YEARBOOK
2019

INSTITUTE OF TECHNICAL PHYSICS AND MATERIALS SCIENCE
CENTRE FOR ENERGY RESEARCH

http://www.mfa.kfki.hu/

Published by
Institute of Technical Physics and Materials Science
Centre for Energy Research

EK MFA Yearbook 2019

Director: Prof. Béla Pécz, D.Sc.

Address: Konkoly-Thege Miklós út 29-33,
H-1121 Budapest, Hungary
Postal: P.O.Box 49, H-1525 Budapest, Hungary
Phone: +36-1-392 2224
E-mail: info@mfa.kfki.hu
URL: http://www.mfa.kfki.hu/

Editor: Krisztina Szakolczai, Ph.D.
Published by: EK MFA, Budapest, Hungary, 2020

Content

GENERAL INFORMATION

Director's foreword

As the director of MFA, it is my pleasure to welcome the reader. I recommend browsing the present yearbook which continues the series of the former ones and contains results achieved in 2019.

2019 was the year when the whole research network of the Academy of Sciences was moved to a separate state owned network Eötvös Roland Research Network (ELKH). The good news is that the structure of institutions was not changed. The bad news is that the salaries remained low and less and less young people join our staff. The new office of the ELKH was set up and created a new research strategy for the whole network with the active participation of the institutions including us. ELKH also requested an increased budget for the network from the state, which is promised by the second half of 2020 by our leaders.

As our institute is a member of World Materials Research Institute we were happy to organise the 8th World Materials Research Institute Forum in Budapest in June 2019. The Forum covered teh following key topics: Advanced Materials for Energy Production, Photovoltaic Materials, Energy Storage Materials, Energy Harvesting Materials and Materials for Quantum Computing. Thanks to the work of our János Volk and many other colleagues the Forum gave an opportunity to meet researchers, industry and funding office leaders.

The International Workshop on Woman in Ceramic Science (WoCeram2019) was organised in Budapest, April 7-9 2019 as well. Beside the scientific talks there was a round table discussion on “Balance between carrier and family in the life of young researchers”. The main organiser of the meeting was our Katalin Balázsi. In both meetings we enjoyed the great help of our Krisztina Szakolczai.

It was an excellent idea of our Péter B. Barna to work on the old 16 mm movies taken some decades ago on crystal growth of element in a transmission electron microscope. By now most of the movies are available in a digital form with the appropriate text. People can now learn the growth, melting and crystallization phenomena of indium, gold, germanium and other elements.

I congratulate to my colleagues: József Gyulai, who was awarded by the Middle Cross with the Star of the Hungarian Order of Merit and István Bársony, who was awarded by the Middle Cross of the Hungarian Order of Merit. We were very happy to learn that our Vilmos Rakovics received the Hungarian Golden Cross of Merit. Csaba Balázsi the prestigious Gábor Dénes prize and József Gyulai received the In Memoriam Gábor Dénes prize.

Then the younger staff of the institute was decorated also very well: Gábor Piszter was awarded by the Junior Prize of the Academy, while Péter Nemes-Incze received the ELFT (Roland Eötvös Physical Society) prize of Zoltán Gyulai for his outstanding results in solid state physics.

We are very proud of our PhD students (Rácz Adél, Ben Zine Haroune, Pósa László, Leelőssyné Tóth Eszter, Fodor Bálint, Furkó Mónika, Oláh Nikolett, Saftics András) who were supervised by colleagues at MFA and defended their thesis successfully in 2019 and got the PhD degree from different universities.

We are also proud of the scientific results achieved by our colleagues, I hope you will enjoy learning them in this book.

Here I note that the former MFA Yearbooks are available electronically at http://www.mfa.kfki.hu/hu/yearbook.

Béla Pécz, D.Sc., Director

Organizational structure

Director: Dr. Béla Pécz, D.Sc.

Scientific Departments	
Thin Film Physics Department	Katalin BALÁZSI, Ph.D.
Complex Systems Department	György SZABÓ, D.Sc.
Photonics Department	Péter PETRIK, D.Sc.
Nanosensorics Laboratory	János VOLK, Ph.D.
Microsystems Department	Péter FÜRJES, Ph.D.
Nanostructures Department and "Lendület" group - 2D Materials	Levente TAPASZTÓ, Ph.D.
"Lendület" group - Topological Nanostructures	Péter NEMES-INCZE, Ph.D.
"Lendület" group - NanoBioSensorics	Róbert HORVÁTH, Ph.D.

Directly supervised functions	
Head of Scientific Advisory Council	János LÁBÁR, D.Sc.
Scientific secretary, projects and PR	Krisztina SZAKOLCZAI, Ph.D.
Quality control, MTMT, REAL admin	Andrea BOLGÁR
Technical support	Károly BODNÁR
Financial administration	Zsuzsanna KELEMEN
Informatics	Gergely TAMÁS
Technology transfer (IPR)	Antal GASPARICS, Ph.D.

Key Financial Figures of MFA

The turnover realised by the institute always reflect the national and international political and financial system and also the efforts of the institute. The domestic subsidies did not change in the last few years; however the overhead increased by approx. 30%. In recent years, there has also been a centrally ordered salary rise for researchers, meanwhile the number of researchers dropped by third in the last 7-8 years.

The recent grants – apart from the fundamental research project – arise from industrial and application driven ideas. Despite all the efforts of colleagues R&D grants require stable strong and research motivated SMEs, which is hard to find in Hungary.

Since 2015 MFA is part of the Centre of Energy Research. The financial operation is only partly transparent, therefore the data shown here for 2015-2019 for MFA are based upon our own estimates.

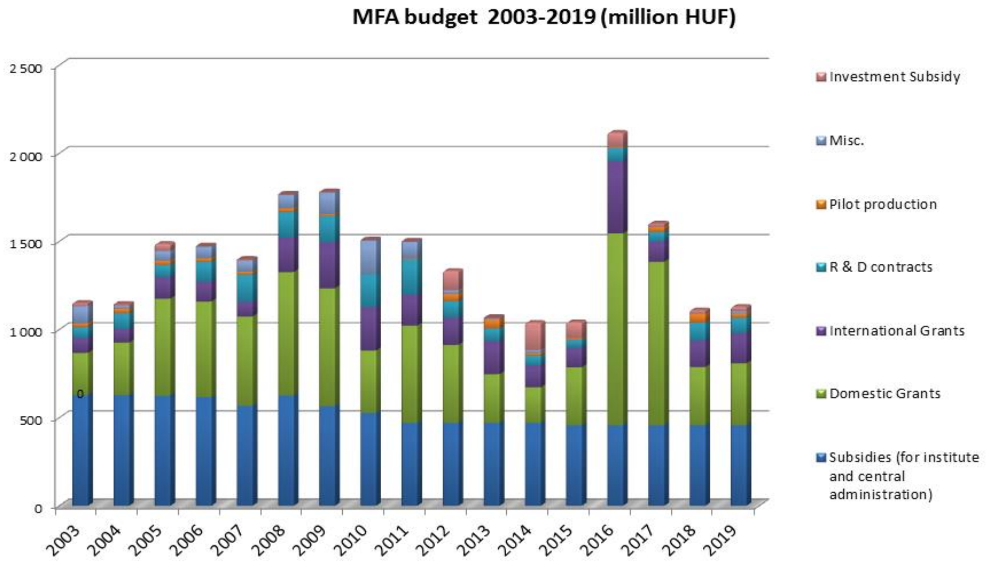
MFA budget 2003-2019 (million HUF)

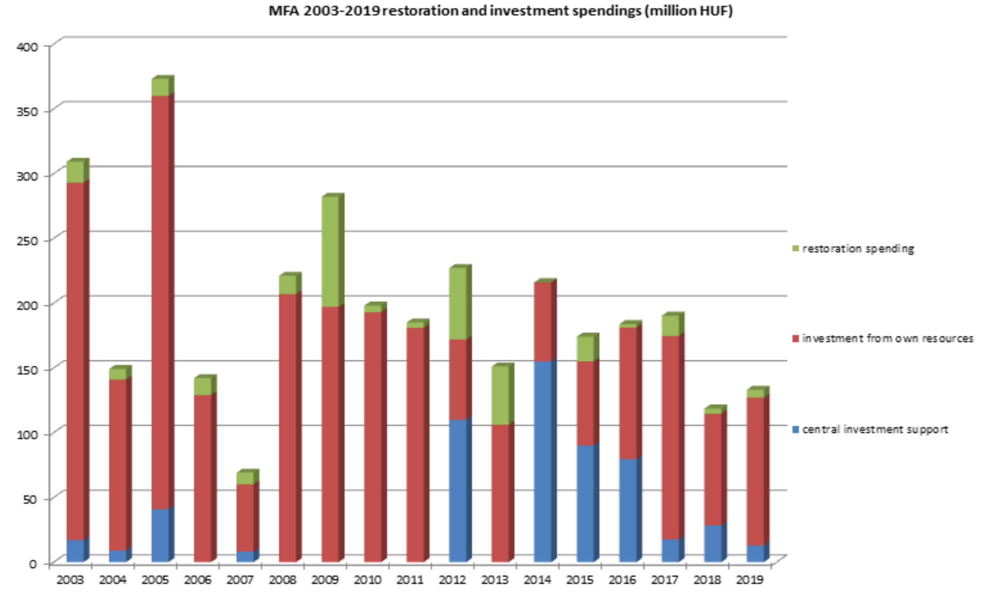
MFA 2003-2019 restoration and investment spendings (million HUF)

Publications and Citations of MFA

According to the Thomson-Reuters ISI "Web of Knowledge", and MTMT2 databases, the Institute has an average publication activity of ca. 100 scientific papers in IF journals a year. The number decreased a bit in the last years, but recently MFA researchers publich in journals with higher impact factor.

MFA and its predecessor's publications

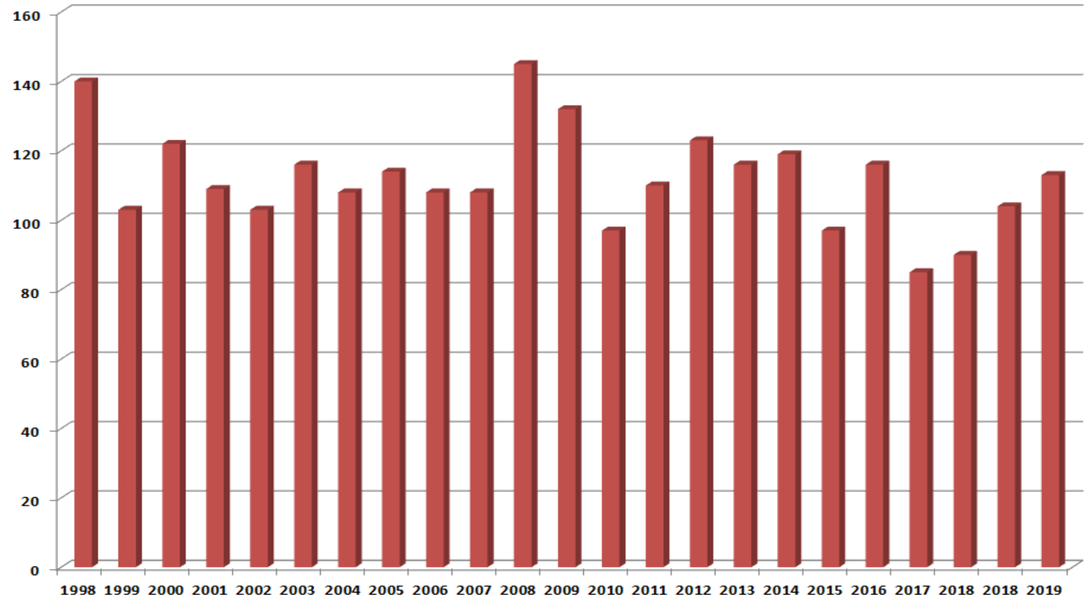

MFA and its predecessor's citations

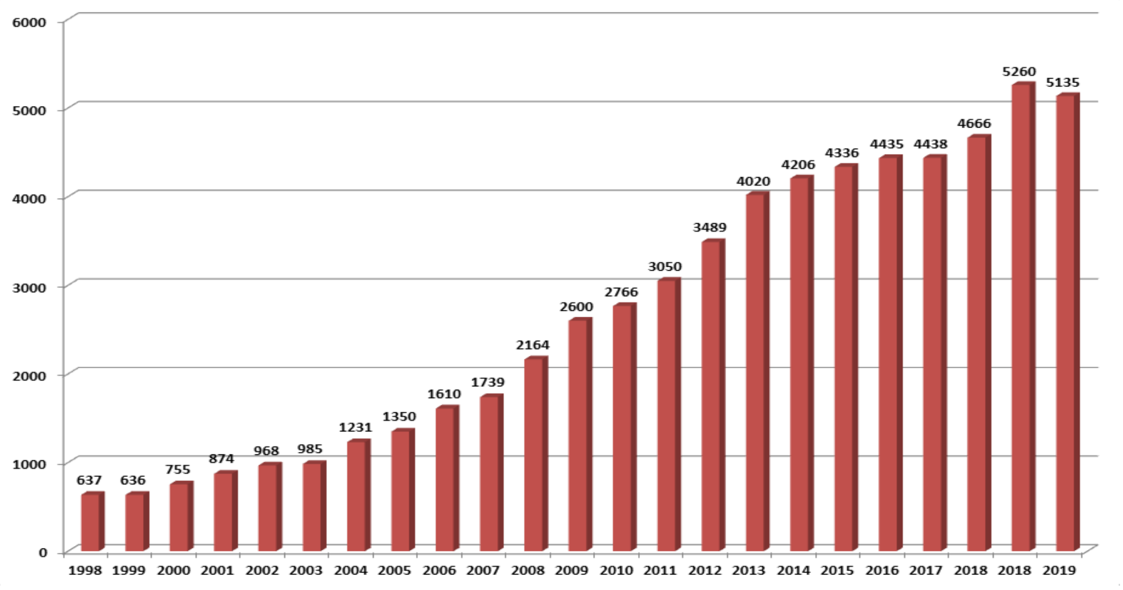

Prizes and Distinctions

	**GYULAI, József**	Order of Merit of the Republic of Hungary Commander's Cross with Star
	**BÁRSONY, István**	Order of Merit of the Republic of Hungary Commander's Cross
	**RAKOVICS, Vilmos**	Order of Merit of the Republic of Hungary Golden Cross
	**BIRÓ, László Péter**	Ordinary member of the Hungarian Academy of Sciences
	**GYULAI, József**	Gábor Dénes Prize
	**BALÁZSI, Csaba**	Gábor Dénes Prize
	**PISZTER, Gábor**	Young researcher award of the Hungarian Academy of Sciences

	**PÉTER, Beatrix**	Young researcher award of the Centre for Energy Research
	**PISZTER, Gábor**	Young researcher award of the Centre for Energy Research
	**NEMES-INCZE, Péter**	ELFT Gyulai Zoltán prize
	**SZOLNOKI, Attila**	Web of Science Highly cited researcher – cross-field
	**RÁCZ, Adél Sarolta**	MFA prize (young researcher)
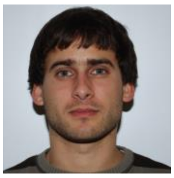	**VANCSÓ, Péter**	MFA prize (postdoctoral)
	**FOGARASSY, Zsolt**	MFA prize (postdoctoral)

President of Hungary János Áder awards Dr. József Gyulai with Order of Merit of the Republic of Hungary Commander's Cross with Star - in recognition of his internationally outstanding scientific achievements in the field of nanostructured semiconductor materials research, his work as a university professor helping the scientific development of younger generations, and his significant scientific organizing activities

President of Hungary János Áder awards Dr. István Bársony with Order of Merit of the Republic of Hungary Commander's Cross - in recognition of his outstanding international work in the field of research and innovative application of functional materials, as well as in recognition of his success in organizing the research field and in educating the next generation of research engineers.

Dr. Vilmos Rakovics received Order of Merit of the Republic of Hungary Golden Cross from Professor László Palkovics, Minister of Innovation and Technology on the occasion of March 15 National Day.

The Young researcher award of the Hungarian Academy of Sciences award was presented by President László Lovász to Gábor Piszter for his work titled "Investigation and application of photonic nanoarchitectures in butterfly scales"

Important events in 2019

MFA Organized the World Materials Research Institutes Forum (WMRIF) Symposium and General Assembly (12-17 June, 2019), chaired by Dr. János Volk. The event was held at the main building of the Hungarian Academy of Sciences. The leaders of the materials research institutes also visited our laboratories.

International Workshop on Women in Ceramic Science (7-9 April, 2019), was organized and co-chaired by Dr. Katalin Balázsi and Dr. Csaba Balázsi.

Girl's day with almost 60 participants from the high schools was held in April 2019, and was organized by Dr. Katalin Balázsi

MFA appeared with its own exhibition stand at the ELECTROSUB conference. Colleagues introduced the R&D achievements on medical and automotive micro- and nanotechnology sensors field.

SCIENTIFIC REPORTS

Highlight of the year

Non-destructive evaluation (NDE) system for the inspection of operation-induced material degradation in nuclear power plants

EU H2020 NFRP-2016-2017-1 -755330 „NOMAD”

A. Gasparics and G. Vértesy

The long-term operation (LTO) of existing nuclear power plants (NPPs) has already been accepted in many countries as a strategic objective to ensure adequate supply of electricity over the coming decades. In order to estimate the remaining useful lifetime of NPP components, LTO requires reliable tools. The objective of NOMAD project is the development, demonstration and validation of a non-destructive evaluation (NDE) tool for the local and volumetric characterization of the embrittlement in operational reactor pressure vessels (RPVs). In order to address these objectives, the following steps should be taken: Development and demonstration of an NDE tool for the characterization of RPV embrittlement; Extension of the existing database of RPV material degradation by adding correlations of mechanical, microstructural and NDE parameters; and application of the developed tool to Charpy geometry samples and also to cladded material resembling the actual RPV inspection scenario.

The MFA contributes to the NOMAD project with own micromagnetic testing method: so called Magnetic Adaptive Testing (MAT). MAT is a recently developed method for nondestructive characterization of ferromagnetic materials, which is based on systematic measurement and evaluation of minor magnetic hysteresis loops. This method is being tested and evaluated regarding its applicability for the determination of the material changes and the variation of the material properties during exposure to neutron irradiation. As shown in our several previous research activities, MAT provides more sensitivity for material degradation than the major hysteresis loop and has an improved feature of measurement error suppression. An additional significant advantage of this method is that there is no need for magnetic saturation of the measured samples, which eases the practical application.

MAT measurements were performed on reactor steel material before and after neutron irradiation and the nondestructively determined magnetic parameters were compared with the destructively measured ductile-to-brittle transition temperature (DBTT) values. Standard Charpy specimens from 22NiMoCr37 type base and from 18MND5 type weld materials were measured. These steel grades are members of the typical RPV steel groups: Mn-Ni-Mo steels (western RPV design). The samples were prepared, irradiated and measured at the Belgian Nuclear Research Centre (SCK•CEN). The samples were irradiated there in the BR2 reactor at 260 ^{o}C temperature by E>1 MeV energy fast neutrons with total neutron fluence in the range of $4.02\text{x}10^{19} – 8.95\text{x}10^{19}$ n/cm^2. Since irradiated samples are radioactive, they can be measured only in hot cell laboratories. A special sample holder was designed and built for this purpose. Charpy impact testing (ASTM-23-16b) was used to determine the 41 Joule transition temperature (T_{41J}). The transition temperature shift (ΔDBTT) is the difference between the neutron irradiated T_{41J} and the as-received (base-line) T_{41J} which is a measure for the embrittlement of the material. In the following figures the correlation between optimally chosen MAT descriptors and the transition temperature shift are shown for the two types of Charpy specimens. MAT descriptors are normalized by the correspondig parameter of the reference (not irradiated) sample. Those parameters were chosen from the calculated big datapool, which characterize most sensitively and at the same time most reliable the material degradation (optimally chosen MAT descriptors).

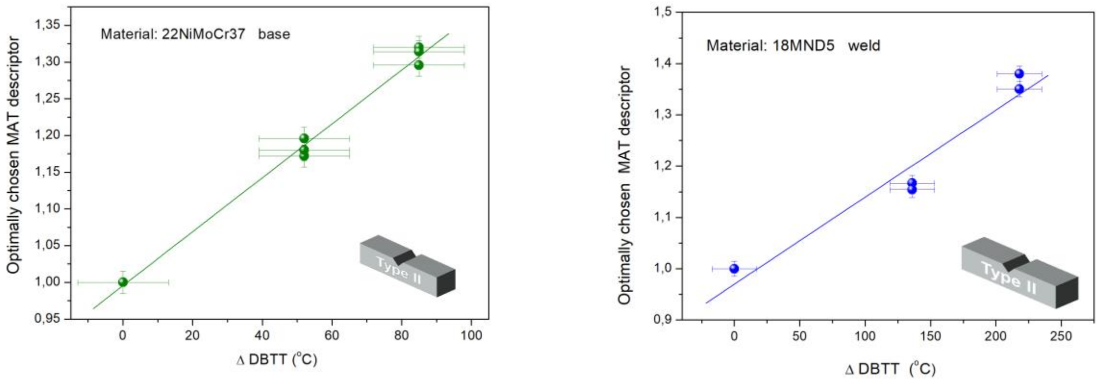

Figure 1.1. *Optimally chosen normalized MAT descriptor as a function of the transition temperature shift for a 22NiMoCr37 type base material and (right) for a 18MND5 type weld material, measured on Charpy samples.*

A linear correlation was found between magnetic parameter and neutron fluence. About 30% increase at 3% error level of the MAT descriptor was detected due to 6x10^{19} n/cm^2 neutron fluence in case of the base material, compared with the not irradiated sample; and close to 40% increase at 5% error level due to 8.5x10^{19} n/cm^2 neutron fluence in case of the weld material. The influence of neutron irradtion is refleceted on the shift of transition temperature, as shown in Fig. 1.1. The linear fit on the measured points is to lead the eye to reflects more visible the character of the correlation. It does not reflect a strict mathematical fitting, because of the limited number of measured points.

In another series of experiments clad and underclad block specimens made of 15H2NMFA material were measured. Blocks were cut from the forged ring as shown in Fig. 1.2. The size of blocks was 115mm x 50mm x 50mm. Cladding (7-10 mm thick) was on the top of the blocks. The clad surface of the real pressure vessels is usually made by submerged strip welding (a special way of the submerged arc welding) in three layers. The surface is either grinded, or roughly machined to provide coupling for the ultrasonic testing. The samples were aged by thermal treatments using a special step cooling technology (details are not given here) used for accelerated evaluation of thermal ageing sensitivity. The main consideration at the selection of the thermal treatment was to produce similar microstructural changes of which occurs at irradiation.

Two types of step cooling were performed, which resulted different material degradations controlled by transition temperature determination. MAT measurements were performed on the clad and underclad blocks. Both sides of the blocks were measured. Regular loops with large amplitude were experienced on base (highly ferromagnetic) material. The situation is different on the top side, which is covered by cladding. Cladding is an austenitic, almost paramagnetic material, which means practically a large air gap between magnetizing yoke and ferromagnetic part of sample. Because of this a very weak magnetic signal was found.

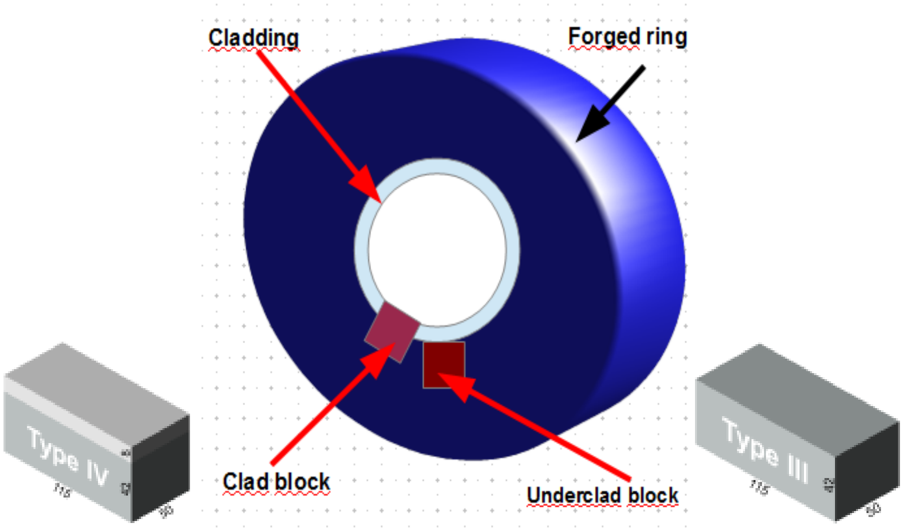

Figure 1.2. Cutting of claded and uncladded blocks from forged ring.

The correlation between MAT parameters and transition temperature in case of blocks is shown in Fig. 1.3. Again excellent, almost perfect linear correlation was found between MAT parameters and transition temperature even if the measurement is performed through the cladding.

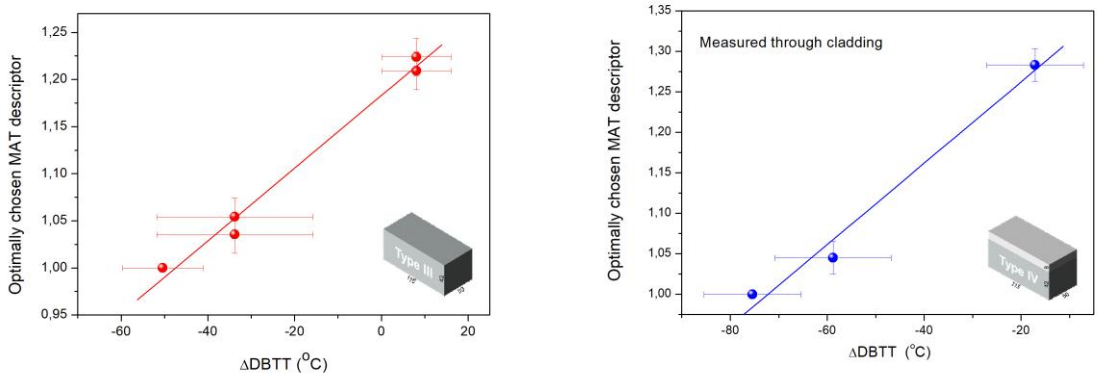

Figure 1.3. *Correlation between normalized MAT parameters and transition temperature, measured directly on base material (left) and on cladding (right).*

An important and novel result of the present work is, that the ferromagnetic base material can be inspected even through the relatively thick cladding, and the measurement through the cladding result the same correlation between magnetic parameters and independent variable as obtained by direct measurement of base material. This fact proves the unique applicability of MAT in nondestructive inspection of degradation of nuclear pressure vessel material.

Another fact, worth of mentioning is, that the error of magnetic measurement is significantly lower than the error of destructive Charpy measurement, which is clearly seen on the above graphs. So magnetic measurement is not only non destructive, but – perhaps – it provides even more precise value about material degradation, than Charpy impact test.

Nanostructures Laboratory

Head: Dr. Levente TAPASZTÓ, Ph.D. research fellow

Research Staff:

- Zsolt Endre HORVÁTH, D.Sc, Deputy Head of Laboratory
- Prof. László Péter Biró, Member of the HAS
- Gergely DOBRIK, PhD
- Krisztián KERTÉSZ, Ph.D
- Antal Adolf KOÓS, Ph.D.
- Géza István MÁRK, Ph.D.
- Péter NEMES-INCZE, Ph.D.
- Zoltán OSVÁTH, Ph.D.
- Gábor Piszter, Ph.D.
- Péter SÜLE, Ph.D
- Péter VANCSÓ, Ph.D.

Ph.D. students:

- Péter KUN Ph.D. student
- András PÁLINKÁS, Ph.D. student
- János PETŐ, Ph.D. student
- Márton SZENDRŐ, Ph.D. student

The research activity of the Nanostructures Laboratory is based on the two-decade-long expertise in the synthesis, characterization and engineering of various nanostructures using scanning probe microscopy as the main experimental technique. Since more than a decade, our research efforts are focused on the investigation of two-dimensional materials. Besides graphene, in the last couple of years, novel 2D materials, mainly form the family of transition metal chalcogenides (TMC) have been intensely studied. Recently, we have further extended our activity with the investigation of layered topological insulator crystals. We have also successfully continued our research on bioinspired photonic nanoarchitectures.

The most notable scientific achievement during 2019 was the publication of an invited perspective article in ACS Energy Letters, on the potential of 2D transition metal chalcogenide crystals to provide an efficient platform for realizing single atom catalysts. Notable distinctions have also been awarded to members of the Nanostructures Department: László P Biró has been elected as full member of the Hungarian Academy of Sciences, as well as Fellow of Academia Europeea, Péter Nemes-Incze received the Zoltán Gyulai prize of the Roland Eötvös Physical Society, and Gábor Piszter was awarded with the Junior Prize of the Hungarian Academy of Sciences.

Transition metal chalcogenide single layers as an active platform for single-atom catalysis

680263-NanoFab2D-ERC-2015-STG, LP2014-14 Lendület , LP2017-9 Lendület, OTKA KH130413, VEKOP-2.3.2-16-2016-00011, Korea-Hungary Joint Laboratory

P. Vancsó, Z. I. Popov (MISiS), J. Pető, T. Ollár, G. Dobrik, J. S. Pap,
C. Hwang (KRISS), P. Sorokin (MISiS), L. Tapasztó

Among the main appeals of single-atom catalysts are the ultimate efficiency of material utilization and the well-defined nature of the active sites, holding the promise of rational catalyst design. A major challenge is the stable decoration of various substrates with a high density of individually dispersed and uniformly active monatomic sites. Transition metal chalcogenides (TMCs) are broadly investigated catalysts, limited by the relative inertness of their pristine basal plane. In this work we proposed that TMC single layers modified by substitutional heteroatoms can harvest the synergistic benefits of stably anchored single-atom catalysts and activated TMC basal planes. These solid-solution TMC catalysts offer advantages such as simple and versatile synthesis, unmatched active site density, and a stable and well-defined single-atom active site chemical environment. Furthermore, 2D crystal substrates are highly convenient, as they can be easily investigated by direct atomic resolution imaging techniques such as high-resolution transmission electron microscopy or scanning tunneling microscopy (STM). Fig. 2.1 shows an example of resolving the individual heteroatom (oxygen) sites embedded into MoS_2 single layer revealed by STM. The sample has been prepared by annealing the exfoliated single layer at 130°C in air for a week.

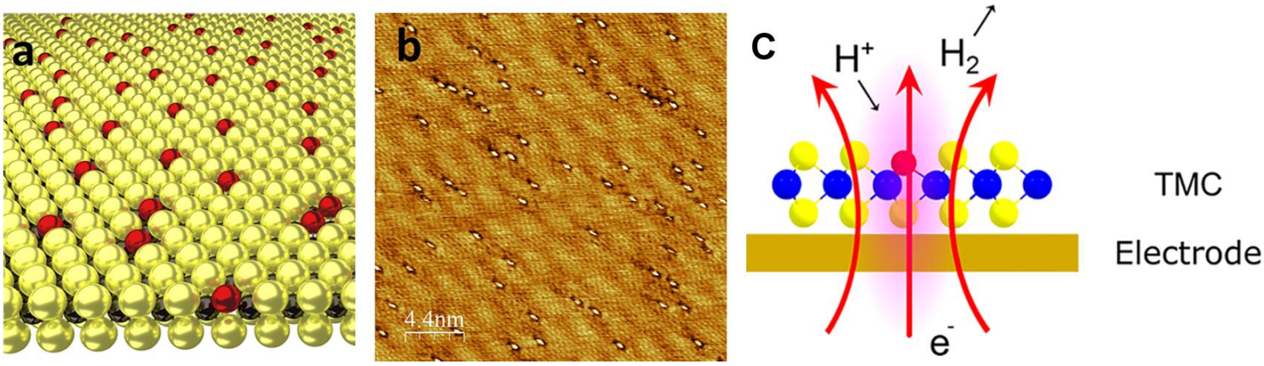

***Figure 2.1**. (a) Schematic model of individually dispersed heteroatoms substituting chalcogenide atoms of 2D transition metal chalcogenide crystals. (b) The practical realization of such structures evidenced by atomic resolution STM images of oxygen-atom-doped MoS_2. (c) Schematic model of the hydrogen evolution reaction in the presence of the heteroatom.*

In order to understand the potential mechanisms responsible for the increased catalytic activity of heteroatoms incorporated by substitution in various TMC crystals (Fig. 1c), we performed DFT calculations for different TMC single layers (2H− MoS_2, $MoSe_2$, $MoTe_2$,WS_2, WSe_2, WTe_2) and investigated the role of oxygen heteroatoms in catalyzing the hydrogen evolution reaction. We observed several common properties related to the catalytic activity of the different TMC single layers.

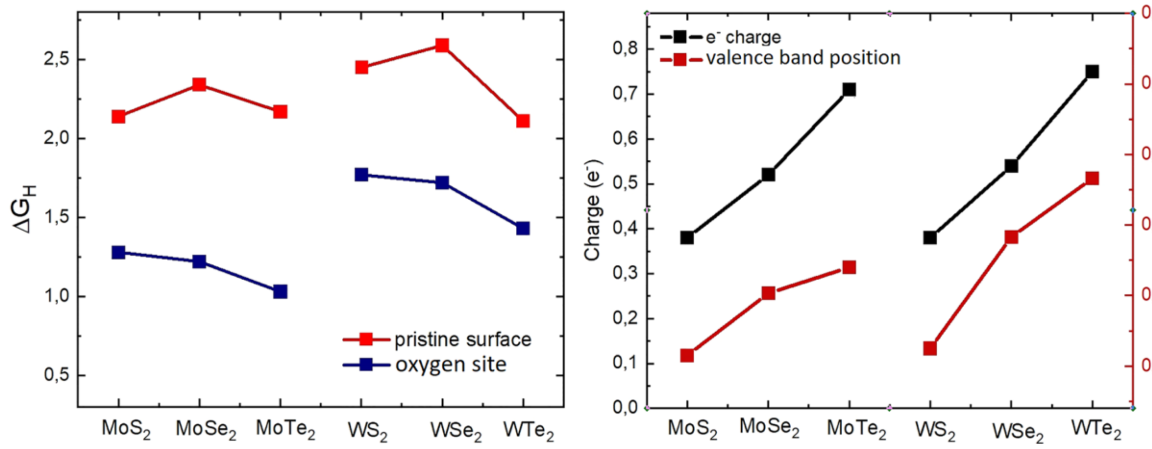

Figure 2.2. *(left) Hydrogen adsorption Gibbs free energy on the basal plane chalcogen sites (red) and O substitution sites (blue). (right) Electron charge surplus on the O sites relative to pristine chalcogen atom sites and the position of the valence band at the Γ point of the Brillouin zone relative to Fermi level for various 2D TMC crystals with O substitution sites.*

First, decreased hydrogen adsorption potential on the oxygen atoms (Fig. 2.2.left) has been calculated from the change of the H atom adsorption Gibbs free energy (ΔG_H), which is a widely used descriptor for the catalytic activity. Second, negatively charged oxygen atoms has been obtained from Bader charge analysis (Fig. 2.2.right), where such negative charges can provide an additional attractive interaction for the positively charged H species, facilitating their adsorption. Finally, increased transversal conductivity around the oxygen atom was revealed resulting an efficient transverse electron transfer for the catalytic process. In the latter case, we found that the presence of oxygen atoms locally enhances the z-like character of the atomic orbitals around the Fermi-level, as it can be seen in the local density of states (LDOS) iso-surface plot (Fig. 2.3). This induces an enhanced overlapping of the O, S, and Mo orbitals, opening sub-nanometer wide transverse conduction channels in the direction perpendicular to the sheet.

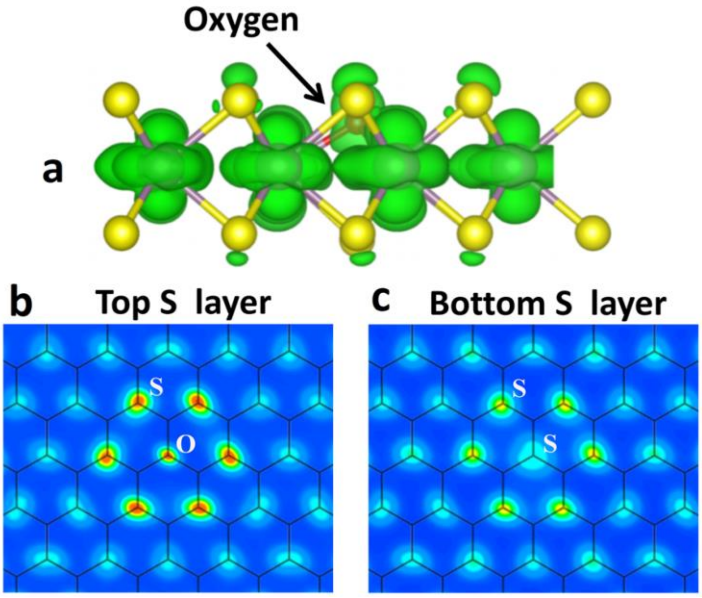

Figure 2.3. *Electronic density of states redistribution near the O substitution site in MoS_2 single layer. In-plane view of the S layers highlighting increased electron density on the nearest neighbor S atoms.*

In conclusion, 2D solid solution TMCs with identical active sites emerge as an excellent platform for single-atom catalysis, where the fully characterized atomic and electronic structure are also expected to provide a new model system for understanding single-atom catalysis.

Visible-frequency graphene plasmons in extremely nanocorrugated graphene sheets

680263-NanoFab2D-ERC-2015-STG, LP2014-14 Lendület, LP2017-9 Lendület

G.Dobrik, P. Nemes-Incze, P. Süle, P. Vancsó, G. Piszter, L. Tapasztó

Graphene plasmons – hybrids of Dirac fermions and photons - are particularly appealing due to their unmatched mode volume confinement, long lifetime and easy tunability. To fully exploit these unique properties, visible-frequency graphene plasmons are desirable, given that our most efficient optical techniques are available for visible light. However, tuning up the resonance frequency from native THz values into the visible range turned out particularly challenging. It has been proposed that graphene structures below 10 nm characteristic size, can scale up plasmon frequencies into the visible. However, this approach is strongly limited by the detrimental effects of edges on plasmon resonances. We have demonstrated the realization of visible graphene plasmons through their edge-free lateral confinement into sub-5 nm graphene nanocorrugations with particularly high aspect ratios. Such graphene sheets with strong nanoscale corrugations were prepared by cyclic thermal annealing between RT and ~400°C. The RMS value characterizing the surface roughness is about 0.5 nm, which is almost the double of the RMS value measured in graphene on SiO_2 (0.27 - 0.35 nm).

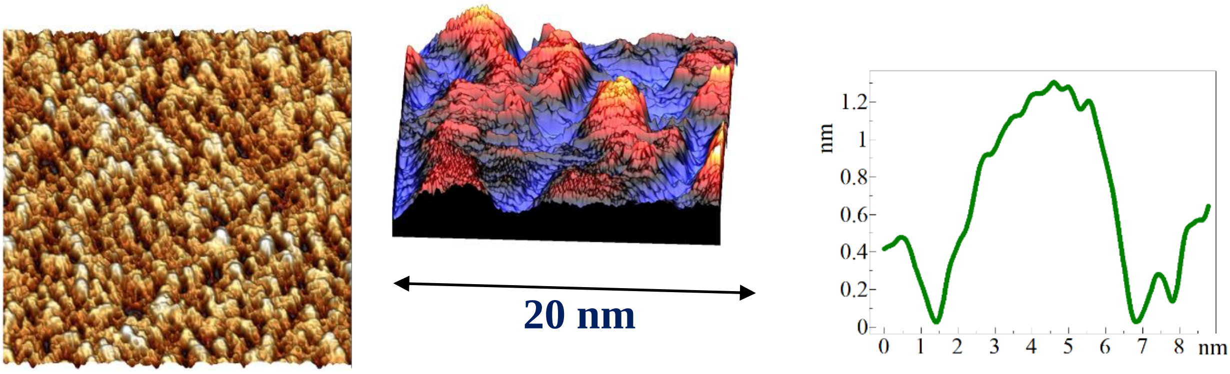

Figure 2.4. *The structure of nanobuckled graphene sheets. STM images of graphene sheets prepared by cyclic thermal annealing displaying a particularly strong nanoscale corrugation, with lateral size below 10 nm, and nanometer height. Line cut displaying a typical graphene nanocorrugation geometry with an aspect ratio of* $h_{max}/R \sim 0.5$.

Graphene corrugations with aspect ratios (h_{max}/R) as high as 0.5 could be easily found. These numbers clearly highlight the extreme nature of the nanoscale deformation (corrugation).The most striking findings were observed when measuring the Raman spectra of corrugated graphene sheets with 633 nm excitation wavelength. Such measurements revealed a huge Raman signal, only by exposing the samples to laboratory air (Fig.2.5.b). Detecting Raman peaks with 20 times higher intensity than the G peak of graphene by only air exposure is truly remarkable, and indicates a strong and robust underlying phenomenon. The huge Raman signal picked up from air, was identified as the fingerprint of copper phthalocyanine (CuPc) molecules. As expected, exposing quasi-flat graphene sheets to the same conditions (i.e. air) does not result in any detectable CuPc signal in the Raman spectra.

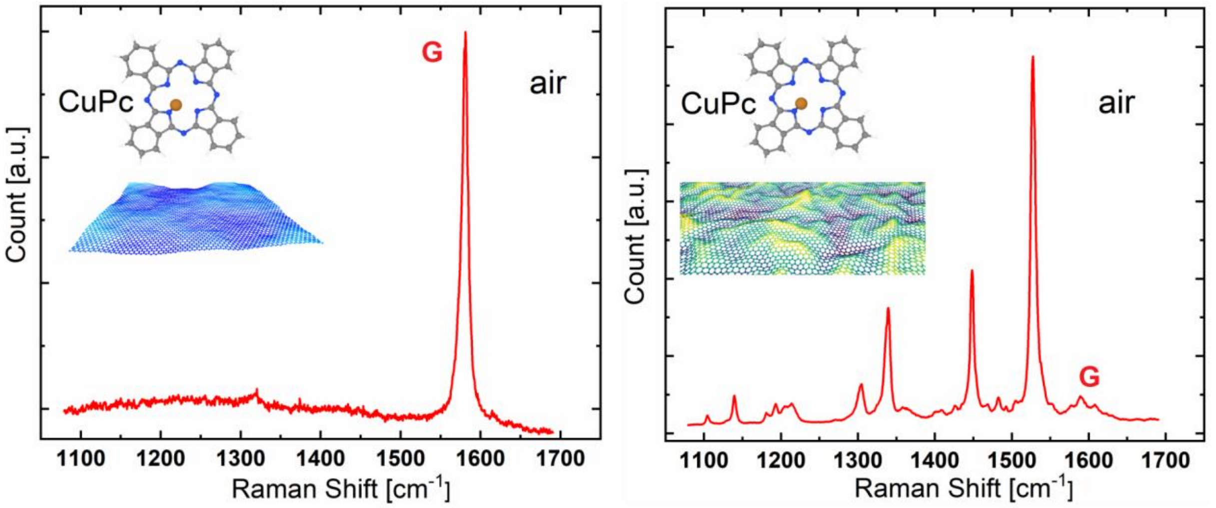

Figure 2.5. *(right) Huge Raman enhancement on nanocorrugated graphene sheets. Detection of CuPc molecules from "clean" air by nanocorrugated graphene sheets. (left)The Raman spectrum of quasi-flat graphene subjected to the same conditions is shown for reference.*

To gain insight into the origin of the increased optical response, we have calculated the electron energy loss spectrum of nanocorrugated graphene that directly reveals plasmon peaks. As apparent in Fig.2.6. several peaks appear in the calculated EELS spectra that can be associated with plasmons or quasi-plasmons of energies in the visible range.

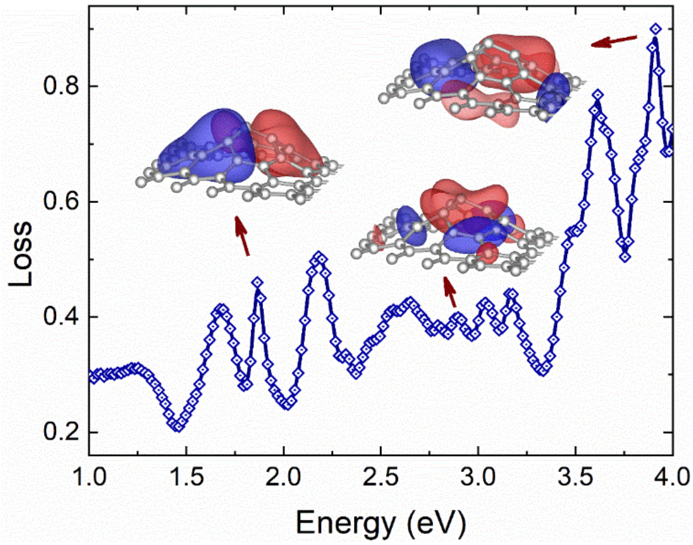

Figure 2.6. *Plasmonic excitations in nanocorrugated graphene. Calculated EELS spectrum of a model graphene nanocorrugation, revealing several loss peaks in the visible range. The insets display the charge distributions of optical excitations corresponding to different loss peaks.*

We have demonstrated the realization of visible graphene plasmons through their edge-free lateral confinement into sub-5 nm graphene nanocorrugations. The emerging strong near-fields of localized visible graphene plasmons provide such exceptional Raman enhancements that enable the detection of specific molecules even from "clean" air. This enormously enhanced interaction of molecules adsorbed on nanocorrugated graphene with visible light opens the way towards highly efficient and tunable SERS substrates and quantum emitters.

Ultra-flat twisted superlattices in 2D heterostructures

680263-NanoFab2D-ERC-2015-STG, LP2014-14 Lendület, LP2017-9 Lendület, Korea-Hungary Joint Laboratory

M. Szendrő, P. Süle, G. Dobrik, L. Tapasztó

When 2D materials are layered on top of each other an interference pattern called the Moiré-pattern is formed due to the lattice mismatch and relative rotation between the layers. Moiré-patterns already host a large variety of exciting physical phenomena e.g.: secondary Dirac cones, Hofstadter's butterfly, superconductivity. However, the corrugation stemming from the pattern is still a largely unexplored field and is lacking a comprehensive theoretical description. The way 2D heterostructures relax strain through out-of-plane deformation can highly influence the properties of such systems. The commonly accepted picture is that the corrugation is a monotonically decreasing function of the twist angle.

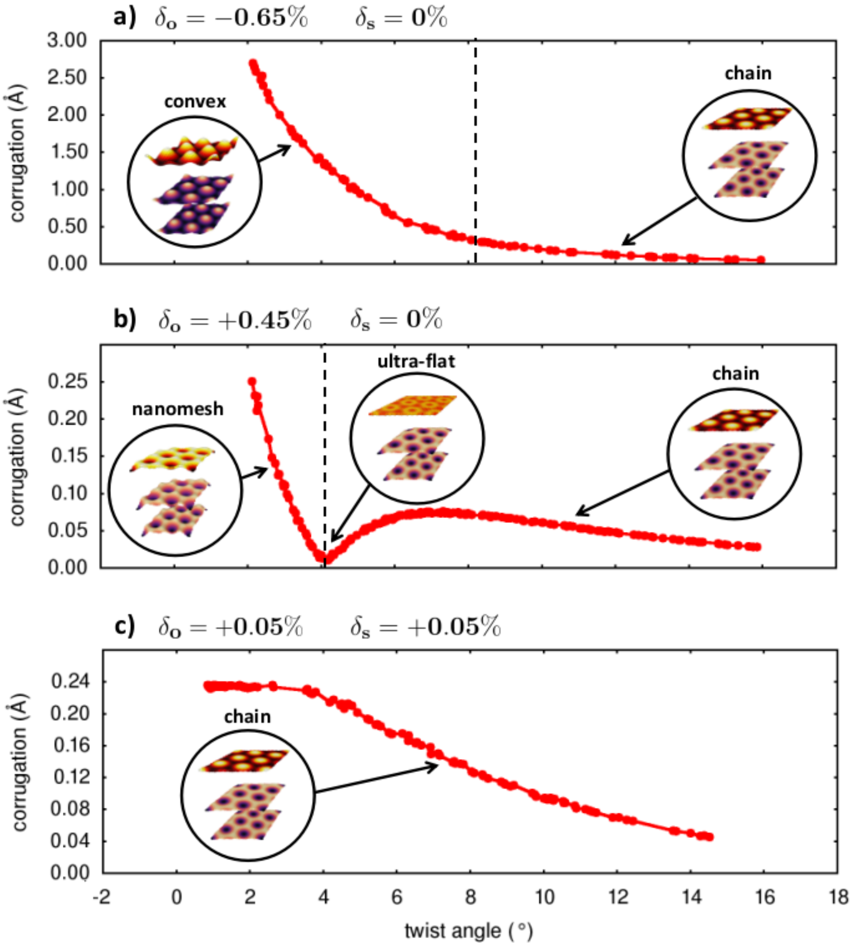

Figure 2.7. *Moiré-superlattice corrugations of the top rotated graphene layer for three differently strained 5-layer graphene systems from molecular mechanics simulations. a) The overlayer is externally compressed with ~0.65% which leads to a convex phase for angles below 8.2° and a chain phase for angles above. b) The overlayer is stretched with ~0.45% strain, inducing a nanomesh phase for angles below 4°, and a chain phase above. Near the phase transition (dashed line), the corrugation vanishes and an ultra-flat phase appears. c) Both overlayer and substrate are stretched with 0.05%. In the range of 0-4° The corrugation is closely constant (plateau-effect).*

Here we found by lattice relaxation of around 8000 different Moiré-superstructures using high scale Classical Molecular Simulations combined with analytical calculations, that even a small amount of strain can substantially change this picture, giving rise to more complex behavior of superlattice corrugation as a function of twist angle. One of the most surprising findings is the emergence of an ultra-flat phase that can be present for arbitrary small twist angles having a much lower corrugation level than the decoupled phase at large angles. A possible experimental realization of the ultra-flat state is revealed by Scanning Tunneling Microscopy (STM) investigations of the graphene/graphite system.

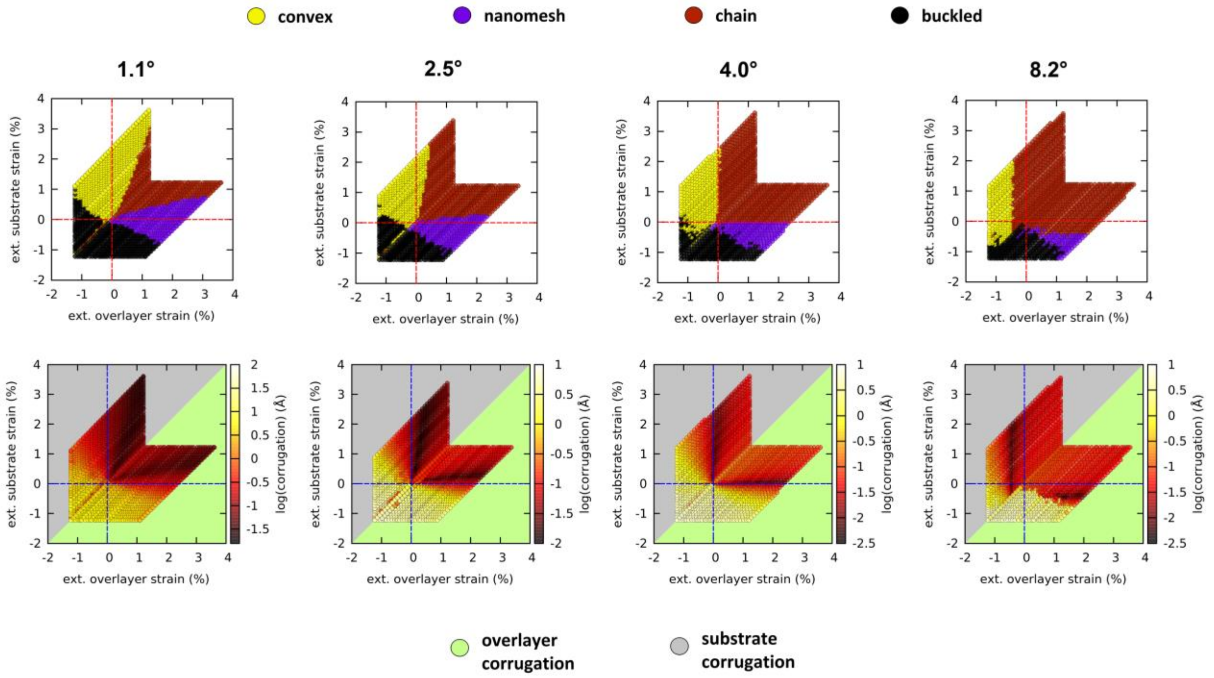

__Figure 1.8.__ Top row: Moiré-phases of the twisted trilayer graphene system for different twist angles in the space of externally applied homogeneous strains (phase-maps). The corresponding Moiré-phases are indicated with different colors (yellow - convex, purple - nanomesh, red - chain). Bottom row: The same phase-maps but colored by the corrugation of the relaxed Moiré-superlattices. The dark areas show the ultra-flat states around the phase boundaries.

We have prepared and analyzed graphene layers deposited at various rotation angles on graphite substrates. We measured the rotation angle, Moiré-periodicity, as well as the Moiré amplitude for various rotation angles. We were able to find a graphene flake where the corrugation was very low, almost undetectable at an intermediate (9°) rotation angle. Consequently, the graphene flake displayed in Fig. 3 b) can be regarded as an experimental realization of an ultra-flat state predicted theoretically, although the exact parameters (heterostrain values) could not be directly inferred.

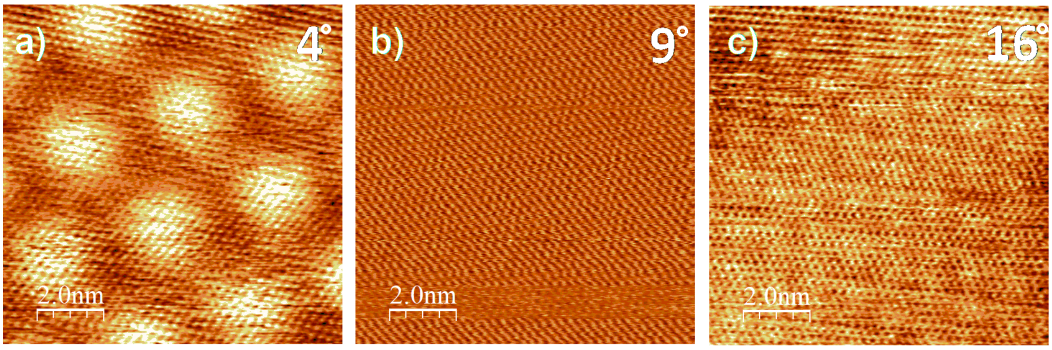

Figure 2.9. *Topographic scanning tunneling microscope images of graphene layers deposited on top of a graphite substrate for various relative rotation angles. The STM image in panel (b) reveals an ultra-flat state, much smoother than observed even for high rotation angles (c). The experimental conditions for image acquisition (*$I_{tunnel} = 1nA$*,* $U_{bias} = 200mV$*), data processing, and graphic display parameters are the same for all panels.*

Anisotropic strain effects in small-twist-angle graphene on graphite

OTKA K119532, OTKA KH129587, Korea-Hungary Joint Laboratory

M. Szendrő, A. Pálinkás, P.Süle, Z.Osváth

Graphene and other two-dimensional (2D) materials are intensively studied from the perspective of building new van der Waals heterostructures by stacking one layer on top of the other. The interaction between stacked 2D layers affects the resulting electronic properties. Already the interaction between two superimposed graphene layers implies rich physics. Moiré patterns can appear when two similar crystalline layers are superimposed, with a spatial period depending on the misfit and the rotation angle between the lattice parameters of the two layers. This moiré superstructure introduces not only a slight geometric corrugation in graphene, but also modulates the local density of states (LDOS). Graphene layers superimposed with small twist angle (~1°) are of peculiar interest due to the decreased Fermi velocity, charge localization, the emergence of flat electronic bands, electron-electron interaction, and also due to the appearance of unconventional superconductivity and correlated insulator behavior.

We have investigated a small-twist-angle (0.64°) graphene on highly oriented pyrolytic graphite (HOPG) by scanning tunneling microscopy (STM) and show that the measured moiré superstructure reflects a locally strained graphene with anisotropic variations of the lattice parameter (Fig. 2.10.).

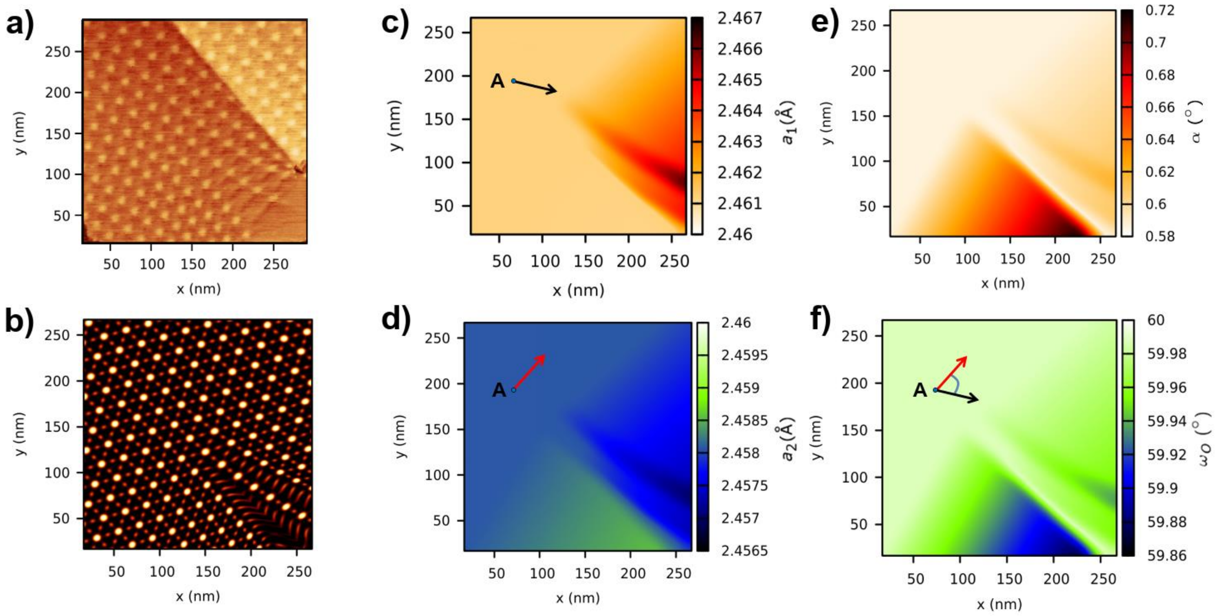

***Figure 2.10**. a) STM image of the moiré pattern. b) Simulated moiré pattern. c)-f) Spatial distributions of the following parameters: c) length of a_1 lattice parameter, d) length of a_2 lattice parameter, e) the twist angle α between the graphene and the HOPG, f) the angle between a_1 and a_2, ω_0. The directions of a_1 and a_2 are marked in point A by black and red vectors, respectively.*

The observed moiré pattern was reproduced by simulation using a rigid lattice Fourier method. The dI/dU spectra obtained from tunneling spectroscopy (STS) measurements (Fig. 2.11.a) show a slightly *p*-doped graphene with the Dirac point at $U_D \cong 50\ mV$, as observed from the spectrum measured in a moiré valley (black line). In contrast, the dI/dU measured on moiré hills reveal significantly higher LDOS near the Dirac point.

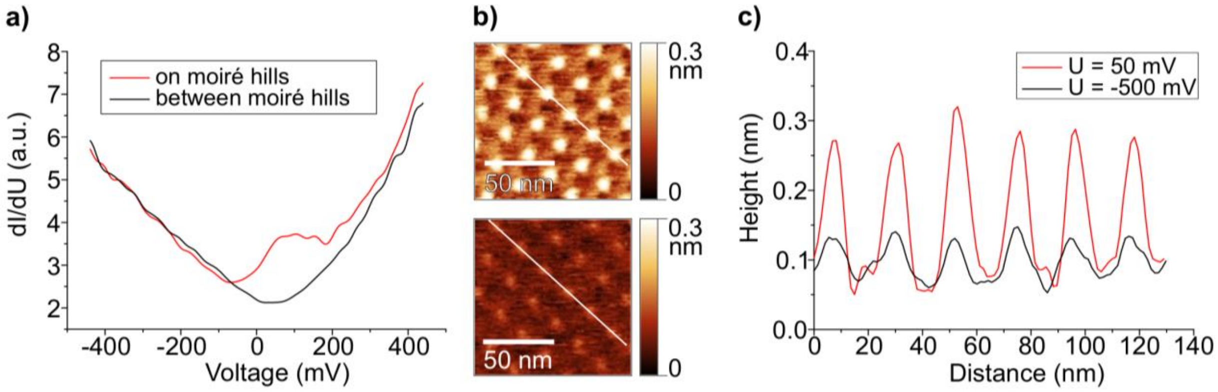

Figure 2.11. *(a) dI/dU spectra measured on moiré hills (red curve) and moiré valleys (black curve). (b) STM images of the same moiré pattern measured with bias voltages of U = 50 mV (top panel) and U = -500 mV (bottom panel). (c) Height profiles taken at U = 50 mV (red) and U = -500 mV (black) along the same moiré hills, marked with white lines in b).*

In order to understand in more detail the observed LDOS peak, DFT calculations have been carried out for trilayer graphene (TLG) supercells with AAB and ABA stackings (pre-optimized by classical molecular dynamics - CMD simulations), which take into account also the uppermost two layers of the HOPG substrate. Full self-consistency calculations performed on AAB-TLG supercell resulted in a band structure as shown in Fig. 2.12.b. The corresponding DOS calculations (Fig. 2.12.a, red) show a double-peak feature near the Dirac point. Note that the DOS of ABA-TLG is featureless near the Fermi energy (Fig. 2.12.a, black). These results capture very well the peak localization in the AA stacked regions and are in good agreement with the measurements, although the peak splitting is not well resolved by room temperature STS. In addition, we performed also a constrained, Harris-functional-like DFT calculation for the full CMD pre-optimized, moiré commensurate bilayer (MCB) supercell, including 33076 atoms at 0.63 twist angle. No peak splitting occurs in the obtained DOS (Fig. 2.12.a, dotted) due to the mixed effect of differently stacked regions.

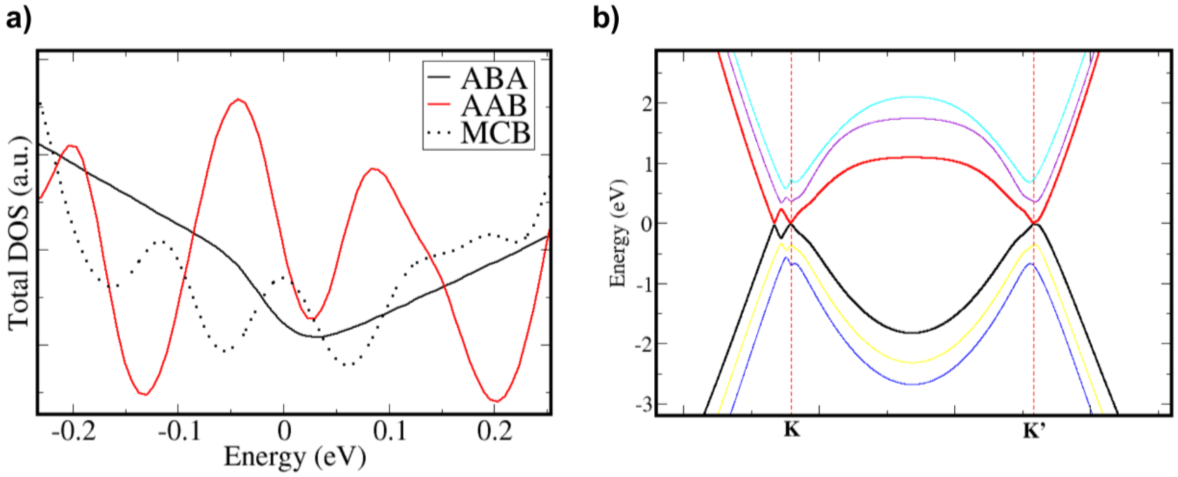

Figure 2.12. *(a) DFT calculations of total DOS for ABA-TLG (black), AAB-TLG (red), and MCB supercell (dotted) at twist angle of 0.63. (b) Calculated band structure for AAB-TLG.*

Optical detection of vapor mixtures using structurally colored butterfly and moth wings

OTKA K111741, OTKA K115724

G. Piszter, K. Kertész, Zs. Bálint, and L. P. Biró

The efficient detection of volatile organic compounds in current applications is highly needed as monitoring air quality in the living environment is becoming increasingly important. The multivariate sensors, based on the photonic nanostructures of butterfly wings, are excellent candidates for this task as their optical readout is relatively easy and their response time is short, while they can operate in ambient air without high operating temperature or vacuum conditions. The sensing process is based on the capillary condensation of the vapors, which results in the conformal change of the chitin-air nanostructures and leads to substance-specific color change signal.

We investigated the optical responses of structurally colored wings of five butterfly and moth species when mixtures of volatile vapors were applied to the surrounding atmosphere. Fig. 2.13 depicts the responses for acetone + ethanol mixtures.

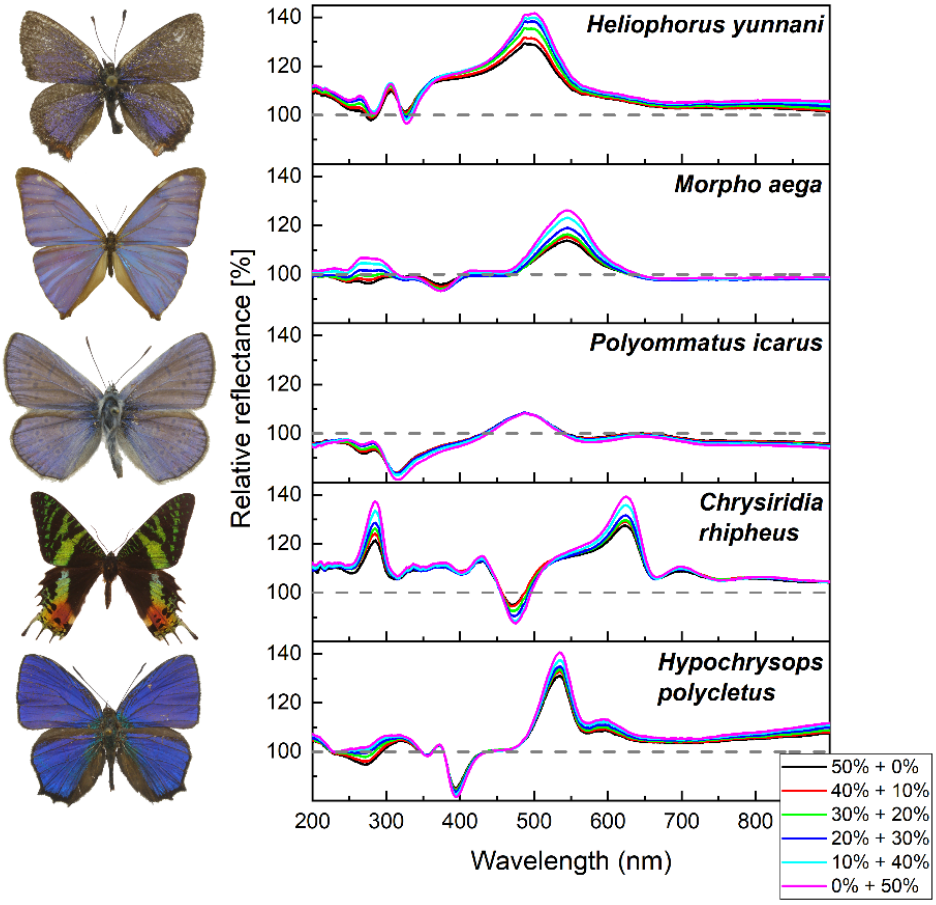

***Figure 2.13**. Optical responses of the wings of five species were investigated when mixtures of acetone + ethanol vapor mixtures were applied. All showed similar color change behavior: the optical responses of the mixtures fell between the color change signals of the pure solvents. The broken lines show the initial relative reflectance spectra used as a reference (100%).*

The changes in the structural colors caused by the different acetone + ethanol vapor mixtures fell between the optical responses generated by the two pure substances in a consecutive order. Therefore, the optical response from a certain vapor mixture consists of the linear combination of the optical responses caused by the vapor components separately. This shows that the photonic nanostructures occurring in the wing scales are capable of chemically selective sensing of vapor mixtures.

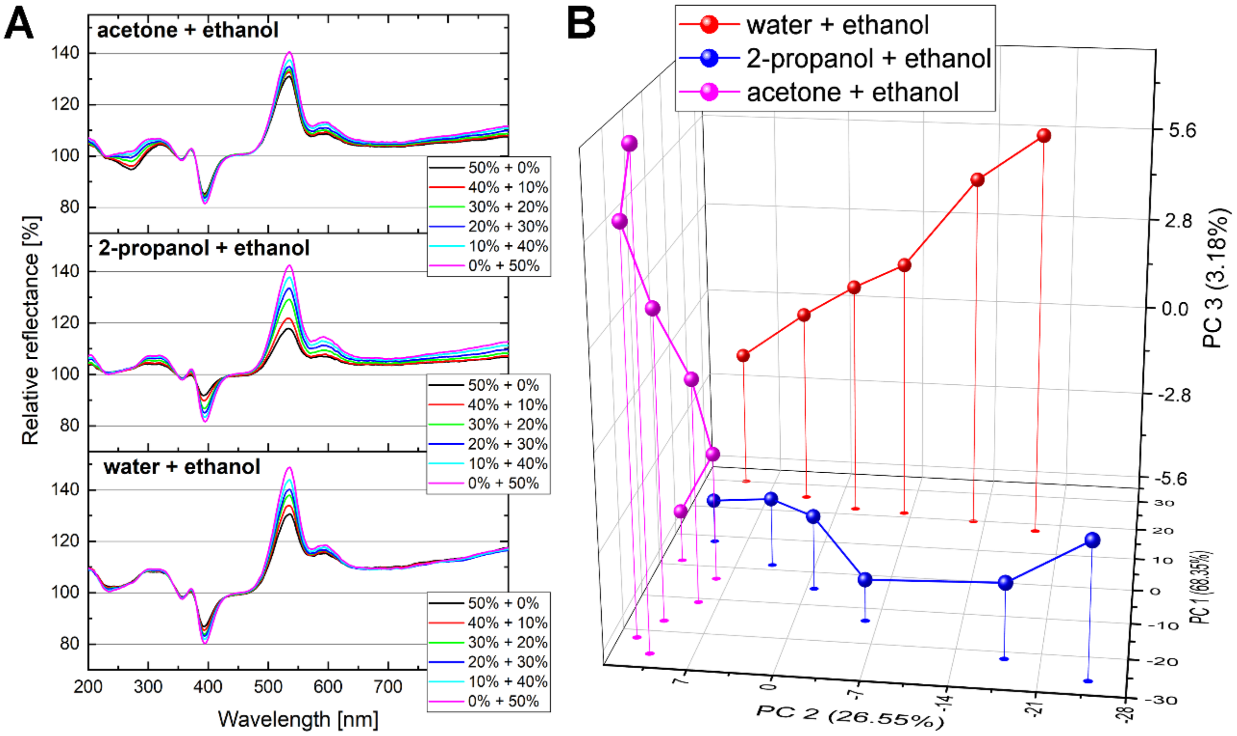

Figure 2.14. Different vapor mixtures generated different optical responses of the wing of a H. polycletus male specimen. (A) The optical responses (relative reflectances) of the three mixtures are characteristically different from each other. (B) The PCA scores plot shows the characteristic trajectories of the three mixtures. The three points close to each other on the left side are the points of the pure ethanol vapor from which the trajectories spread apart.

To investigate the chemically selective behavior of the butterfly wings in detail, a *Hypochrysops polycletus* specimen with bright blue structural color was used in the vapor sensing experiment and three different vapor mixtures were applied. The measured optical responses, i.e., the color changes of the wing in the case of acetone + ethanol, 2-propanol + ethanol, and water + ethanol vapor mixtures were recorded, and the results are depicted in Fig. 2.14.A. All vapor mixtures showed similar behavior, as described earlier, as the optical responses of the mixtures fell between the pure substances.

To analyze the vapor-specific behavior, the measured data were evaluated with principal component analysis (PCA). Figure 2.14.B provides the PC scores plot, which contains the vapor sensing trajectories of the three different vapor mixtures. The three data points on the left that are close to each other, from which the trajectories originate, are the points of the pure ethanol vapor spectrum. Away from this, the curves spread apart, as the compositions of the mixtures shift to their other component. These results demonstrate that butterfly wing-based sensor materials can discriminate between different vapor mixtures very efficiently, as the optical responses of these biological photonic nanostructures are highly substance-specific.

Reproducible phenotype alteration due to prolonged cooling of the pupae of *Polyommatus icarus* butterflies

OTKA K111741, OTKA K115724

G. Piszter, K. Kertész, Z. E. Horváth, Zs. Bálint, and L. P. Biró

The phenotypic changes induced by prolonged cooling (2 – 12 weeks at 5 °C in the dark) of freshly formed *Polyommatus icarus* pupae were investigated. We used more than 200 pupae in our laboratory. Cooling halted the imaginal development of pupae collected shortly after transformation from the larval stage. After cooling, the pupae were allowed to continue their developmental cycle. The wings of the eclosed specimens were investigated by optical microscopy, scanning and cross-sectional transmission electron microscopy, UV-VIS spectroscopy and microspectroscopy. The eclosed adults presented phenotypic alterations that reproduced results that we published previously for smaller groups of individuals remarkably well (see Fig. 2.15); these changes included i) a linear increase in the magnitude of quantified deviation from normal ventral wing patterns with increasing cooling time; ii) slight alteration of the blue coloration of males; and iii) an increasing number of blue scales on the dorsal wing surface of females with increasing cooling time. Several independent factors, including disordering of regular scale rows in males, the number of blue scales in females, eclosion probability and the probability of defect-free eclosion, showed that the cooling time can be divided into three periods: 0 – 4 weeks, 4 – 8 weeks, and 8 – 12 weeks, each of which is characterized by specific changes. The shift from brown female scales to first blue scales with a female-specific shape and then to blue scales with a male-specific shape with longer cooling times suggests slow decomposition of a substance governing scale formation.

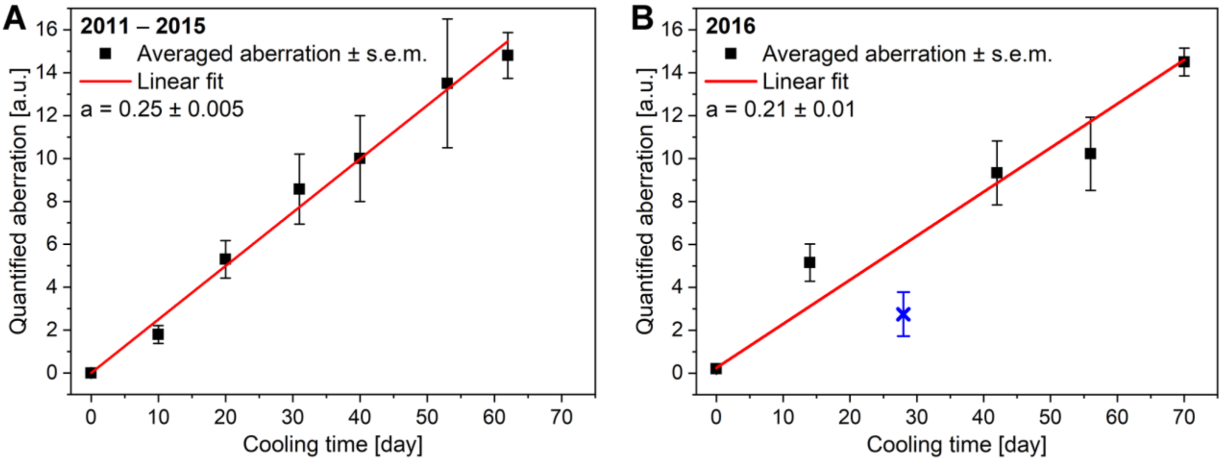

Figure 2.15*. Quantification of the aberration of the pigment-based pattern on the ventral wing surfaces of P. icarus butterflies. (A) Previously reported results; (B) results of the set of cooling experiments conducted to check reproducibility. (s.e.m. = standard error of the mean)*

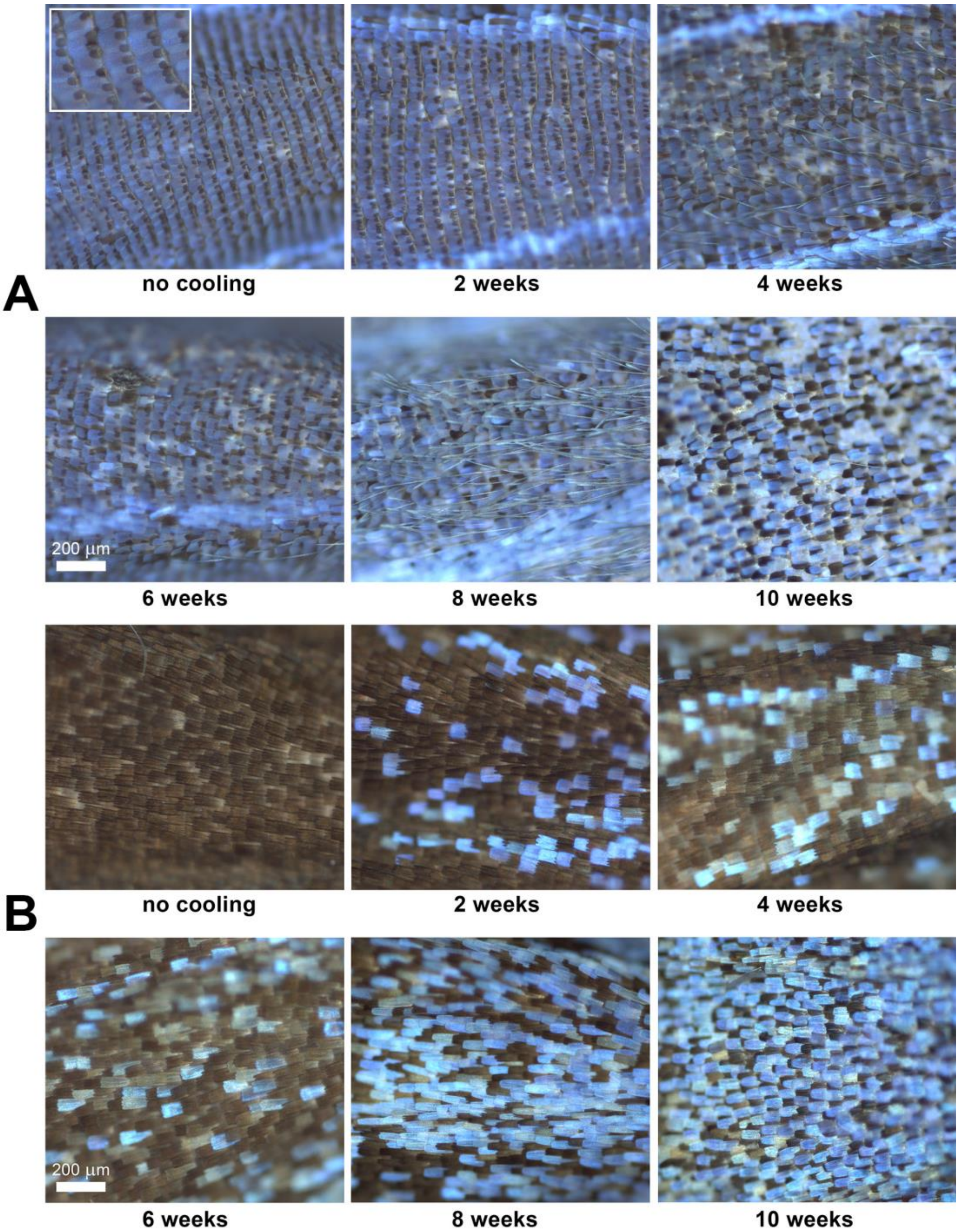

Figure 2.16. *Changes in the dorsal wing scales of P. icarus specimens with increasing cooling times, as seen under an optical microscope. Male (A) and female (B) specimens. The inset in the top left corner of (A) shows the androconia separating the regular rows of the cover scales of the males.*

The normally brown females developed an increasing number of blue scales as the cooling time was increased (see Fig. 2.16.) and exhibited greater deviation in the spectral position of the blue reflectance peak associated with blue scales than males. We attribute this difference to the fact that the genes regulating the production of the blue-generating nanoarchitecture of females are not subjected to reproductive selection, in contrast to those of the males, as the production of their blue scales is induced only under special conditions.

Photonics Department

Head: Dr. Peter PETRIK, D.Sc., scientific advisor

Research Staff:

- Miklós FRIED, D.Sc., Head of Ellipsometry Laboratory
- András DEÁK, Ph.D., Head of Chemical Nanostructures Laboratory
- Miklós SERÉNYI, D.Sc.
- Gábor VÉRTESY, D.Sc.
- Antal GASPARICS, Ph.D.
- Norbert NAGY, Ph.D.
- Zoltán LÁBADI, Ph.D.
- Ferenc RIESZ, C.Sc.
- Dániel ZÁMBÓ, Ph.D. on leave
- Emil AGÓCS, Ph.D., on leave
- György KÁDÁR, D.Sc., Prof. emeritus
- Tivadar LOHNER, D.Sc., Prof. emeritus
- János MAKAI, C.Sc., retired
- András HÁMORI, dr. univ., retired
- György JUHÁSZ, dr. univ., retired

Students:

- Benjamin KALAS, Ph.D.
- Szilárd POTHORSZKY, Ph.D.
- Alekszej ROMANENKO, M.Sc., Ph.D.
- Dániel SZEKRÉNYES, Ph.D.
- Dávid KOVÁCS, M.Sc.
- Rita NÉMEDI, B.Sc

The Photonics Department develops unique methods and tools for non-destructive optical and magnetic measurement of surface nanostructures and materials (spectroscopy; magnetic material testing; biosensors; surface curvature measurement; surface testing; water contamination). One of the most important tasks of the Department is patenting and application of the methods in international projects with partners representing the industry and the high technology.

Key achievements of the Photonics Department in 2019:

- The degradation of the heat-treated reactor steel was investigated by non-destructive magnetic method. The self-developed, so-called "magnetic adaptive test" (MAT) is capable of high sensitivity, fast and non-destructive testing of material quality (e.g. brittleness).
- Surface modification and measurement techniques have been developed to control and characterize the self-assembly of nanoparticles. Gold nanoparticles with opposite surface charges have been created to study in-situ formation of individual dimers in a liquid medium. It has been shown that single particle spectroscopy is capable of determining the spatial configuration of interconnected particle pairs.
- Capillary probe methods have been developed and equipment for high-precision edge angle measurement has been developed, which offers an indirect, non-destructive, fast and sensitive determination of surface properties, including purity, pinholes, and many other technologically important properties. In addition to the extremely high sensitivity of the method, it has been

possible to reduce the measurement accuracy of the edge angle to 0.1° even in measuring ranges where conventional methods are not applicable or the measurement error is several times higher.

- The cyclic voltammetry method has been optimized for the detection of arsenic and nickel in drinking water. Properly immobilized genetically modified flagellar filaments allow greater sensitivity on the gold surface. The stability and regenerability of the sensor surfaces have been demonstrated, which is an important aspect for the practical use of a handheld instrument for field application. An optical method for real-time monitoring and structural modelling of the surface adsorption of filaments has been developed.
- Makyoh ("magic mirror") topography method created a new geometric model to take into account global curvature. The developed method shows that the error can be analytically corrected by knowing the equivalent sample-screen distance and the global curvature parameters.
- The method of combinatorial materials science has been improved in both sample preparation and analytical applications. Metal-oxide structures, which are characterized by optical and ion-beam mapping techniques, have been created by multi-source large-area magnetron sputtering to understand lateral distribution of properties, develop measurement evaluation models, and create optical databases over a wide range of compositions.
- The optical monitoring method for the optical inspection of the surface of zirconium rods used in nuclear power reactors has been further developed. The method can also test small diameter tubes (<1 cm) in a controlled atmosphere at temperatures ranging from 25 to 600 °C. A diffusion model has been developed to understand the oxidation process, which provides a better understanding of high temperature processes compared to measurement data.
- Using the spectroscopic ellipsometry method, the dielectric function of germanium amorphized by ion implantation was determined. Implantation parameters that allow the formation of a compact amorphous layer are used, and bubbles in the layer are avoided. Optical references are important for studying ion implanted semiconductors, embedded nanodots, and complex structures that can be studied in the medium of sensing and microelectronics.

Combinatorial Investigation of WO3-MoO3 Mixed Layers by Spectroscopic Ellipsometry using Different Optical Models

M-ERA.NET Transnational Call 2018 VOC-DETECT, OTKA NN131269, OTKA K129009

R. Bogar, Z. Labadi, Z. E. Horvath, Z. Zolnai, M. Fried

Protection against heat waves through the glass windows, the electrochromic film as a smart window is the most useful tool to reduce heat in buildings. This type of glass consists of a layer of electrochromic film bounded by metal oxide layers able to change their transparency under DC bias. Typical materials for this purpose are MoO_3 and WO_3 but relatively little attention is paid for the applicability of their mixed oxides. In our work we investigated mixed oxides deposited by combinatorial reactive sputtering. Metal oxides were deposited onto glass substrates by using Argon-Oxygene plasma for sputtering metallic targets, while combinatorial method meant that substrates were in cyclic movement under two different plasma streams.

W- and Mo-targets were placed separately into the sputtering chamber and 30x30 cm glass substrates were slowly moved under the two separated targets. Two possible arrangements of the targets can be seen in Fig. 3.1. In the first arrangement, the two targets were placed at 35 cm, in the second arrangement they were placed at 70 cm distance from each other. According to the measurements, in the first arrangement the two „material streams" overlapped around the centre position, while in the second arrangement the two „material streams" were separated.

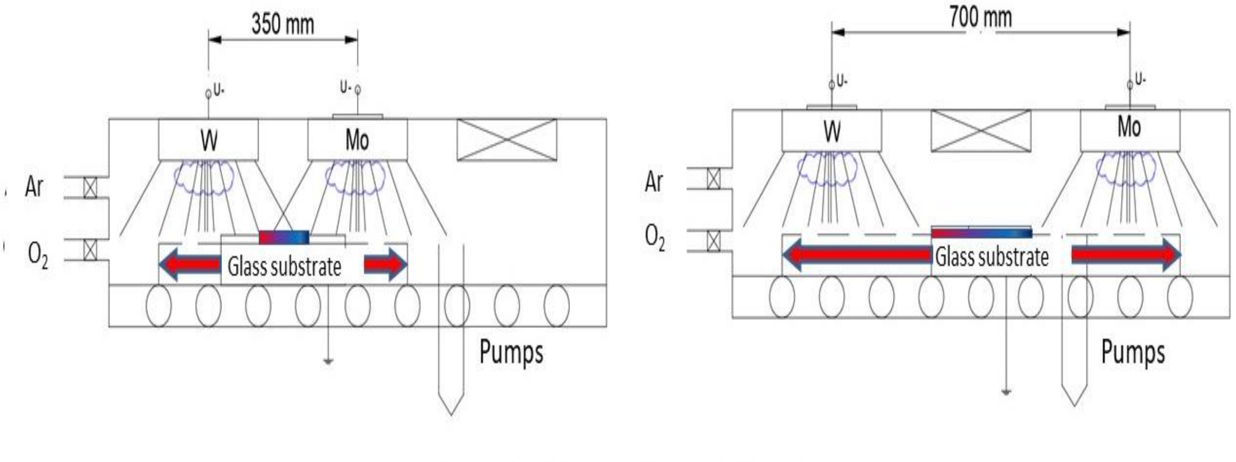

8th International Conference on Spectroscopic Ellipsometry

Figure 3.1. *Two arrangements of the targets: a) the two targets in closer position (35 cm from each other) b) the two targets in distant position (70 cm from each other).*

Reactive sputtered mixed oxide layers were investigated and mapped by Spectroscopic Ellipsometry (SE) We used different (oscillator- and Effective Medium Approximation, EMA-based) optical models to obtain the thickness and composition map of the sample layer relatively quickly, and in a cheap and contactless way. In a set of experiments, we changed the position of the sputtering targets, the speed and cycle number of the substrate motion. Our aim was to compare the "goodness" of the different optical models depending upon the sample preparation conditions.

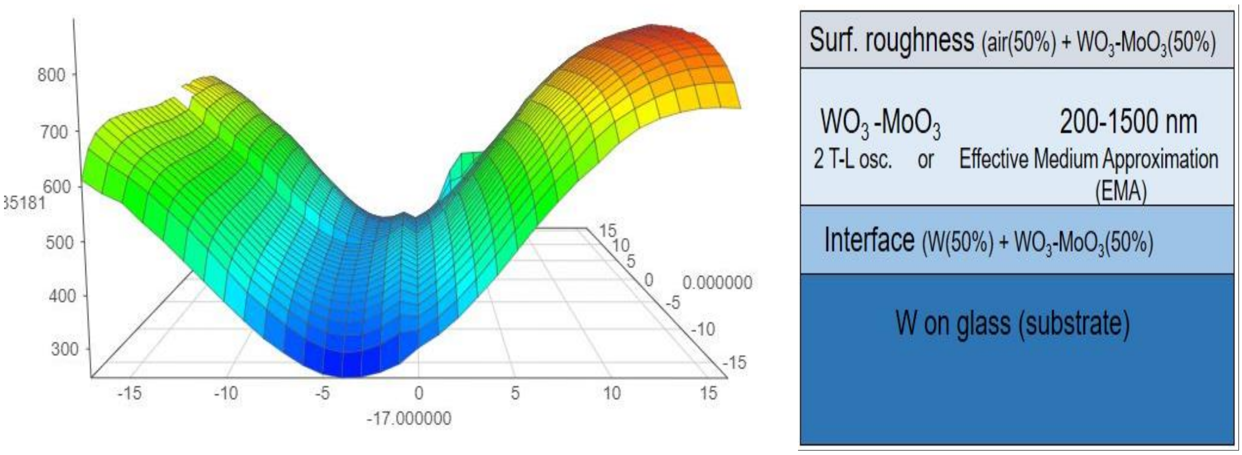

Figure 3.2. *Thickness-map based on Tauc-Lorentz oscillator model*

Figure 3.2 shows a typical SE map of the deposited layer (together with the schematic optical model). We have also used Rutherford Backscattering Spectrometry (RBS) to check the SE results (see Fig. 3.3). We showed that we were able to produce mixed oxide layers using the combinatorial approach in a magnetron sputtering system. These samples can be mapped (thickness and composition maps, too) by fast and non-destructive manner by Spectroscopic Ellipsometry. We can choose between appropriate optical models (2-Tauc-Lorentz-oscillator model versus the Bruggeman Effective Medium Approximation, BEMA) depending on the process parameters.

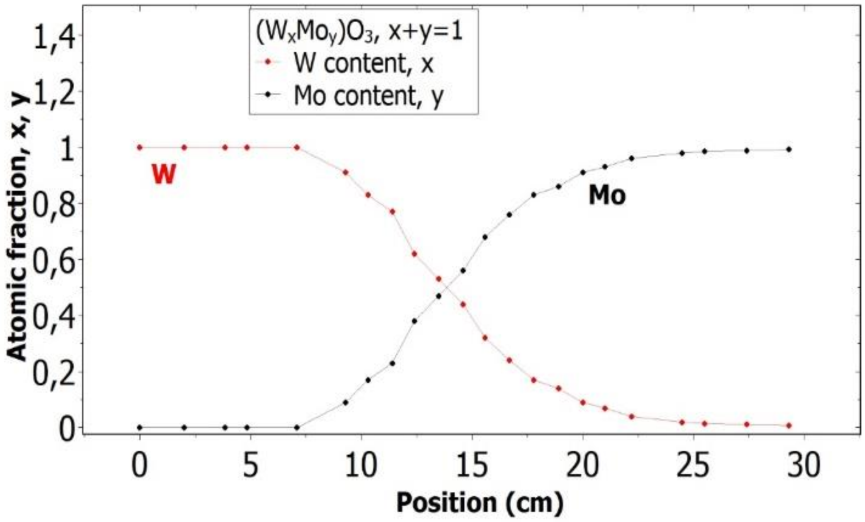

Figure 3.3. *Composition-map along a line by Rutherford Backscattering Spectrometry*

Our further aim is to investigate the goodness of WO3-MoO3 mixed layers as electrochromic materials for „smart" windows (transparency ratio, switching speed, coloration efficiency).

Sensing layer for Ni detection in water created by immobilization of bio-engineered flagellar nanotubes on gold surfaces

OTKA NN117847, OTKA NN117849, OTKA K131515,
INFRANANOCHEM - Nr. 19/01.03.2009

Z. Labadi, B. Kalas, A. Saftics, L. Illes, H. Jankovics, É. Bereczk-Tompa, A. Sebestyén, É. Tóth, B. Kakasi, C. Moldovan, B. Firtat, M. Gartner, M. Gheorghe, F. Vonderviszt, M. Fried, P. Petrik

Environmental monitoring of Ni is needed around the WHO threshold limit of 0.34 µM. This sensitivity target can usually only be met by time consuming and expensive laboratory measurements. There is a need for cheap field-applicable methods, even if it is only used for signalling the necessity of a more accurate laboratory investigation.

In this work bio-engineered bacterial Ni-binding flagellin variants were fabricated and their applicability in capture layers was tested. Nanotubes of mutant flagellins were built by in vitro polymerization (Fig. 3.4.).

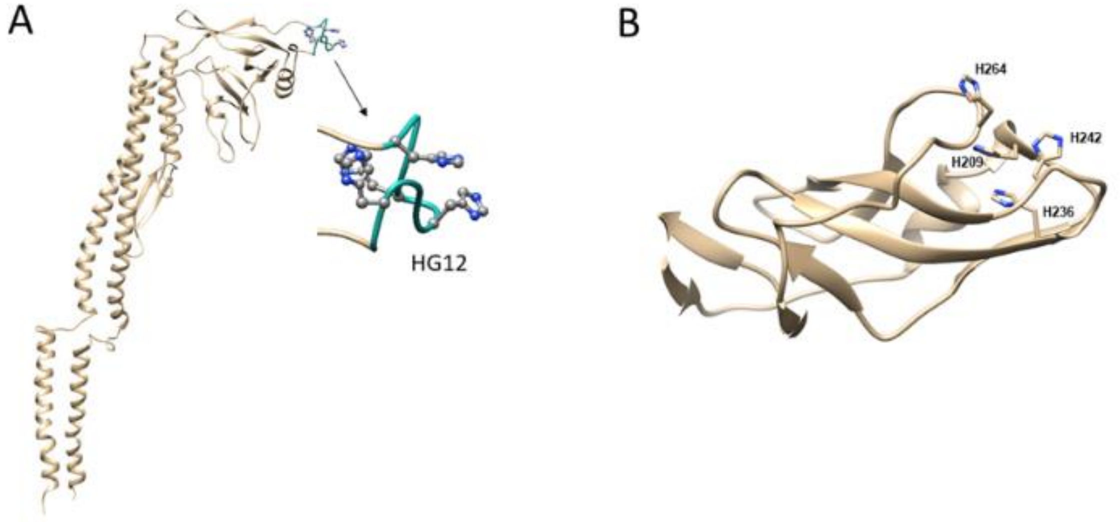

Figure 3.4. *Construction of Ni-binding flagellin variants. (A) The D3 domain of Salmonella flagellin was replaced by a Ni-binding motif. (B) The Ca backbone trace of the D3 domain of flagellin is displayed showing residues mutated for histidine.*

A large surface density of the nanotubes on the sensor surface was achieved by covalent immobilization chemistry based on an optimized dithiobis(succimidyl propionate) (DSP) crosslinking. Surface coverage was monitored by using *in situ* plasmon enhanced spectroscopic ellipsometry (Fig. 3.5.).

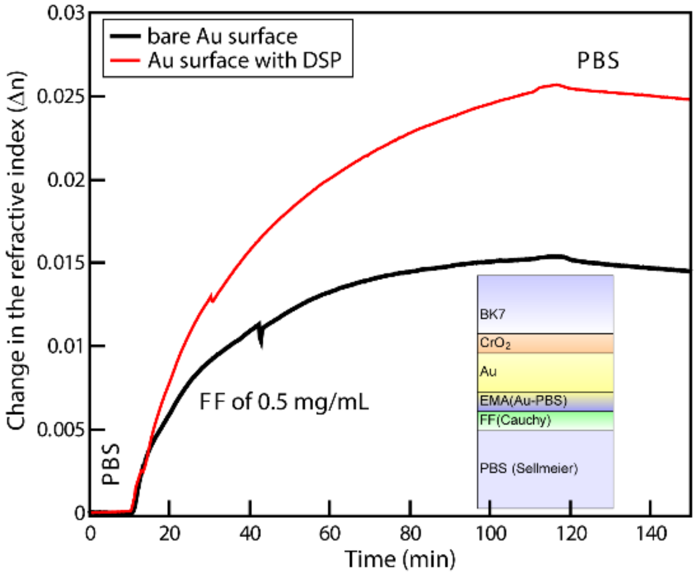

***Figure 3.5**. Increase of refractive index (at the wavelength of 633 nm) in the layer modelling the filaments at the interface during adsorption to gold surface with (red line) and without (black line) a DSP layer for covalent bonding. The change of refractive index corresponds to surface densities of 391 ng/cm^2 and 184 ng/cm^2, for DSP-covered and non-covered surfaces, respectively.*

Nickel detecting capability of the filament layers was tested by cyclic voltammetry using added $NiSO_4$ in different concentrations. Fig. 3.6.left shows that a cathodic peak associated with the Ni^{2+} ion reduction appears in the potential range around -250 mV, and the peak intensity monotonously increases with the Ni^{2+} concentration, up to saturation. Regeneration of the samples was also successfully realized (Fig 3.6.right).

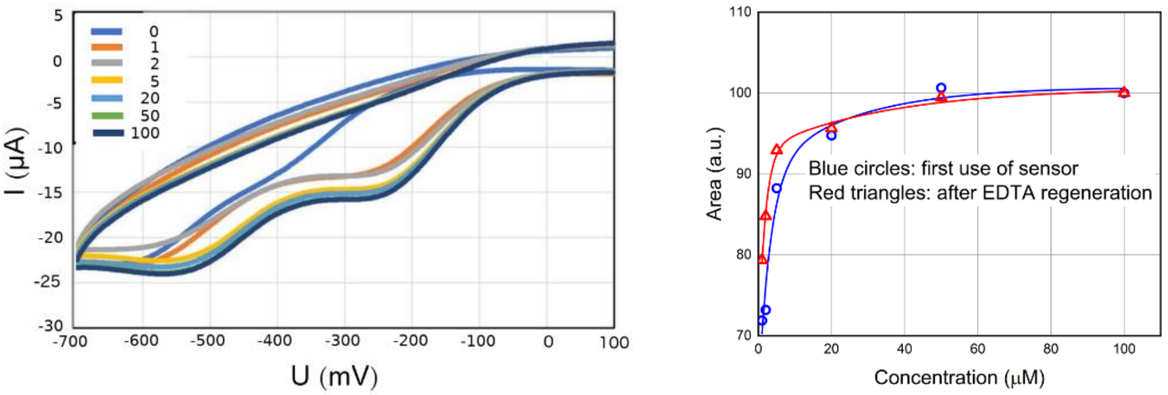

***Figure 3.6** (left) Set of CV curves measured in the presence of Ni(II) on flagellar nanotubes. (right) Ni peak areas are represented for first use (blue) and for regenerated (red) samples.*

Our work demonstrates [Ref. 3.1] that mutant flagellar filaments have the potential to form protein-based Ni sensing layers on a Si substrate which can be employed in low-cost portable electrochemical biosensors to fulfil the requirements for sensing Ni in water at concentration as low as the WHO health threshold limit.

Optical properties of hydrogenated amorphous $Si_{1-x}Ge_x$ for the entire range of compositions

OTKA K131515, OTKA K129009 and M-ERA.NET Transnational Call 2018 VOC-DETECT

B. Kalas, Z. Zolnai, G. Sáfrán, M. Serenyi, E. Agocs, T. Lohner, A. Nemeth, M. Fried, and P. Petrik

The optical parameters of hydrogenated amorphous a-$Si_{1-x}Ge_x$:H layers were measured with focused beam mapping ellipsometry for photon energies from 0.7 to 6.5 eV. The applied single-sample micro-combinatorial technique enables the preparation of a-$Si_{1-x}Ge_x$:H with full range composition spread. Linearly variable composition profile was revealed along the 20 mm long gradient part of the sample by Rutherford backscattering spectrometry and elastic recoil detection analysis. The Cody-Lorentz approach was identified as the best model to describe the optical dispersion of the alloy. The effect of incorporated hydrogen on the optical absorption is explained by the lowering of the density of localized states in the mobility gap. It is shown that in the low-dispersion near infrared range the refractive index of the a-$Si_{1-x}Ge_x$ alloy can be comprehended as a linear combination of the optical parameters of the components [Ref.3.2.].

The micro-combinatorial sample preparation with mapping ellipsometry is not only suitable for the fabrication of samples with controlled lateral distribution of the concentrations, but also opens new prospects in creating databases of compounds for optical and optoelectronic applications.

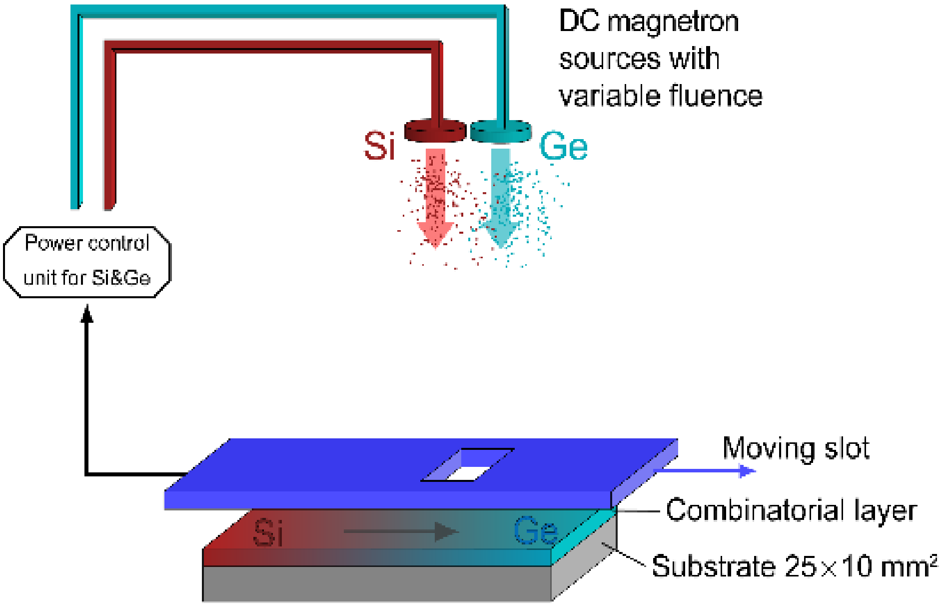

Figure 3.7. *Setup used for the "single-sample concept" combinatorial deposition.*

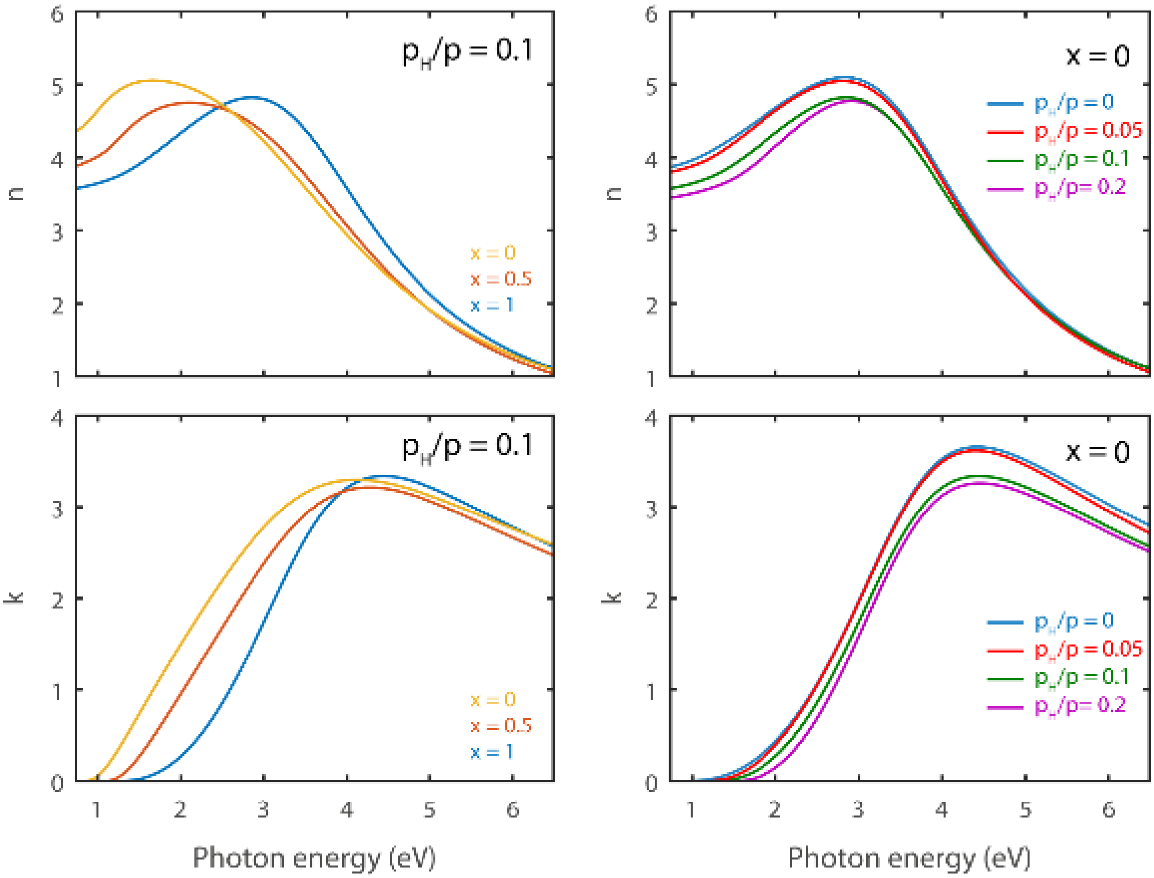

Figure 3.8. *Real and imaginary parts of the complex refractive indices of a-*$Si_{1-x}Ge_x$*:H with* $p_H/p=0.1$ *for different compositions (left-hand side) and for different H contents for x=0 given as* p_H/p *values written next to the corresponding curves (right-hand side).*

Determination of complex dielectric function of ion-implanted amorphous germanium by spectroscopic ellipsometry

OTKA K131515, OTKA K129009

T. Lohner, E. Szilágyi, Zs. Zolnai, A. Németh, Zs. Fogarassy, L. Illés, E. Kótai, P. Petrik, M. Fried

Accurate reference dielectric functions play important role in the research and development of optical materials. Libraries of such data are required in a broad range of applications from integrated optics to photovoltaics. Amorphous semiconductors are gaining increasing interest in optoelectronics and many other applications. Measuring with a spectroscopic ellipsometer (SE) in the wavelength range from 210 to 1690 nm we determined the complex dielectric function of fully amorphized Ge (a-Ge) layer produced by a two-step implantation (120 and 300 keV) of Al ions into single-crystalline Ge. The reason for selecting a relatively light mass projectile (Al) was to avoid void formation in case of implantation of heavy mass ions. The evaluation of ellipsometric spectra at multiple angles of incidence was performed using a two-layer optical model: an a-Ge layer with a GeO_2 surface layer. The complex dielectric function of a-Ge was modelled using the Tauc-Lorentz or the Cody-Lorentz dispersion relations (Fig. 3.9.). The thickness of the a-Ge layer was determined by Rutherford backscattering spectrometry (RBS) in combination with channelling and by cross-sectional transmission electron microscopy (XTEM). The thickness values evaluated from SE, RBS and XTEM measurements agree within the experimental limits of accuracy. The complementary investigations revealed a high-quality amorphous layer, suitable for providing optical reference data [Ref.3.3.].

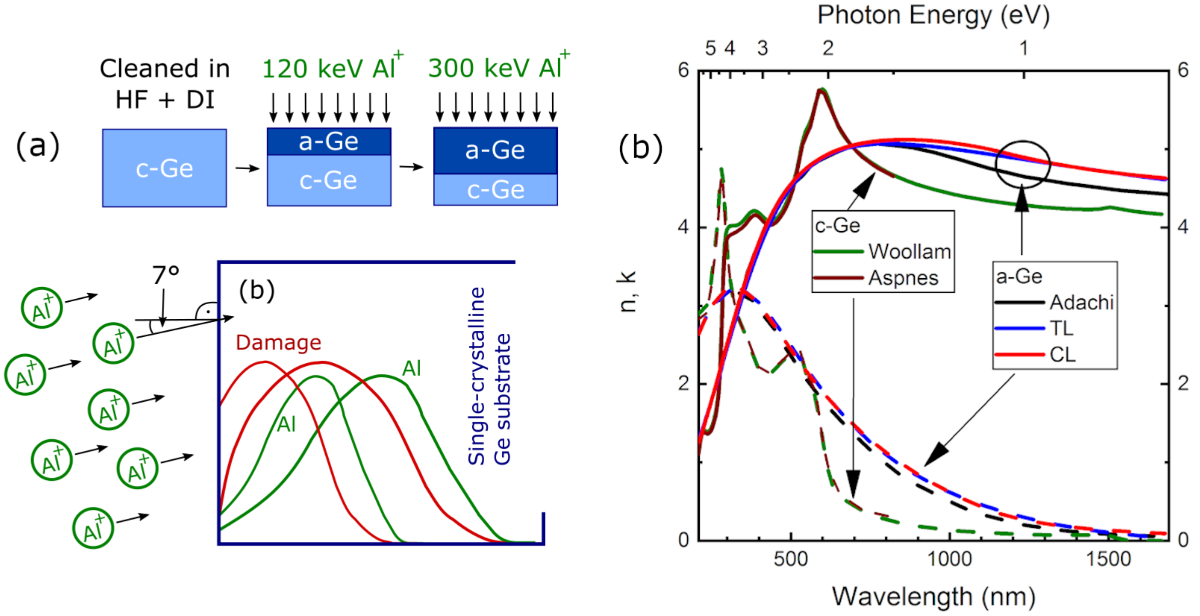

Figure 3.9. *(a) Dual-energy ion implantation to create amorphous Ge. (b) Refractive index (n, solid lines) and extinction coefficient (k, dashed lines) spectra measured by ellipsometry using the Cody-Lorentz (CL) and the Tauc-Lorentz (TL) dispersions. For comparison, the data of c-Ge and evaporated a-Ge (Adachi) are also presented.*

Optical spectroscopy studies on nanoparticles

OTKA FK128327, OTKA KH129578, 2018-2.1.13-TÉT-FR-2018-00002

D.P. Szekrényes, D. Zámbó, A. Deák

Our earlier works on gold nanoparticle heterodimers have shown that it is possible to site-selectively surface modify gold nanorods with specific molecules that in turn enables the region-selective assembly of nanosphere/nanorod heterodimers [Ref.3.4., Ref.3.5.]. We also demonstrated that the assembly process of such patchy colloids can be captured in-situ in the aqueous environment even at the single particle level by relying on the scattering spectrum measurement of individual heterodimers [Ref.3.6.].

In our recent work we push these studies one step further by systematically investigating the polarization resolved scattering spectra of sphere/rod heterodimers with the aim to conclude on the relative spatial arrangement on the particles more precisely [Ref.3.7.]. For the measurements we use a custom developed dark-field microscopy-based setup, which allows the measurement of the scattering spectrum of individual nanoparticles via a high sensitivity imaging spectrometer. As we use gold nanoparticles for the experiments, their localised plasmon resonance determined scattering spectrum will drastically change upon binding of a second particle due to plasmon coupling. The scattering spectrum of such a particle dimer contains rich details when the dimer is formed by a sphere and a rod. One prominent feature is the Fano resonance arising due to the destructive interference of the spatially and energetically overlapping rod and sphere plasmon modes. Polarization resolved scattering measurements performed on individual heterodimers reveals, however, that apparently identical scattering spectra of sphere/rod heterodimers belonging to different relative particle arrangements (namely top or bottom arranged in term of the spheres' position with respect to the nanorod), show markedly different behaviour as an analyser Is placed at different azimuthal angles in the beam path (Fig. 3.10.).

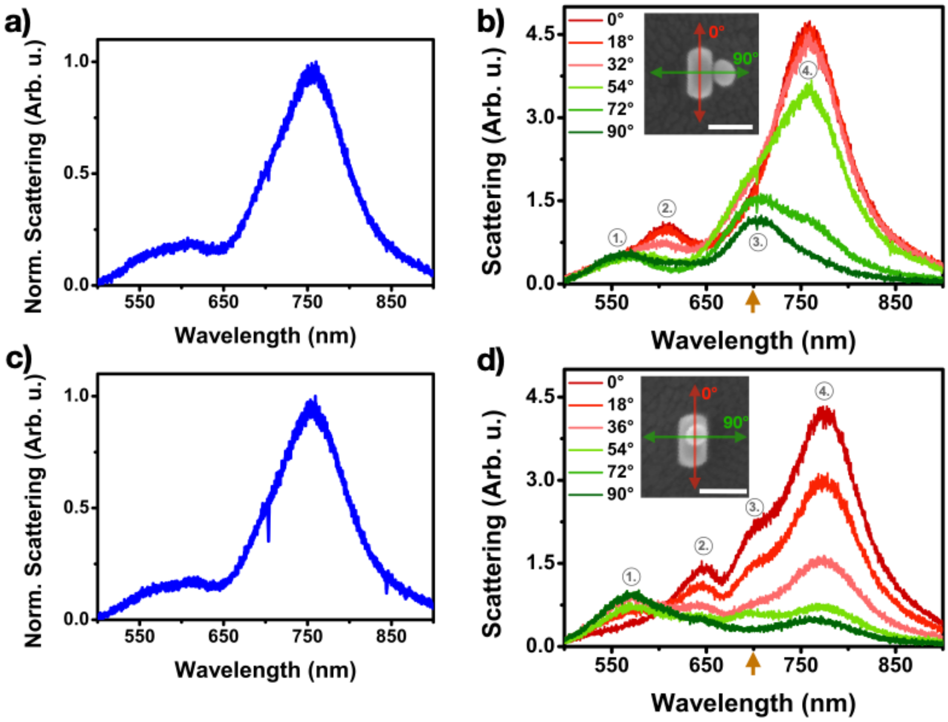

Figure 3.10. White light scattering spectra obtained for sphere/rod heterodimers featuring different nanosphere arrangements (side: a, top: c). The scattering spectrum of the same heterodimers obtained using a linear analyser at different angles with respect to the rod longitudinal axis (b,d).

It has to be stressed that in the polarisation resolved spectra there is a peak (marked '3' in Fig. 3.10.b, 3.10.d) that behaves markedly differently for the two arrangements. This peak – supported by optical simulations on the structures – can be attributed to the coupled sphere dipole/rod transversal mode. The different intensity modulation of this mode with the analyser angle can be expected as the coupling axis is different for the two arrangements. For the side arranged case the peak is fairly pronounced at 90°, as in this case the coupling axis is parallel to the analyser direction and the coupled dipole radiates effectively towards the collecting optical system. For the top arranged case, however, its intensity remains fairly low and constant at all angles, as the coupling axis is vertical and radiation from this coupled mode propagates largely towards the sides. This implies that the polarisation dependence of this coupled mode can be used to conclude on the relative arrangement of the particles in the direction perpendicular to the substrate (side or top arranged). We successfully exploited this strategy to investigate the formation of individual heterodimers in aqueous environment and their eventual rearrangement upon drying the very same structure. We provided evidence for the structural rearrangement of such a rod/sphere heterodimer based on correlative spectroscopic / scanning electron microscopic investigations [Ref.3.7.].

Another direction of the research is centred on the controlled preparation of nanosphere dimers at solid/liquid interface with the specific aim to investigate their arrangement and surface separation in-situ in the aqueous environment by optical microspectroscopic measurements. As the coupled spectrum of such dimers is well known change sensitively with the surface-to-surface separation, it could provide a platform to study in the (attractive) interaction between nanoparticles featuring dissimilar surface molecular coatings. We prepared colloidal systems from gold nanospheres that are individually stable, but have high affinity towards each other owing to their opposite surface charge. One of these attractive particle types are PEGylated to provide an additional steric repulsion. PEG is used as a benchmark molecule in bio-related fields as it can significantly improve the stealth capability of nanosized materials introduced into the body. The goal will be to correlate the effective particle separations with the relevant colloidal interactions, including the steric repulsion due to the presence of the PEG chains. At the preliminary stage of this work the model systems have been prepared and their assembly potential verified based on bulk spectroscopy measurement (Fig. 3.11). In the next phase of the work these systems will be used to carry out the single particle (dimer) spectroscopy measurements.

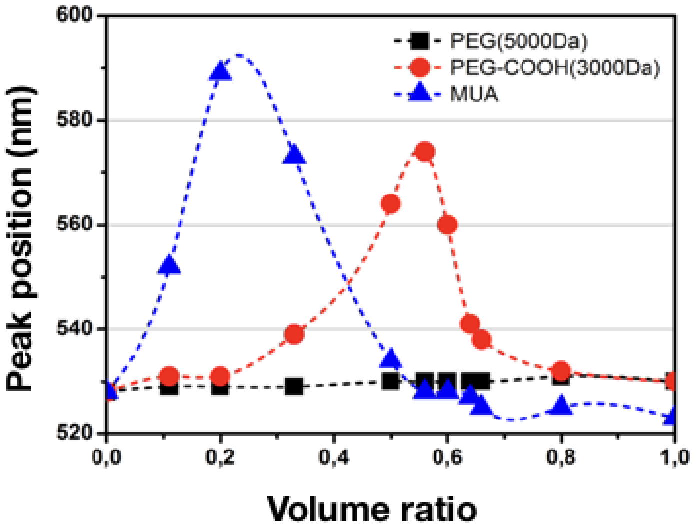

Figure 3.11. *Spectral peak position changes upon mixing positively charged ((11-Mercaptoundecyl)-N,N,N-trimethyl-ammonium bromide coated) gold nanoparticles with negatively charged ones (carboxy-PEG; 3000 Da and 11-mercaptoundecanoic acid coated). As a reference only PEG covered particles (5000 Da) are used where no changes in the optical spectrum are observed, underlining the role of the electric double layer attraction in the assembly process.*

In the framework of a bilateral project we also work with a French partner, Doru Constantin from the Laboratoire de Physique des Solides (Orsay) on the detailed SAXS investigation of our PEGylated gold nanoparticles, that we used earlier successfully demonstrate the ionic strength and temperature triggered clustering of the particles [Ref.3.8.]. We successfully repeated our earlier experiments and amended the characterization with the SAXS data, from which the equilibrium distance between the particles within the clusters was obtained. We compare this to theoretical calculations on the soft-sphere type interaction between the nanoparticles. The results are planned to be published next year.

Robust contact angle determination for sessile drops without apex

OTKA FK128901

E. Albert, B. Tegze, Z. Hajnal, D. Zámbó, D. P. Szekrényes, A. Deák, Z. Hórvölgyi, N. Nagy

The polynomial fitting to the profile of a sessile drop is widely used in those cases when the drop apex is not visible. The major disadvantage of this approach is that the resulted contact angle is highly sensitive to the applied polynomial order and the number of pixels to which the polynomial was fitted. In order to overcome these uncertainties, an easily implementable method was introduced.

Circumcircles are constructed independently for the left and right unperturbed parts of the profile. Polynomial is fitted to the vertical difference between the circumcircle and the profile, see Fig. 3.12.

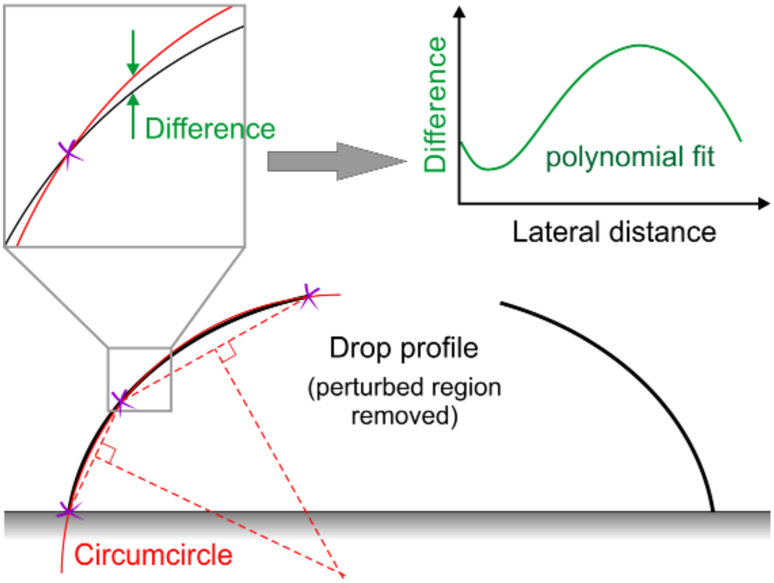

Figure 3.12. *Schematics of the circumcircle and difference fitting method are shown. That region of the profile is intentionally omitted, which is affected by the needle. Three points are selected from each resulted arc: the endpoints and the point at the half of maximum height. Circumscribed circles that pass through these points are constructed independently and polynomial is fitted to the difference between the circle and the profile as a function of the lateral distance from the contact point.*

The contact angle is calculated from the sum of the slope of the circumscribed circle and the polynomial curve at the three-phase contact point for each side. The derivative of the circumcircle at the contact point can be calculated analytically. The slope of the polynomial curve at the contact point does not change significantly with the contact angle or with the drop volume.

The method was validated in the contact angle range of 20°–150° with two different image resolutions (1280 × 1024 and 750 × 600 pixels) by comparing the results to the values calculated by the Young-Laplace fit (Fig. 3.13). The accuracy of the method was found to be $\leq 0.6°$ and it does not show significant dependence on the actual contact angle and on the resolution of the captured image. In comparison, the accuracy of the most sophisticated polynomial method is $\geq 1°$.

Needle-in-drop measurements were carried out on a thermal SiO_2 surface for demonstration the capability of the present method (Fig. 3.14). Two syringes were applied with different needle diameter and the determined contact angles were in good agreement considering their standard deviation. The results obtained using the small-diameter needle were a bit closer to the values resulted from the Young-Laplace fit [Ref.3.9.].

The method improves the accuracy of the evaluation of the needle-in-drop measurements in sessile drop, captive bubble, electrowetting, and electrodewetting experiments and it might be useful also for tilted plate measurements as well.

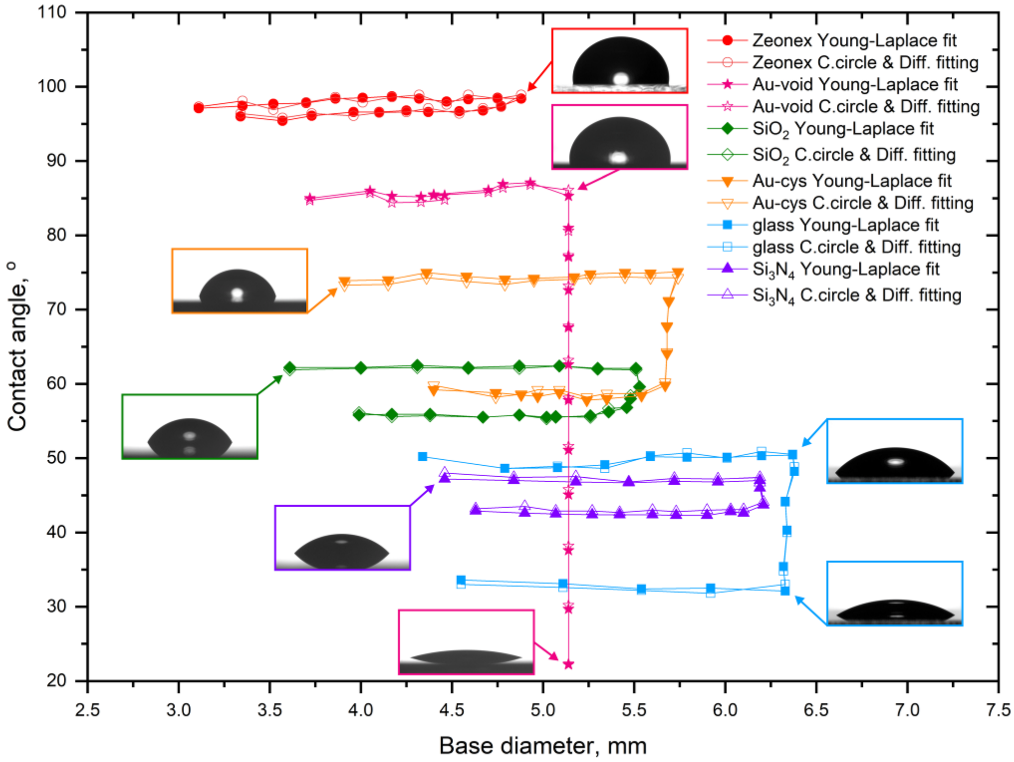

Figure 3.13. *Contact angles as a function of the drop's base diameter. The values determined by the Young-Laplace fit are shown by filled markers. The hollow markers designate the values determined by the proposed circumcircle and differential fitting. The insets show droplet images corresponding to the marked points. The contact line pinning on the gold nanovoid surface is obvious.*

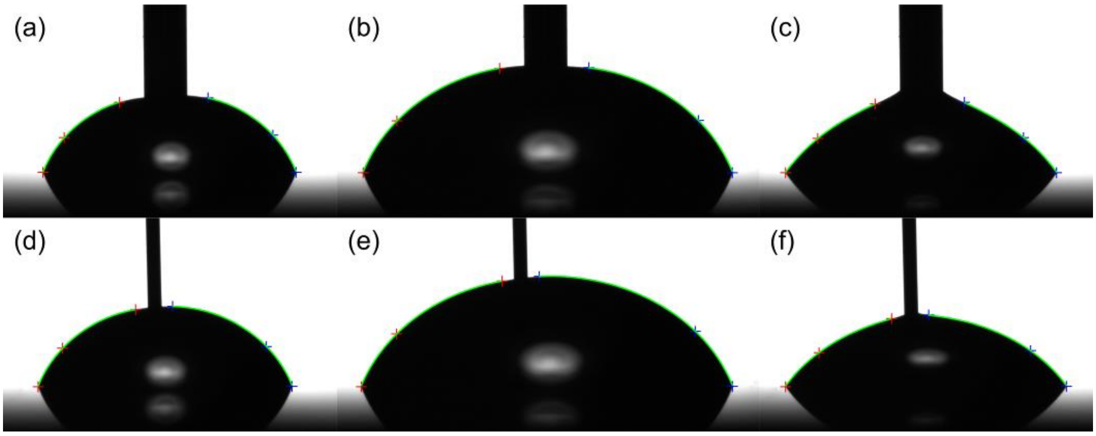

Figure 3.14. *Evaluated images of water droplets with the volume of 10 µL (a,c,d,f) and 30 µL (b,e) captured in the advancing (a,b,d,e) and the receding phase (c,f). The measurements were carried out on the SiO_2 sample using two different needles with the diameter of 0.718 mm (a-c) and 0.235 mm (d-f). The red and blue crosses designate the points for the circumcircle construction, the green curves show the resulted profile after difference fitting.*

Contact angle determination on super hydrophilic surfaces by using capillary bridges

OTKA FK 128901

N. Nagy

Measurement of low contact angles is challenging. The developed indirect Capillary Bridge Probe method combines the accuracy of the Wilhelmy method and the general usability of the sessile drop method without their limitations.

The method is based on the use of a liquid bridge as a probe: the capillary bridge of the test liquid is stretched between the rim of the base of a cylinder and the investigated surface under equilibrium conditions. The advancing contact angle on the sample can be measured during the stepwise decrease of the bridge length. The receding contact angle is determined during the retraction of the cylinder. The contact angle is calculated from Delaunay's analytical solution, while the necessary parameters are obtained from the measured capillary force and from the automated analysis of the captured image of the liquid bridge. The bridge is formed from a pendant drop. This unique feature ensures that the advancing contact line finds dry (not prewetted) surface.

A new effect was observed during the measurements on freshly acid-cleaned glass surfaces, *i.e.* in complete wetting situations. The receding contact line starts to advance again during the increase of the bridge length, see Figure 3.15.

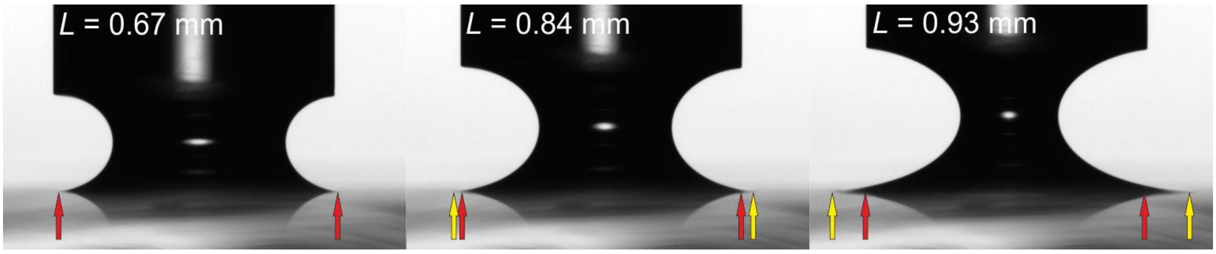

Figure 3.15. *Images of a water capillary bridge taken during the retraction of the cylinder. The receding contact line starts to advance again after a given bridge length (L). The capillary bridge was formed on a glass slide treated freshly in sulphuric acid. Note that images show equilibrium states, not snapshots of a dynamic process.*

The measured capillary force does not exhibit hysteresis. The contact radius started to increase in the retraction phase, around the bridge length corresponding to bridge formation (Fig. 3.16.a). It can be observed in Fig. 3.16.b that the advancing and receding contact angles are equal within their standard deviation: 4.7° ± 0.3° and 4.5° ± 0.3°, respectively. The measured contact angle in the readvancing phase, *i.e.* the readvancing contact angle is much lower, its value is 1.0° ± 0.1°. When the receding contact line starts to advance again, it finds prewetted surface, therefore the resulted contact angle is much smaller.

As a demonstration of the capability of capillary bridge probe method, lightly corroded glass slides were investigated: how does the water contact angle change as a function of the exposure time to air. Microscope glass slides were cleaned and soaked in 3:1 Piranha-solution. The glass slides were rinsed thoroughly in hot ultrapure water. The measurement was started directly after the cleaning process on a glass slide, while other samples were soaked for four days at room temperature. Before the samples were inserted into the chamber they were dried thoroughly under filtered nitrogen flow. The samples were measured periodically in different positions, and they were left in the humid atmosphere (94%) of the sample chamber between the measurements.

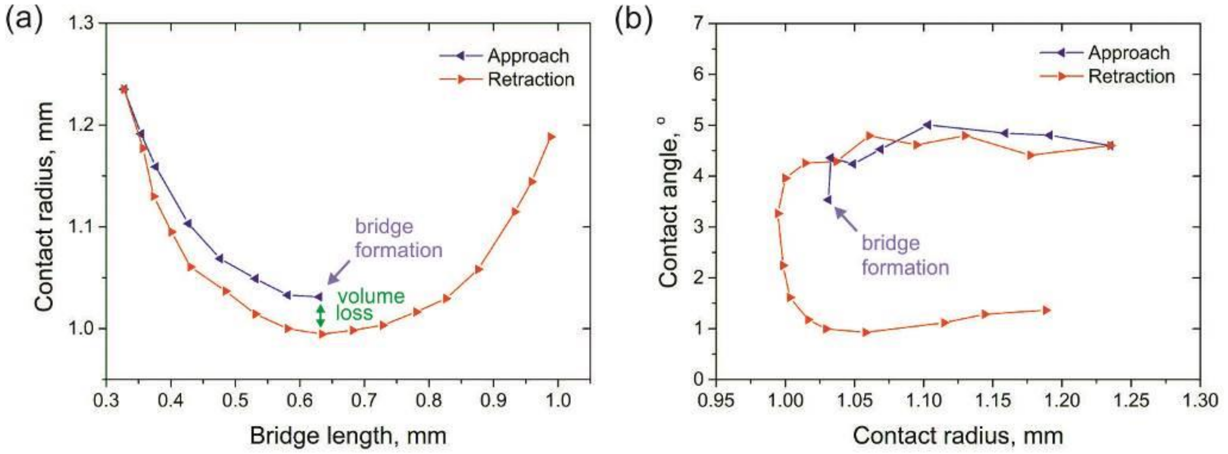

Figure 3.16. *(a) Contact radius as a function of the bridge length measured on a glass surface treated in concentrated sulfuric acid. The contact radius increases after a given point during the increase of the bridge length. The small difference between the approaching and retraction phase refers to small volume loss. (b) Contact angle on the glass surface versus the contact radius. Advancing and receding contact angles are equal, while the readvancing contact angle is lower, because the readvancing contact line finds prewetted surface. The volume of the liquid bridge was 1.17 μL.*

The advancing and receding contact angles were determined to be equal (3.6° ± 0.1° and 3.6° ± 0.4°, respectively) by the first measurement. Their values remain equal for ca. 150 min, and finally significant hysteresis can be observed, while the readvancing phase disappears. The increased standard deviations of the last measurement can be connected to the increasing amount of surface inhomogeneity, while the surface hydroxyl group density decreases. On the contrary, the advancing, receding, and readvancing contact angles on the soaked sample remain almost unchanged, although the increase of the amount of surface contamination can be similar to the previous sample. The advancing and receding contact angles were measured to be 3.8° ± 0.1° and 3.6° ± 0.2° in the first position. A slight increase of ca. 1° can be observed for both after 260 min [Ref.3.10.].

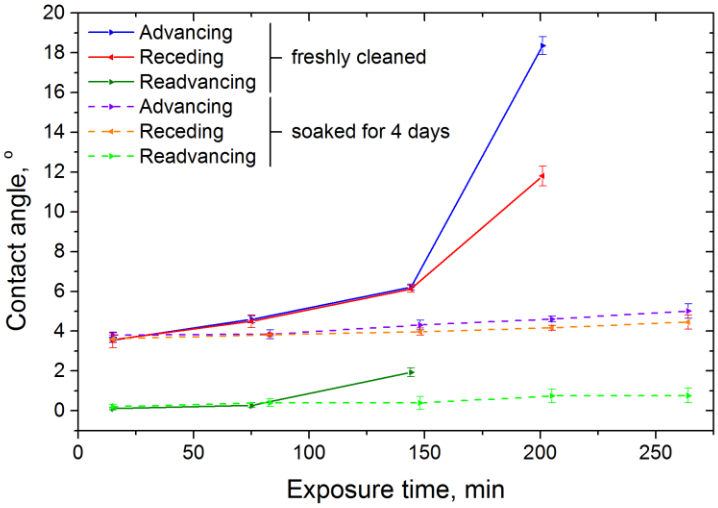

Figure 3.17. *Advancing, receding, and readvancing contact angles on glass slides as a function of exposure time to humid air (94%) of the sample chamber. The capillary bridge probe measurements were performed directly after the cleaning process (continuous lines), and after soaking the sample in ultrapure water for four days (dashed lines). The super-hydrophilic character and the readvancing phase of the directly measured surface disappear, while the alteration zone formed by corrosion preserves the super-hydrophilicity.*

Makyoh topography

F. Riesz

Makyoh topography is an optical tool for the qualitative flatness testing of specular surfaces, based on the defocused detection of a collimated light beam reflected from the tested surface. By inserting a square grid into the path of the illuminated beam, the height map can be calculated by integrating the gradients obtained from the distortion of the grid's reflected image (quantitative extension).

In the past year, activities were concentrated both on methodology and applications as follows.

The effect of the global sample curvature on the qualitative-mode Makyoh imaging was analysed based on a geometrical optical model. It was shown that the global curvature can be taken into account by establishing an equivalent screen-to-sample distance formula containing the global curvature radius. The different regimes of the imaging were analysed in detail [Ref.3.11.].

The swirl defects in *p*-type Si wafers were studied (see Fig. 3.18). White-light interference microscopy confirmed the existence of the circular-structure relief pattern of the wafers. The geometrical optical origin of the swirl-like pattern in the Makyoh image was proven. In addition, a visual swirl pattern in the rough backside was observed in certain wafers, not always correlated with the front swirl pattern.

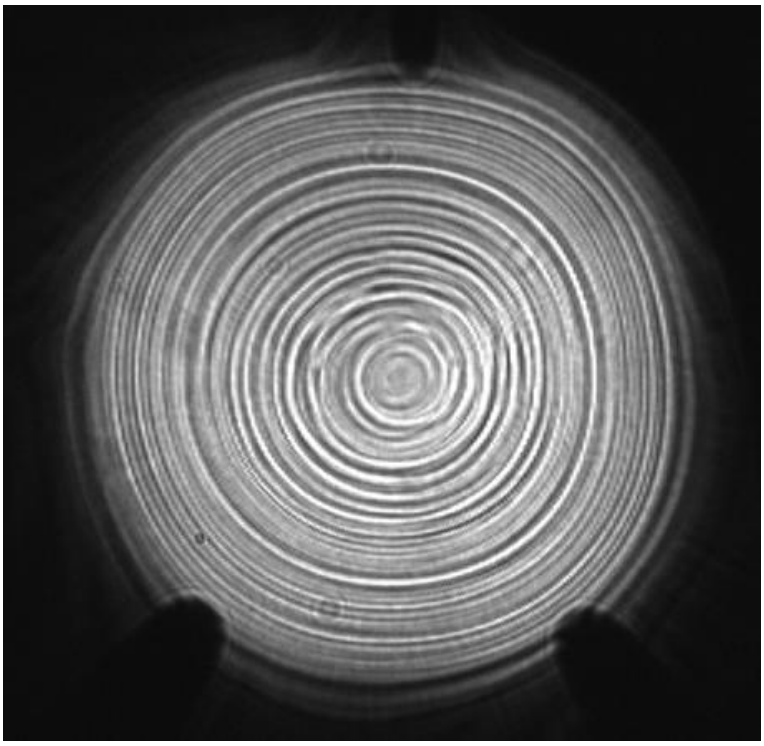

***Figure 3.18**. Typical Makyoh-topography image of a swirl defect in a p-type Si wafer.*

Nanosensors Laboratory

Head: Dr. János VOLK, Ph.D., senior research fellow

Research Staff:

- Gábor BATTISTIG, D.Sc., Deputy Head of Department (part time)
- Zsófia BAJI, Ph.D.
- Nguyen Quoc KHÁNH, Ph.D.
- István Endre LUKÁCS, Ph.D.
- György MOLNÁR, Ph.D.
- Andrea Edit PAP, Ph.D. (part time)
- Zsolt ZOLNAI, Ph.D.

Technical Staff:

- Tamás CSUKÁS, engineer
- János FERENCZ, engineer
- Levente ILLÉS, engineer
- Attila NAGY, technician
- Miklós SZAPPANOS, engineer
- Erika TUNYOGI, engineer

Ph.D. students / Diploma workers:

- János Márk BOZORÁDI, B.Sc. student
- Lucky Kenda PETER, M.Sc. student
- László PÓSA, Ph.D. student
- János RADÓ, Ph.D. student (part time)
- Saeedeh SOLEIMANI, Ph.D. student
- Máté SÜTŐ, M.Sc. student

The Nanosensors Laboratory was established at the beginning of the year from the former Department of Microtechnology. The core infrastructure, having two semiconductor clean rooms, is shared and operated together with the Microsystems Laboratory. Our Mission is to utilize the emerging results of nanotechnology and materials science for novel physical sensors, particularly for micro- and nanometer sized electromechanical systems (MEMS/NEMS). The research activities include the exploration of piezoelectric thin films, the development of semiconductor sensors and low-power consumption or even autonomous sensor networks. The activity of the research group is related to and supported by five domestic projects and several scientific collaborations with national and international partners. Besides, the group also provided characterization- and fabrication-related services for industrial partners, such as Light-Tech Hungary or Semilab.

In the most significant project of the group, titled ‘Advanced Functional Materials for Autonomous Sensor Networks’, the work was divided into three levels: i) research of CMOS compatible piezoelectric alloys; ii) development of MEMS energy harvester and sensor devices; iii) development of wireless proof-of-concept (PoC) sensor nodes. The developed PoC systems aim to monitor different parameters such as tire deformation, machine vibration, and bicycle traffic or gamma radiation. These PoC systems utilize different commercial and in-house developed low-power RF communication protocols.

Nanotechnology related research was carried out mainly in collaboration with Physics Department of BME. On the one hand, the group continued the work on spintronic devices as well, in the framework of National Quantumtechnology Program (HunQuTec). In 2019 we could downscale the period of the electrode pattern to 50 nm and optimized the deposition of superconducting NbTiN thin films. On the other hand, we had also progress in the field of memristors and started to work on the phase-changing VO_2 layers. Besides, the Nanosensors Laboratory conducted research in the field of betha-Ga_2O_3 and plasmonic Au nanoparticles as described below.

Optimization of co-sputtered $Cr_xAl_{1-x}N$ thin films for piezoelectric MEMS devices

NVKP_16-1-2016-0018 “KoFAH”

S. Soleimani, Z. E. Horváth, Zs. Zolnai, Zs. Czigány, and J. Volk

CrAlN alloys can play an important role in the improvement of next generation piezoelectric MEMS devices. However, enhanced piezoelectric constants require high degree of uniaxial orientation in the polycrystalline thin film. In this work $Cr_xAl_{1-x}N$ thin films of varying compositions were deposited at different substrate temperatures by reactive DC co-sputtering technique and compared with respect to their microstructure and optical properties. The relationship between the atomic composition of the layers and the plasma powers over the Al and Cr targets during co-sputtering was revealed accurately by Rutherford Backscattering Spectrometry (RBS). As it was revealed by X-ray and selective area electron diffraction methods, thin films in the range of x=0-0.23 show hexagonal wurzite-type phase, which changes to cubic rock-salt-type structure between $0.23<x<0.31$. At lower Cr cation concentration, like x=0.12 the wurtzite type polycrystalline film indicates uniaxial texture, whereas it is almost randomly oriented at x=0.23. Among the compared compositions $Cr_{0.12}Al_{0.88}N$ showed the strongest c-axis orientation, whereas the optimal substrate temperature was found to be T=350°C. While the refractive index measured by ellipsometry monotonously increases increasing Cr from 2.07 to 2.64 with cation concentration in the range of x=0-0.31, the optical band gap shrinks from 2.65 to 2.23 eV. These optical data can serve as reference in future contactless wafer-scale optical monitoring process.

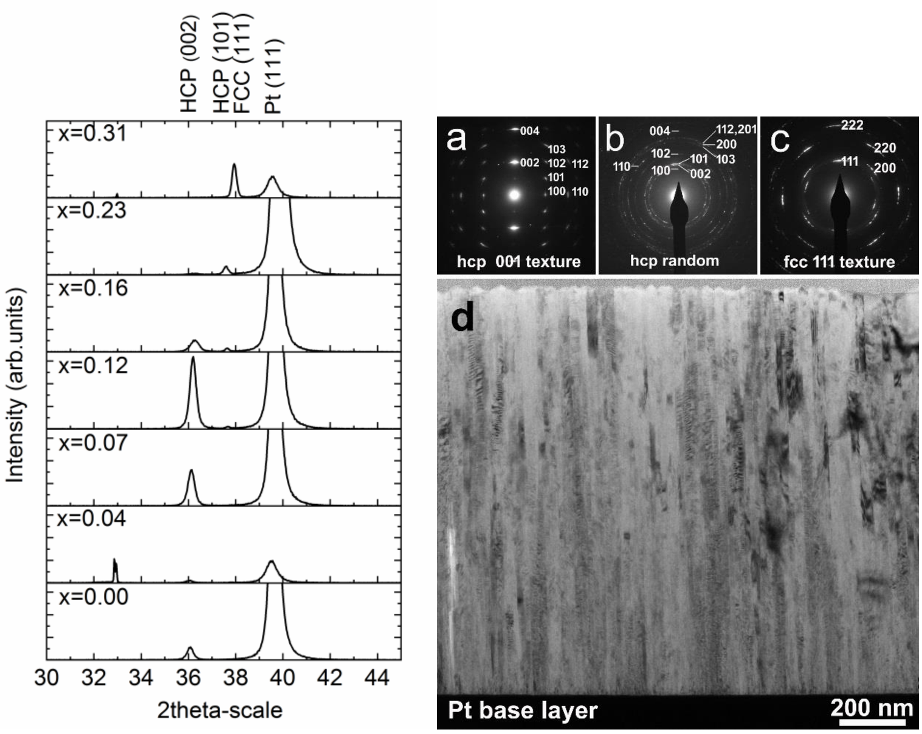

Figure 4.1. *XRD spectra of $Cr_xAl_{1-x}N$ films (x= 0.04, 0.07, 0.12, 0.16, 0.23, and 0.31) (left); SAED pattern of $Cr_xAl_{1-x}N$ films at x=0.12 (a) x=0.23 (b), and x=0.31 (c) cation ratios showing a changing crystal structure (textured hcp, random hcp, and textured fcc, respectively). d) TEM overview image of $Cr_{0.12}Al_{0.88}N$ cross section.*

Energy harvester powered vibration analyzer

NVKP_16-1-2016-0018 "KoFAH"

M. Szappanos, J. Volk

We continued to work on our vibration analyser – or *VibrAn* for short – and improved 1) the measurement range, 2) the energy management system, 3) the wireless transmitter module and 4) introduced the device to the internet, effectively making it an IoT application with a well-defined infrastructure. This device (or rather system) can be used to monitor the vibrations, while the embedded Fourier-transform algorithms provide real-time analyzation features. The device is powered by energy harvesting (piezoelectric, thermoelectric, photovoltaic).

1) The device by now is capable to measure vibrations ranging up to 1.6 kHz with an average precision of 1 mg. This was achieved with a dual accelerometer topology: one of the accelerometers has ultra-low power consumption and can measure up to 200 Hz, while another accelerometer may provide frequency range up to 1.6 kHz albeit with higher energy consumption.

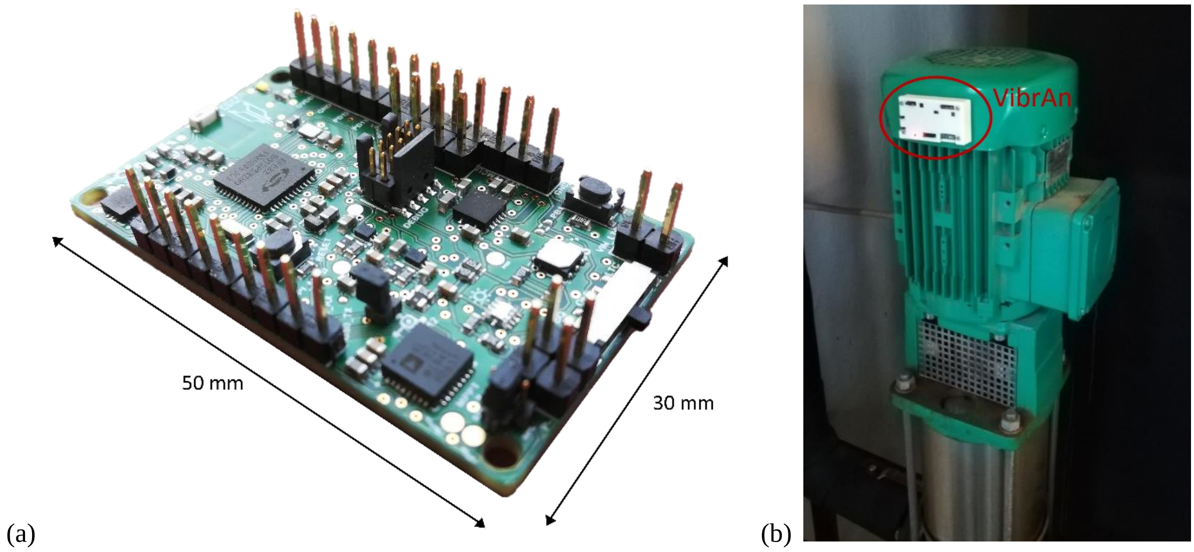

(a) (b)

Figure 4.2. *(a) The vibration analyser circuit board and (b) measurement setup in the engine room of building 29/B attached to an air-ventilation pump*

2) With the upgraded energy management system, it is now possible to harvest energy from three different sources simultaneously, for example connecting a piezoelectric cantilever, a solar cell and a thermoelectric generator to the device will all charge the same on-board super capacitor. Furthermore, both low impedance (thermoelectric generator) and high impedance (piezoelectric cantilever, solar cell) sources are applicable. These features are achieved by having two energy management integrated circuits, one for low and another for high impedance sources.

3) We designed our own radio frequency protocol and transceivers with the help of partners Bonn Hungary Electronics and Datalist Ltd. The protocol operates using the principle of time-to-digital conversion (TDC), thus by creating a radiofrequency transmission with a very low duty-cycle (<1%) of the transmitter radio signal. This short active time makes this an ideal protocol for energy harvesting applications, where low-power operation is critical.

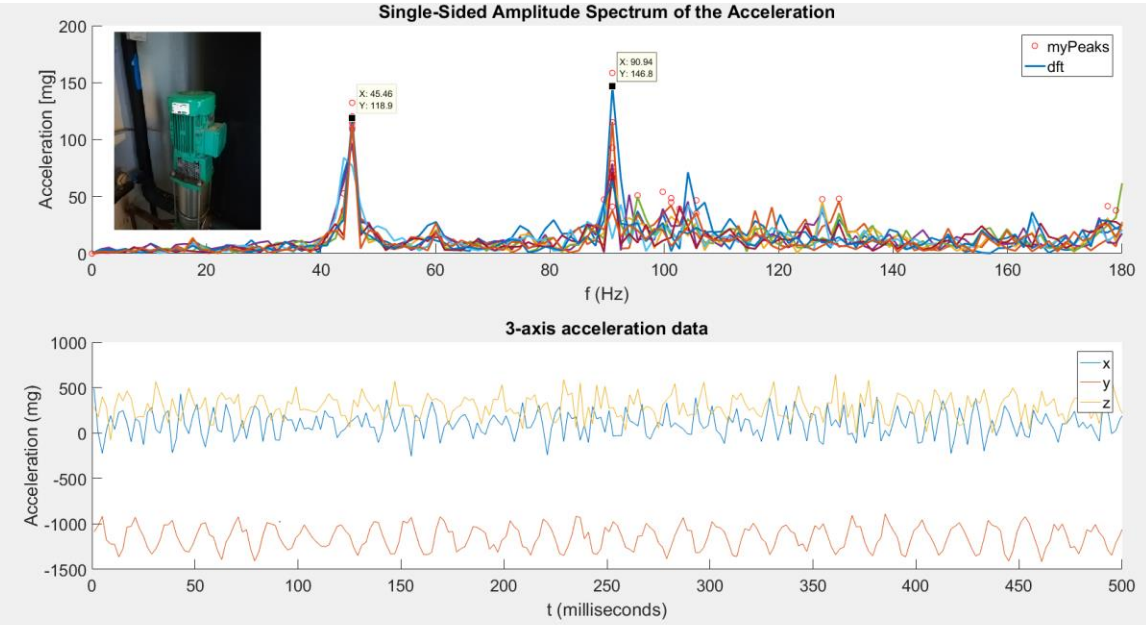

Figure 4.3 *Vibration analyser measurement results on an air-ventilation pump, these results are essential to tune a piezoelectric cantilever for energy harvesting*

4.) The device seen in Fig. 4.2. represents a sensor node in our system. These sensor nodes operate from energy harvesting and they transmit the vibration analysis results to a radio receiver unit. A radio receiver unit can collect data from up to 32 numbers of devices. All the measurement results then get transmitted to a database and can be loaded and further inspected from this (see Fig. 4.4.).

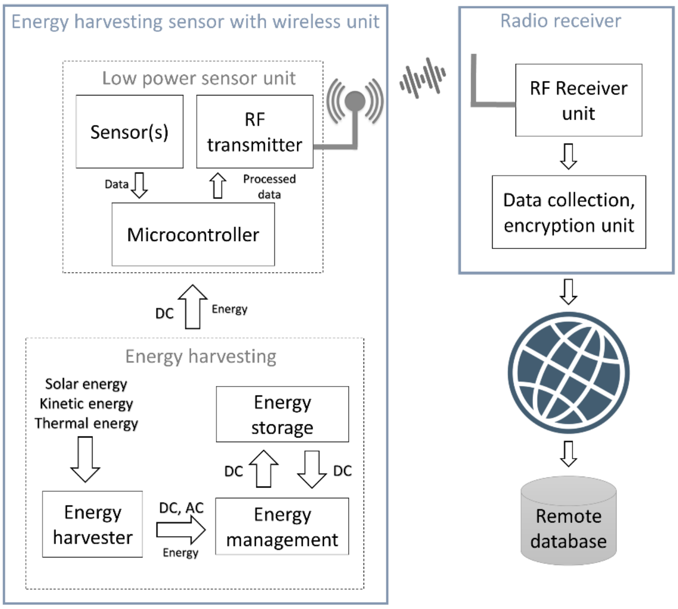

Figure 4.4 *Block diagram of a sensor node with the receiver unit and the connection to the database on the internet*

The system was already tested in a few live demonstrations (the latest at the PowerMEMS 2019 conference during December 2-6) and currently the utilization of this system in a real application is pursued.

Wireless environmental radiation monitoring system – DOZINET

NVKP_16-1-2016-0018 "KoFAH"

E. Tunyogi, M. Szappanos, J. Volk

The primary objective of the DoziNet project is to demonstrate that the radiation detector system, developed by the Space Dosimetry Research Group for rocket experiments, can be combined with the communication units and protocol used and developed by the Nanosensor Laboratory for scalable networks. The targeted system can be integrated into the network of Geiger–Müller (GM) probes installed and operated by the Environmental Protection Service at the KFKI Campus. The same communication protocol will also be used for transmitting data of the airflow sensors to the server.

The electrical design of the GM system was adapted to the ZP1220 and ZP1301 GM tubes used in the GM probes of the Environmental Protection service. The signal is measured on the cathode resistor of the GM tubes. The signal processing unit comprises a pulse shaper (differentiator-integrator unit) and a comparator. At the output of the signal processing unit a monostable multi-vibrator provides square pulses of fixed amplitude and length. The counter/data processing unit is realized by a Happy Gecko EFM32 type microcontroller unit. The measured count rates, in counts per minute, are transmitted to the server via an RN2483 LoRa® transceiver module. Therefore, as an outdoor gateway, a PDTIOT-ISS00 IoT Wirnet Station was also installed on rooftop of building 29B with Ethernet connection and protection against rain and lightning. A GPS module was connected to the Happy Gecko developer kit to provide GPS coordinates as metadata. Measurement data are displayed using NodeRed/ThingSpeak and saved into mysql database. In addition, for demonstration purposes an airflow meter used at the aerosol stations at the KFKI campus was also connected to the Lora Network.

The first breadboard model of the DoziNet system was completed and tested. The prototype of the relocatable GM unit successfully measured the background radiation at the campus and transmitted the measured data to the LoRaWan server. Data were successfully processed and displayed on the web-based NodeRed data viewer (Fig. 4.5).

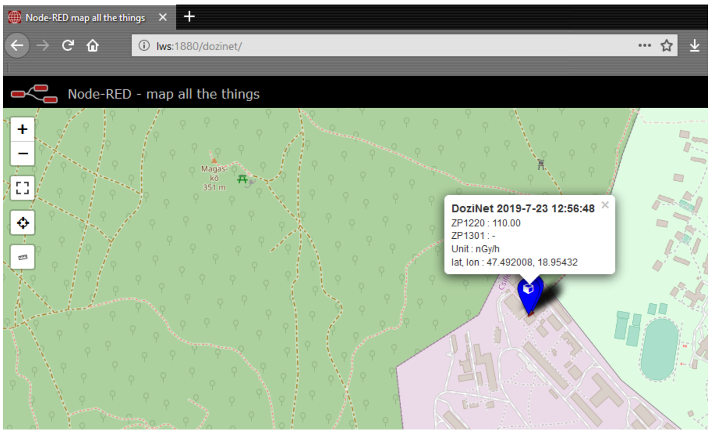

DoziNet 2019-7-23 12:56:48
ZP1220 : 110.00
ZP1301 : -
Unit : nGy/h
lat, lon : 47.492008, 18.95432

Figure 4.5 *The NodeRed based data viewer of the prototype of the DoziNet system*

In the next phase of the project, 3-5 relocatable GM probes, connected by the LoRaWan network to the main server will be added to the present network of GM probes. A similar unit will be optimized for use on radiation protection vehicle (DoziMobile).

Bicycle traffic monitoring system

NVKP_16-1-2016-0018 “KoFAH”

A. Nagy, M. Szappanos, E. Tunyogi, T. Csukás, J. Volk

We designed and built a sensor strip (approximately 1 m long, see Fig. 4.6.), which not only provides bicycle counting and shows the direction with calculated speed of the biker in the traffic, but with a 2-3 cm precision detects the accurate position where the cyclist crossed the sensor strip.

Figure 4.6 *Sensor strip (covered with red adhesive tape) across a bicycle lane*

Figure 4.7 *“I Bike Budapest” (2019.04.28.) bicycle parade with our 6 m long sensor strip (with green adhesive tape)*

The project fits well with KOFAH as in order to transmit the measured bicycle traffic data we need a network. The network used here is called LoRaWAN, which is a wide area network aimed for low power applications and the transmission distance can reach tens of kilometres. We tested this system near Margaret Bridge during a 10 day period (Fig. 4.6.), when the data (time, direction, speed, section) of almost 40.000 cyclists were collected. We also installed the sensor during a big bicycle event (Fig. 4.7.) and successfully covered a 6 m wide road surface. The project results are by now matured enough to move to fabrication by the newly established spin-off company LogLine Sensing Kft.

Nanometer-scale resistive switches

OTKA K128534

L. Pósa, I. E. Lukács

Resistive switching phenomena were detected recently in a wide range of material systems. In proper device geometries these materials exhibit a reversible change of their resistance as voltage is applied. Our studies mainly focus on the fabrication of resistive switches below the resolution of current lithography techniques and the demonstration of complex operation on single or a few devices utilizing their multiple physical timescales. This year the following device constructions were realized studied using our nanofabrication facilities.

Sub-10 nm sized graphene-SiO_x-graphene resistive switch was investigated regarding electrical noise in steady state and during the switching process. The ultra-small active region was formed in graphene nanogap created by controlled electrical breakdown of a 200 nm wide graphene nanoribbon (Fig. 4.8.a-b). The noise spectra were already studied during the graphene breakdown process offering information about the origin of the large resistance fluctuation in graphene nanogap systems. Since the SiO_x resistive switch has several physical timescales, time resolved noise measurements were carried out to gain information about the evolution of the mechanisms in conduction and switching. The SiO_x memristive system was also investigated in nanofabricated Nb-SiO_x-Nb structure. In this case few nanometer size active regions could not be generated by the electromigration of an initially continuous nanowire due to the formation of NbO_x. To exclude the formation of NbO_x, the Nb electrodes were placed 24-34 nm far from each other by electron-beam lithography. Compare to the devices with graphene electrodes, all relevant parameters were similar, however the switching stability and the device-to-device variations were poorer. We demonstrated the multi-level programming capability, and also the 1/f type electrical noise was investigated. In the near future, owing to the superconductive behaviour of Nb, Andreev spectroscopy will be performed to reveal the conduction channels of the resistive switch.

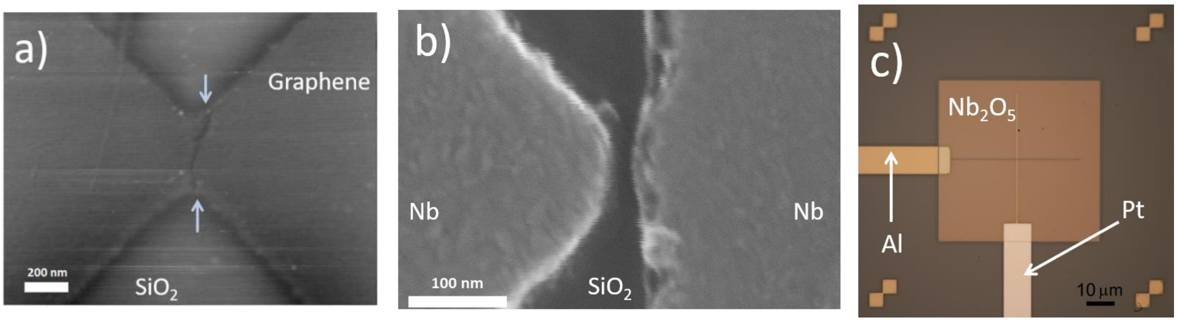

Figure 4.8. *SEM image of graphene constriction after electrical breakdown and electroformation of SiO_2 at the nanogap region. The gap in the graphene is visible as a thin line, marked with arrows. b) A SEM image of the Nb-SiO_x-Nb resistive switch after the sample preparation. The gap between the two Nb electrodes is 24 nm. c) Optical image of Pt/Nb_2O_5/Al vertical resistive switch.*

Resistive switching memories can also be created from atomic-sized contact, in which the switching mechanism is attributed to voltage induced reversible movement of a single atom. Such devices can be realized in many systems: electromigrated nanowire, notched wire MCBJ or STM, however these arrangements either do not have high enough mechanical stability, or a new contact cannot be defined again after complete rupture of the wire. Nanofabricated suspended silver nanowire can combine the advantages of these arrangements, it has high stability and the contact can be pushed several times. The structure lies on a spring steel substrate covered by polyimide providing smooth surface for the nanofabricated structure. During the mechanical rupture we could observe conduction quantization at room temperature and the resistive switching of atomic sized contact was also demonstrated.

The switching behaviour of Nb_2O_5 is attributed to the valence change effect, in which the conductive filament is built up by local enrichment of oxygen vacancies. Typically, one of the contacts serves as an oxygen reservoir in forming oxides, while the other one is inert (i.e. Pt). This year three different device structures were fabricated in vertical arrangement, where two metal wires cross each other perpendicularly (Fig. 4.8.c). Widths of the metal wires were varied between 100 nm and 5 μm. The inert electrode was 50 nm thick Pt for all types of devices (bottom electrode), while the other electrode was either aluminium or titanium (top electrode). Between the two metal electrodes an about 16 nm thick Nb_2O_5 layer was deposited by reactive sputtering. In case of one set of devices with aluminium top electrode the Nb_2O_5 layer was exposed to argon plasma for 2 min, which typically aids the electroforming process, when the insulator layer transforms into switchable state. The devices with Ti top electrode did not show robust switching effect, only weak resistance changes: less than 1.5 switching ratio could be observed for 100 cycles. In case of Al top electrode we could induce stable resistive switching independently of the plasma treatment and the wire width. The electroforming voltage for the plasma etched devices was lower; it decreased from 2.8 V to 2.3 V. We could switch these devices more than 10 thousand times under ambient condition for 5 months. We demonstrated signal detection in a noisy background using only single device and we also studied their 1/f type electrical noise.

The work was done in collaboration with Physics Department at BME.

Optimization of VO_2 thin films for memristors

OTKA K128534

Gy. Molnár, L. Pósa

The metal-insulator transition phenomenon accompanied by a rapid reversible phase transition in vanadium dioxide (VO_2) has attracted great attention both from scientific and from technological point of view due to the various potential applications. Vanadium dioxide thin films are prepared by different physical and chemical vapour deposition methods.

During our experiments, thin vanadium oxide films were prepared by electron gun evaporation of vanadium metal in a high vacuum environment followed by the annealing in the presence of air. According to the available literature, initially, glass plates were used as substrates. It was shown, that in contrast to the literature the expected VO_2 phase was not present in the layers. The detailed x-ray diffraction measurements revealed that the sodium content of the glass substrates interacted with the layer, and three different sodium-vanadium-oxygen phases were formed (NaV_3O_8, $Na_{0.76}V_6O_{15}$, $Na_5V_{12}O_{32}$) instead. The replacement of the glass substrates by SiO_2 covered Si wafers resulted in the appearance of the desired VO_2 phase. The substrates were: (a) 100 nm SiO_2 covered Si wafers, and (b) 1.3 μm SiO_2 covered Si wafers. 200 nm vanadium metal was evaporated by electron gun onto the substrates in a high vacuum environment. The heat treatment was carried out in a tube furnace at temperatures of 350-500°C. The annealing times ranged 1 - 4 hours. Initially, the samples were inserted into the hot furnace, and removed at the end of heat treatment. Later, slow temperature ramping and slow cooling processes were applied, too. X-ray diffraction measurement confirmed the presence of the VO_2 phase in the layers. For temperature dependent resistivity measurements, 1 mm diameter Cr/Au contacts were evaporated onto the vanadium oxide through a contact mask. According to the electric measurements the metal-insulator transition could be detected in some samples. The best results were achieved in case of 400°C and 3 hours annealing, the resistance change almost reached two orders of magnitude. In some cases, the heat treatment caused the appearance of bubbles in the layers. The quantity of bubbles depended on the temperature and time of the annealing, and on the thickness of the SiO_2 layer of the substrates too. The work was done in collaboration with Physics Department at BME.

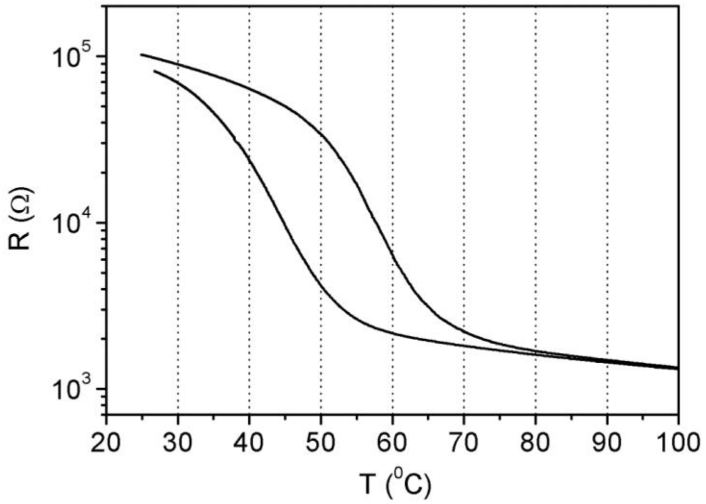

Figure 4.9. *Temperature dependence of electrical resistance of a VO_x film on SiO_2/Si substrates after annealing at 400°C for 3 hours*

Optimization of superconducting microwave resonators and high spatial resolution bottom gates

National Quantum Technology Program (HunQuTech)

I. Lukács, M. Sütő

In 2019 we continued our cooperation with the consortium of the National Quantum Technology Program in the field of generating, sharing, and developing quantum information networks. Low dimensional nanosystems and quantum nano-circuits were implemented by our group whereas the consortium partners are responsible for theoretical models and measurements. The charge density in InAs nanowires can be well manipulated by an electrical potential on high resolution gate electrodes resulting in quantum dots of adjustable width and depth. Topological phases of matter are accompanied by protected surface states or exotic degenerate excitations such as Majorana modes or Haldane's localized spinons as well as Weyl degeneracies. According to the literature, the high-frequency modulation of the potential of quantum dots rotates the quantum bit through spin-orbit coupling. The coupling of quantum circuits to superconducting resonators enables faster characterization of quantum circuits, for example by reading the charge and spin quantum bits.

NbTiN layer on intrinsic silicon wafer is a good choice to prepare superconducting resonator due to its chemical stability, higher critical temperature and simplicity to be produced by reactive sputtering. We used an AJA UHV system for deposition at a DC sputtering power of 150W on a 3 inch diameter Nb(60%)Ti(40%) source. The applied Argon flow rate was 10 sccm and the gate valve of TMP was fixed at a chamber pressure of 2.5 mTorr. In order to optimize the NbTiN layer we deposited 14 samples at several nitrogen flow rates. In some cases we also used additional RF bias plasma at a power of 5 W on the sample holder.

Sample name	**N_2 flow rate**	**Bias plasma**	**T_c (K)**
S_2.0	2.0	Off	12.8±0.3
S_2.2	2.2	Off	13±0.3
S_2.4	2.4	Off	12.8±0.3
S_2.6	2.6	Off	12.8±0.1
S_2.8	2.8	Off	12.1±0.1
S_3.2	3.2	Off	11.2±0.5
S_3.6	3.6	Off	10±0.8
S_4.0	4.0	Off	10.1±0.3
S_6.0	6.0	Off	6±0.1
S_8.0	8.0	Off	<5
S_2.2_RF	2.2	On	14±1
S_2.4_RF	2.4	On	14.6±0.5
S_2.6_RF	2.6	On	14±1
S_2.8_RF	2.8	On	10.1±0.3

Table 4.1. *Deposited layers with its critical temperatures*

The designed resonators with several geometries were formed by electron beam lithography and reactive ion etching of NbTiN on sample S_2.4_RF (Fig. 4.10.a). From geometry (Fig. 4.10.b) and transmission measurements (Fig. 4.11.) of the coplanar transmission line the inner and coupling quality factors, the specific capacity, the magnetic inductance, the effective dielectric constant, the kinetic inductance and the square kinetic inductance of the system (Table 4.2) can be determined.

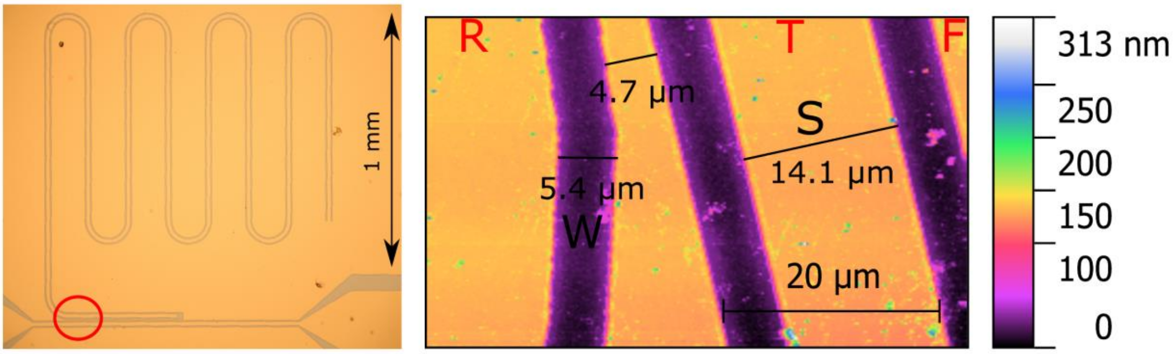

(a) (b)

Figure 4.10. *(a) Optical microscope image of a superconductor resonator and (b)AFM image with the relevant geometric data*

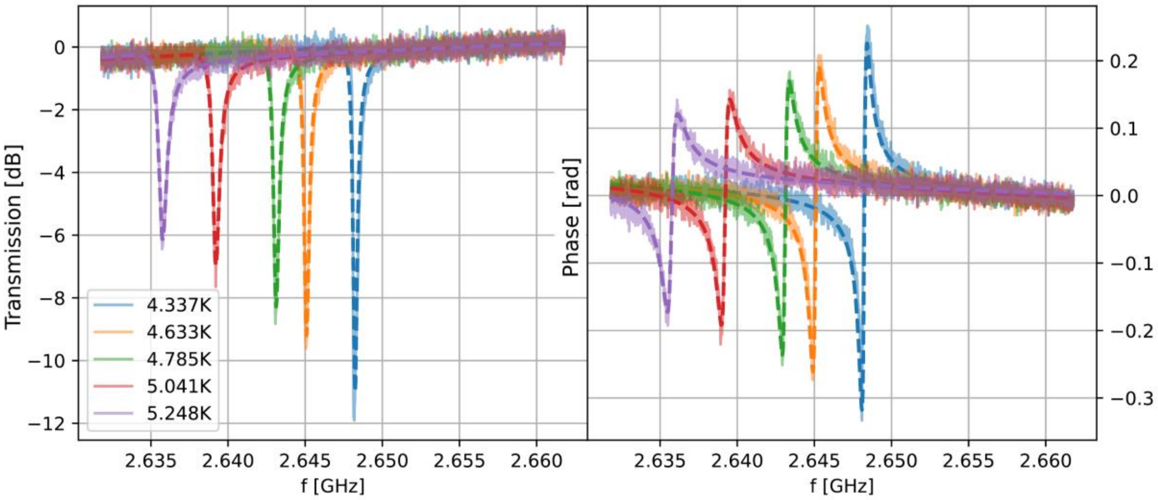

Figure 4.11. *Transmission measurements of the resonator shown in Figure 1 at various temperatures*

Q_i	Q_c	C pF/m	ε_{eff}	L (nH/m)	L_m (nH/m)	L_k (nH/m)	$L_k^{\square}$(pH/□)
7787	14972	186	12.12	727	380	347	4.4

Table 4.2. *The calculated characteristic values of the shown CTL*

In order to increase the resolution of electron transmission measurements through tunable quantum dot system in InAs nanowire, it is necessary to decrease the spatial period of the gate electrodes. Previously gate electrodes were fabricated from Ti/Au vaporized on silica layer by lift-off technology. By reducing the distance between the Ti/Au gate electrodes, gold can easily migrate on the surface of the chip at low temperature, causing an open or short circuit in the electrode system. By substituting the gold to platinum and optimizing the sample preparation processes we can reduce the spatial resolution of bottom gates from 80 nm to 50 nm (Fig. 4.12.).

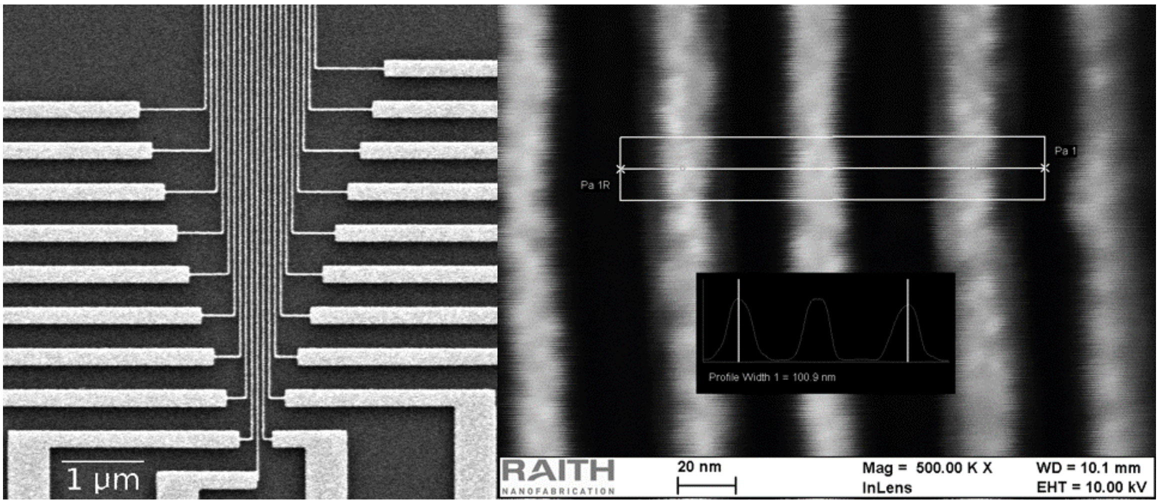

Figure 4.12. *SEM images of high spatial resolution Ti/Pt bottom gates on* SiO_2

Atomic layer deposition and characterisation of Ga_2O_3 films

OTKA PD116579

Zs. Baji, I. Cora, Z. Szabó, Zs. E. Horváth, E. Agócs

Gallium oxide (Ga_2O_3) is a wide bandgap (4,7-4,9eV) semiconducting material with a number of crucial applications in sensorics, optoelectronics and catalysis. Due to its UV transparency and its absorption of deep-UV, it may find important applications in photonics and as a DUV photo-detector. The present work focuses on the atomic layer deposition and annealing of Ga_2O_3 prepared with $Ga_2(NMe_2)_6$, which promises some advantages over the other often used chemicals, such as a lower deposition temperature. The Ga_2O_3 films in this work were prepared at deposition temperatures between 100°C and 300°C. Although it has been shown to be possible to grow such films in a temperature range of 100°C to 300°C, the precursor source had to be heated to 130°C to achieve sufficient vapour pressure. At temperatures exceeding 270°C, the precursor decomposes resulting in growth of inhomogeneous rough CVD-like film. The growth rate within the ALD window is 0.4 - 0.8 Å/cycle at 130°C - 270°C. The films prepared with these optimised parameters are homogeneous, and as can be seen in Fig. 4.13., their roughness is below 1nm. All the as deposited films are amorphous.

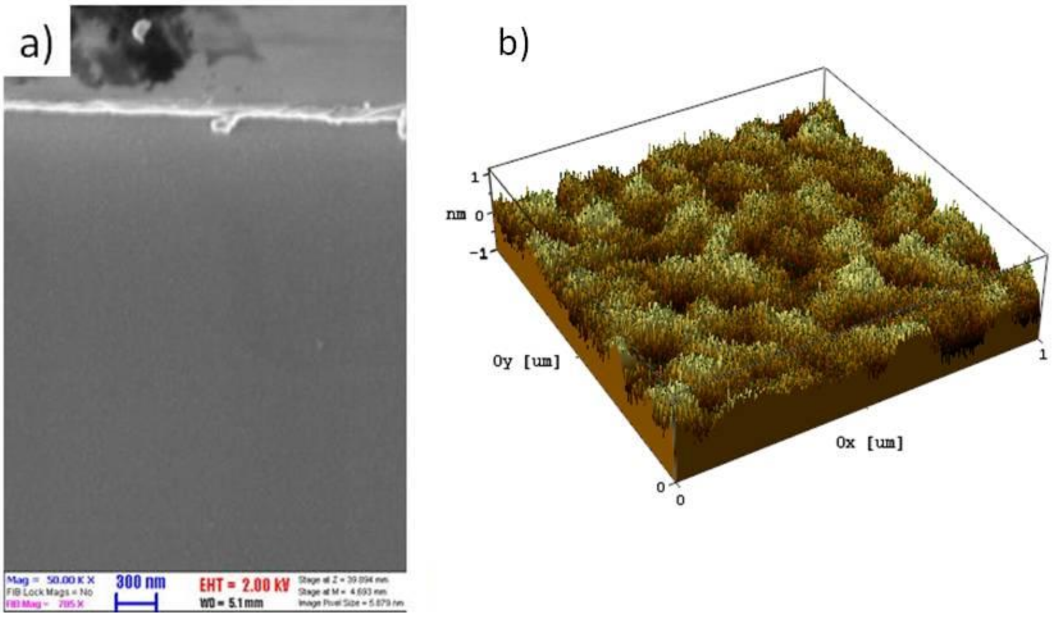

Figure 4.13. *The morphology of the Ga_2O_3 layer deposited at 130°C*

To induce a crystallisation in the ALD Ga_2O_3 films, different annealing procedures were tested. 3 hour long heat treatments at 900°C were required to achieve crystalline films. Fig 2a shows that in the film annealed in nitrogen atmosphere a crystallisation started, but according to XRD measurements, these films remained still mainly amorphous. On the other hand, annealing in oxygen resulted in crystalline β-Ga_2O_3 films with large crystallites on the surface, as it is shown in fig. 2.b and c. The films are textured and oriented mainly in the (-204) direction.

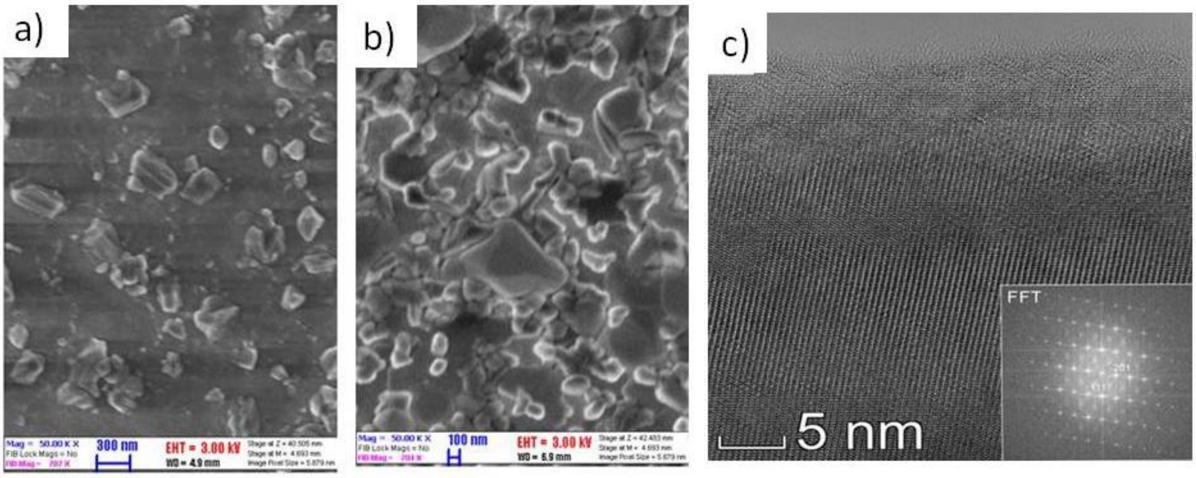

Figure 4.14. *SEM image of the film after annealing in nitrogen (a), and oxygen (b) at 900°C for 3 hours, and the TEM image of the latter one*

To determine the electrical parameters of the layers, spectroscopic ellipsometric measurements were conducted. As it is shown in Fig. 4.15., the bandgaps of all deposited layers were within the regime predicted by the literature: between 4eV and 4.8 eV. The deposition temperature also affected the bandgap of the films; the ones deposited at 130°C had the widest bandgap. The dielectric constants are between 3.2 and 3.5, i.e. this property was not significantly influenced by the deposition temperature. The annealing reduced the dielectric constants of the layers significantly.

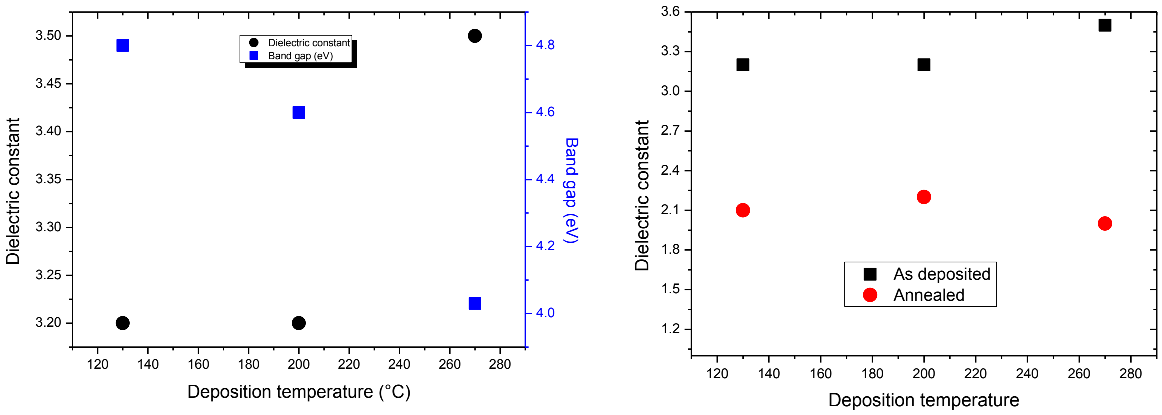

Figure 4.15. *Dielectric constants and bandgaps of the as deposited and annealed films as determined by spectroscopic ellipsometry.*

Radiative damping of surface plasmon resonance in gold nanoparticles: the influence of shape, size, and substrate material

Z. Zolnai, D. Zámbó, D. P. Szekrényes, and A. Deák

In the surface plasmon resonance (SPR) of metal nanoparticles (NPs) the linewidth and spectral intensity – besides the shape and size of the particles – is determined by radiative and non-radiative damping terms. So far mainly the role of surface/chemical interface damping term was investigated in the detection of different ligand molecules bound to the surface of the NPs, and less attention was paid to the role of radiation damping (Γ_{Rad}) in plasmonic NPs. Nevertheless, to evaluate the intensity and the overall damping, i.e., full width at half maximum of the SPR spectra a reliable estimation of Γ_{Rad} is also required. The value of Γ_{Rad} and thus spectral intensity depends on the local environment of NPs, that is, the substrate material and the dielectric function of the surrounding media. In case of polarizable substrates supporting plasmonic NPs the dipole moment of the NP is coupled to the dipole moment induced by the mirror charge appearing in the substrate (or, in the NP shell for core-shell NPs).

In this work we investigated the effect of the underlying material on the radiation damping for gold nanospheres (NS) and nanorods (NR) with dark-field single-particle scattering spectroscopy correlated with scanning electron microscopy analysis. Besides spectrum shape, the relative intensities of the optical spectra were also considered as the detector system is corrected for spectral intensity vs. the excitation wavelength. Au NPs on glass, Si, and SiC, i.e., on substrates with significantly different refractive indices were analyzed. The effect of the anisotropic environment was taken into account through an effective dielectric constant which is extracted from the resonance frequency of SPR.

Through the correlation of the optical scattering spectra with the NP size extracted from SEM analysis, significantly higher relative spectral intensity and radiation damping was found for nanospheres deposited on Si and SiC as compared to the nanospheres deposited on glass. For nanorods an opposite effect was observed, i.e., higher relative intensity, but lower radiation damping was observed for NRs on glass as compared to NRs on Si. These findings can be explained by a dipole oscillator model that relates the spectral intensity with the net polarization of the system, the SPR frequency, and the effective dielectric constant of the NP environment. For spheres (rods), the substrate mirror charge induced polarization is parallel (opposite) to the transversal (longitudinal) polarization of the Au NPs induced by the excitation light source. As the induced polarization of the substrate is higher for higher refractive index, the observed trends in Γ_{Rad} and intensity can be understood considering the net polarization of the different systems. We note that besides the oscillator model, possible influence due to reflectance of the incident light and the NPs dipole radiation on the substrate surface and the spectral transmittance of the substrate/air interface on the detected intensity were estimated.

This work can pave the way toward the detection of ligand molecules and local dielectric environment through the parameters of the SPR resonance of metal nanoparticles.

Investigation of atomic or molecular processes induced by ultrashort laser and/or electron pulses

2018-1.2.1-NKP-2018-00010

G. Battistig

The collaboration of the three institutions (University of Pécs, Faculty of Sciences, Institute of Physics, Institute for Nuclear Research and MFA) of complementary competencies develops a new tool able to study atomic and molecular processes triggered by the combined action of photons and electrons. The ultra-short pulses of electrons needed for the process will be produced by terahertz radiation. The new scientific tool is planned to be setup and operate at ELI-ALP.

The task of MFA in the project is aimed at producing micro- and nano-sized structures and devices in which the terahertz electromagnetic space can accelerate electron packets with great efficiency. For the production and processing of semiconductor and dielectric structures in the required micrometer size range, only the MFA Microtechnology Laboratories provide the appropriate technology and expertise.

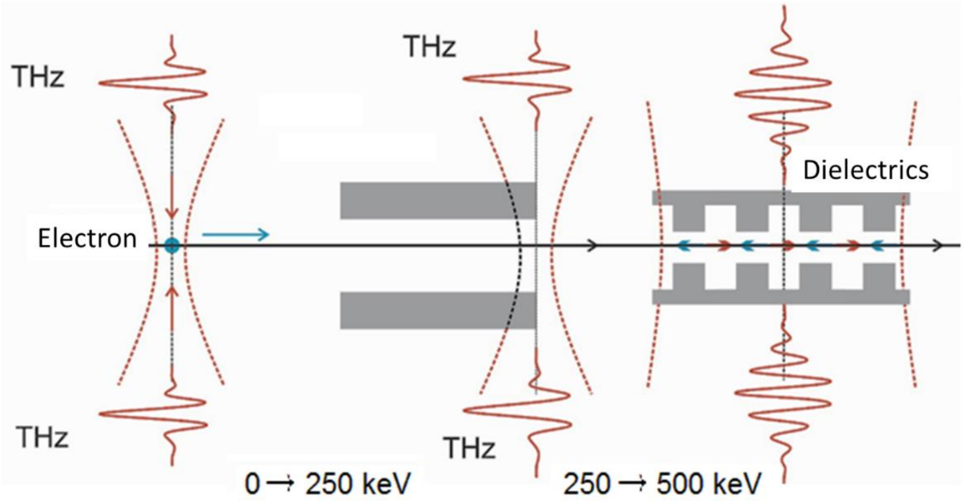

Figure 4.16. *Principle of electron acceleration by electromagnetic field of THz radiation*

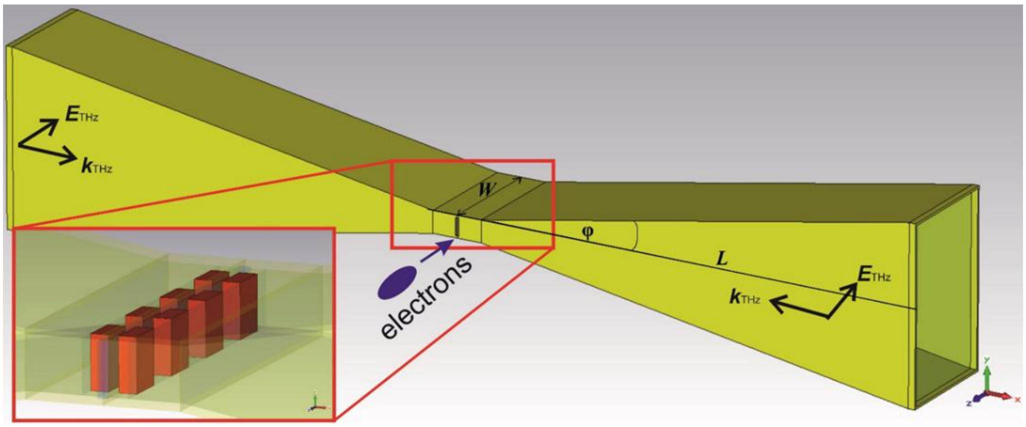

Figure 4.17. *The planned setup: THz illumination of the dielectric microstructure (inset) through the waveguides. The electromagnetic field across the structure accelerates the electron packets flying through the microstructure.*

Microsystems Laboratory

Head: Dr. Péter FÜRJES, Ph.D., senior research fellow

Researchers:

- István BÁRSONY, member of HAS,
- Orsolya BÁLINT-HAKKEL, Ph.D. , maternity leave
- Ferenc BÍRÓ, Ph.D.
- Csaba DÜCSŐ, Ph.D.
- Péter FÖLDESY, Ph.D.
- Péter FÜRJES, Ph.D.
- Zoltán HAJNAL, Ph.D.
- István RÉTI, Ph.D.
- Zoltán SZABÓ, PhD.

PhD Students:

- Anita BÁNYAI (ÓE Uni Óbuda)
- János RADÓ (ÓE Uni Óbuda)
- Eszter Leellősyné Tóth (Pazmany Peter Cath. Uni– defence in 2019)

Engineers / technicians:

- György ALTMANN, technician
- Gabriella BÍRÓ, technician
- Tibor CSARNAI, technician
- Magda ERŐS, technician
- János FERENCZ, electrical engineer
- Petra HERMANN, bioengineer
- Róbert HODOVÁN, mechatronic engineer
- Csaba LÁZÁR, electrical engineer
- Margit PAJER, technician
- Zsuzsanna Brigitta SIK, bioengineer

The main goal of the Microsystems Laboratory is to research and develop integrated sensors and sensor systems, MEMS and BioMEMS devices fabricated by silicon or polymer micro- and nanomachining technology. The activity covers the characterisation, materials systems and technology solutions and the development of sensing principles. The application of micromachining technology enables the miniaturisation of analytical systems and integration of various functions of sample preparation, sensing, readout, actuation or communication, respectively. The laboratory is focusing on the development of mechanical, physical, chemical (and biochemical) sensors, functional micro- and nanofluidic devices, implantable microsystems and infrared LED.

Our medium-term goal is to broaden the spectra of perspective research topics of MEMS systems and to develop a systematic organisation and form a dynamic and growing research group in the Microsystems Laboratory. Considering the financial environment our research directions fit to the European and Hungarian strategic roadmaps and direct ives (S3 - National Smart Specialisation Strategy) by the following research topics:

- Healthy society & wellbeing: BioMEMS, Lab-on-a-Chip, Organ-on-a-Chip, microfluidic systems, implantable, wearable devices, personal medicine, continuous monitoring, etc.
- Vehicle technologies: Driving safety sensors
- Clean and renewable energies: Low consumption electronics, sensors for energy industry, characterisation photovoltaic systems,

- Sustainable environment: Environment safety sensors (water monitoring), gas sensors (smart home, smart clothes)
- Healthy food: Food safety sensors, spectroscopy

Research group structure in the Laboratory

The development of MEMS devices requires solid design capacity and advanced cooperation among the research and technical staffs for precise operation of the full micromachining fabrication line. Actually, 9 researchers, 5 engineers / PhD student and 5 technicians work for the Laboratory with close and flexible cooperation with the colleagues of the Nanosensors Laboratory.

- **MEMS / smart sensors (Csaba Dücső, Ferenc Bíró, János Radó):** The team's primary expertise is traditional MEMS sensor development, such as gas, environmental and mechanical sensors with an emphasis on the technology of 3D microstructure implementation.
- **BioMEMS, medical applications (Péter Fürjes, Csaba Dücső, János Radó):** Silicon based sensor development and their electro-mechanical integration, specifically for medical applications, are the long-term goals in this topic. The medical field demands the development of tools in low numbers that have extensive added value, which also aligns with the European strategic directives. The topic includes Si and flexible integrated microstructure development as subcontractors in the NAP project.
- **Lab-on-a-Chip / Organ-on-a-Chip (Péter Fürjes, Orsolya Hakkel):** The LoC and OoC systems are essential building blocks of Point-of-Care diagnostic tools in the medical field. We have vast experience in this topic, especially in microfluidics. Accordingly, we actively collaborate with companies in this field (77 Elektronika Kft., Diagnosticum Zrt.) as well.
- **IRLED (Zoltán Szabó, Ferenc Bíró, István Réti):** We fabricate and develop a few thousand infrared LEDs per year (partners: Anton Paar, Senop). Additionally, we envisaged a larger scope spectroscopic development and application in the frame of an actual ECSEL grant. Environmental analytics and food safety applications could be important goals for IR spectroscopy and other optical developments.
- **Integrated systems / Heterogeous integration /IoT (Péter Földesy):** Research grants ask for a certain level of preparedness, which usually includes demo systems (sometimes prototypes). Therefore, the requirements of developed instruments and their electro-mechanical integration are becoming a greater task.
- **Technology, FEM / Multiphysics Modelling (Zoltán Hajnal):** Modelling, such as digital twin, is a widely applied method in engineering practice. It speeds up development and manufacturing time of prototypes while also lowering costs. The application of these methods is not as straight forward for the development of microstructures due to the effects of microenvironments. However, the use of these simulations is indispensable. The group is effectively corroborating the research and development tasks.

Infrastructure and technological competencies

This is a unique infrastructure in Hungary accordingly its sustainable operation and development is strategic goal. The infrastructure is open for academic and industrial partners to realize complex, purpose-designed microsystems, nanocircuits, as well as Lab-on-a-Chip devices.

The high-tech microtechnology related fabrication and characterisation systems work in a class 10 cleanroom facility. The laboratory is dedicated for 3D processing of 3” and 4” Si / glass / polymer substrates with maximal resolution of 1µm, together with lithographic mask manufacturing. Electron beam lithography and focused ion beam (FIB) milling are also available with resolution of 20nm. The structural design and development are also supported by multi-domain Finite-Element Modelling (FEM), and process simulation. Wide spectra of characterisation techniques are also available: optical (fluorescent) and electron microscopy (SEM and EDS), atomic force microscopy (AFM), profilometry, optical and electrical measurements, electrochemical impedance spectroscopy, microfluidic characterisation, mechanical vibration and climate test chambers, UV / VIS / IR / FTIR spectroscopy, etc.

Available micromachining techniques:

- Patterning – mask design, laser pattern generator, photolithography, (double side) alignment, electron beam lithography (E-Beam), Focused Ion Beam processing – FIB milling, nanoimprinting
- Structured polymer layers – PMMA, PI, SU8 patterning, micromoulding, soft lithography – PDMS
- Wet chemistry – chemical wafer cleaning, isotropic and anisotropic etching techniques
- Dry etching – deep reactive ion etching, plasma etching techniques (DRIE, RIE)
- High temperature processes – thermal oxidation, diffusion, annealing, rapid thermal annealing (RTA)
- Physical thin film depositions – Thermal and electron beam evaporation, DC and RF Sputtering
- Chemical thin film depositions – Atmospheric and Low Pressure Chemical Vapour Deposition (CVD, LPCVD, LTO), thermal and plasma enhanced Atomic Layer Deposition (ALD)
- Liquid Phase Epitaxy of III-V compound semiconductors (LED manufacturing)
- Wafer bonding – Si-glass, glass-glass, polymer-glass anodic and thermal bonding
- Chip dicing, wire bonding especially for sensor applications
- Special packaging techniques and methods

Cooperations

Apart from the European and bilateral international R&D projects wide cooperative and knowledge network was established by the large number of joint research projects with Hungarian research centres (ATOMKI, BME, PPKE, SE, SZBK, PTE, WIGNER, SZTAKI) and research groups to perform interdisciplinary research. We are supporting the National Quantum Technology Programme (HunQuTech) and the National Brain Programme by our infrastructural background. Besides the scientific projects, the Lab offers technology development services, with these industrial partners (SEMILAB ZRt, Diagnosticum ZRt, 77 Elektronika Kft, CellSorter, Mirrotron Kft., Z-Microsystems (Austria), Anton Paar (Austria), Senop (Finland), FRK (Poland), Philips (The Netherlands)) the higher technology readiness levels are also achievable (TRL 2 → 6).

The technological and scientific results are directly transferred into the higher education, by means of several lectures, laboratory practices, TDK, diploma and PhD works. Our researchers give lectures at various departments of BME, PPKE, ÓE, DE, ELTE.

Major research projects

The researchers of the Microsystems Laboratory are involved in development, fabrication and integration micro- and nanosystems, sensor structures to open new perspectives in the field of medical diagnostics, Minimal Invasive Surgery techniques, energy-efficient autonomous systems (sensor networks, autonomous driving). Our interest covers the topics of optical analytics (spectroscopy), environmental and safety (gas detectors) sensors.

- A pilot line for the next generation of smart catheters and implants – POSITION-II, ECSEL 2017-2-783132
- Low power consumption-type nano-sensors for gas detection in harsh environment – Hungarian-Russian Collaborative Research Program - 2017-2.3.4-TéT-RU-2017-00006
- Development of the microtechnology infrastructure to achieve European compatibility - VEKOP-2.3.3-15-2016-00010
- Development of Rapid Urine Bacteria Analyzer – VEKOP-2.2.1-16-2017-00001-„ Versenyképességi és Kiválósági Együttműködések”

- Investigation of novel implant materials for high-resolution, multiparametric imaging of cortical activity, OTKA K120143
- Application chiptechnology for improvement the success of human in vitro fertilisation – GINOP-2.3.2-15 „Stratégiai K+F műhelyek kiválósága”
- Manufacturing optrode devices applied in the NKP_17 „National Brain Programme” - 2017_1.2.1-NKP-2017-00002
- Development and manufacturing near infrared LED devices

Low power consumption-type nano-sensors for gas detection in harsh environment

Hungarian-Russian Collaborative Research Program 2017-2.3.4-TéT-RU-2017-00006

F. Bíró, Z. Hajnal, I. Bársony, Cs. Dücső

The ultimate goal of the project is to develop a novel calorimetric gas sensor family what is able to detect CH_4, NH_3 and CO up to their lower explosion limits (LEL), i.e. 5, 15 and 12,5%, respectively. The sensors can be operated in harsh environment without any risk of ignition even over LEL concentrations. Beside the optical and electrochemical approaches and the corresponding systems, sensors operate with catalytic-calorimetric principle are still among the dominant devices in safety systems.

The catalytic device is expected to detect lower gas concentration and exhibit better sensitivity, than the heat-conductivity type device which is simpler and still in use in practice. Still a more sophisticated device applies both sensors, thereby extending the detection range and improves the detection reliability.

Another advantage is the commonly used filament or micro-hotplate structure. Therefore, to develop a micro-hotplate meets all the mechanical, electrical and chemical requirements is essential for a reliable and commercialized device.

The activity of the Microsystems Lab can be described in 2 sections (1) Development and testing of the final micro-hotplate structure optimized for high temperature thermal-catalytic sensing processes and (2) Joint decision making on the selection of the final structures, components of the device for the demonstration at the end of the project; and the construction of heat conductivity type sensing device.

The optimum layer structure of the full membrane micro-hotplate was elaborated and finalized. The vertical structure was set to parallel provide minimum stress (~100MPa, but definitely below 200MPa), protection of the filaments from the environment - and vice-versa! - as well as appropriate thermal and electrical isolation. Nevertheless, the geometry of the filament is determining both in terms of lifetime and sensor response. The catalysis requires operation at elevated temperature. Depending on the catalyst applied it must be 500-700^{o}C. There are two substantial issues; the temperature and its gradient along the filament as well as along the heated area of the hotplate must be kept as low as possible, thereby the temperature of the active hotplate surface must be uniform. Having concluded the deterioration mechanisms we designed and processed alternative filament geometries. Thereby we tuned the geometry of the filament to exhibit better uniformity, smaller gradient but still having large cross sections to withstand migration related deterioration.

Using the high resolution visible pyrometry method we analysed the latest structures and found very good temperature uniformity. The heated area exhibits less than ±5 ^{o}C temperature difference at 550^{o}C for the appropriately tailored heater structure. This structure will be used for testing catalyst and also in the demo devices. The targeted operation temperature is 550^{o}C or below, which can be achieved with max. 27mW/element. We have been testing the long time performance of micro-hotplates. After 6 months continuous operation at 600 ^{o}C the resistance change of the filament is around 1.1-1.2%, therefore we conclude that in a Wheatstone-bridge configuration the resistance drift will be much less than the required 1%/year.

As the heat conductivity mode is also feasible for hydrogen or higher concentration methane detection we constructed chips for testing this operation. One of the hotplates of chips presented above was encapsulated with a dome like Si element and vacuum-sealed around the cover and also around the bottom of the chip. Fig. 5.1. shows the structure.

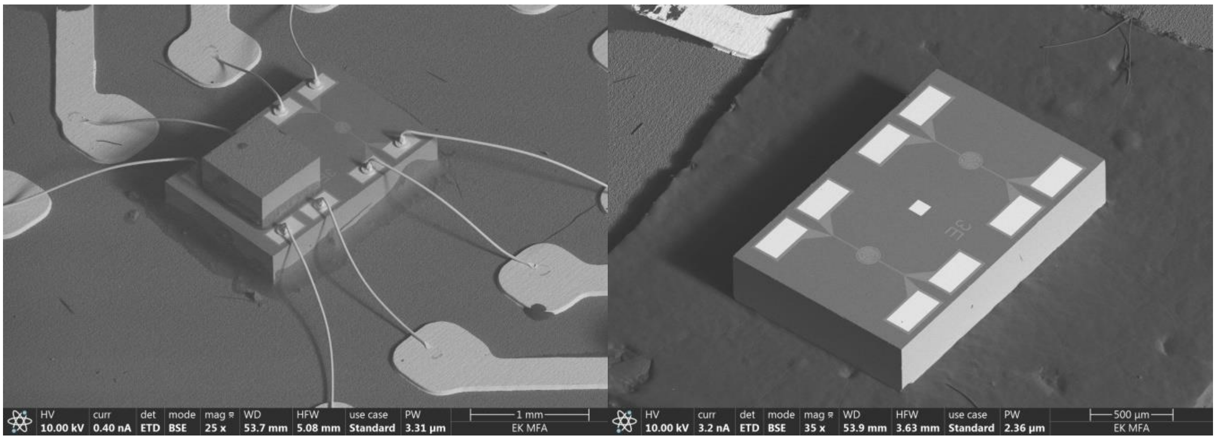

Figure 5.1. *Construction of the heat conductivity sensor. The two identical micro-hotplates (left) and one of the hotplates are vacuum-sealed(right). The chip is mounted on a small PCB for testing.*

Thermal conductivity sensors formed from micro-heaters were tested in synthetic air-methane gas mixture. Before test every filament was heated in synthetic air for at least 3 hours by 21 mW. Active and reference element were connected in Wheatstone-bridge arrangement and supplied by constant voltage.

Design and development of a 3D Flex-to-Rigid compatible force sensor

H2020-ECSEL-2017-2-783132 “POSITION-II”, 2018-2.1.6-NEMZ-ECSEL-2018-00001

J. Radó, P. Asztalos, Z. Hajnal, P. Földesy, Gy. Molnár, P. Fürjes, Cs. Dücső

The main objective of the POSITION-II project is the realization of a pilot line for the fabrication of the next generation of smart medical instruments. This second generation of smart medical instruments offers improved performance through better sensors and transducers combined with an improved manufacturability and lower cost. The task of our research group is to develop and demonstrate the applicability of a capacitive force sensor integrable in the tip of an electrophysiological catheter.

The F2R compatible 3D force sensors exploit the capacitive read-out; thereby three capacitors positioned symmetrically on a deforming membrane are needed to resolve the vector components of the loading force. The Partners agreed upon the basic structure, i.e. a force transferring and amplifying rod will be formed from the handle layer of the SOI wafer, whereas the deforming membrane will be the 40µm thick device layer with isolated capacitors on top. Two types of surface micro-machined capacitors will be investigated; the cavity/oxide dielectric capacitor presented by Philips in the CMUT device and an alternative structure having an oxide/compressible PDMS dielectric (Fig.5.2). The Laboratory has to develop the PDMS base sensor and also to adapt the CMUT like chip to force sensing purposes.

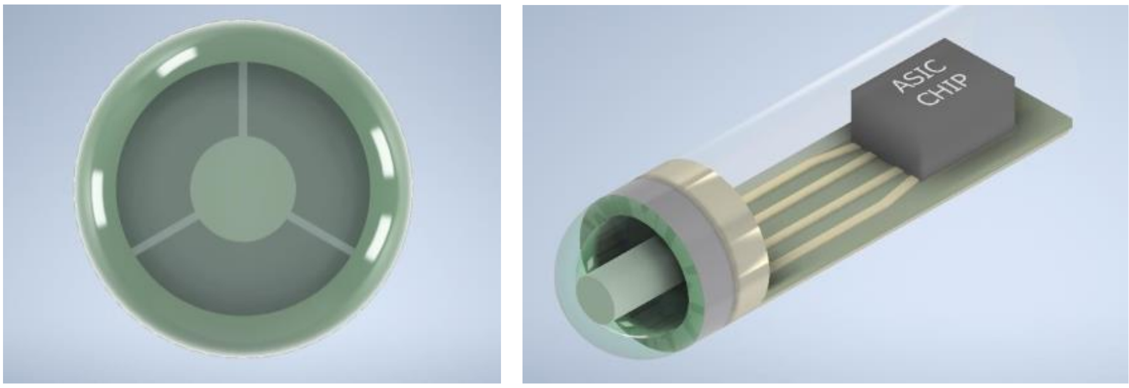

Figure 5.2. *Schematic cross section of the catheter head with the fixed sensor at the tip (left). The front view of the tip symbolises the position of the 3 capacitors (right). (The diameter of the catheter is in the mm range.)*

On the basis of general geometric requirements FEM models were set to predict functional properties of the deforming capacitor. The simplified model is applied to see the geometric changes of the capacitors under load. In the first step the deformation vs. applied force was modelled. Following the deformation the change of capacitance was calculated. Typical C-F responses were found to be around 0.5-1.0 pF/N. As in this specific task the thin film membrane “sandwich” structure cannot be neglected. Nevertheless, its aspect ratio (lateral dimensions vs. thickness of individual components) is in several orders of magnitude, their mechanical behaviour was only simulated at a moderate level of applied forces (~0.2 N). The elastic response of the membrane becomes more and more non-linear above that load, which would require enormous extension of the mesh-refinement for mathematically convergent results. However, the mechanical “real-life” behaviour can probably be considered linear at a much broader range of forces.

Parallel with modelling, the additional thin film compatible elastic PDMS processing steps were elaborated. Due to the lateral size limitations of the capacitors the thickness of the elastic dielectric must be definitely below 1µm to exhibit capacitance in the pF range. Test structures were manufactured on SOI wafer to verify model calculations and determine geometric constrains. The diameter of the sensor is varied between 300-2500µm. Due to the assembly issues and the construction of force sensing measurement setup the 2 x 2cm^2 test chips contain 9 sensor elements of the above lateral sizes. Force transferring rods are formed in the handle wafer whereas the capacitors (3/sensor) and wire contacts on the device layer. In order to limit the deformation in the PDMS layer a solid backside Si element was bonded on the device layer side (Fig. 5.3.).

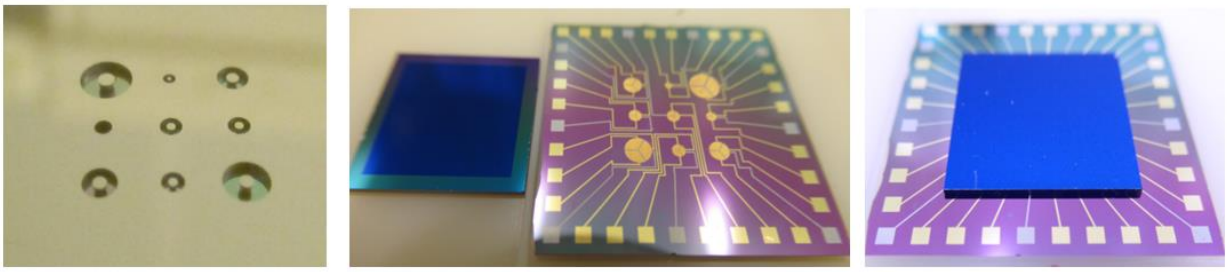

Figure 5.3. *Processed test chip with 9 force sensors of different lateral geiometry. Force transferring rods in the handle wafer (left), 9x3 capacitors on the device layer side and the supplementary Si chip with a 1µm frame to prevent membrane deformation (centre) and test chip with back-side bonded deformation limiting Si element (right).*

The test chips were mounted on rigid PCB elements and measured by a manual 3D loading and force sensing setup. The on-going measurements have proven the validity of the concept (Fig. 5.4.), however the actual signal level is still below 1pF. It has to be increased in order to improve the signal/noise ratio and minimize the effect of parasitic capacitances. We found measurable signals up to 100fF / sensing elements for up to 2N load but resolving load directions is still to be improved. Due to the low signal/noise ratio on site filtering will be a must in the final device.

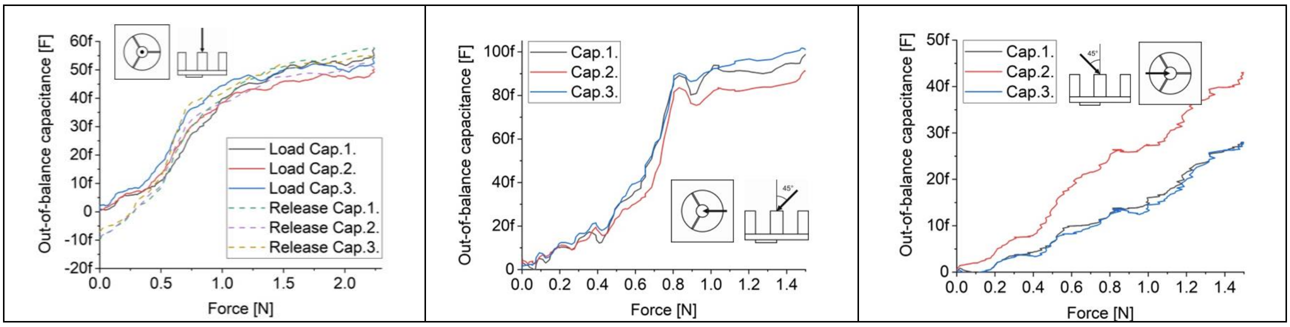

Figure 5.4. *Responses of the three elements for the three characteristic directions as indicated with the insets.*

Manufacturing implantable microelectrode arrays

OTKA K120143, 2017-1.2.1-NKP-2017-00002 „Nemzeti Agykutatási Program 2.0”

A. Zátonyi, Á. Horváth, A. Pongrácz, A. Nagy, R. Hodován, Z. Fekete

The PPKE “Implantable microsystems” group contributed to the development of an implantable microelectrode array, which is able to change its Youngs-modulus from 2 GPa to 300 MPa if being exposed to physiological temperature (see Fig. 5.5.). Besides the micromachining of the thiolene-acrylate based microdevice, packaging of the system was optimized to meet the demands of long-term operation in the living body. After successful electrochemical aging tests involving thiolene-acrylate neural probes, acute in vivo recordings have been carried out and repeated from the rat hippocampus several times.

As spatial resolution tests through Parylene HT based ECoG devices using fluorescent two-photon imaging provided promising data, the focus of experiments moved to application of the microsystem in living subjects instead of in vitro cultures. The concurrent use of high-density electrophysiology and Ca imaging was presented in awake mice and the dataset in both the optical and electrical domain is being evaluated. Besides the preparation of in vivo experiments, our group made further efforts to confirm the mechanical and electrochemical stability of these Parylene HT/ITO devices (see Fig. 5.6.).

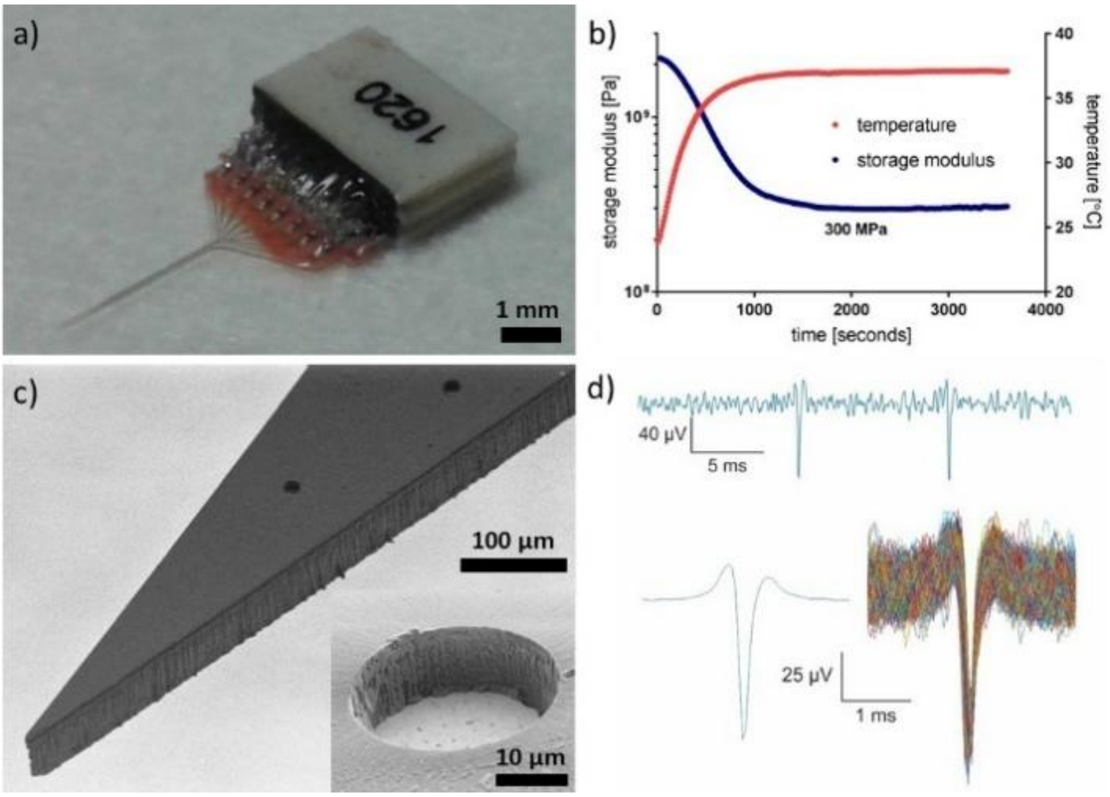

Figure 5.5. *(a) Ready-to-use neural probe for hippocampus recording. (b) Scanning electron microscopy view on the sidewall profile (b) on a reference recording site (c) Softening of a polymer sample upon immersion into room temperature saline solution and heating to 37 °C. (d) Representative filtered waveform of action potentials in vivo.*

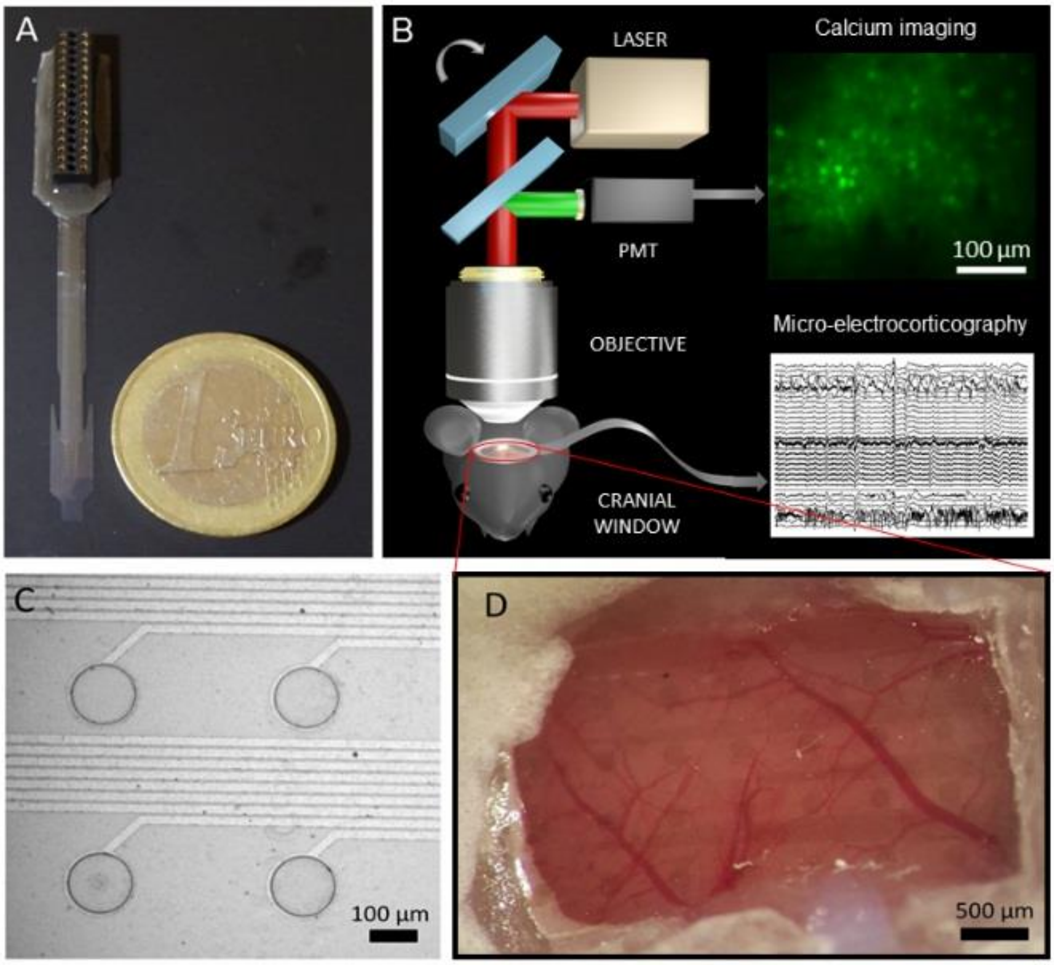

Figure 5.6. *(A) transparent microECoG array made of low-autofluorescent Parylene HT substrate. (B) Schematic figure representing the experimental design for simultaneous Ca*$^{2+}$ *imaging and electrophysiology in vivo. (C) Close view of recording sites and wires made of sputter-deposited indium-tin-oxide. (D) Epidurally implanted microECoG array prepared for two-photon imaging in freely moving mouse.*

The group contributed to the in vitro and in vivo demonstration of a multimodal implantable actuator (Fig. 5.7.), which comprises of monolithically integrated infrared waveguide, a temperature sensor and electrophysiological recording sites. A coupled mechanical—optical-thermal model has been created and validated to estimate the surrounding temperature in the deep neural tissue. During the first in vivo experiments, controlled elevation of the background temperature using the integrated device resulted in reversible excitation or inhibition of cellular activity depending on the targeted brain region and cell type. [Ref. 5.3., Ref. 5.4., Ref. 5.5.]

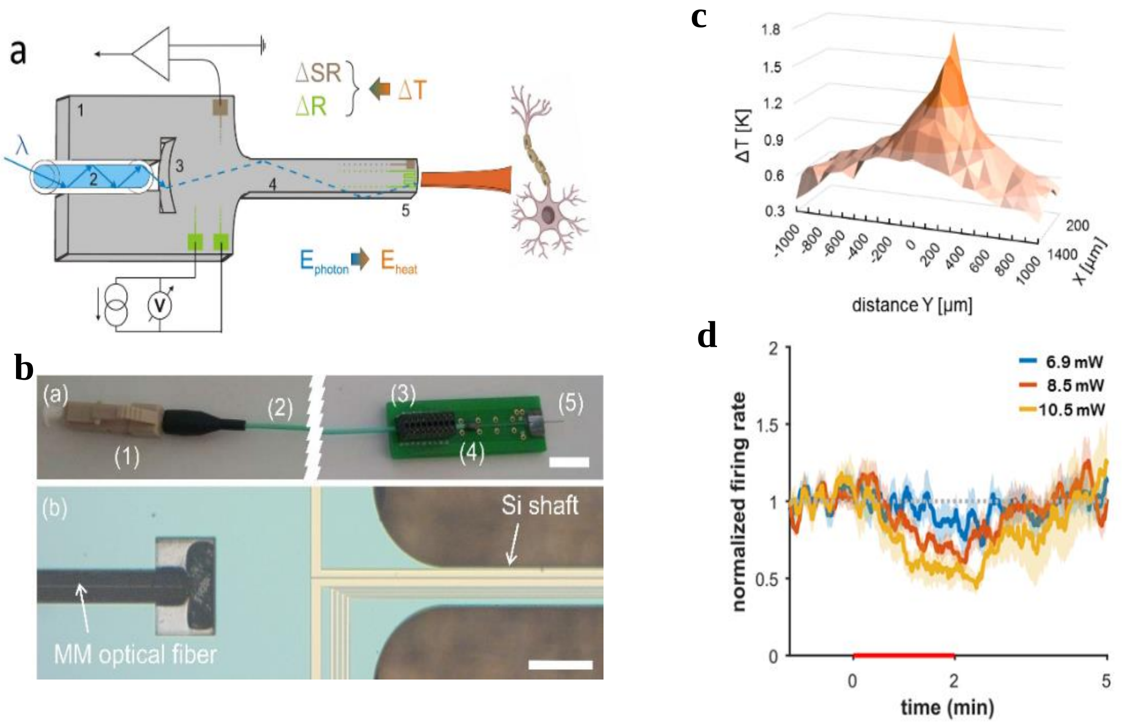

Figure 5.7. *(a) Operation of the multifunctional probe chip designed to deliver infrared light into the neural tissue and monitor electrophysiology concurrently. (b) Photo on the ready-to-use device (top) and microscopy image of coupling region of the chip (bottom). Denoted parts: (1) optical connector, (2) optical fiber, (3) electrical connector, (4) PCB, (5) silicon chip. (c) Measured spatial distribution of temperature change evoked by the absorbed IR light around the probe shaft. (d) Representative cellular response in the cortex to IR stimulation at various input optical power.*

Polymer based autonomous microfluidic systems for medical diagnostics

GINOP-2.3.2-15 „Stratégiai K+F műhelyek kiválósága - Chiptechnológia alkalmazása a humán in vitro fertilizáció eredményességének javításában”

O. Hakkel, A. Füredi, P. Hermann, L. Bató, L. Illés, P. Fürjes

Precise and fast PoC monitoring of marker molecules or bacteria levels in body fluids or cell culture media could be crucial in effective diagnostics and choosing therapies. Due to the specific tools and novel microtechnology processes the cost-effective, complex but miniaturised analytical systems, such as Lab-on-a-Chip (LoC) and microfluidic devices have become available and applicable for implementing the overall sample analysis from the preparation to the molecular detection. The microfluidic system has to transport the sample and the washing buffer to the active area of the chip meanwhile mix and incubate the sample with the reagents. As the incubation and read-out needs a specified time, precise sample handling and flow control are crucial. The perspective of our work is to develop a polymer based microfluidic cartridge suitable to autonomously controlled sample transport or preparation for integrated bioanalytical device.

In a previous project (Multiparaméteres Point of Care in vitro diagnosztikai rendszerek fejlesztése, KTIA VKSZ_14-1-2015-0004) an autonomous microfluidic system was designed and manufactured for transporting blood or plasma by precisely controlled sample rate. These autonomous sample transport systems were integrated into Point-of-Care Lab-on-a-Chip based diagnostic devices. The developed systems are to be applied for detection cardiovascular diseases in cooperation with 77 Elektronika Ltd. Based on these results we are developing Lab-on-a-Chip based diagnostic device for a specific project of the University of Pécs dedicated to support human in-vitro fertilisation with the 77 Elektronika Ltd. In the actual period the geometry of the microfluidic systems was modified according to the additional requirements of the optical detection method and the real sample. Accordingly a new, actualised microfluidic structure was designed (see Fig. 5.8) to be compatible with the applied bioanalytical specifications (targeted detection limits, surface blocking, etc.):

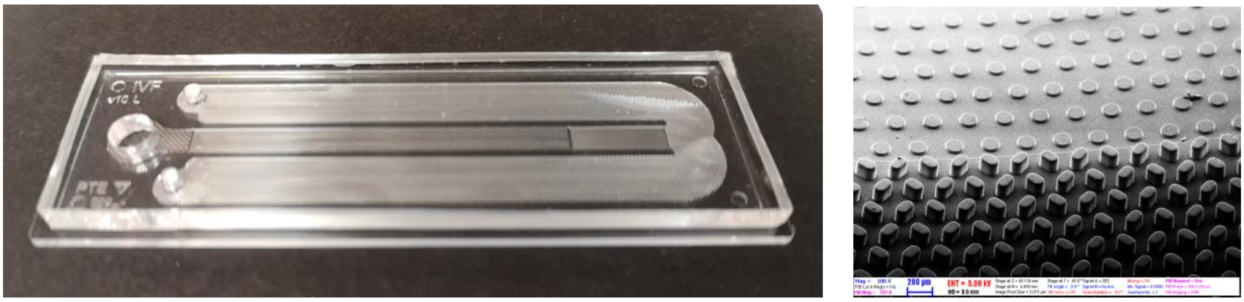

Figure 5.8. *The autonomous microfluidic cartridge proposed for transport culture media applied in human in-vitro fertilisation (left) and its microstructure (SEM image).*

The material composition of the pre-industrial / laboratory stage cartridge was optimised according to the required sample flow rate, the optical and mechanical properties. The embedding protocol of PDMS-PEO molecules was optimised considering the applied molecular weight, concentration and the physical parameters of the PDMS polymerisation process (temperature, time, surface treatments of the molding master). The long term stability of the modification is continuously verified. According to the project requirements the geometry and the fabrication protocol will able to be improved.

Microfluidic sample preparation system for rapid urine bacteria analysis

VEKOP-2.2.1-16-2017-00001

A. Bányai, O. Hakkel, P. Hermann, Zs. B. Sik, Z. Hajnal, P. Fürjes

The goal was to develop a single-channel microfluidic cartridge for certain subtasks of sample preparation and handling, which then can be integrated into a measuring instrument. During the optical measurements of bioanalytical tests, the sample handling is solved in an integrated Lab-on-a-Chip cartridge. The cartridge includes transport and filtration of the liquid sample, positioning of bacteria in the detection chamber over the sensing layer, and a microfluidic component for storage of used sample. Accordingly, we focused our attention to develop a passive hydrodynamic unit that is capable of filtering larger elements (>6um) in urine samples and positioning permeated bacteria laterally. In order to achieve this goal, we designed and characterized such units. Simultaneously, single-channel cuvettes were made to test the optical system with the sample solution.

1. The previously designed DLD (deterministic lateral displacement) structures were modified, manufactured and analysed their flow profile with finite element method in COMSOL Multiphysics.
2. A so-called crossflow type filtration system was designed and implemented that is more advantageous regarding high-speed fluid handling. This system provides a continuous mechanical filtration in a microfluidic environment due to its longitudinal arrangement. Conclusions were based on the efficiency of each of the separation geometry.
3. The lateral focusing of the bacteria was accomplished by a hydrodynamic method. The focusing depends on the particle to channel size ratio, which was investigated in an asymmetric fluidic system with variable parameters and special geometry.
4. Single-channel cuvettes were made to optimize the optical measurements. The design advanced over several iterations in order to sufficiently detect the bacteria in the sample solution. The flow profiles were analysed with finite element method and experimentally.

Size dependent sorting of components is essential for effective sample preparation in Lab-on-a-Chip systems. Our goal is to achieve separation of bacteria from residues of urine having diverse sizes, shapes. DLD microchannels were fabricated by soft lithography with six pillar cross-sections: circle, square and triangles with various orientations to test the separation efficiency depending on their shape and arrangement (Fig. 5.9.).

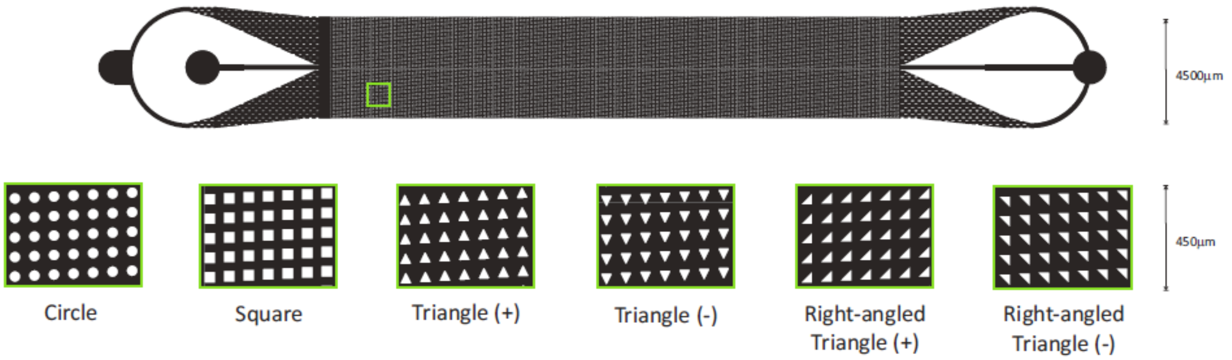

Figure 5.9. *Layout and pillar types of the proposed DLD structure.*

A suspension of fluorescently labelled microbeads (with 16.5 and 20.4 µm diameters) and Human Serum Albumin (FITC-HSA) were focused between buffer fluids in the device. The separation efficiencies of the individual structures were quantified by the range of bead-deflection from the centred flow. Molecular diffusion was captured by recording the concentration of the diluted FITC-HSA along the channel. Pillars' shape and configuration strongly influence not only the DLD effect, but the concentration profiles determined mainly by diffusion in laminar flow. Deflection of particles and spreading of focused sample stream were explained by FEM simulation considering the pressure distribution and transversal flow generated by inhomogeneous hydrodynamic resistance due to asymmetries as presented in Fig. 5.10.

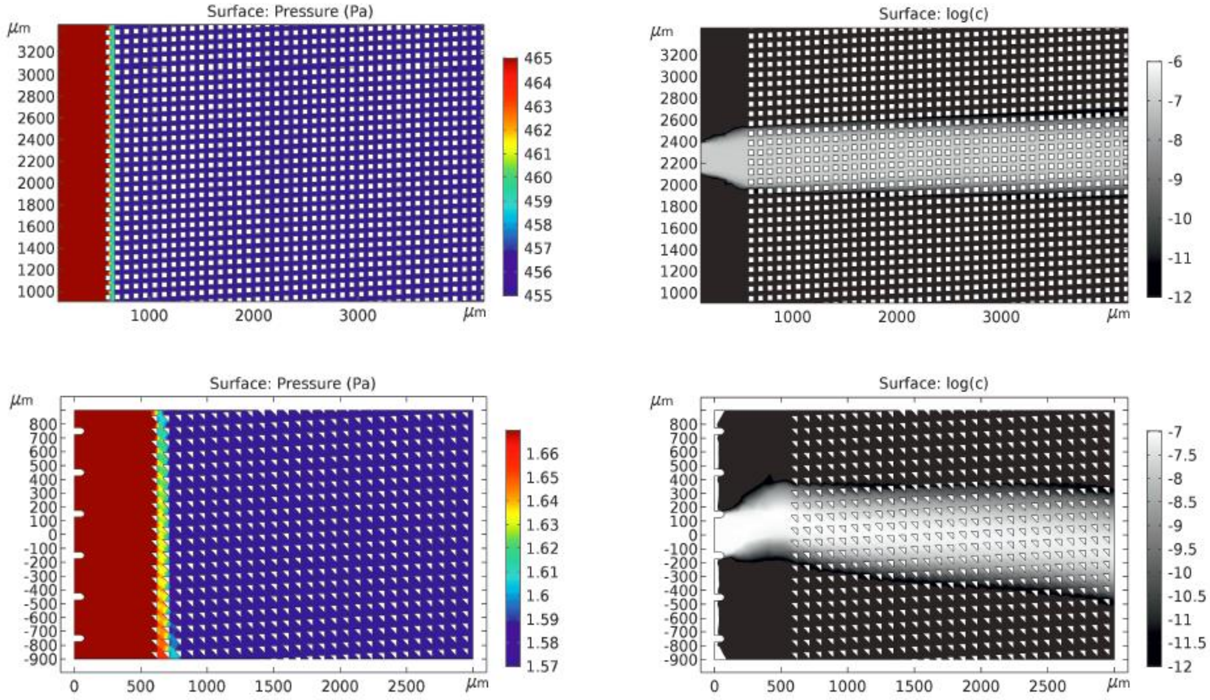

Figure 5.10. *FEM simulation of the flow characteristics in different DLD separation systems.*

The effects of pillar geometry in microfluidic DLD systems were analysed experimentally and simulated by FEM regarding their separation efficiency. Deflection of particles and spreading of the focused sample stream were recorded and explained by theoretical considerations.

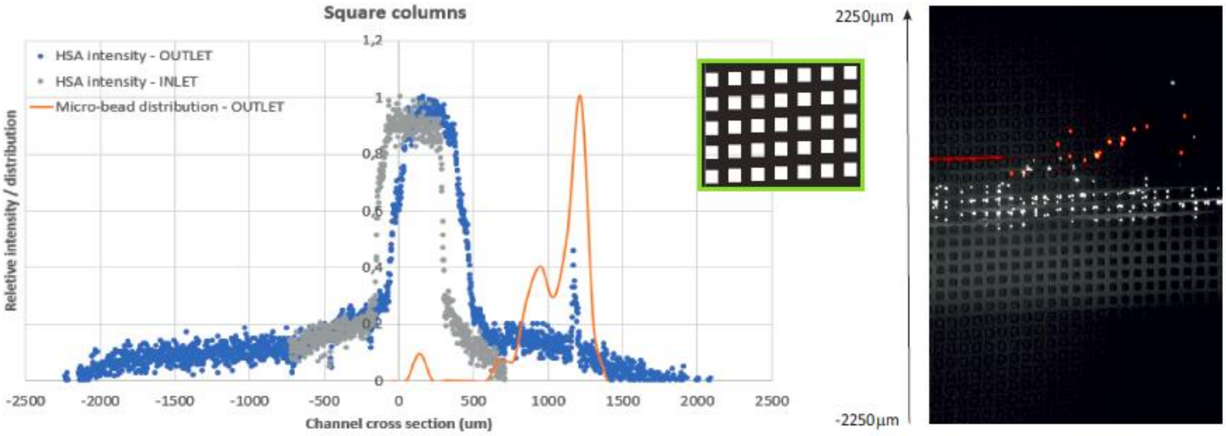

Figure 5.11. *Experimental characterisation of the separation efficiency of the square shaped pillar based DLD microfluidic structure. Bead diameter: 16.5µm (white) / 20.4µm (red) (in the right fluorescent picture).*

In order to handle the liquid sample with high-speed in the corresponding volume, the application of crossflow type separation / filtration system proved to be beneficial. The crossflow system achieves a continuous mechanical filtration within a microfluidic environment. The size of the permeable particles determines the geometry of the microchannels, which then filters any particle that is larger in size. Moreover, the longitudinal arrangement allows larger sample volumes without clogging. We tested several geometrically variant separation structures with fluorescent microbeads (diameter ranging from 4.8 µm to 15.8 µm) and different flow velocities.

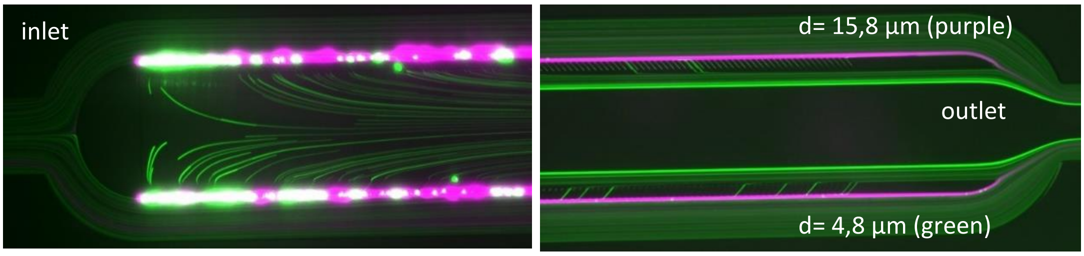

Figure 5.12. *Size dependent filtration of different fluorescent beads in cross-flow type microfluidic separation system (at 3µL/s flow rate).*

More efficient filtration achieved at lower flow velocities in the structures, where the surface of the filter is parallel to the flow direction. While the filter surface is less prone to clogging, and bubble trapping. Similar efficiency can be achieved at higher flow velocities in structures, where the surface of the filter is perpendicular to the flow direction. The system is less sensitive to bubble formation; however, clogging is strongly dependent on the particle concentration and saturation is quick.

After filtering every larger component of the urine sample, the permeated bacteria must be vertically and possibly laterally focused in the detection chamber in order to achieve high trapping efficiency on the functionalized surface. The lateral focusing was achieved by a hydrodynamic method. The efficiency of the hydrodynamic focusing depends mainly on the characteristics of the fluidic system and on the particle to channel size ratio. The position of the particle within the flow profile is determined by forces acting on the particle in the fluidic system. The focusing was carried out in an asymmetric microfluidic system with alternating geometric parameters. Fluorescent beads were used in order to mimic the size range of the E. coli bacteria. The efficiency of the focusing increased with both the flow velocity and the growing inhomogeneity of the alternating geometric structure (Fig. 5.13). The behaviour of the microfluidic systems was characterized by finite element methods as well (Fig. 5.14.). [Ref. 5.7., Ref. 5.8., Ref. 5.9.]

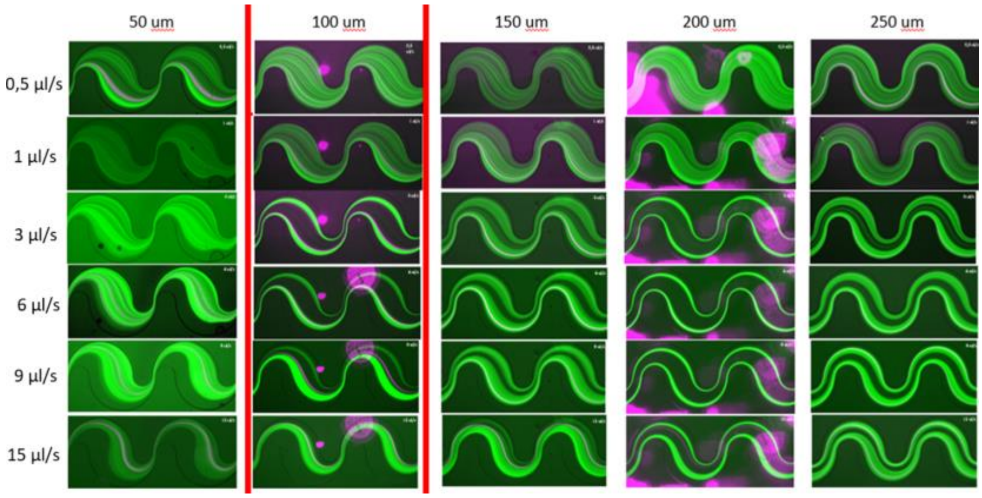

Figure 5.13. *Lateral focusing of fluorescent microbeads (d = 4.8µm) in asymmetrically altering microfluidic channels affected by the flow rate and asymmetry parameter (lateral size of the constrains of the channel).*

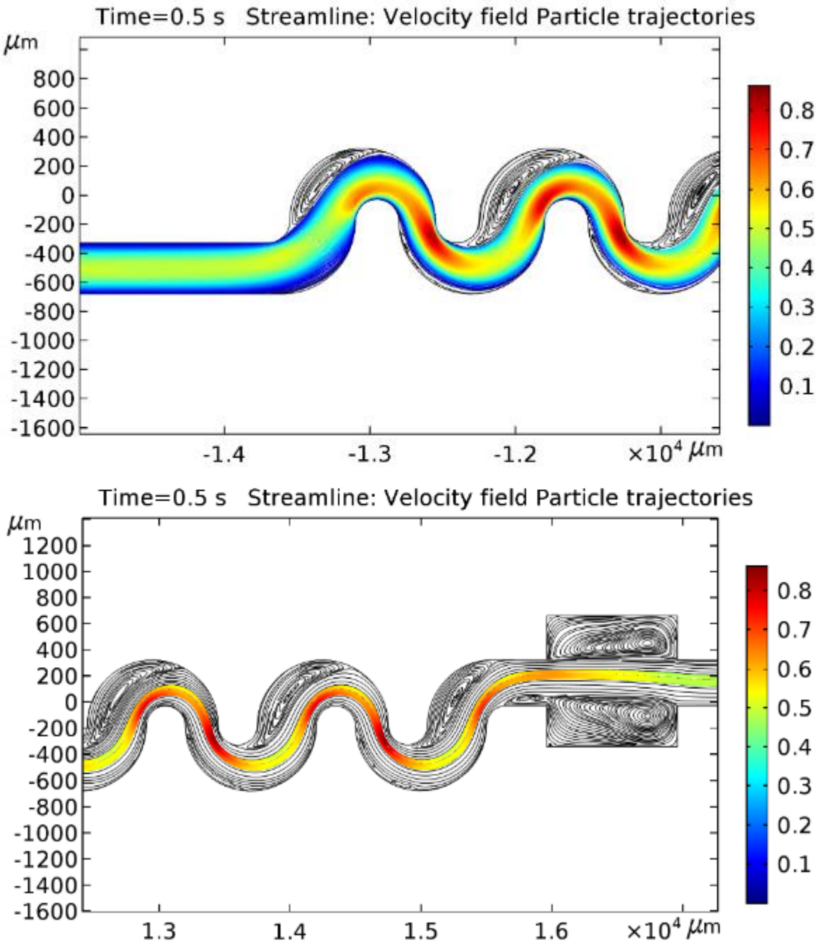

Figure 5.14. *Streamlines and particle trajectories in the focusing microfluidic system at the inlet (left) and the outlet (right) of the 250/1000µm channel.*

Microfluidically integrated SERS active cell trap array for analysis red blood cells

O. Hakkel, R. Öcsi, Zs. Zolnai, I. Rigó (Wigner FKK), M. Veres (Wigner FKK), P. Fürjes

Surface Enhanced Raman Scattering (SERS) is applied to enhance the Raman signal by several orders of magnitude and significantly improve the sensitivity of the ordinary scattering method. As a result of the electromagnetic enhancement emerging in the vicinity of metallic nanostructures the sensitivity of molecule detection can achieve attomolar concentrations. Thus by using this method efficient detection method can be developed for the analysis of low concentration biological samples assuming that sample transport and preparation system is also integrable. In our case the 3D SERS active structure is simultaneously forming the cell trapping array of the microfluidic system, in line with the concept presented previously.

According to our approach a perforated membrane of tailored size and shape was prepared to be applicable for cell entrapment and highly sensitive detection of molecular components also. Arrays of periodic inverse pyramids were prepared in the 5μm thick device layer of SOI (silicon-on-insulator) wafers. The 3D structure was shaped by alkaline etching after development of appropriate masking pattern. By the definition of the initial pattern and the device layer thickness the geometry of the truncated pyramids could be fitted to the estimated cell size. Vertical microchannels were revealed by etching away the back-side handler silicon and buried oxide and coated with a 50nm thick evaporated layer of gold. The resulted structure was used as an array of particle traps and SERS substrate simultaneously. Additional sample injection microfluidic channels were formed over the SERS substrate to support the blood transport to the sensing area. Normal blood sample was diluted and injected onto the 3D structure and RBCs were captured on its surface and in the perforated inverse pyramids. The lateral distribution of the cells was characterized by bright field microscopy and later by scanning electron microscopy (SEM) as presented in Fig. 5.15.

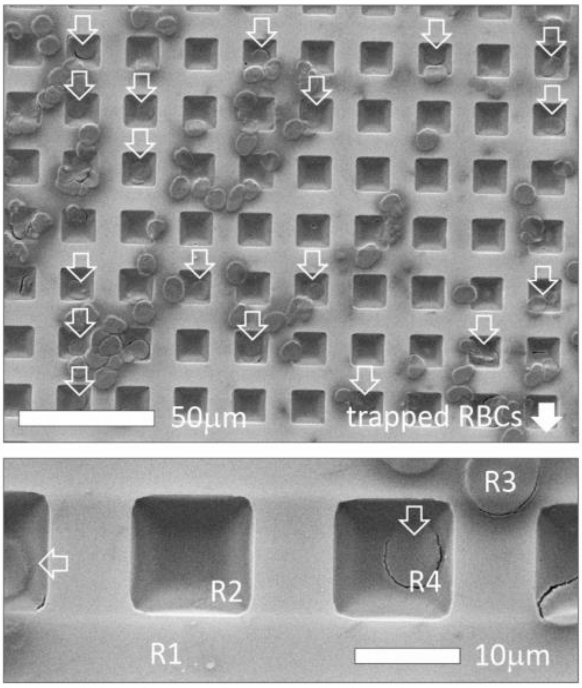

Figure 5.15. *SEM image of the entrapped RBCs on the SERS substrate. The empty wells are filled by plasma. Note, that the structure was covered with a 50nm Au layer before SEM microscopy.*

Trapped RBCs and blood plasma were also analysed on the flat gold surface and in the inverse pyramid structures by Raman spectroscopy. Centrifuged blood plasma was also analysed on a specific SERS substrate, where the hierarchically combined micro- and nanostructures achieve significant SERS enhancement. The SERS spectra of the RBC and blood plasma were compared. The differential spectrum is demonstrated and the most relevant molecular components of the Red Blood Cells are indicated in Fig. 5.16. The primary component of the RBCs is the hemoglobin molecule which has significant resonant peaks at: 570cm^{-1} (FeO_2), 670cm^{-1} and 750cm^{-1} (pyrrole), 820cm^{-1} and 1550cm^{-1} (tyrosine and phenylalanine), 1227cm^{-1} (CH group of hemoglobin). These peaks refer to the major molecular components of the RBCs, as membrane lipids, hemoglobin, etc. The applicability of special perforated periodic 3D SERS structure was demonstrated for simultaneous cell trapping and sensitive Surface-Enhanced Raman Spectroscopy based detection of characteristic molecular vibrations of the blood and red blood cell components. [Ref. 5.10., Ref. 5.11]

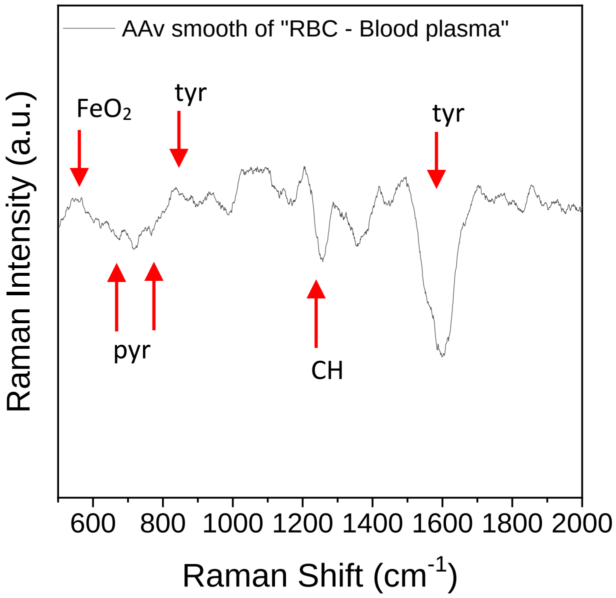

Figure 5.16. *Differential SERS spectrum of the RBC and plasma, obtained by subtraction of normalized plasma SERS spectrum from RBC SERS spectrum. Peaks at: 570cm^{-1} (FeO_2), 670cm^{-1} and 750cm^{-1} (pyrrole - pyr), 820cm^{-1} and 1550cm^{-1} (tyrosine - tyr and phenylalanine), 1227cm^{-1} (CH group of hemoglobin).*

Modelling and analysing of fluid dynamic phenomena in two-phase microfluidic systems

Zs. Szomor, Z. Hajnal, P. Fürjes

We are facing many problems that necessitate moving, manipulating, sorting, counting or analysing localised cells and particles with commensurate dimensions. The response of the individual cells to physical and chemical effects can be precisely analysed in the cell-size scale micro-environment. Two-phase microfluidic systems can create such a specific environment by generating monodisperse microemulsions as cell traps. The long-term goal of our research is to design and create a microfluidic system that generates a specific chemical environment in cell-size trapping in containers. However, understanding and designing physical processes on the microscale is quite challenging, thus deeper characterisation of the behaviour of the fluids in such environment is crucial. During the work, we have investigated the design, preparation and analysis of two-phased microfluidic devices, being able to generate controlled microdroplets and change the chemical environment within them.

Two-phase microfluidic systems have been manufactured by soft lithography technology in Polydimethylsiloxane (PDMS) polymer. A stable emulsion of an oil and water phase was prepared in the devices and the influence of the hydrodynamic and geometric parameters on the droplet sizes was determined.

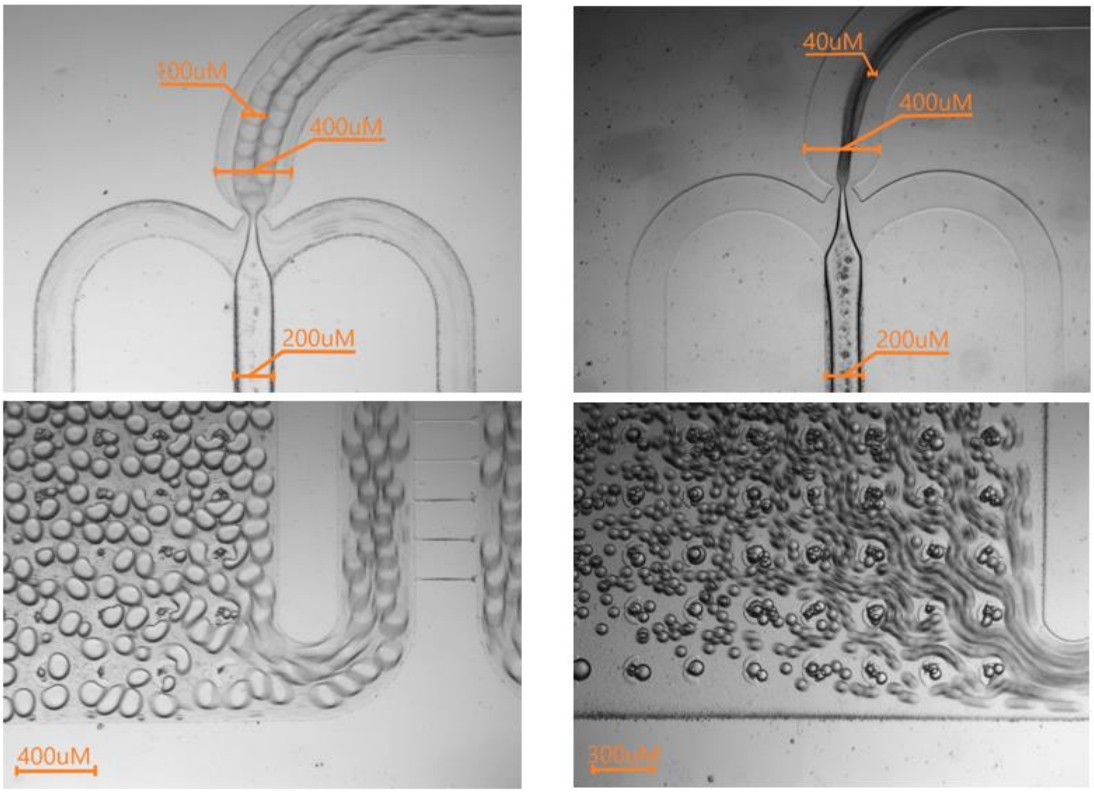

Figure 5.17. *Droplet generation in junction type two-phase microfluidic system in case different flow rates of the dispersed (water) and continuous (oil) phase. The applied flow rates are: water – 0.1µl/s / oil – 0.3µl/s (left) and 0.4µl/s (right).*

The key parameters of the droplet formation have also been studied by finite element modelling (FEM) and simulations, using available standard methods of multiphase dynamics in Comsol Multiphysics. The influence of volume flow ratio at the inlets, viscosity of the fluids, and interface tension were determined in successive parametric sweep simulations as presented in Fig. 5.18. The advantages and disadvantages of the different design geometries haves been revealed also. [Ref. 5.12.]

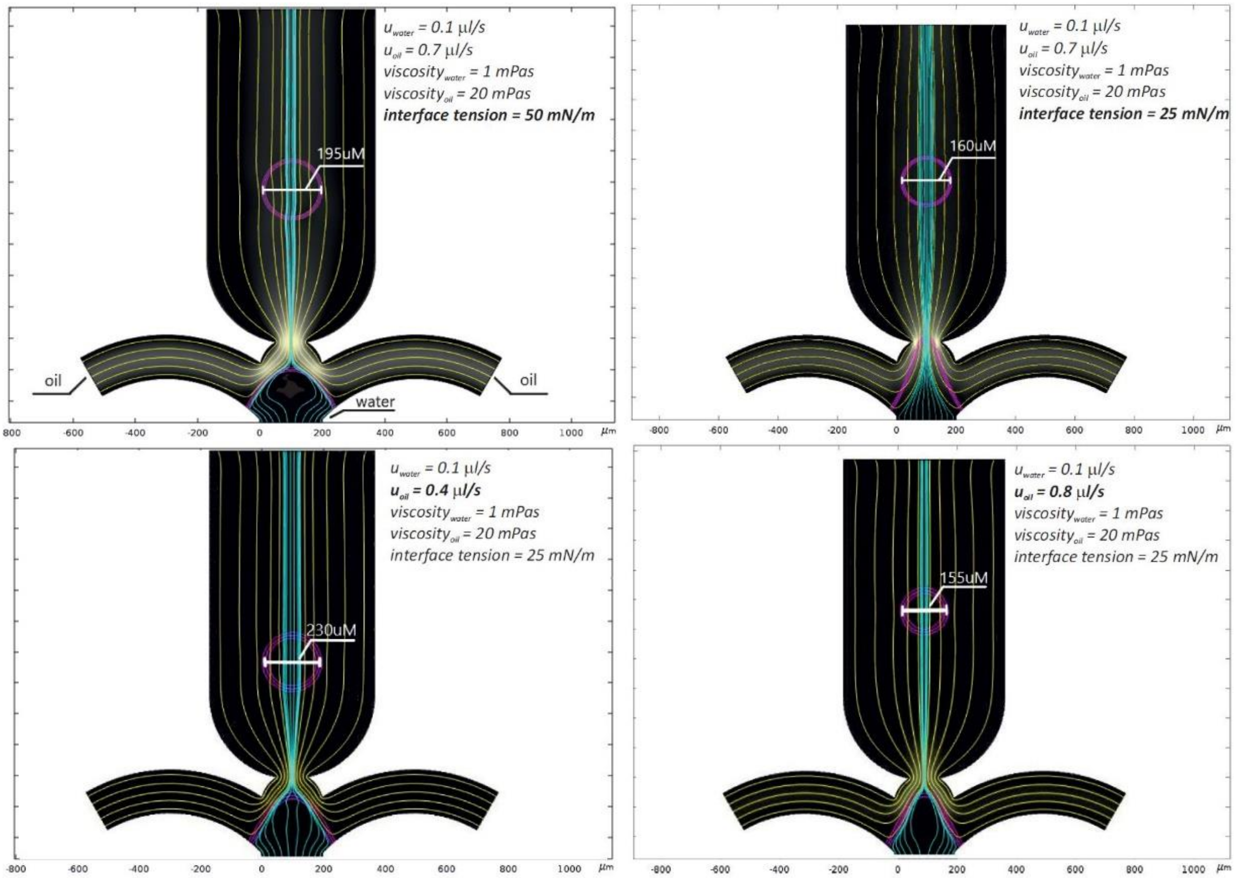

Figure 5.18. *Influence of the interface tension and flow rate ratios on the droplet formation process (droplet size) – FEM simulation.*

Near InfraRed LED devices for spectroscopic applications: Development and small scale production of near infrared LEDs and LED based devices

F. Bíró, I. Réti, G. Battistig, Z. Szabó

Infrared spectroscopy is a very popular measurement technique especially in food industry, pharmaceutical industry and agriculture for the detection and measurement of organic materials. The -OH, -NH and -CH functional groups found in organic substances can frequently be detected by spectroscopy through absorbance measurements at the resonance wavelength of valence-bond vibrations. The measured wavelengths are 4-2.5μm, while the signal to noise ratio of photon detectors is low due to moderate thermal noise at room temperature. The 1st-3rd harmonic absorption bands are located in the range of the near infrared (NIR), where smaller signals can be measured effectively in practice. NIR LEDs have narrow wavelength, therefore they are suitable for measurements at given wavelength. Further advantages of LEDs compared to incandescent lamps are their small dimensions, high efficiency, and low power consumption, which is critical in small handheld devices.

GaInAsP/InP is an ideal material system for the fabrication of double heterostructure devices as the emission wavelength is easily tuneable between 0.950-1.650 μm. As InP has higher bandgap than the lattice-matched GaInAsP active layer the absorption losses inside the device structure can be minimized. In order to tune the emission wavelength of the LED, the composition of the semiconductor light-emitting layer has to be properly set. When a secondary or multi-peak emission is preferred e.g. in spectroscopic applications, various solid-state solutions can be considered:

1. Application of LED array of different single-peak emissions to cover the whole spectrum or emit at specific peaks the application requires. This approach is widely known and viable, however it suffers from geometric constrains and also from the different temperature dependence of emission of each LED. This makes the intensity control complicated.
2. A more viable solution is our novel single chips what exhibit multiple emission peaks. As we demonstrated earlier (patent pending and publications in 2017) the source of the primary electroluminescent light is the active layer of the diode, but this light also excites a second smaller band gap layer, thereof producing secondary light by photoluminescence. The key element of chip production is liquid-phase epitaxy. Our recent and ongoing development is twofold: Demonstration a measuring technique using double-wavelength LED as light source and wavelength-selective photodiodes as photodetectors.

The photodiodes were fabricated similarly to the NIR LEDs and mounted in a single TO-package. We have chosen ethanol-water system and matching wavelengths to certain -OH and -CH absorption peaks to be able to measure ethanol concentration with 0.1% resolution. Fig. 5.19. represents the transmission spectra of EtOH-H_2O mixtures as illuminated by a double peak LED.

Moreover, the modified LEDs can be used as photodiodes with proper cut-off at the required wavelength. Also the proper modification of the double-peak LED provides a selective narrow band photodiodes. Demonstration device have constructed using double wavelength LED, two photodiodes in single TO-package and custom-made analogue and digital electronics. The sealed sensor head containing the light source, the photodiodes and a mirror in trans-reflectance configuration sinks in the measured liquid. [Ref. 5.13.]

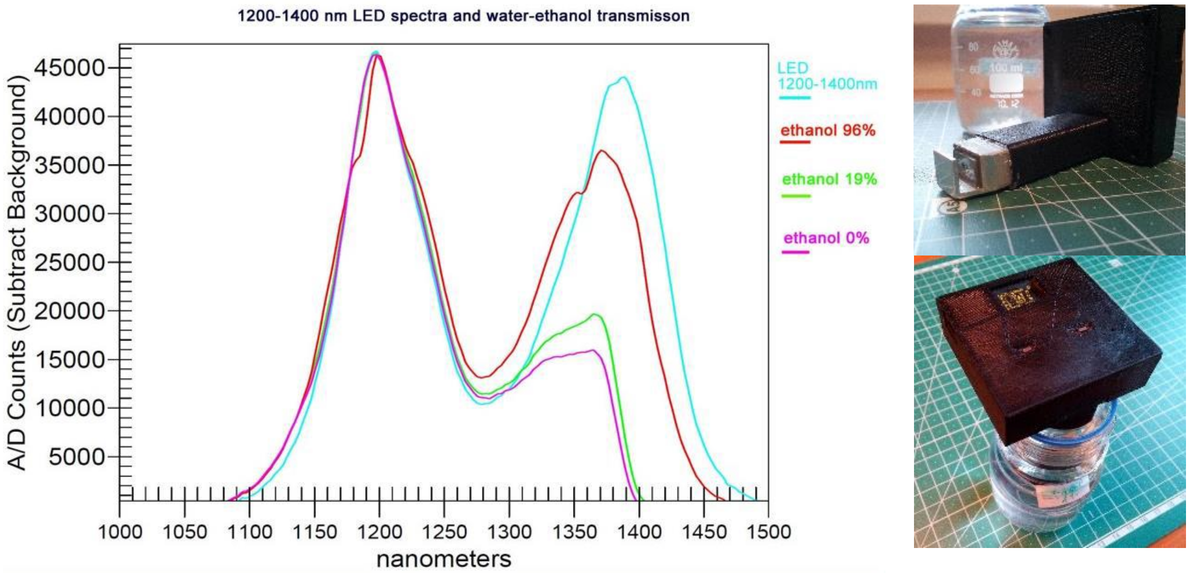

Figure 5.19. *Transmission spectra of water-ethanol mixtures illuminated by a double peak single-chip LED (light blue) (left) and the demonstration device for selective spectroscopic application using dual-wavelength LED (right).*

The feasibility of both the 3- and 4-peak single chip LEDs were successfully demonstrated and the early results were presented in the E-MRS 2019 Spring Meeting (Fig. 5.20.). However, the reliable fabrication technology is still under development before entering in the market. The promise is to be able to produce a wide band (1000-1700nm) NIR LED with excellent optical and thermal parameters. Manufacturing wide spectra point-like light source opens the way towards miniature spectroscopic devices.

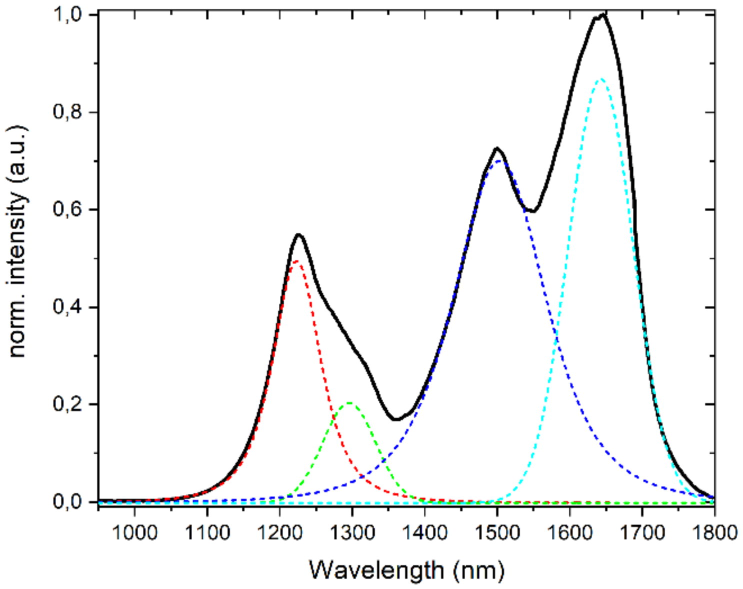

Figure 5.20. *Emission spectrum of the fabricated single LED chip emitting at 4 different wavelengths.*

Our business partners are SENOP Oy (Fi) and Anton Paar Ltd. (At). Another Canadian tech company is also interested in high power single emission peak LEDs of the upper wavelength regime for solar simulator purposes.

Nanobiosensorics Momentum Group

Head: Róbert HORVÁTH, Ph.D., Senior Scientist

Research Staff

- Róbert HORVÁTH, Ph.D.
- Sándor KURUNCZI, Ph.D.
- Inna SZÉKÁCS, Ph.D.
- Beatrix PÉTER, Ph.D.
- Boglárka KOVÁCS, Ph.D.
- András SAFTICS, Ph.D.
- Zoltán SZITTNER, Ph.D.
- Nicolett KANYÓ, M.Sc.
- Eleonóra HATY, M.Sc.

Ph.D. students / Diploma workers

- Enikő FARKAS, Ph.D. student
- Ágoston NAGY, Ph.D. student
- Tamás GERECSEI, Ph.D. student
- Kristóf KLIMENT, Ph.D. student
- Milán SZTILKOVICS, M.Sc. student
- Kinga Dóra KOVÁCS, M.Sc. student
- Bálint KOVÁCS, M.Sc. student
- Norbert PAP, B.Sc. student
- Róbert TARR, B.Sc. student
- Péter CHRENKÓ, M.Sc. student

The research profile of the Nanobiosensorics Group is related to the development and application of label-free optical biosensors and the mathematical modeling of the relevant biological and biophysical processes. Building on their broad national and international collaborative network the group conducts research in the fields of instrument development, monitoring of cell secreted extracellular vesicles, development of protein-based functional coatings, adhesion studies on human cancer and immune cells, and theoretical modeling. In 2014, the application for an ERC Consolidator Grant by the head of the research group received “qualification category A (fully meets the ERC excellence criteria and should be funded if sufficient funds are available)” after the interview in Brussels, but the funding line did not reach this proposal due to budgetary constraints. However, using this achievement the Group could successfully apply for funding from NKFIH in the framework of the ERC_HU call. In the framework of this project they aim single cell manipulation and label-free sensing. Building on this expertise, in 2018 they won an Élvonal (NKFIH, OTKA KKP129936) research project for single cell biosensing. The research group also conducts industry oriented research on bacteria sensing (NKFIH, VEKOP-2.2.1-16-2017-00001).

Adhesion force measurements on functionalized microbeads: An in-depth comparison of computer controlled micropipette and fluidic force microscopy

ÚNKP-18-3, LP2012-26/2012 Lendület, OTKA KKP129936, OTKA KH126900, OTKA ERC_HU117755

T. Gerecsei, I. Erdődi, B. Peter, Cs. Hős, S. Kurunczi, I. Derényi, B. Szabó, R. Horváth

Characterization of the binding of functionalized microparticles to surfaces with a specific chemistry sheds light on molecular scale interactions. Polymer or protein adsorption are often monitored by colloid particle deposition. Force measurements on microbeads by atomic force microscopy (AFM) or optical tweezers are standard methods in molecular biophysics, but typically have low throughput. Washing and centrifuge assays with (bio)chemically decorated microbeads provide better statistics, but only qualitative results without a calibrated binding force or energy value. In the present work we demonstrate that a computer controlled micropipette (CCMP) is a straightforward and high-throughput alternative to quantify the surface adhesion of functionalized microparticles. However, being an indirect force measurement technique, its in-depth comparison with a direct force measurement is a prerequisite of applications requiring calibrated adhesion force values. To this end, we attached polystyrene microbeads to a solid support by the avidin-biotin linkage. We measured the adhesion strength of the microbeads with both a specialized robotic fluid force microscope (FluidFM BOT) and CCMP. Furthermore, the bead-support contact zone was directly characterized on an optical waveguide biosensor to determine the density of avidin molecules. Distribution of the detachment force recorded on ~50 individual beads by FluidFM BOT was compared to the adhesion distribution obtained from CCMP measurements on hundreds of individual beads. We found that both methods provide unimodal histograms. We conclude that FluidFM BOT can directly measure the detachment force curve of 50 microbeads in 150 min. CCMP can provide calibrated binding/adhesion force values of 120 microbeads in an hour. Schematic illustration of the mentioned methods is in Fig.6.1. [Ref.6.1.].

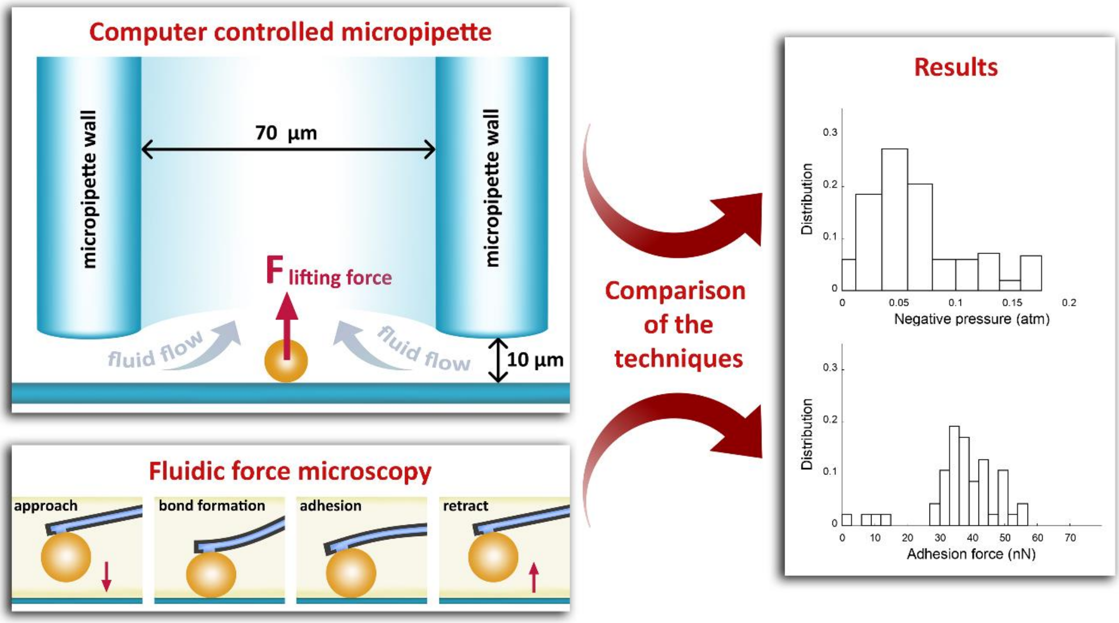

Figure 6.1. *Schematic illustration of the methods. Adhesion force measurements on microbeads were performed by using computer controlled micropipette (CCMP) and Fluidic force microscopy. The obtained results by-the two techniques had been compared.*

Spring constant and sensitivity calibration of FluidFM micropipette cantilevers for force spectroscopy measurements

LP2012-26/2012 Lendület, OTKA KKP129936, OTKA KH126900, OTKA ERC_HU117755

Á. G. Nagy, J. Kámán, R. Horváth, A. Bonyár

FluidFM technique can be considered as the nanofluidic extension of the atomic force microscope (AFM). Schematic illustration of the method is in Fig 6.2. This novel instrument facilitates the experimental procedure and data acquisition of force spectroscopy (FS) and is also used for the determination of single-cell adhesion forces (SCFS) and elasticity. FluidFM uses special probes with an integrated nanochannel inside the cantilevers supported by parallel rows of pillars. However, little is known about how the properties of these hollow cantilevers affect the most important parameters which directly scale the obtained spectroscopic data: the inverse optical lever sensitivity (InvOLS) and the spring constant (k). The precise determination of these parameters during calibration is essential in order to gain reliable, comparable and consistent results with SCFS. Demonstrated by our literature survey, the standard error of previously published SCFS results obtained with FluidFM ranges from 11.8% to 50%. The question arises whether this can be accounted for by biological diversity, or this may be just the consequence of improper calibration. Thus the aim of our work was to investigate the calibration accuracy of these parameters and their dependence on: (1) the aperture size (2, 4 and 8 µm) of the hollow micropipette type cantilever; (2) the position of the laser spot on the back of the cantilever; (3) the substrate used for calibration (silicon or polystyrene). It was found that both the obtained InvOLS and spring constant values depend significantly on the position of the laser spot. Apart from the theoretically expectable monotonous increase in InvOLS (from the tip to the base of the cantilever, as function of the laser spot's position), we discerned a well-defined and reproducible fluctuation, which can be as high as ±30%, regardless of the used aperture size or substrate type. The calibration of spring constant also showed an error in the range of −13/+20%, measured at the first 40 µm from the tip of the cantilever. Based on our results a calibration strategy is proposed. The optimal laser-spot position which yields the most reliable spring constant values was determined and found to be on the first pair of pillars. The proposed method helps in reducing the error introduced via improper calibration and thus increases the reliability of subsequent cell adhesion force or elasticity measurements with FluidFM [Ref.6.2.].

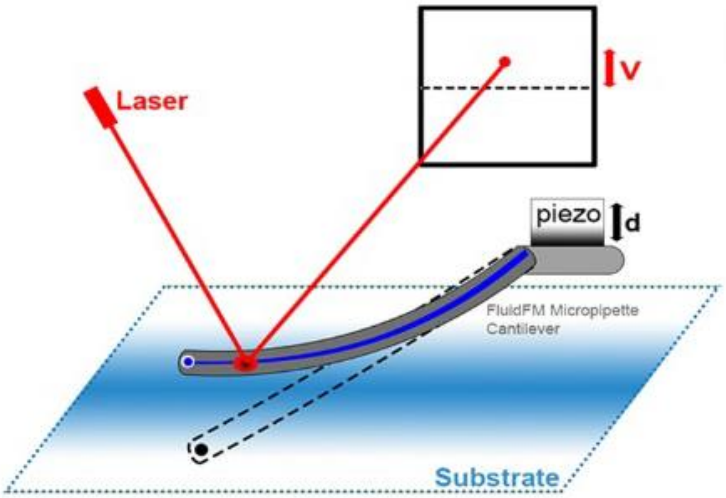

***Figure 6.2**. Illustration of the laser beam reflection based optical setup of the FluidFM system.*

A practical review on the measurement tools for cellular adhesion force

LP2012-26/2012 Lendület, OTKA KKP129936, OTKA KH126900, OTKA ERC_HU117755, PD 124559, Bolyai Scholarship

R. Ungai-Salánki, B. Peter, T. Gerecsei, N. Orgován, R. Horváth, B. Szabó

Cell–cell and cell–matrix adhesions are fundamental in all multicellular organisms. They play a key role in cellular growth, differentiation, pattern formation and migration. Cell-cell adhesion is substantial in the immune response, pathogen-host interactions, and tumour development. The success of tissue engineering and stem cell implantations strongly depends on the fine control of live cell adhesion on the surface of natural or biomimetic scaffolds. Therefore, the quantitative and precise measurement of the adhesion strength of living cells is critical, not only in basic research but in modern technologies, too. Several techniques have been developed to quantify cell adhesion. All of them have their pros and cons, which has to be carefully considered before the experiments and interpretation of the recorded data. The current review provides guidance to choose the appropriate technique to answer a specific biological question or to complete a biomedical test by measuring cell adhesion (Fig.6.3.) [Ref.6.3.].

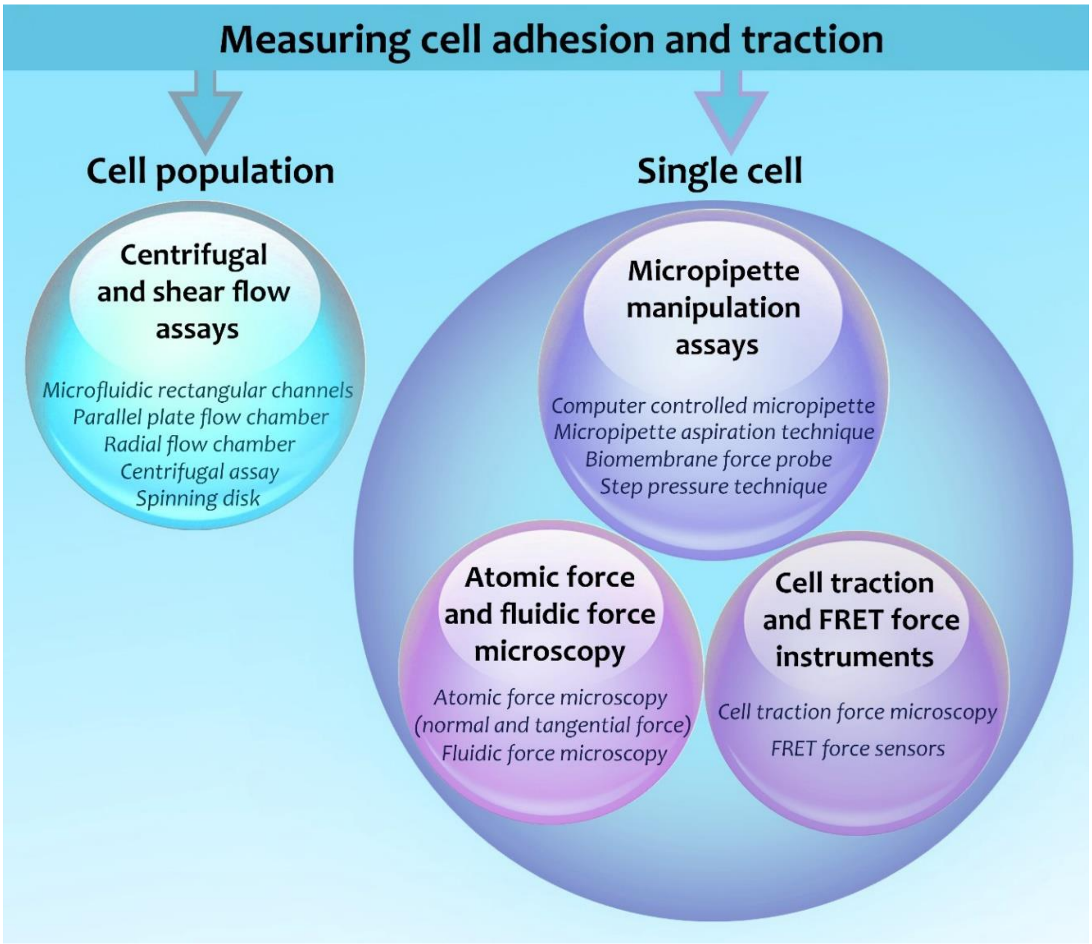

Figure 6.3. *Assays to measure cell adhesion and traction. These techniques are discussed in the review article.*

Modeling of label-free optical waveguide biosensors with surfaces covered partially by vertically homogeneous and inhomogeneous films

LP2012-26/2012 Lendület, OTKA KKP129936, OTKA KH126900, OTKA ERC_HU117755

B. Kovács, R. Horváth

Optical Waveguide Lightmode Spectroscopy (OWLS) is widely applied to monitor protein adsorption, polymer self-assembly, and living cells on the surface of the sensor in a label-free manner. Typically, to determine the optogeometrical parameters of the analyte layer (adlayer), the homogeneous and isotropic thin adlayer model is used to analyze the recorded OWLS data. However, in most practical situations, the analyte layer is neither homogeneous nor isotropic. Therefore, the measurement with two waveguide modes and the applied model cannot supply enough information about the parameters of the possible adlayer inhomogeneity and anisotropy. Only the so-called quasi-homogeneous adlayer refractive index, layer thickness, and surface mass can be determined. In the present work, we construct an inhomogeneous adlayer model (Fig.6.4.). In our model, the adlayer covers the waveguide surface only partially and it has a given refractive index profile perpendicular to the surface of the sensor. Using analytical and numerical model calculations, the step-index and exponential refractive index profiles are investigated with varying surface coverages from 0 to 100%. The relevant equations are summarized and three typically employed waveguide sensor structures are studied in detail. We predict the errors in the calculated optogeometrical parameters of the adlayer by simulating the OWLS measurement on an assumed inhomogeneous adlayer.

We found that the surface coverage has negligible influence on the calculated refractive index for film thicknesses below 5 nm; the calculated refractive index is close to the refractive index of the adlayer islands. But the determined quasi-homogeneous adlayer refractive index and surface mass are always underrated; the calculated quasi-homogeneous thickness is heavily influenced by the surface coverage. Depending on the refractive index profile, waveguide geometry, and surface coverage, the thickness obtained from the homogeneous and isotropic modelling can possess negative and largely overestimated values, too. Therefore, experimentally obtained unrealistic adlayer values, which were dismissed previously, might be important indicators of the layer structure [Ref.6.4.].

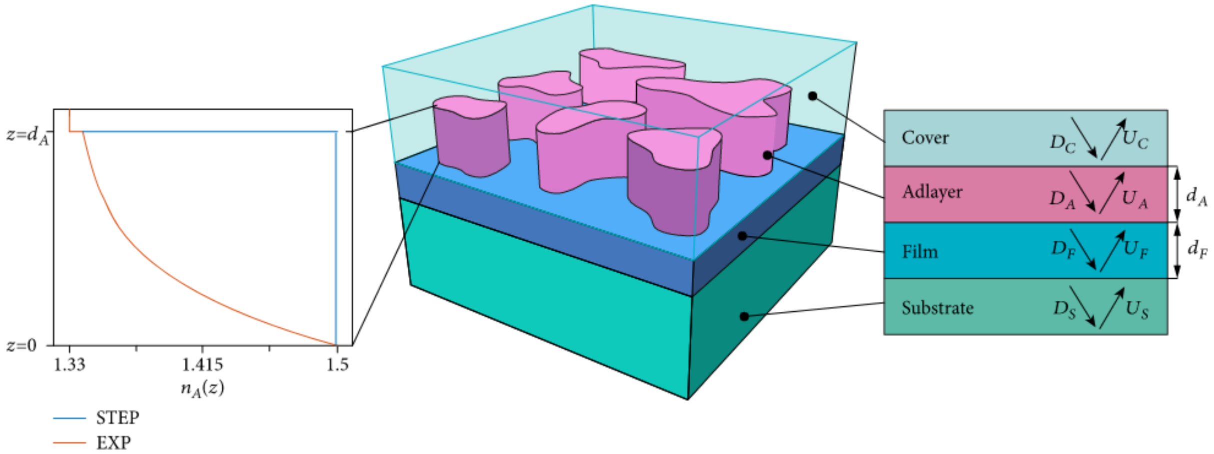

Figure 6.4. *The structure of the modelled OWLS waveguide chips with inhomogeneous adlayer. The modelled multilayered assembly consists of 4 layers: substrate, waveguide film, adlayer, and cover.*

Biomimetic Dextran-Based Hydrogel Layers for Cell Micropatterning over Large Areas Using the FluidFM BOT Technology

LP2012-26/2012 Lendület, OTKA KKP129936, OTKA KH126900, OTKA ERC_HU117755, OTKA FK128901, Bolyai Scholarship

A. Saftics, B. Türk, A. Sulyok, N. Nagy, T. Gerecsei, I. Székács, S. Kurunczi, R. Horváth

Micropatterning of living single cells and cell clusters over millimeter–centimeter scale areas is of high demand in the development of cell-based biosensors. Micropatterning methodologies require both a suitable biomimetic support and a printing technology. In this work, we present the micropatterning of living mammalian cells on carboxymethyl dextran (CMD) hydrogel layers using the FluidFM BOT technology (Fig.6.5.). In contrast to the ultrathin (few nanometers thick in dry state) CMD films generally used in label-free biosensor applications, we developed CMD layers with thickness of several tens of nanometers in order to provide support for the controlled adhesion of living cells. The fabrication method and detailed characterization of the CMD layers are also described. The antifouling ability of the CMD surfaces is demonstrated by in situ optical waveguide lightmode spectroscopy measurements using serum modeling proteins with different electrostatic properties and molecular weights. Cell micropatterning on the CMD surface was obtained by printing cell adhesion mediating cRGDfK peptide molecules (cyclo(Arg-Gly-Asp-d-Phe-Lys)) directly from aqueous solution using microchanneled cantilevers with subsequent incubation of the printed surfaces in the living cell culture. Uniquely, we present cell patterns with different geometries (spot, line, and grid arrays) covering both micrometer and millimeter–centimeter scale areas. The adhered patterns were analyzed by phase contrast microscopy and the adhesion process on the patterns was real-time monitored by digital holographic microscopy, enabling to quantify the survival and migration of cells on the printed cRGDfK arrays [Ref.6.5.].

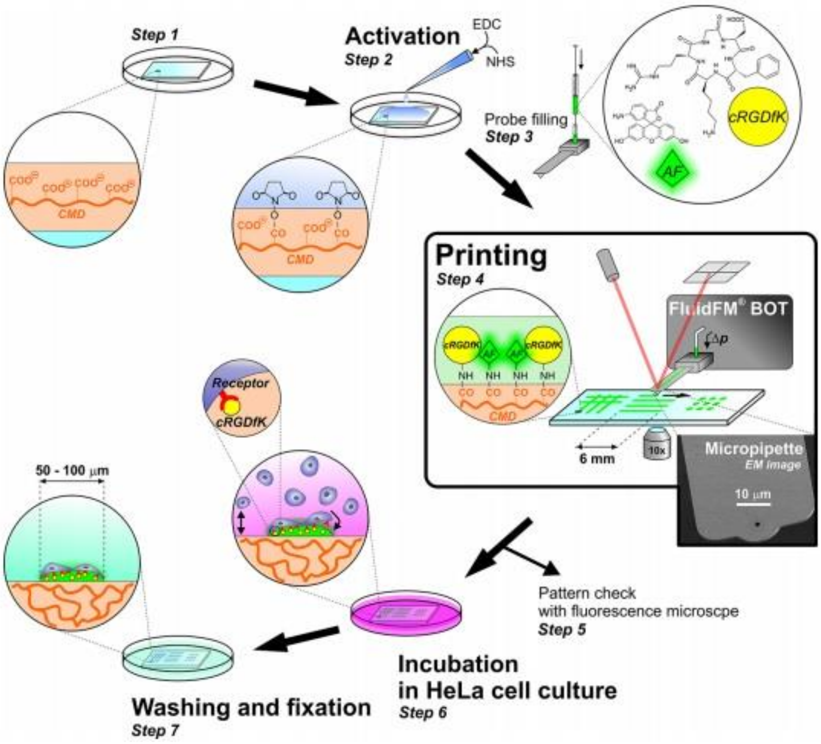

***Figure 6.5**. Method used for cell adhesion experiments on the cRGDfK-printed CMD surface, where microprinting was performed with the FluidFM technique.*

Oxidization increases the binding of EGCG to serum albumin revealed by kinetic data from label-free optical biosensor with reference channel

LP2012-26/2012 Lendület, OTKA KKP129936, OTKA KH126900, OTKA ERC_HU117755

B. Péter, A. Saftics, B. Kovács, S. Kurunczi, R. Horváth

Epigallocatechin-gallate (EGCG) is the main polyphenol ingredient of green tea. This compound is a strong antioxidant and oxidizes easily. Numerous studies demonstrated its beneficial effects on the human health, for example its anticancer and anti-inflammatory activity. In the body, EGCG is transported by serum albumin. EGCG easily oxidizes and the interactions of the oxidized form presumably present significant differences. However, the presence of oxidized EGCG is usually neglected in the literature and its effects have not been investigated in detail. Here, we applied the label-free grating coupled interferometry method that performs dual-channel measurements. The measured kinetic signal can be compensated with a signal of a reference channel at each measurement time (Fig.6.6.). By testing both hydrophilic and hydrophobic platforms, we found that EGCG can bind to a wide range of surfaces. Exploiting the dual-channel referencing ability as well as the unique sensitivity and throughput of the employed label-free technique, the experiments revealed the specific interactions between bovine serum albumin (BSA) and EGCG and determined the characteristic dissociation constant (K_d) of the binding equilibrium. The obtained binding constants were compared to literature values, showing reasonable agreement with NMR data. Besides the native EGCG, the oxidized form of EGCG was also examined, whose binding behaviors to serum albumins have never been studied. Over-stoichiometric binding obtained; BSA has stronger and weaker binding sites, which could be characterized by two separate K_d values. Furthermore, EGCG oxidization increased the bound amount [Ref.6.6].

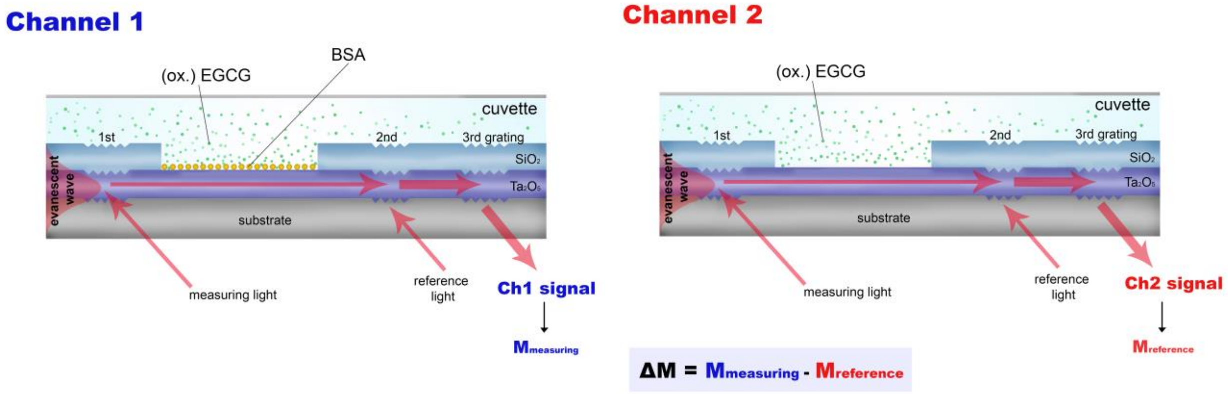

***Figure 6.6**. The sensor chips used in the WAVE instrument have two channels; one for measuring the interaction between the immobilized bioreceptor and the analyte (measuring channel, channel 1) and one for subtracting the channel 1 signal by a reference signal (reference channel, channel 2). In our case, BSA was immobilized on channel 1 surface, while channel 2 remained unmodified.*

In vitro SOD-like activity of mono- and di-copper complexes with a phosphonate substituted SALAN-type ligand

LP2012-26/2012 Lendület, OTKA KKP129936, OTKA KH126900, OTKA ERC_HU117755, OTKA FK128901, Bolyai Scholarship

I. Székács, P. Tokarz, R. Horváth, K. Kovács, A. Kubas, M. Shimura, J. Brasun, V. Murzing, W. Caliebe, Z. Szewczuk, A. Paluch, L. Wojnárovits, T. Tóth, J. S.Pap, Ł. Szyrwiel

SALEN- and SALAN-based complexes with catalytically active metal centers are very promising small molecules to be utilized as part of antioxidant therapies. Here we discuss a modified SALAN-type molecule armed with two phosphonate groups that significantly increase its water solubility and aid to furnish mono- or di-nuclear complexes with Cu^{2+} ions. The regulation of the SOD-mimicking (i.e., catalytic) disproportionation reaction of the superoxide radical anion (O_2 •−) at pH ~7.5 could be achieved by adjusting the metal-to-ligand stoichiometry as confirmed by McCord-Fridovich and pulse radiolysis tests. The higher antioxidant activity of the dicopper complex can be explained by the better access of O_2 •− to the copper centers and their more positive Cu(II)/Cu(I) redox potential. Simultaneously the analysis of in vitro effect on cells morphology (Fig.6.7.) indicates that cytotoxicity is also affected by the metal-to-ligand ratio, however, the active complex molecules do not show notable cytotoxicity that, together with the observed SOD-like activities, makes them potential candidates for antioxidant therapies [Ref.6.7.].

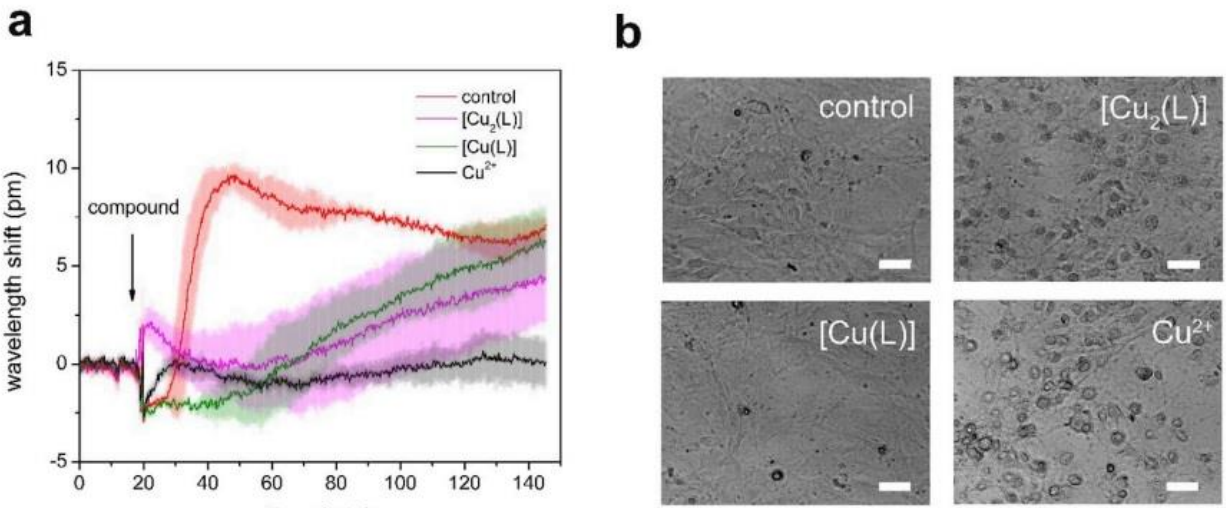

Figure 6.7. *Response of the MC3T3-E1 cells to the treatment with Cu-complexes detected with Epic BT (a). Phase contrast images (scale bar: 50 µm) show morphology of cells on the biosensor surfaces after 24 h incubation with tested compounds (b).*

An improved 96 well plate format lipid quantification assay for standardisation of experiments with extracellular vesicles

LP2012-26/2012 Lendület, OTKA KKP129936, OTKA KH126900, OTKA ERC_HU117755

T. Visnovitz, X. Osteikoetxea, B. W. Sódar, J. Mihály, P. Lőrincz, K. V. Vukman, E. Á. Tóth, A. Koncz, I. Székács, R. Horváth, Z. Varga, E. I. Buzás

The field of extracellular vesicles (EVs) is an exponentially growing segment of biomedical sciences. However, the problems of normalisation and quantification of EV samples have not been completely solved. Currently, EV samples are standardised on the basis of their protein content sometimes combined with determination of the particle number. However, even this combined approach may result in inaccuracy and overestimation of the EV concentration. Lipid bilayers are indispensable components of EVs. Therefore, a lipid-based quantification, in combination with the determination of particle count and/or protein content, appears to be a straightforward and logical approach for the EV field. In this study, we set the goal to improve the previously reported sulfo-phospho-vanillin (SPV) lipid assay. We introduced an aqueous phase liposome standard (DOPC) to replace the purified lipid standards in organic solvents (used commonly in previous studies). Furthermore, we optimised the concentration of the vanillin reagent in the assay. We found that elimination of organic solvents from the reaction mixture could abolish the background colour that interfered with the assay. Comparison of the optimised assay with a commercial lipid kit (based on the original SPV lipid assay) showed an increase of sensitivity by approximately one order of magnitude. Thus, here we report a quick, reliable and sensitive test that may fill an existing gap in EV standardisation. When using the optimised lipid assay reported here, EV lipid measurements can be more reliable than protein-based measurements. Furthermore, this novel assay is almost as sensitive and as easy as measuring proteins with a simple BCA test (Fig.6.8) [Ref.6.8.].

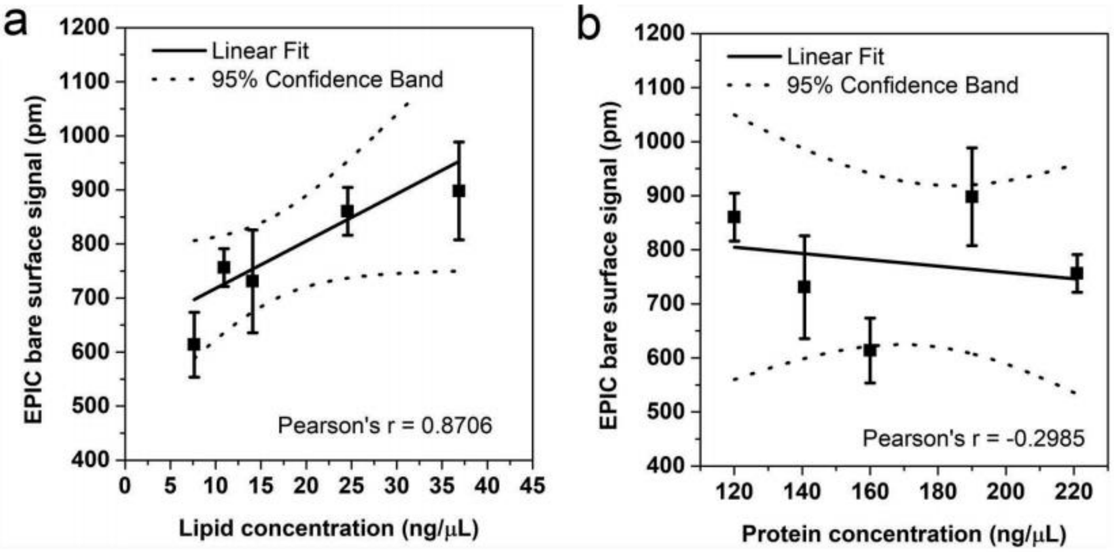

Figure 6.8*. Correlation between the lipid and protein concentrations of EVs with the "bare surface signal" of an EPIC optical biosensor. Correlation between the EPIC "bare surface signal" and the lipid concentration (a) and the protein concentration (b). Small EVs were isolated from serum-free conditioned medium of THP-1 cells. Data points are average of three replicates, error bars represent SD.*

Thin Film Physics Department

Head: Dr. Katalin BALÁZSI, Ph.D., senior scientist

Research Staff:
- Ildikó CORA, Ph.D.
- Zsolt CZIGÁNY, D.Sc.
- Zsolt FOGARASSY, Ph.D.
- Mónika FURKÓ
- Viktória KOVÁCSNÉ-KIS, Ph.D.
- János LÁBÁR, D.Sc.
- Riku LOVICS, Ph.D., left in October
- Fanni MISJÁK, Ph.D., left in October
- Nikolett OLÁH left in November
- Béla PÉCZ, D.Sc., deputy general director of Centre for Energy Res., MFA director
- György Zoltán RADNÓCZI, Ph.D.
- György SÁFRÁN, C.Sc.
- Attila SULYOK, Ph.D.
- Fruzsina SZIRA, Ph.D. left in May
- Orsolya TAPASZTÓ, Ph.D.
- Lajos TÓTH, C.Sc., retired in September
- Árpád BARNA, D.Sc., Prof. emeritus
- Péter B. BARNA, D.Sc., Prof. emeritus
- György GERGELY, D.Sc., Prof. emeritus.
- Miklós MENYHÁRD, D.Sc., Prof. emeritus
- György RADNÓCZI, D.Sc., Prof. emeritus

Ph.D. students:
- Erzsébet DÓDONY
- Klára HAJAGOS-NAGY (maternity leave)
- Nikolett HEGEDŰS
- Tamás KOLONITS
- Adél RÁCZ
- Haroune Rashid BEN ZINE (Hungaricum stipendium)
- Soukaina LAMNINI (Hungaricum stipendium)
- Mohamed AFROIU (Hungaricum stipendium)

Technical Staff:
- Andrea J. FENYVESINÉ
- Valéria OSVÁTH (maternity leave)
- Tamás ZAGYVA (leave from October)
- Noémi SZÁSZ
- Sándor GURBÁN
- Andor KOVÁCS
- Viktor VARGA

The scientific results of the Thin Film Physics Department are related to thin film and ceramic fields. The main research topics are in line with modern trends of materials science with the respect to a 50 years long history of the department. In 2019, the important base research field was the development of the thin films, especially, modern semiconductor layers, hetero transitions and 2D semiconductor layers supported by several international basic scientific projects and collaborations.

Basic and applied research of ceramics, as another important research line, was continued. Si_3N_4 / multi-layered graphene and different calcium phosphate based bioceramics were developed as framework of the research projects. Finally, as uniqueness of the Department (in national and international level) was the transmission electron microscopy. The effect of the structure on the developed materials properties was demonstrated by a TEM study and they showed that the optimal structure could be achieved in a controlled way. All topics supported by methodical developments based on electron diffraction.

In 2019, 51 papers appeared in refereed journals with a cumulative impact factor of 142. In addition, 7 papers in conference proceedings were published with no impact factor. Members of the group presented 6 invited lectures, 28 oral talks and 9 posters at national and international conferences and filed one patent. The group received 2132 independent citations in the examined interval of the last two years. Members of Thin Film Physics Department organized the International Workshop on Woman in Ceramic Science – the JECS TRUST event of the European Ceramic Society - in Budapest between April 7 and 9.

Research members of the group lectured three courses at universities and four member held laboratory practices. All courses were for full semester (Eötvös Lóránd University - ELTE, and Budapest University of Technology and Economics - BME, and Óbuda University - OE). In addition, 12 PhD students were supervised 4 of them successfully defended her/his PhD thesis.

Social activity of the group is landmarked by 15 memberships in different committees of the Hungarian Academy of Sciences and in boards of societies, giving one elected representative to the General Assembly of the Hungarian Academy of Sciences.

Graphene added multilayer ceramic sandwich (GMCS) porous structure prepared by HIP and SPS techniques

FLAG-ERA.NET “Ceranea”, OTKA NN127723

K. Balázsi, M. Furkó, Z. Liao, V. Varga, S. Gurbán, A. Kovács, L. Illés, J. Gluch, Zs. Fogarassy, D. Medved, E. Zschech, J. Dusza, C. Balázsi

Multilayer ceramic composites (MCC) consist of two ceramic materials and, considering basic properties, they can be divided into two groups: multilayer composites with weak interfaces and composites with strong interfaces. The sintering of ceramic matrix composites is usually carried out by raising the sintering temperature below melting point of components.

Graphene added multilayer ceramic sandwich (GMCS) structure can be manufactured using various methods, such as the stacking of ceramic sheets produced by tape casting or powder lamination or with in situ layer formation by slip casting, centrifugation or sequential electrophoretic deposition, sintering, among others. Spark plasma sintering (SPS) and hot isostatic pressing (HIP) were used. Multilayered graphene (MLG) and graphene oxide (GrO) were added to Si_3N_4 ceramic matrix in various amount; 5 wt% and 30 wt% (Fig. 7.1.a). The influence of reinforcing phase on final properties and the relationship between density, porosity and 3-point bending strength of composites were studied. It was shown, that both types of graphene addition had similar trend to the modulus of elasticity, namely, the decrease of strength with increasing graphene content [Ref.7.1., Ref.7.2.].

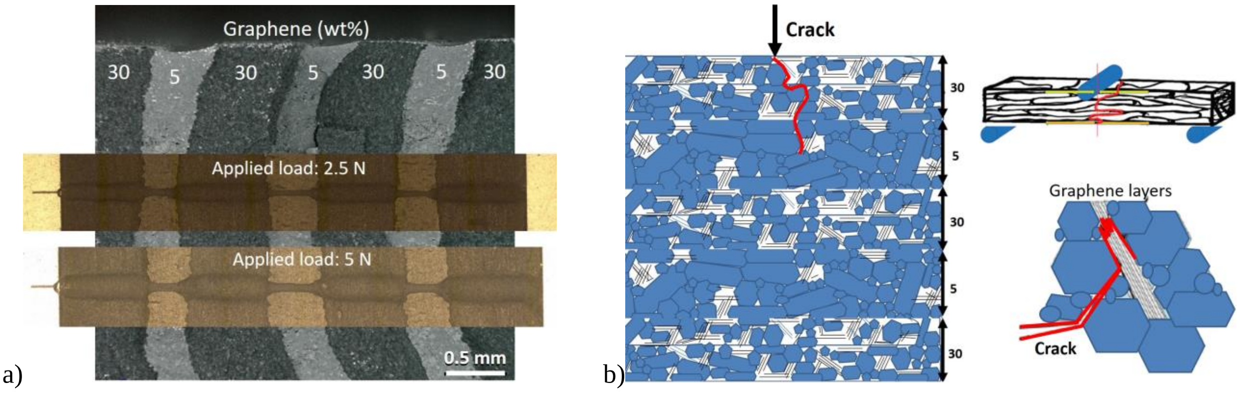

***Figure 7.1**. GMCS with 7 multilayers.*
a) SEM image with depth profile, b) schematic view of the crack propagation mechanism in GMCS structure.

Detailed elemental analysis of the layers proved the presence of graphene phase after HIP (Fig. 2) and SPS sintering process, as well, the ZrO_2 contamination. The graphene was well dispersed in matrix layers and remained non-oxidized after sintering (Fig 7.2.). The high-temperature liquid phase provided the vehicle for rapid mass transport and the driving force for densification. The 30 wt% of graphene reinforcing phase dispersed between ceramic matrix grains creating a “barrier” layer and blocked the transformation from α to β phase [Ref.7.3.].

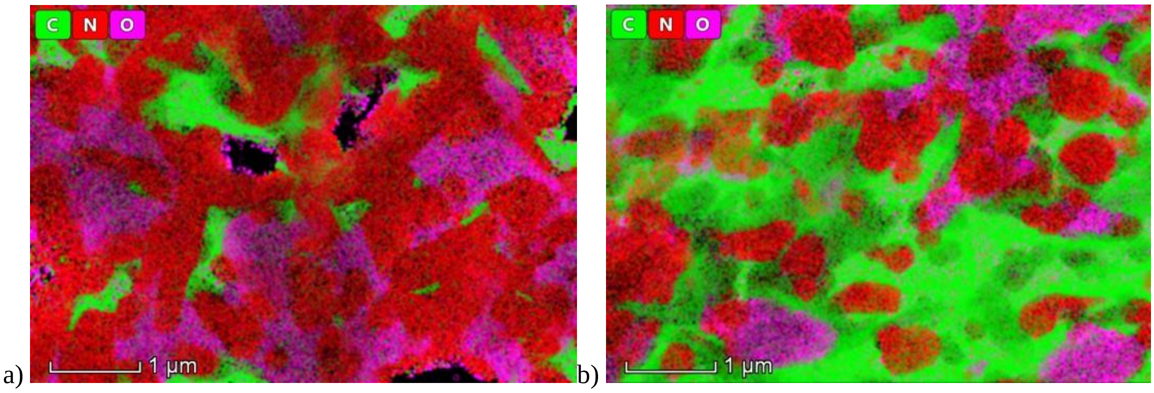

***Figure 7.2**. Elemental maps of graphene reinforced Si_3N_4 based composites.*
a) 5 wt% graphene, b) 30 wt% graphene.

The Si_3N_4 / graphene composites exhibited lower friction coefficient (Fig. 7.3.). A four-time reduction was observed for 30 wt% graphene content, independent of graphene type (MLG, GrO). The friction coefficient (COF) for 5 wt% MLG and GrO containing composites changed between 0.35 and 0.4, while for composites with 30 wt% MLG and GrO content had almost similar COF values of 0.2. These low values are related to the carbon containing tribofilms, the porous structure and characteristic of Si_3N_4 ceramic matrix [Ref.7.4.].

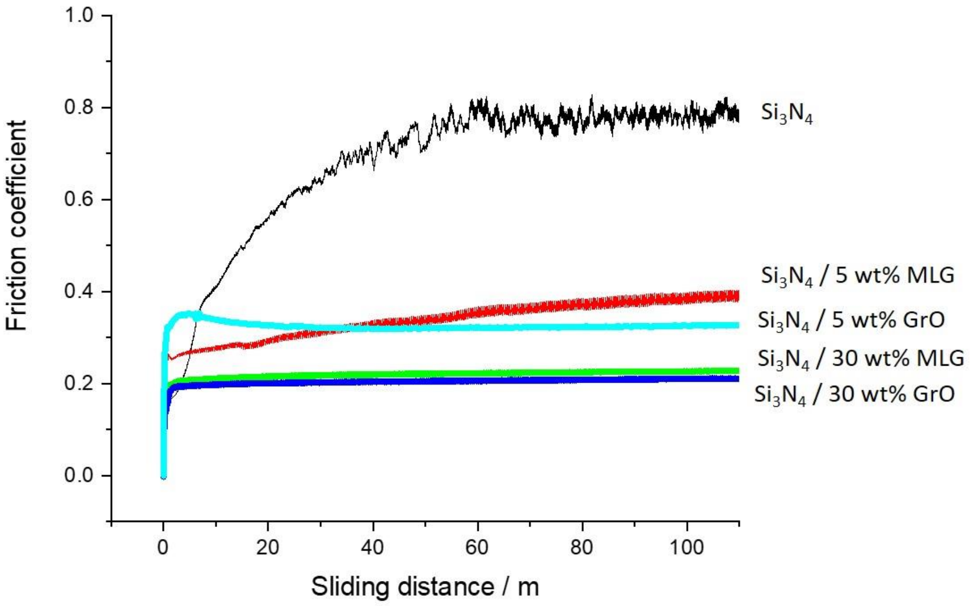

***Figure 7.3.** Friction coefficient measurement of Si_3N_4 based composites prepared by SPS.*

In conclusion, the uniaxial-pressure assisted sintering such as SPS resulted in a preferential alignment of graphene in the ceramic matrix, leading to highly anisotropic properties with lower mechanical behaviour. In the case of HIP, the high-temperature liquid phase provided the vehicle for rapid mass transport and the driving force for densification. The 30 wt% of graphene reinforcing phase dispersed between ceramic matrix grains creating a “barrier” layer and blocked the transformation from α to β phase. In both sintering processes, the homogeneity of graphene addition, the effect of layered structure and porosity influenced the final properties of GMCS structure.

An economic and facile method for graphene oxide preparation from graphite powder

FLAG-ERA.NET “Ceranea”, OTKA NN127723

M. Furkó, Zs. Fogarassy, L. Illés, K. Balázsi and C. Balázsi

A new method for preparing multi-layered graphene oxide powder was developed. In this method the raw material was commercially available micro-sized graphite powder. The graphite powder was milled by high-speed attritor mill to reduce the particle size of graphite to nanometre and to exfoliate the graphite into multi-layered graphene particles (Fig. 7.4.). The graphene particles were then oxidized into graphene oxide using the combination of strong oxidizing agents, thermal oxidizing and sonication [Ref.7.5.]. Thorough morphological characterizations were carried out to reveal the structure and the size of GrO particles. Results confirmed that the oxidation process was successful (Fig. 7.5.).

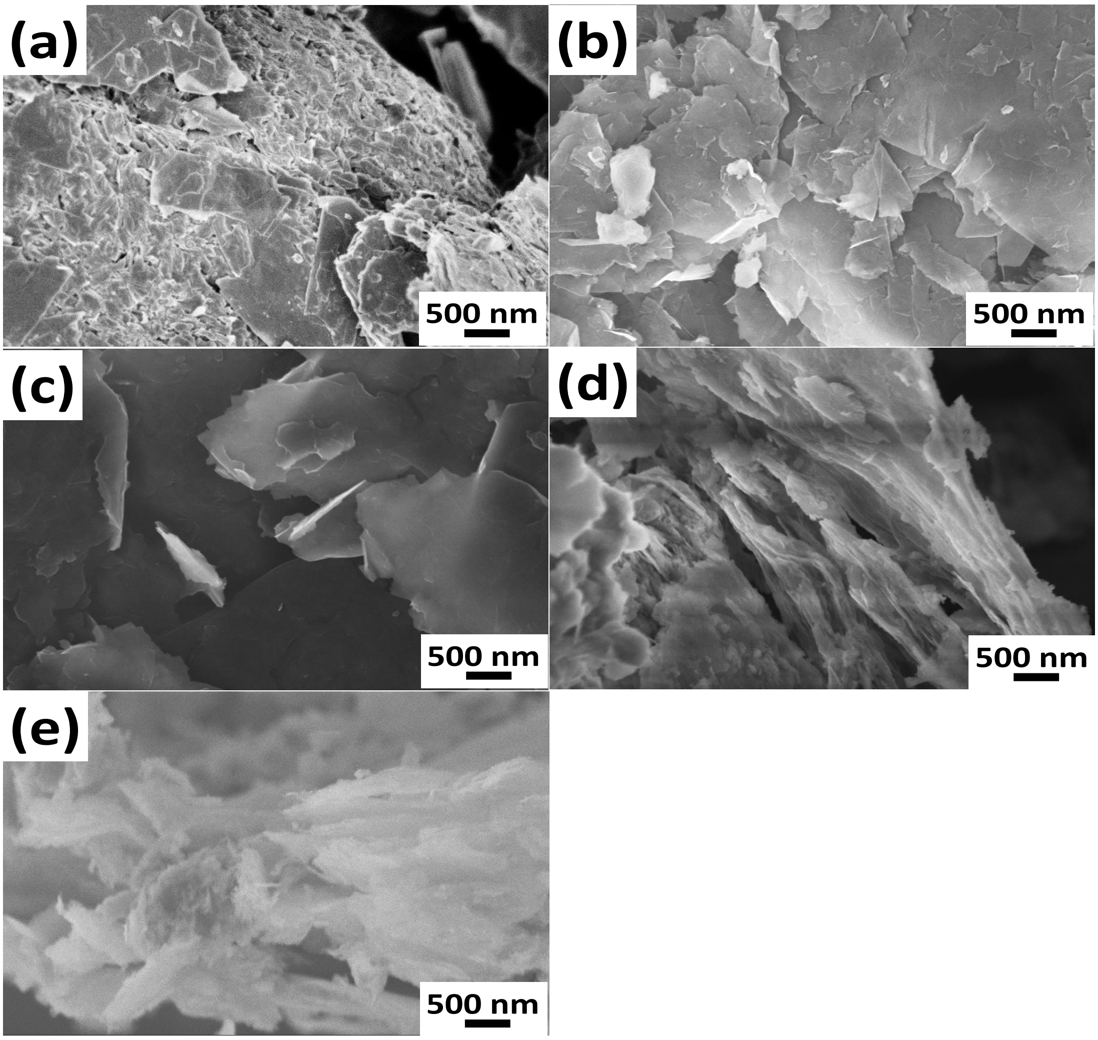

Figure 7.4. *SEM images of graphite (a), grapheme platelets (b) and different graphene oxide powders: after oxidation step first (c), oxidation step second (d) and oxidation step third(e).*

The graphene nanosheets were oxidized in three steps. First, the powders were dispersed in cc. HNO_3 solution and stirred at 80 °C for 4 hours then 50% H_2O_2 was added to the dispersion under continuous stirring and kept at room temperature for 16 hours. The dispersion was then filtered using filter paper grade 3, the filtrate washed/rinsed with 30% H_2O_2 and 96% ethanol and dried at 150 °C in air. In the second step, the dried powders were collected and put into oven and heat treated at 850 °C for thermal oxidation. Finally, a portion of treated powders were dispersed again in 96% ethanol and sonicated in ultrasonic bath for 3 hours at 70 °C to examine the effect of ultrasound on the exfoliation rate of graphene oxide multilayers, then the solvent was evaporated at 80 °C.

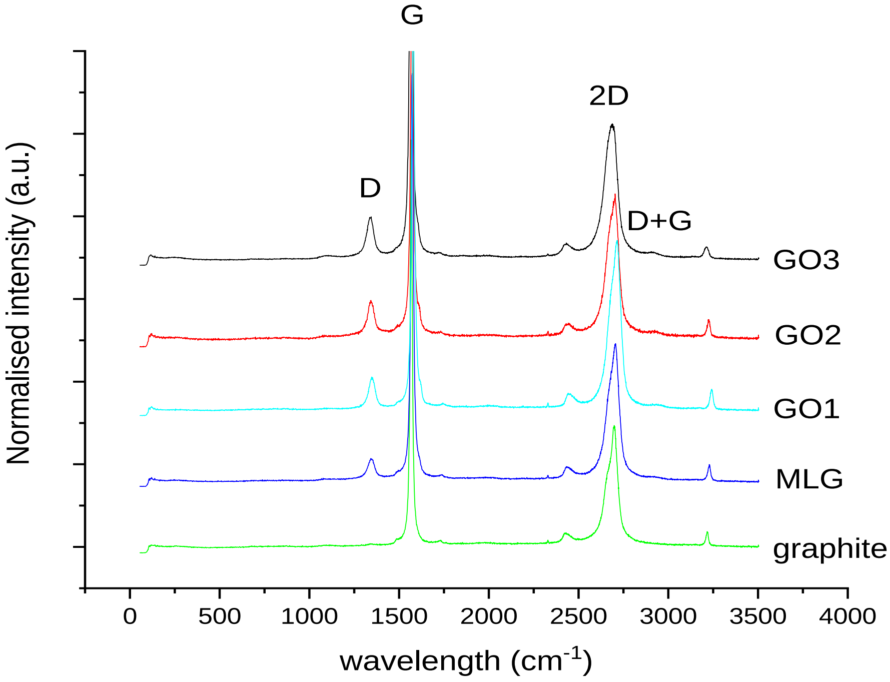

***Figure 7.5**. Raman spectra of graphite, MLG and different graphene oxide samples.*

Examination of novel electrosprayed biogenic hydroxyapatite coatings on Si_3N_4 and Si_3N_4 /MWCNT ceramic composite

T. Zagyva, K. Balázsi, C. Balázsi

Several types of biomaterials are used for total knee and hip replacements in orthopaedic surgery since the 1970s. Metallic materials, such as titanium alloys and cobalt-chromium have been widely used due to their excellent mechanical strength and corrosion resistance. Silicon nitride (Si_3N_4) ceramic, beside these advantageous properties exert two or three times better fracture toughness than metals, thanks to its microstructure. The high fracture toughness is resulted from the extended crack path along the surface of the elongated grains. Although there is no chemical reaction between bioinert ceramics (e.g. Si_3N_4) and the living tissue, bioactive materials can induce tissue reactions in human body. Using a biodegradable and bioactive temporary coating (e.g., hydroxyapatite HAP) on the implant's surface could induce tissue reactions and help avoid the rejection from the body in the critical early few days, after the operation.

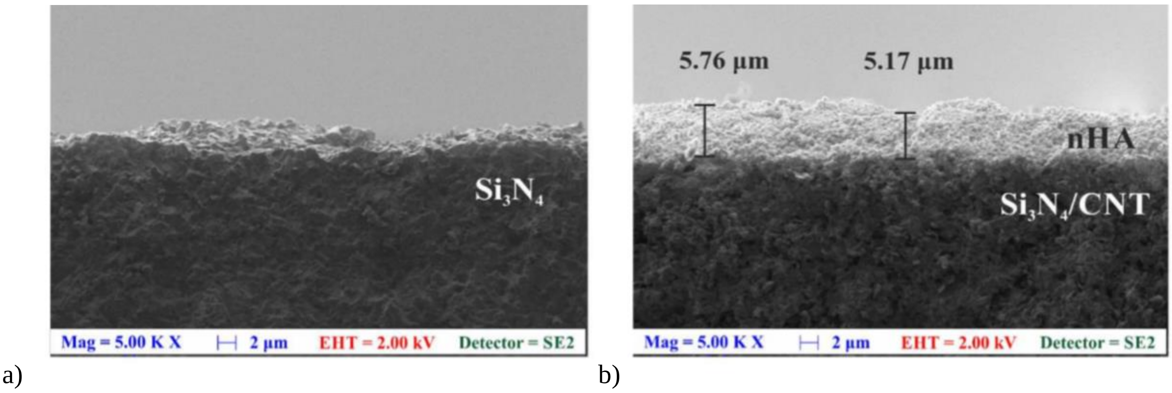

a) b)

Figure 7.6. *Electrosprayed nHAP layer after 45-minute-long ESD process with the same deposition parameter. a) Si_3N_4, b) Si_3N_4/MWCNT substrates.*

The aim of our study was to produce thin nanosized HAP layer on silicon nitride implant material by electrospray deposition (Fig. 6). To the best of our knowledge, this is the first time that electrosprayed nanosized hydroxyapatite coatings were deposited on the ceramics, although this method is more cost-efficient than other widely used deposition techniques like plasma spraying, pulsed laser deposition or RF-magnetron sputtering. In case of electrospraying, electrically conductive materials are required as substrates. Ceramics are mostly insulators, therefore special treatments (e.g., doping) are necessary for creating appropriate substrates for the deposition process. Multiwall carbon nanotubes (3wt.%) were ideal dopants for increasing the conductivity of Si_3N_4. The carbon nanotubes occurred only inside the substrate. Using the same deposition parameters, a thin (5μm) nHAP coating was deposited on the MWCNT doped silicon nitride in 45 minutes (Fig. 6b), while continuous nHAP layer could not form on the pure (insulator) Si_3N_4 surface during this time (Fig. 6a) [Ref.7.6.].

Eco-friendly AlON processing

OTKA NNE129976

K. Balázsi, M. Furkó, V. Varga, S. Gurbán, L. Illés, S. Lamnini, F. Szira, C. Balázsi

Aluminium oxynitride (AlON) has a unique thermal and chemical stability that makes it a perfect candidate for a wide range of applications. Currently commercially available AlON material exhibit average grain size in the order of 150–200 μm; however, development of new methods to control grain size, especially, at the nano-scale could create materials with improved properties. The most promising techniques for AlON preparation are hot pressing (HP), hot isostatic pressing (HIP) and spark plasma sintering (SPS).

According to the thoroughly studied literature data and the state of the art on AlON preparation, the currently available and used techniques are still all expensive, as well as being energy and time consuming [Ref.7.7.]. High temperature above 1600–1900 °C is needed for a long time to achieve appropriate phase and densification. We intend to develop an eco-friendly preparation method of AlON in which we develop a novel way to reduce the temperature and/or time thus requiring lower energy (technique, temperature and so on). Moreover, we are planning to recycle and utilize the industrial by-products or aluminium waste (such as aluminium cans) as Al source.

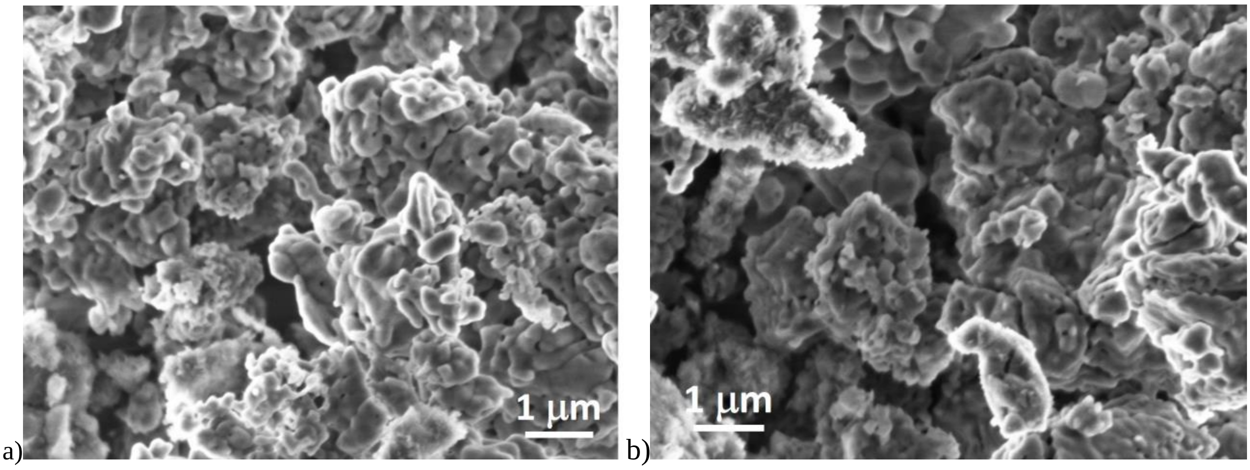

Figure 7.7. *SEM image of oxidized AlN powder. a) 3 h, b) 10 h.*

The aim of our research is a preparation of cheap AlON by eco-friendly technology. The oxidization of base AlN powder with specific surface area 4.0 -8.0 m²/g and an average particle size of 0.80 -1.8 μm for 3, 6 and 10h at 900°C in air atmosphere was the first step (Fig. 7.7.). Hot isostatic pressing for 5h at 1700°C in nitrogen was used for sintering of oxidized powders. The increasing the oxidation time significantly improved the tensile strength of sintered samples compared to the reference (Fig. 7.8). In the case of reference AlN, the measured value is 13.8 MPa on average for the 4-point bending test and 159.2 MPa after 10 h oxidation. It shown the significant increasing with oxidation time. The oxidation time has influence not only on mechanical properties. We showed, that the increasing of oxidizing time, the higher density, the lower porosity showed the AlON after 10h oxidization [Ref.7.8.].

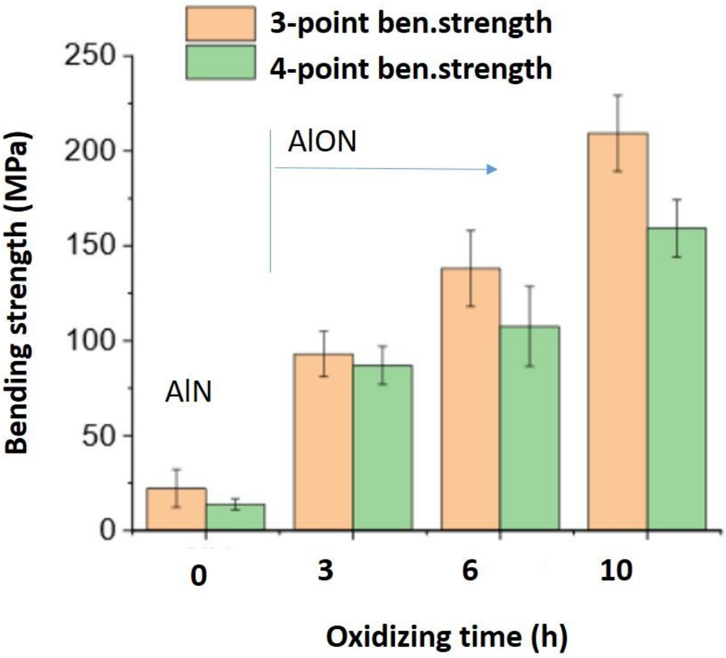

Figure 7.8. Bending strength of reference (AlN) and sintered AlON ceramics with different oxidation times.

Development of of multiwall carbon nanotube reinforced yttria stabilized zirconia composites

S. Lamnini, L. Illés, Zs. Horváth, Zs. Fogarassy, V. Varga, K. Balázsi and C. Balázsi

Zirconia (ZrO_2) based materials belong to the most widely investigated and technologically powerful ceramics applied in several fields. Nowadays, multiwall carbon nanotube (MWCNT) reinforced ZrO_2 composites are attracting growing interest, thanks to their ability of self-healing of the crack and the possibility to tailor the desired nanostructured properties. The aim of this PhD work was the experimental synthesis of 8mol% yttria-stabilized zirconia (8YSZ) containing 1, 5 and 10 wt% MWCNTs and study of the microstructure effect on the mechanical and tribological properties of composites (Fig. 7.9). The powder morphology of pure 8YSZ has been significantly modified after attrition milling to a refined and homogeneous microstructure sized of approximately 400 nm with soft grain edges.

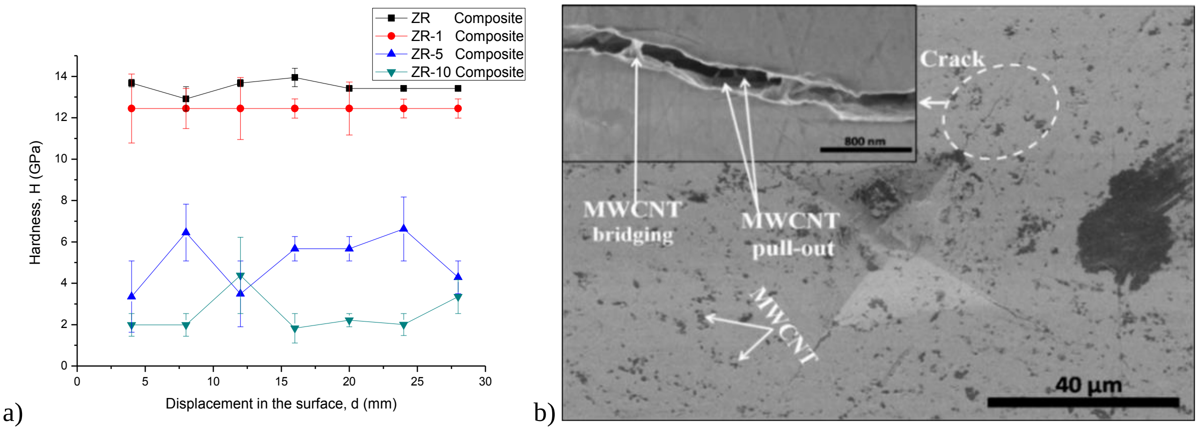

Figure 7.9. *Mechanical properties of 8YSZ/MWCNTs composites. a) hardness measurements, b) crack propagation in composite with 1 wt% MWCNTs.*

8YSZ / 1 wt% MWCNTs sintered composite owns the highest density 6.76 g/cm^3, hardness 12 GPa (Fig. 7.9.a) and bending strength of 502 MPa besides the lowest porosity of 16.5 % among all the tested composites.

The analysis of the crack propagation modes showed the presence of MWCNT pull-out, crack bridging and crack deflections besides more restrained and tapered crack path in the 8YSZ /1 MWCNTs wt% composite compared to the reference (Fig. 7.9.b). It was showed that these toughening mechanisms played a vital role in enhancing the resistance to crack propagation. The high degradation of the mechanical and indentation fracture toughness was well approved in case of 5 wt% and 10 wt% MWCNTs addition. This was associated with incoherent and discontinuous matrix, reduced interfacial bonding due to the deep open pores on the surface, which caused a long unrestrained crack path. It was shown an outstanding wear improvement of composite with 1 wt% MWCNTs at low (0.036 m/s) and high (0.11 m/s) sliding speeds attributed to the formation of a perfectly continuous, uniform tribofilm and the improved flexural strength and density. Further, the steady state friction coefficient marked significant decrease at higher sliding speed with 5 and 10 wt% of MWCNTs content [Ref.7.9.,Ref.7.10.].

Novel method for the production of SiC micro and nanopatterns

A.S. Rácz, D. Zámbó, G. Dobrik, I. Lukács, Z. Zolnai, A. Németh, P. Panjan,
A. Deák, G. Battistig, M. Menyhárd

Recently we have shown that it is possible to produce SiC nano-coating at room temperature by applying ion beam mixing (IBM) on C/Si multilayer structures. Herein we show that the combination of masking layers with IBM allows the fabrication of patterned SiC structures at room temperature and the achievable patterned area is scalable up to wafer size. For this purpose IBM was applied on a Si/C system covered by masks obtained by either conventional lithography technique or nanosphere lithography.

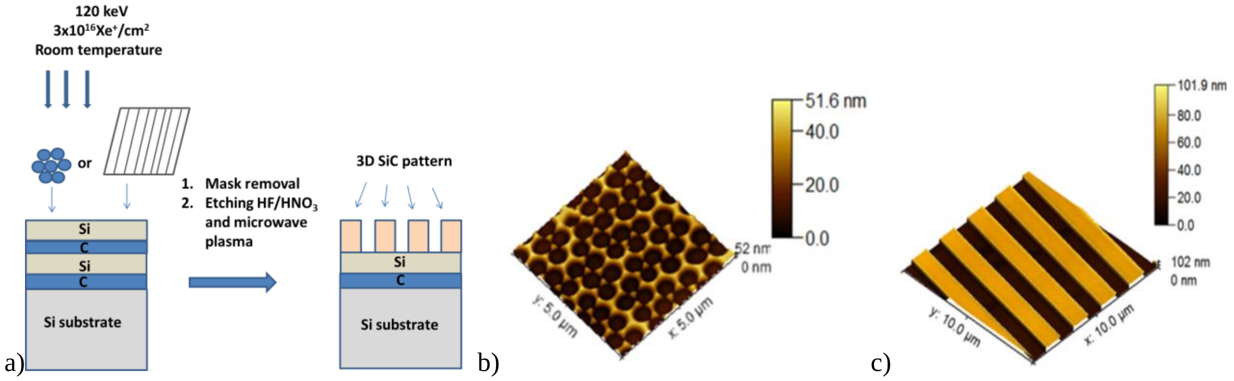

Figure 7.10. *a) Process of producing 3D structures b) AFM image of the LB-masked sample after mask removal and one step HF/HNO_3 etching and one step oxidation. c) AFM image the grid-masked sample after mask removal and HF/HNO_3 etching, oxidation and additional HF/HNO_3 etching*

The irradiation conditions were chosen by TRIDYN simulation. Due to IBM a SiC rich layer formation on the non-covered parts of the sample was demonstrated using AES depth-profiling, while the covered regions have not changed. Thus, in a single-step (the compound formation and the creation of patterns happened in one step) a tailor made 2D nanopattern of SiC rich regions alongside pure Si has been constructed at room temperature. Applying additional etching and oxidation processes the 2D pattern has been transformed to a 3D one consisting SiC rich regions in their original place and holes of given depths with either C or Si bottom. The scheme of the 3D structure production is depicted in Fig. 7.10.a, while Fig. 7.10.b and 7.10.c provide the AFM images of the different 3D structures. One of the 3D structure produced by applying the Langmuir-Blodgett film was tested for surface-enhanced Raman scattering (SERS) application. To our knowledge IBM have not been used to produce SERS substrates, yet. The gold coated 3D structure proved to be SERS active allowing the high sensitivity detection of biomolecules both in mild and harsh environments. [Ref.7.11.]

Investigation of the nanostructural background of functionality in the case of biogenic and biocompatible mineral apatite

OTKA K125100

1) Crystal structure study of bone apatite nanocrystals

V. Kovács Kis, Zs. Czigány, Zs. Dallos, D. Nagy, I. Dódony

While synthesis and characterization of calcium phosphate biomaterials for biomedical applications relies on their similar composition to bone and teeth mineral apatite, the atomic structure and nucleation processes of the biological calcium phosphates themselves are poorly known. Transmission electron microscopy is a powerful tool for studying structures on the nanoscale. While the atomic structure of individual tooth enamel apatite, which have much less organic content (< 5%), has been successfully investigated by HRTEM, nanoscale electron diffraction techniques indicating non-centrosymmetry of the enamel apatite nanocrystals [Ref.7.12.], no published atomic level structural information on bone apatite nanocrystals is known up to now.

In [Ref.7.13.] we present the first crystal structure model for bone apatite based on the analysis of individual nanocrystals by high-resolution transmission electron microscopy (HRTEM) see Fig. 7.11.

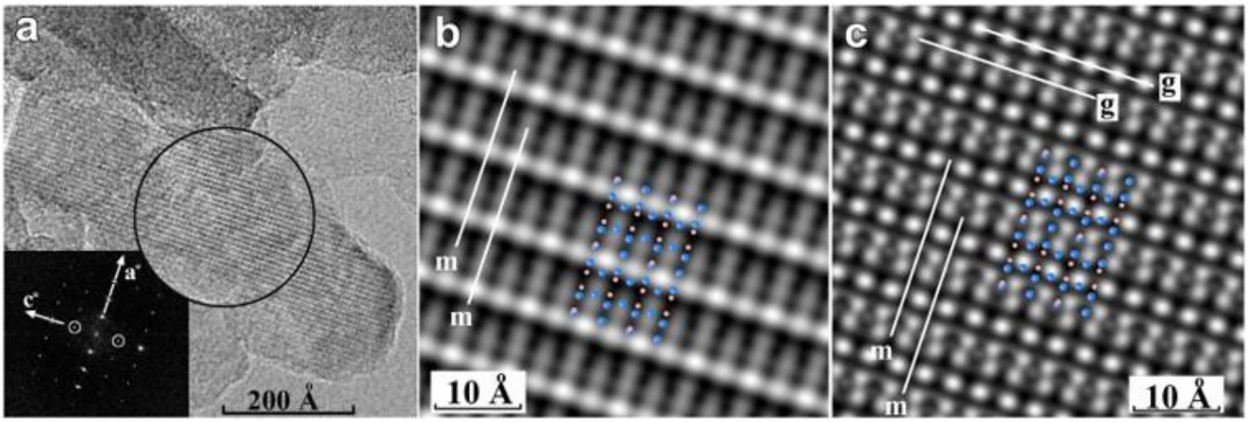

Figure 7.11. *a) [100] HRTEM image of bone apatite nanocrystal is shown with its Fourier transform inserted in the lower left corner. Fourier components forbidden by $P6_3/m$ space group symmetry are encircled. b) Enlarged symmetry imposed image, mirror planes (m) are marked. The inset is the structure model of $P6_3/m$ apatite for 2 × 2 unitcells. c) Calculated [100] HRTEM image of $P6_3/m$ F-apatite with 2 Å resolution. The 2D symmetry elements, mirror plane (m) and glide plane (g), are marked. The inset is the structure model of $P6_3/m$ apatite for 2 × 2 unit cells. Calcium (orange) and phosphorus (blue) atoms are shown, other atoms are omitted for clarity.*

By crystallographic image processing we show the loss of hexagonal symmetry along the c axis. To explain our observations, we propose a structure model for B-type carbonate substitution with O vacancies localized in the structural channel along the c axis (Fig. 7.12.). This model is in agreement with the observed absence of the [001] 6_3 screw axis, and the shift of mirror plane perpendicular to the c axis. Carbonate substitution is deduced from the measured Ca/P=2 ratio.

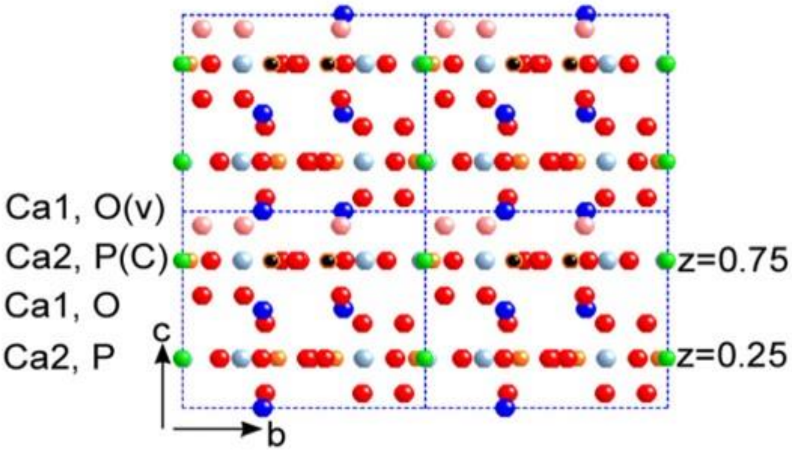

Figure 7.12. *Proposed structural model for carbonated F-apatite to interpret HRTEM observations on bone apatite nanocrystals, 2 × 2 unit cells. Representation of atoms: blue – Ca (dark and light blue are Ca1 and Ca2 positions, respectively), orange – P, black – C, red – O, pale red – O vacancies, green – F. [100] zone projection.*

Besides symmetry reduction, we give evidence for polarity along [010] direction of bone apatite, which implies chemically distinct (0*k*0) surfaces [Ref.7.12.]. First principles study [Ref.7.14.] indicate different water adsorption capacities of the two types of surfaces. Bone apatite nanocrystals, which are platy on (010), have relatively large (0*k*0) surfaces, which according to our results [Ref.7.13.], are either Ca or P rich. Ca release in exchange for two hydrogens proved to be energetically favourable [Ref.7.14.], promoting surface hydratation. Therefore, we propose that the relative orientation of (0*k*0) facets has prominent role in resorption processes and also in the adhesion of apatite nanocrystals to the collagen fibers [Ref.7.13.].

2) Primary dental enamel: nanostructure and mechanical properties

V. Kovács Kis, Zs. Kovács , M. Hegedűs, A. Sulyok, A. Jakab, L. Illés, K. Hajagos-Nagy, Gy. Radnóczi

“XPS clean” surfaces of deciduous dental enamel, obtained according to the cleaning protocol established in the previous year, has been subjected to Mg-exchange experiments. The aim of these experiments was to study under controlled conditions the correlation between Mg-content and mechanical properties, reported in the first year. To check the effect of crystallinity, morphology and particle size on Mg incorporation, nanocrystalline hydroxylapatite and amorphous calcium phosphate (ACP) nanoparticles together with crystalline apatite of pegmatitic origin were also included into the study. Our results indicate that enamel incorporates more Mg than nanocrystalline hydroxylapatite, in spite of its smaller specific surface (related to its character of compact ceramics). ACP dissolves and re-precipitates via forming a metastable nanocrystalline Ca-phosphate phase with stoichiometry Ca:Mg:P = 1:1:2.

Regarding the effect of Mg incorporation on mechanical properties, nanoindentation measurements were performed in parallel on two halves of the same molar, one subjected to the Mg exchange procedure, the other not. This method excludes the effect of individual variations in the thickness of the aprismatic layer, which as reported in the last year, correlates both with native Mg content and with nanohardness. According to our results, Mg incorporation into dental enamel induces a nanohardness increase by cca. 20

% with respect to the initial values (Fig. 7.13). According to preliminary HRTEM, this significant increase is related to a decrease of crystallite size during Mg uptake. These results were presented at two conferences: full-length papers are in preparation.

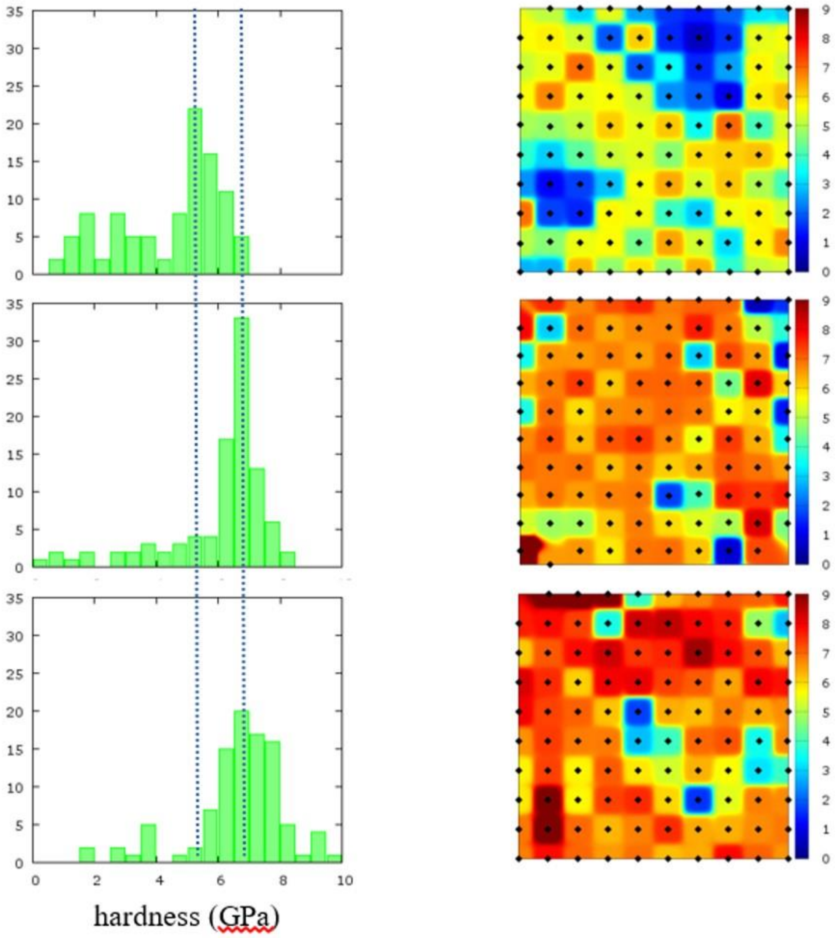

Figure 7.13. *Nanoindentation measurements on pristine (upper row) and Mg-treated (middle and bottom row) primary molar surfaces, array of 10x10 measurement points, 50 μm step size.*

Nanostructure investigation of Mg-NbO-carbon nanotube composite materials for hydrogen storage applications

M. Gajdics, T. Spassov, V. Kovács Kis, E. Schafler, Á. Révész

Mg-based nanostructured materials have considerable potential for future applications in hydrogen storage, the main focus of ongoing research activities is improving the desorption properties by applying different additives and processing techniques. In collaboration with colleagues from the Eötvös University, several Mg based nanocomposites before and after absorption-desorption cycles were studied using HRTEM and the effect of the applied additives (Nb_2O_5, carbon nanotubes (CNT) [Ref.7.15., Ref.7.16.], titania nanotubes [Ref.7.17.] and their combinations) and processing techniques (ball milling, high pressure torsion (HPT)) on the nanostructure was investigated.

According to our results [Ref.7.15., Ref.7.16.], in the ball milled Mg-CNT nanocomposite sample the interior of the Mg particles contains fairly long CNT sections (several tens of nanometers), which are slightly bent and mainly intact. After HPT, CNTs are still recognized in the disks; however, they are heavily bent considerably shorter than the nanotubes in the corresponding as-milled powder. It is evident from the HRTEM that the torsion procedure does not completely destroy the nanotube structure, which is crucial for the catalytic effect.

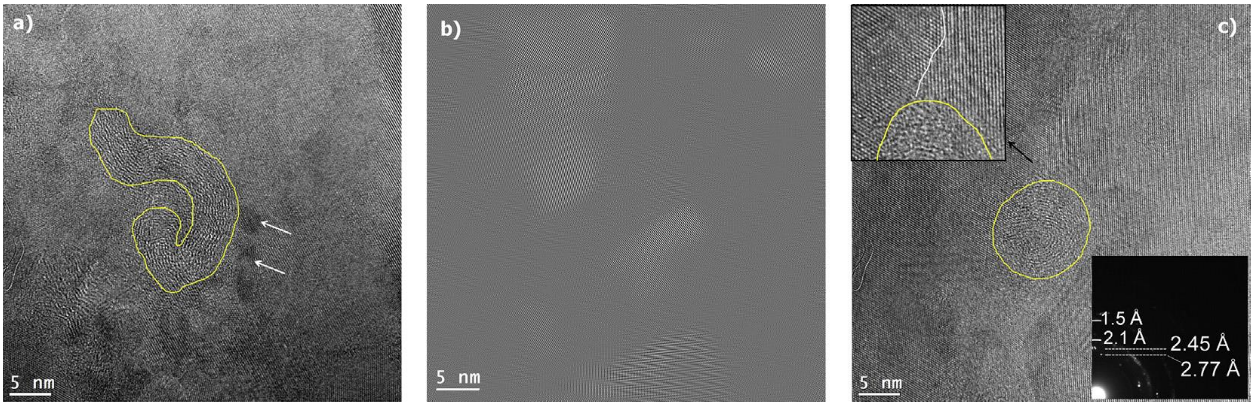

Figure 7.14. *a) A HRTEM images of Mg-NbO-CNT_HPT containing a short nanotube section, b) the corresponding IFFT image using Nb_2O_5 Fourier maxima. Yellow lines mark the egde of CNT, c) A nanotube lying parallel to the viewing direction close to a grain boundary, marked by white line on the enlarged image at the top left corner. The inset at the bottom right corner shows a typical SAED pattern.*

It is noteworthy that CNTs and Nb_2O_5 nanoparticles, when applied together, are located in close proximity to each other in the HPT processed samples, which is even more evident on HRTEM images after hydrogen cycling (Fig. 7.14.a) [Ref.7.15.]. We propose that the presence of this kind of agglomerated catalyst structures might be the reason of the noticeably improved sorption kinetics of the Mg catalyzed applying both CNT and Nb_2O_5 (Fig. 7.14.b-c).

Structural and electrical properties of AlN thin films on GaN substrates grown by plasma enhanced-Atomic Layer Deposition

FLAG-ERA.NET 'Grifone"

E. Schilirò, F. Giannazzo, F. Roccaforte,Zs. Fogarassy, I. Cora, B. Pécz

Aluminum nitride (AlN) thin films have been deposited by Plasma Enhanced Atomic Layer Deposition (PE-ALD) onto GaN-sapphire substrates [Ref.7.18.] The morphological, structural and electrical properties of AlN films with different thicknesses (from 5 to 15 nm see Fig. 7.15.) have been investigated. They uniformly cover the underlying GaN substrate without pinholes and cracks. All the AlN thin films show c-axis orientation and their in-plane crystalline arrangement perfectly matches the hexagonal structure of GaN substrate. In particular, the cross-sectional TEM analysis demonstrated that the first AlN layers are well aligned with respect to the GaN (001) substrate, while stacking faults formation is observed in the upper part of the films.

Finally, electrical measurements by Hg-probe on as-deposited AlN showed very low current leakage across these layers and the presence of a high density two dimensional electron gas (> 2×10^{13} cm^{-2}) at the AlN/GaN interface. This latter is a consequence of the above discussed good epitaxial quality of the PE-ALD grown AlN thin films on GaN. These results are promising for future integration of low-temperature deposited AlN thin films with GaN devices technology.

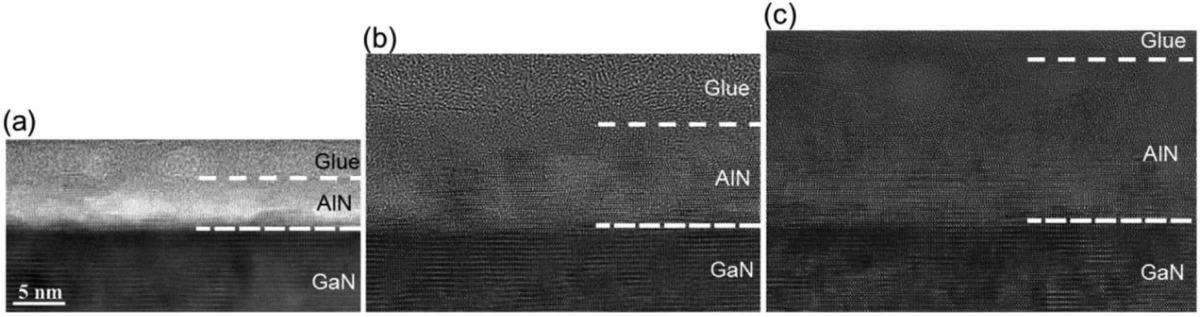

Figure 7.15. *High-resolution cross-sectional TEM images acquired on the AlN layers with 5 nm (a), 10 nm (b) and 15 nm (c) nominal thickness.*

Structure, mechanical properties and thermal stability of WBC and MoBC coatings

M. Alishahi, S. Mirzaei, P. Soucek, L. Zábransky, V. Buršíková, M. Stupavská, V. Peřina, K. Balázsi, Zs. Czigány, P. Vašina

Characterization of sputtered WBC and MoBC was performed in cooperation with Department of Physical Electronics of Masaryk University, Brno, Czech Republic (Brno) and Nuclear Physics Institute of Academy of Sciences of the Czech Republic, Rež (Rež). The cooperation, which started in 2016 is promising since deposition of layers that are both hard and fracture tough is difficult. The recently applied ceramic coatings are generally fragile. The apparently contradictory properties of high hardness and ductility may be realized in X_2BC systems (X = Ti, V, Zr, Nb, Mo, Hf, Ta, W) by an-initio calculations. In this cooperation WBC [Ref. 7.19., Ref.7.20., 7.21.] and MoBC [Ref.7.22.] films were investigated.

In our previous experiments, we have investigated the effect of C/W ratio on bond structure, microstructure, hardness, fracture toughness and scratch resistance at constant B content. This year we added the investigation of the effect of B/W ratio at constant C content. The new results verify former observations. The layers are mostly amorphous, however, a certain level of short range ordering can be observed even in the amorphous films, which are manifested in short, curved and irregular lattice fringes in the HRTEM images. Coatings in the vicinity of W_2BC composition are nanocomposites containing nanocrystals with size of ~ 5nm embedded into an amorphous matrix. All the layers exhibited high hardness (>20GPa) so they all can be classified as hard coatings. The level of crystallinity played no crucial role in determining the hardness of the coating, while the effect of the coating structure and bonding was clear – the densest coating with the highest relative amount of W-B bonds exhibited the highest hardness of ~ 29 GPa. Furthermore, the presented coatings exhibited high adhesion to industrially important substrates as well as scratch and crack resistance unmatchable by current top-of-the-shelf industrial protective coatings of comparable hardness. The bond state and structure of the amorphous and nanocrystalline WBC coatings were compared with ab-initio calculations [Ref. 7.21.].

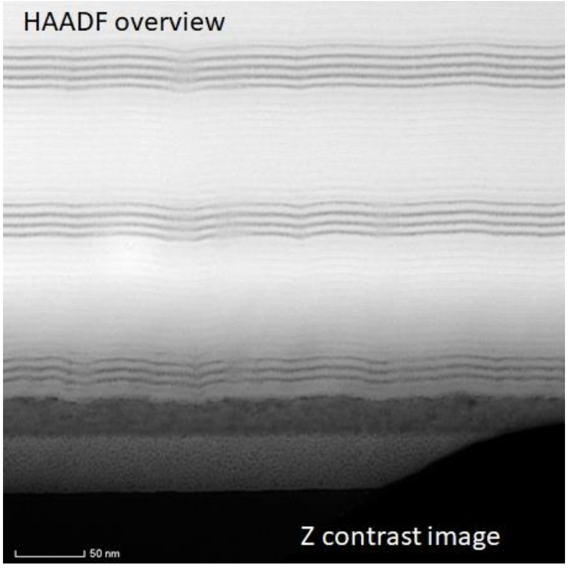

Figure 7.16. *STEM-HAADF image of a WBC coating sputtered in an industrial chamber. The hierarchic multilayer structure, composed of ~5nm layers, was formed due to the double rotation mechanism of the sample holder.*

WBC coatings might pave the way to the next generation of coatings for tool protection. As an example the STEM HAADF image of a WBC coating deposited in an industrial chamber is shown in Fig.7.16. Based on HAADF and Spectrum Images a hierarchical multilayer structure was revealed which is composed of ~5nm layers. The complicated multilayer structure was formed due to the double rotation mechanism of the sample holder [Ref.7.20].

After annealing at 1000°C of MoBC films Mo_2C and Mo_2BC phases were formed embedded in a nanocrystalline matrix [Ref.7.22].At high Mo content nanocrystalline Mo_2C phase, at low Mo content Mo_2BC phases were formed. At medium Mo content the structure was almost amorphous. The hardness and elastic modulus of the layers always increased after annealing, in some cases reaching the 29GPa and 500GPa values, respectively. Co diffusion from the WC(6%Co) substrate and the formed nanocrystalline phases were identified based on HRTEM, STEM HAADF and EDS elemental maps (Fig. 7.17).

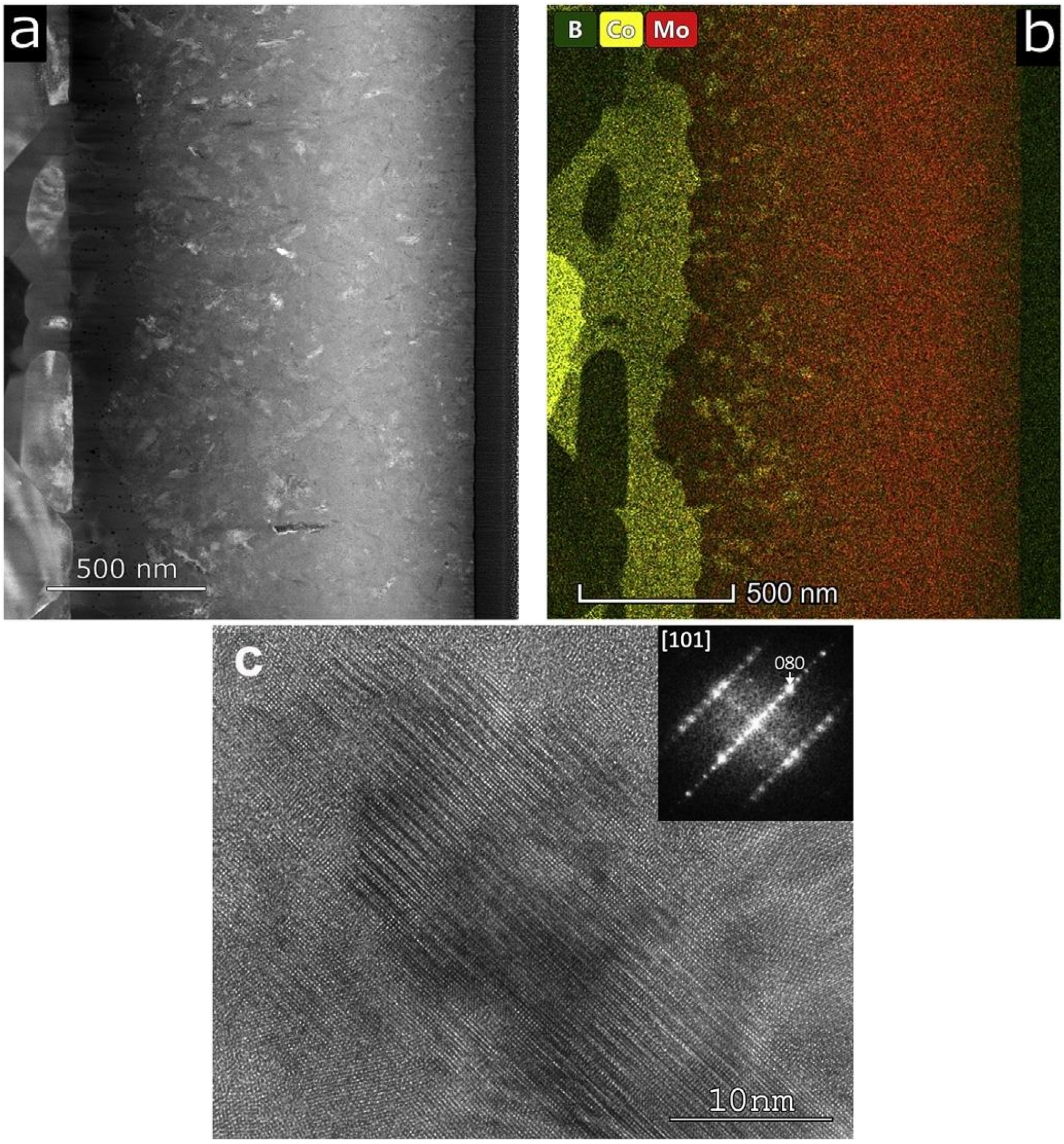

Figure 7.17. *a) HAADF image of a MoBC film with 45 at% Mo content after annealing at 1000°C, b) its EDS elemental map. The interaction between the WC(6%Co) substrate and the film can be observed in the EDS elemental map: the Co content of the substrate diffuses into the film to 100-200nm depth. By the Fourier transform of the HRTEM image (c) orthorhombic Mo_2BC phase can be identified embedded in a nanocrystalline matrix.*

Influence of bath additives on the thermal stability of the nanostructure and hardness of Ni films processed by electrodeposition

T. Kolonits, L. Péter, I. Bakonyi, J. Gubicza and Zs. Czigány

The effect of various organic additives (such as saccharin and trisodium-cytrate) on the microstructure (grain size, dislocation and twin densities), mechanical properties and thermal stability of electrodeposited Ni films was investigated by X-ray diffraction (XRD) line profile analysis and transmission electron microscopy (TEM). The main task of the project is to investigate the thermal stability of different initial microstructures, which could be formed by solving organic additives in the original electrolyte.

The electrodeposited layers were deposited at room temperature at low current density onto copper substrate. The basic electrolyte mainly contained nickel-sulphate ($NiSO_4 \cdot 7\ H_2O$) and boric acid (H_3BO_3). XRD and TEM grain size and phase analysis was carried out to determine the microstructure. Hardness tests were made to examine the mechanical properties. Heat treatment (at 400, 500, 600, 750 and 1000 K) was applied to investigate the stability of the micro and macro properties.

During this work, three different initial microstructures were formed: the organic additive free bath resulted a large grain size (90-130 nm), a low dislocation density ($13 \times 10^{14}\,m^{-2}$) and a (220) type texture. Trisodium citrate resulted a moderate grain size (60-80 nm) and dislocation density ($30 \times 10^{14}\,m^{-2}$) and the direction of the texture changed into (200). The additive saccharin resulted in the smallest grain size (20-30 nm), the largest defect density ($160 \times 10^{14}\,m^{-2}$), the highest hardness and the texture was eliminated.

The changes of the hardness and the microstructure during the heat treatment can be followed on Fig. 7.18. It was found that the layer with additive saccharin which showed the highest hardness at room temperature has the worst thermal stability since the high defect density led to a large driving force for recrystallization; the recrystallization process occurred between 750-1000 K and took place in a few minutes. The best thermal stability was achieved in the layer processed with trisodium-cytrate as recrystallization has not been observed even after heating up to 1000 K [Ref.7.23.].

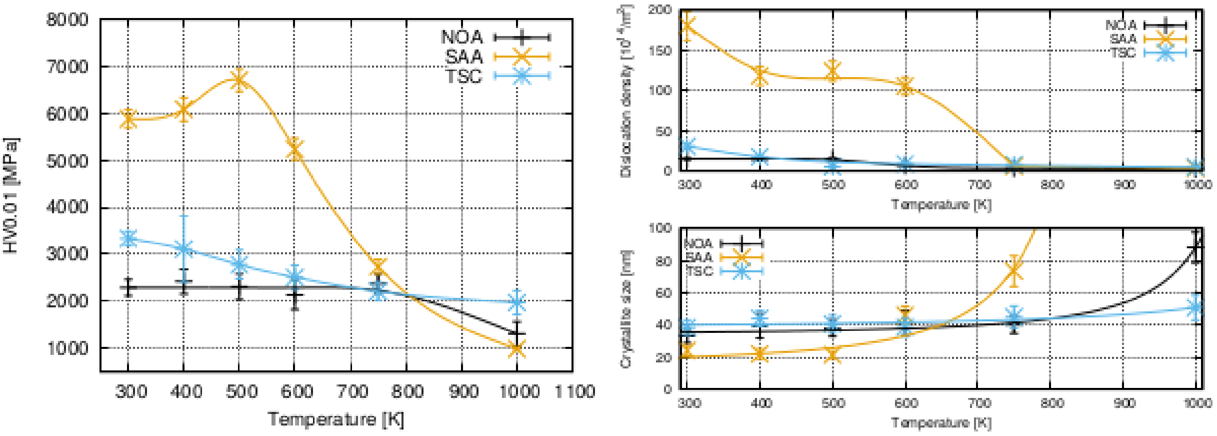

Figure 7.18. *Hardness, dislocation density and crystallite size of heat-treated electrodeposited nanocrystalline nickel layers.*

TEM study of nickel silicides

E. Dódony, Gy. Z. Radnóczi

Controlled formation of nickel silicide materials is still extensively studied, due to their impact in microelectronics. As the industry is heading towards ever smaller device sizes, new challenges arise. The phase formation and sequence of the nickel silicides differ from the results of the bulk experiments, because of the restricted dimensions. In order to make and optimize devices and their performance, it is necessary to learn how the used materials are formed, what is their atomic structure, and how it transforms as a function of elapsed time.

Due to their importance, we are studying the formation of copper-silicides in thin amorphous silicon (a-Si) films, with the focus on the development and structure of the γ phase $Ni_{31}Si_{12}$. The samples – 10nm thick a-Si foils, supported by a Ni microgrid – were heated in-situ to temperatures up to 600 °C, and the silicide formation was investigated. The model structure was created by DC magnetron sputtering a layer of Si in Ar on cleaved NaCl substrate, then, the a-Si layer was transferred to the Ni microgrid by dipping the NaCl in water. The grid acted as the metal source for the silicide formation, where the phases were identified through selected area diffraction (SAED) patterns and high-resolution transmission electron microscopic (HRTEM) images. We have observed polymorphs of the γ phase $Ni_{31}Si_{12}$ with c_0=(6, 12, 18, 24 and 36) Å - so called $S_{6,}$ S_{12}, S_{18}, S_{24}, S_{36}. While working on the new Themis microscope of the Thin Film Department, we have observed the S_6 polymorph, which was not documented to date. We have determined its structure using techniques of electron crystallography. The good match between simulated (JEMS) and the gathered experimental data validated the new crystal structure in the $Ni_{31}Si_{12}$ composition (Fig. 7.19). (To be published.)

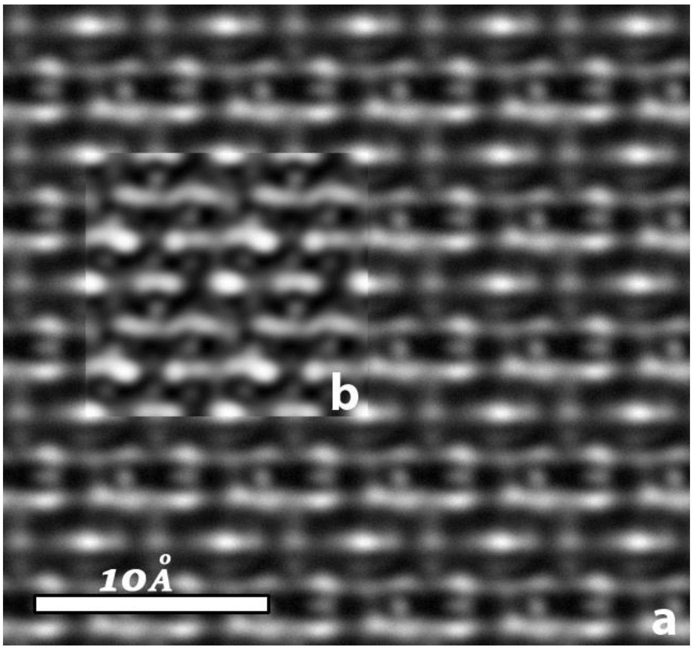

Figure7.19. *a) Fourier-filtered experimental HRTEM image of S6 and b) it's built structure's simulated HRTEM image*

A micro-combinatorial study of the optical properties of a-SiGe:H towards a database for optoelectronics

B. Kalas, Zs. Zolnai, G. Sáfrán, M. Serényi, N. Szász, G. Dobrik, E. Agocs, Tivadar Lohner, Attila Németh, Nguyen Quoc Khanh, M. Fried and P. Petrik

In a co-operation with the Photonics Laboratory the optical parameters of hydrogenated amorphous a-Si1-xGex:H layers were measured with focused beam mapping ellipsometry for photon energies from 0.7 to 6.5 eV. The single-sample micro-combinatorial technique developed at the Thin Films Physics Department enables the preparation of thin binary samples with full range composition spread. Linearly variable composition profile was revealed along the 20 mm long gradient part of the sample by Rutherford backscattering spectrometry and elastic recoil detection analysis. The Cody-Lorentz approach was identified as the best method to describe the optical dispersion of the alloy.

Amorphous Si$_{1-x}$Ge$_x$:H samples were prepared on 10 mm x 25 mm size Si wafers by ”single-sample” micro-combinatory that resulted in gradient composition of Si$_{1-x}$Ge$_x$ with x ranging in $0 \leq x \geq 1$. The layers with thicknesses of about 100 nm were deposited in an UHV system by dual DC magnetron sputtering using a patented, scaled-up technique and device originally developed for synthesizing micro-combinatorial TEM samples [Ref.7.24., Ref.7.25.]. The device sweeps a shutter with a 1 mm x10 mm slot in fine steps above the wafer meanwhile the power of the two DC magnetron sources is regulated in sync with the slot movement that creates a gradient of the composition. The details were described earlier for non-hydrogenated a- Si$_{1-x}$Ge$_x$ samples [Ref.7.26.]. The present samples were deposited at a sputtering rate of 0.4 nm/s, in a mixture of H and Ar. The H partial pressures (p_H/p) were 0, 0.05, 0.1 and 0.2 and the total plasma pressure (p) was kept at 3x10^{-3} mbar.

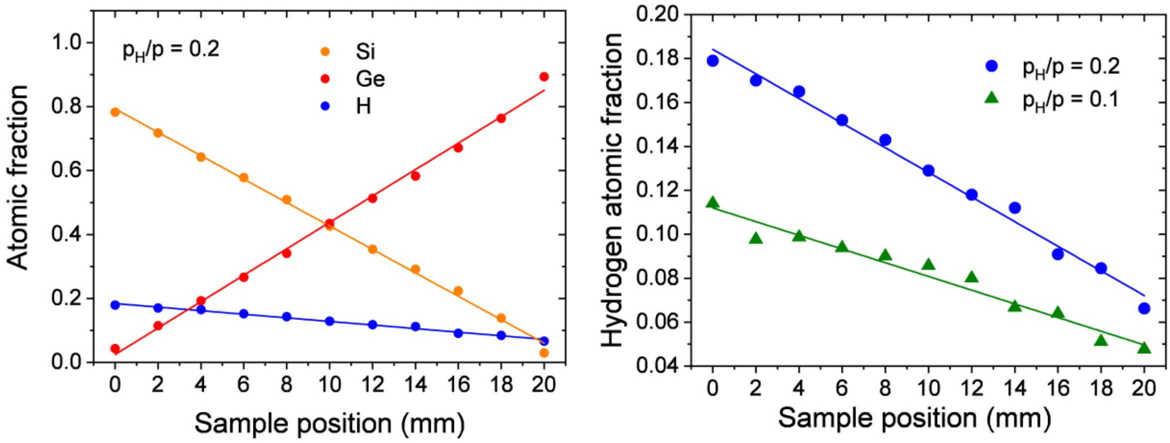

Figure 7.20. *a) Atomic fractions of Si and Ge showing the incorporated H for pH/p = 0.2 of the SiGe layer along the sample measured by RBS, b) atomic fractions of H evaluated from ERDA spectra applying simulations by the RBX software [4] for samples with* $p_H/p = 0.1$ *and 0.2, respectively).*

The 25 mm long samples exhibit a 20 mm long gradient a-Si$_{1-x}$Ge$_x$:H track enclosed between 2.5 mm long lead-in sections of pure Si and Ge, respectively. The sample position “0” belongs to the Si-rich side of the gradient track. Fig.7.20.a depicts highly linear curves of Si, Ge and H atomic fractions, along the sample, measured by RBS and ERDA, while Fig. 7.20.b represents the H-content change with the position from Si-rich to Ge-rich layer, that proves different H-incorporation into Si and Ge. [Ref.7.27.].

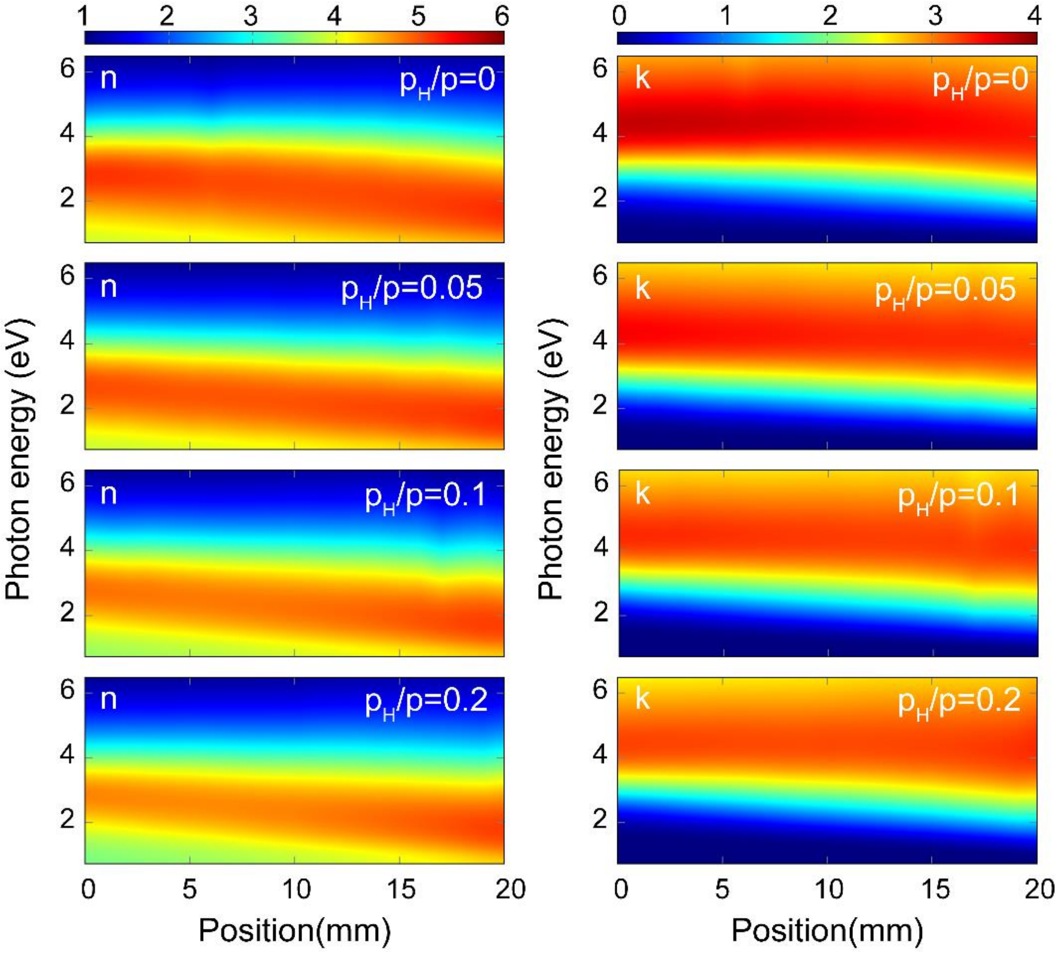

Figure 7.21. *Real and imaginary parts of the complex refractive indices of a-$Si_{1-x}Ge_x$:H thin films (left and right column, respectively) with different partial pressures of H (pH/p = 0;0:05, 0.1 and 0.2) as a function of both the position along the 20 mm long gradient section (composition) and photon energy. According to the RBS plots, the position at 0 mm corresponds to the Si-side of the sample.*

Fig. 7.21 shows maps of both n and the extinction coefficient (k) of all samples (pH/p = 0, 0.05, 0.1 and 0.2) in the whole range of compositions, for photon energies from 0.7 to 6.5 eV. n and k were obtained by fitting the measured spectra using the Cody-Lorentz (CL) optical model. The features in both n and k show a linear change with the position, hence, also with the composition. The single broad peak, characteristic of amorphous semiconductors can clearly be identified in all maps. The peaks are shifted to smaller photon energies as the composition changes from Si to Ge (positions from 0 to 20 mm). There is also a remarkable shift of the peaks vs. H content towards a higher band gap, smaller amplitude and broadening. The maps in Fig. 7.21 represent a complete database for optical properties of a-$Si_{1-x}Ge_x$:H.
The effect of incorporated H on the optical absorption is explained by the lowering of the density of localized states in the mobility gap. It is shown that in the low-dispersion near infrared range the refractive index of the $Si1_{-x}Ge_x$ alloy can be comprehended as a linear combination of the optical parameters of the components. The results revealed above prove that micro-combinatorial sample preparation combined with mapping ellipsometry is not only suitable for the fabrication of samples with controlled lateral distribution of the concentrations, but also opens new prospects in creating databases of composition dependent properties of compounds for optical and optoelectonic applications.

This work was supported by the Economic Development Innovation and Operative Program. GINOP # 2.1.7-15.

Ceramic dispersion strengthened sintered stainless steels after thermal ageing

MTA Hungarian – Japan Bilateral project (CeramODS)

C. Balázsi, K. Balázsi, H. R. Ben Zine, M. Furkó, Zs. Czigány, L. Almásy, V. Ryukhtin, H Murakami, G. Göller, O. Yucel, F. C. Sahin, S. Kobayashi, Á. Horváth

Oxide dispersion strengthened (ODS) ferritic steels can be used as large scale structural materials in many industrial applications owing to their excellent corrosion resistance in oxidising and/or sulphidising environments. The ODS are useful base materials for boilers and turbines of power generation plant co-firing coal or gas with renewable fuels such as biomass for high temperature, high pressure tubing applications, fast breeder reactors and blanket applications for fusion reactors.

The aim of research was the development of the ultrafine grained silicon nitride by powder technology has been studied. The effect of the yttria addition to the morphological, structural, mechanical and magnetic properties of the ceramic dispersion strengthened 316L stainless steels was studied.

Two composites have been prepared: 316L/0.33 wt% Si_3N_4 and 316L/1 wt% Si_3N_4 (CDS). Spark plasma sintering (SPS) was used for fast compaction of milled composite powders (Fig. 7.22.a) [Ref.7.28.].

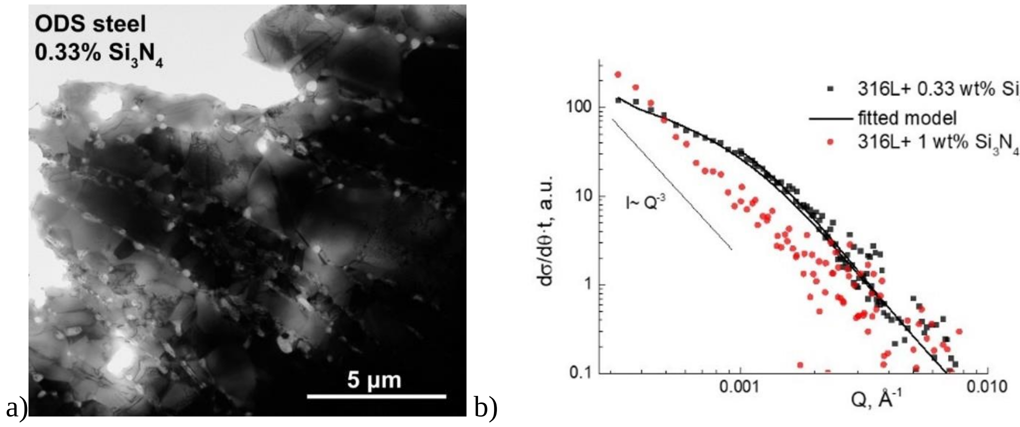

***Figure 7.22**. Si_3N_4 ceramic dispersed strengthened steel. a) structure, b) SANS measurements.*

The samples were enclosed in a vacuum quartz tube and then aged at 600 °C in a high-temperature furnace up to 10 h and 20 h. For CDS with 1wt% Si_3N_4 ageing was carried out also at 800 °C. The hardness values have been found to be twice as higher (300 HV) in the cases of CDS samples in comparison to reference sample.

SANS data measured on the sintered samples at DBC-SANS facility are presented in Fig. 7.22.b. The scattering curves obey Porod law (I~Q-3) over the whole measured q-range. This corresponds to the interface scattering from particles larger than several micrometers. This scattering behaviour is observed for sample with 1wt% of Si_3N_4 (Fig. 7.22.b). However, SANS on 316L+ 0.33 wt% of Si_3N_4 has demonstrated presence of smaller (submicron) size particles. The scattering data were fitted to a model scattering of spherical particles with log-normal size distribution, and the fitted averaged diameter is obtained as $\langle D \rangle = 441 \pm 33$ nm. The presence of smaller grains in this sample is probably caused by their better dispersion in the steel matrix, and contribute to the favourable mechanical properties of these CDS.

To investigate possible microstructural changes with ageing, EBSD measurements were performed for CDS sample with 1.0 wt.% Si_3N_4 aged at 800^{o}C. The average grain size is ~14 microns and small amount of bcc iron structure (< ~ 0.2%) was also detected for this sample (Fig. 7.23.a). The magnetic characterization of samples demonstrated that the samples exhibit ferromagnetic property already before ageing and a larger ferromagnetic component was observed as a result of thermal aging.

Fig. 7.23.b shows data for CDS samples with 1.0 wt% Si_3N_4 inclusion, aged at 800°C. The sample exhibits ferromagnetic property before ageing, associated with a hysteresis around zero magnetic field. In particular, for the sample used for ageing at 800°C, we observed a large ferromagnetic component, which evolves with thermal ageing.

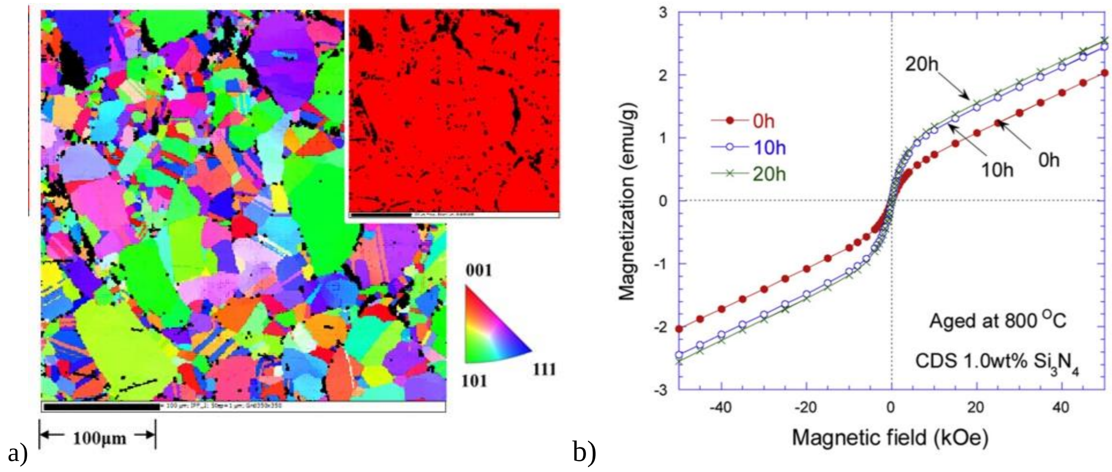

Figure 7.23. *a) EBSD inverse pole figure (IPF) map of CDS samples with 1.0 wt%* Si_3N_4 *for ageing time of 20 h, showing crystal orientation along the normal direction of sample surface. The insets show phase color map. The crystal structure of* Si_3N_4 *was not considered in this analysis, b) Magnetization curves for 1.0 wt.%* Si_3N_4 *CDS samples aged at 800°C.*

The magnetic characterization of samples demonstrated that the samples exhibit ferromagnetic property before ageing and a large ferromagnetic component was observed, which evolved with thermal aging [Ref.7.29.]. It was proven that for ODS and CDS samples with a low amount of Y_2O_3 or Si_3N_4, the saturation magnetization was slightly dependent on ageing time, however, it exhibited a noticeable change with ageing both at 600 and 800 °C for samples containing higher amount of additives.

Si(B) a prospective material for quantum electronic applications

VEKOP-2.3.3-15-2016-00002

J.L. Lábár, M. Menyhárd, A. Sulyok, L. Illés, F.Chiodi, S. Lequien, F. Lefloch, F. Nemouchi

Gas Immersion Laser Doping (GILD) of Si with boron provided shallow, box-like regions, where B concentration exceeds thermodynamic equilibrium level without forming precipitates. In such material, superconductivity was measured below 1 K. However, to detect either the concentration, or spatial distribution of B is a difficult task. In the present paper, we show a TEM-based method for measuring B concentration and determining the extent of the heavily B-doped region.

Preparation of the TEM lamella and examination of the native sample with SEM/EDS was done in a SCIOS-2 type dual-beam FEG-SEM/FIB equipped with Oxford X-maxN 20 type EDS. FIB-lamellae were cut by Ga+-ions with special care taken to avoid heating of the samples during preparation. The selected region was protected by Pt-deposition prior to cutting. First an <100 nm thick Pt was deposited by e-beam assisted deposition (2 kV, 3.2 nA), followed by a thicker (1.5 µm) ion-beam assisted deposited Pt layer (30 kV, 300 pA). The trenches at the two sides of the lamella were milled with a 30 kV Ga-ion beam (15 nA). When the lamella reached 3 µm thickness, it was further thinned in the bulk with 30kV, 7 nA ion current down to a thickness of 1.5 µm. Then it was cut out (30 kV, 5 nA) and welded to the TEM-grid (using back-sputtering at 30kV 5 nA) for further thinning. The thinning started with 16 kV 50 pA Ga-beam. Polishing in two steps: 5 kV 48 pA followed by 2 kV 27 pA till proper transparency.

TEM and energy-disperse X-ray spectroscopy (EDS) examinations were performed in a Titan Themis G2 200 STEM equipped with a four-segment Super-X EDS detector. The corrector for the spherical aberration (C_s) was applied at the imaging part, while no probe-correction was present. Image resolution limit is 0.08 nm in phase-contrast HRTEM mode, while resolution is 0.16 nm in STEM Z-contrast imaging mode (by using a Fishione high-angle annular dark-field (HAADF) detector). HRTEM images were recorded at 200 keV with a 4k × 4k CETA 16 CMOS camera.

Auger Electron Spectroscopy (AES) depth profiling of B was done in STAIB DESA 150 analyser with pre-retarded CMA. Depth profiling with AES did not require any preparation prior to insertion into the UHV. Depth profiling: projectile Ar+, energy 1 keV, angle of incidence 75° (with respect to surface normal), specimen rotation during sputtering. Using these parameters for sputter removal, bombardment induced roughness is not expected.

First, we proved that the layer close to the surface really contains B, as expected. A sample without any prior preparation was inserted into the SEM and an EDS spectrum was recorded with 1 kV primary electron beam energy, to ensure that the excited volume is within the top 30 nm of the sample. Fig.7.24. shows that B K-line and Si L-line are clearly present. However, the commercial program of the EDS could not give quantitative result at that energy with the Si L-line.

Next, Auger electron depth profiling was carried out starting from the native surface. Fig. 7.25 demonstrates that B is only present in the layer close to the surface and its concentration does not vary with depth. Thus, the procedure resulted in a good quality homogeneous B doping. Both the depth scale and the concentration value were fitted to the TEM result.

Finally, the cross-sectional TEM lamella was examined by TEM. Note that EDS in the TEM was unable to measure B properly, due to the extremely high overvoltage. Electron diffraction proved that the crystal structure in the layer is identical to that of Si. Measurement of both the B concentration and the thickness of the B-doped layer were based on observation of the change in the lattice parameter due to the difference in the atomic radii of Si and B. The resulting strain and lattice defects made the layer visible even in the bright field (BF) image in the TEM. However, it was only the lattice resolution image (HRTEM) recorded by phase contrast (Fig. 7.26.), that facilitated measuring the change in the local lattice parameter quantitatively. That difference in lattice parameter was converted into local B concentration by using the Vegard's law. Boron in pure form cannot be found in cubic structure, so Vegard's law cannot be applied to the pure end-members of the oversaturated Si(B). However, the x-ray diffraction database contains Si-1%B, which has the same crystal structure as Si, which still allows to rely on Vegard's law. As it is seen in Fig.7.26, the thickness of the B-doped layer is 30 nm. It also contains stacking faults occasionally. Selecting regions without crystal defects, we can measure the lattice parameter both in the layer and in the pure Si substrate. The latter one was used to fine-tune the calibration of the magnification of the TEM. Table 7.1 summarizes the measurement results on several images. As a result the B-content is 7,15±2,86 at% in a 30 nm thick layer. The scatter is probably a superposition of both local variation and measurement uncertainty.

FFT #	Miller index	d-in-layer	d-in-Si	d-in-Si-1%B	B[at%]	Magnification of HRTEM
915	333	1,035	1,0450	1,0424	3,88	630 k
921	333	1,033	1,0450	1,0424	4,85	800 k
923	333	1,029	1,0450	1,0424	6,21	380 k
924	333	1,015	1,0450	1,0424	11,65	380 k
927	333	1,022	1,0450	1,0424	9,13	380 k

Table 7.1. *B-concentration determined from HRTEM images on the basis of Vegard's law.*

This research was supported by VEKOP-2.3.3-15-2016-00002 of the European Structural and Investment Funds.

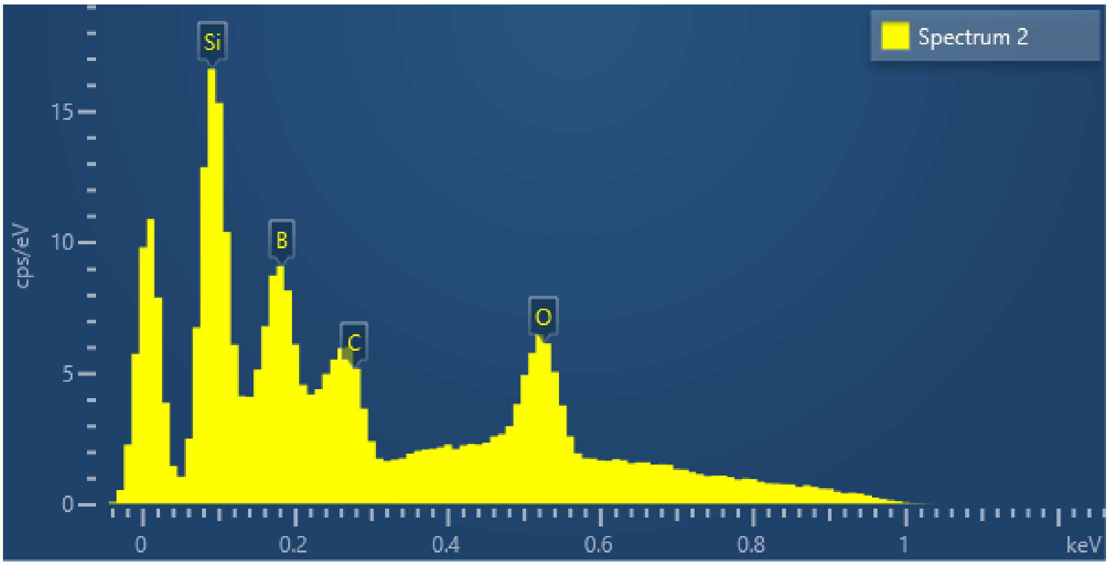

Figure 7.24. *EDS spectrum recorded at 1 kV in the SEM from native surface of the implanted layer.*

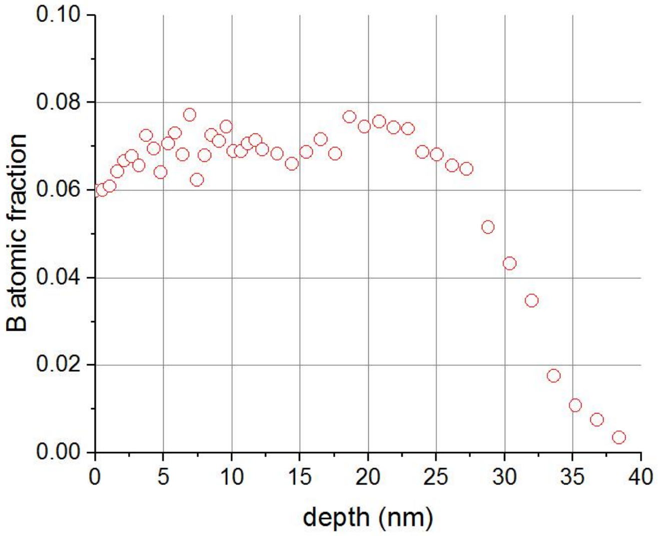

Figure 7.25. *AES depth profile from native surface of the implanted layer.*

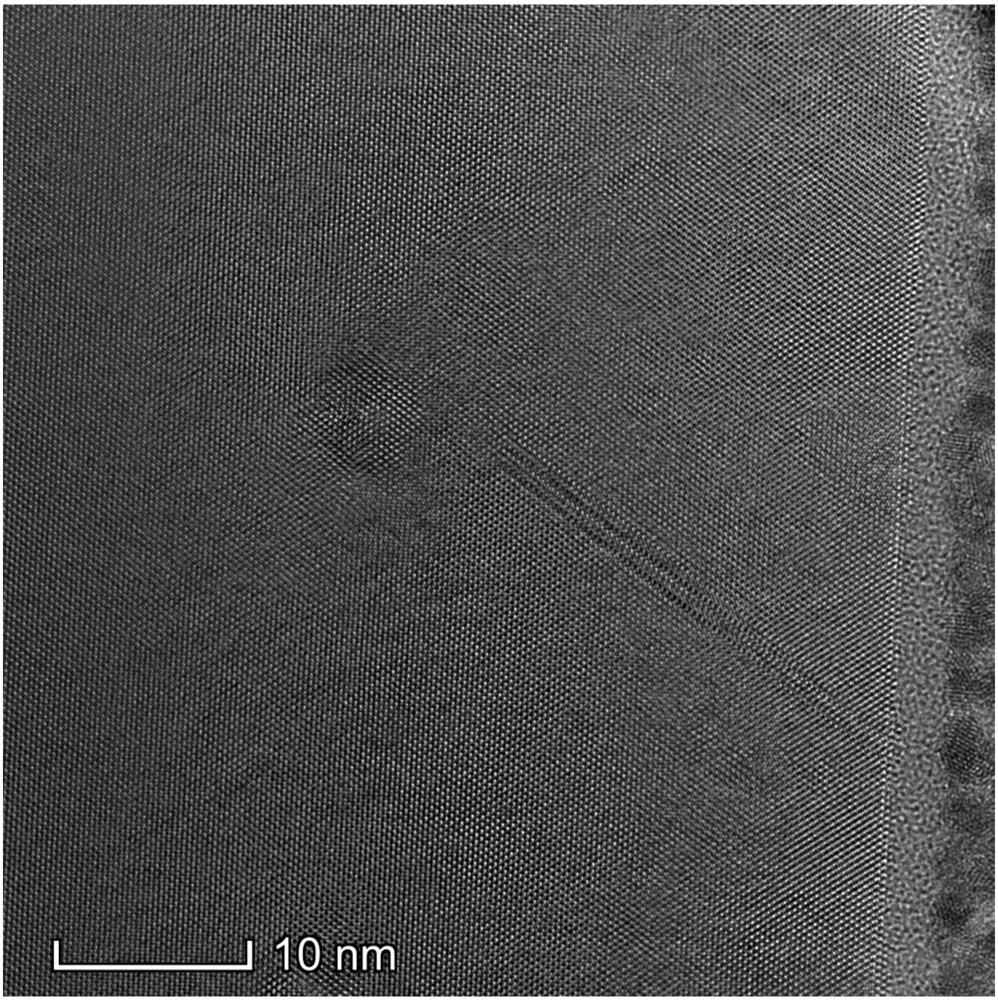

Figure 7.26. *HRTEM image from a cross section of the sample.*

Complex Systems Department

Head: Dr. György SZABÓ, D.Sc., scientific advisor

Research Staff:

- Balázs Király
- István Borsos
- Zoltán Juhász PhD
- Géza Ódor D.Sc., scientific advisor
- Attila Szolnoki D.Sc., scientific advisor

Ph.D. students / Diploma workers:

- Kristóf Hódsági (BME, BSc-MSc student)
- Gergely Bunth (BME, BSc-MSc student)
- Beatriz de Simeoni (BME, MSc student)

The research field of the group is the investigation of complex systems by the methods of statistical physics in equilibrium as well as non-equilibrium states. The theoretical investigation of multi-agent evolutionary game models studies processes supporting fair behavior of individuals by numerically analyzing mathematical models when a player's own interest opposes that of the community. Mathematical models have been used to investigate the effect of one kind of penalties, the combinations of the rules of strategy updates, and systems in which the income of the players is obtained from two or three interconnection systems (communities). Decomposing matrices into elementary (orthogonal) components allows the identification and frequency analysis of elementary interactions causing social dilemmas in potential games. The systematic examination of elementary interactions of evolutionary matrix games unearthed two newer versions of social dilemmas. In the first case the macroscopic system develops into a state of higher average income, because of the greater number of possible microscopic states. In the second case the anomalous consequence of cyclic symmetry-breaking forces the system develops into the state of lower average income. Because of the cyclic dominance, however, this system returns to the initial state, where the newer and newer similar avalanche phenomena cause huge fluctuations both in the proportions of the strategies and in the incomes.

Using traditional concepts and methods of statistical physics the critical dynamical properties of synchronization phenomena were analyzed in Kuramoto type models appearing in brain and electrical power-grid models. They extend the investigation of the general characteristics of the Griffiths phase to inhomogeneous networks of modular structures. In these models frustrated synchronization and chimera states emerge, slowing down the dynamics and causing non-universal power-law distributions in the synchronization times.

The increase of data in folk music and genetic data sets implies the continuous improvement of algorithms to analyze them. The newly developed algorithms are able both to identify clusters and to follow the evolutionary inheritance of clusters, both in genetic (haplogroup) features and in popular characteristics of folk music tunes.

Bursts in three-strategy evolutionary games on a square lattice

OTKA K120785

G. Szabó, B. Király, and K. Hódsági

The evolutionary potential games exhibit thermodynamic behaviour if the strategy updates are controlled by the so-called logit rule which is a consecutive selfish one-site strategy updates resembling dynamics used widely in Monte Carlo analyses of many-particle systems. Now we have considered three-strategy evolutionary games on a square lattice when the pair interactions are composed of three types of elementary interactions. The first component is equivalent to the three-state Potts model and it results in the formation of one of the three equivalent homogeneous states at low noise levels. The second component favours the first strategy similarly to the application of a suitable external field in spin systems. The third component describes Rock-Paper-Scissors type cyclic dominance. In contrary to the naive expectation the presence of cyclic component yields paradoxical effect. Namely, instead of the externally supported (first) strategy the system will be dominated by its predator (second strategy). The homogeneous state of the second strategy, however, is unstable. Due to the cyclic dominance a sufficiently large island of the third strategy can expand as illustrated in Fig. 8.1.

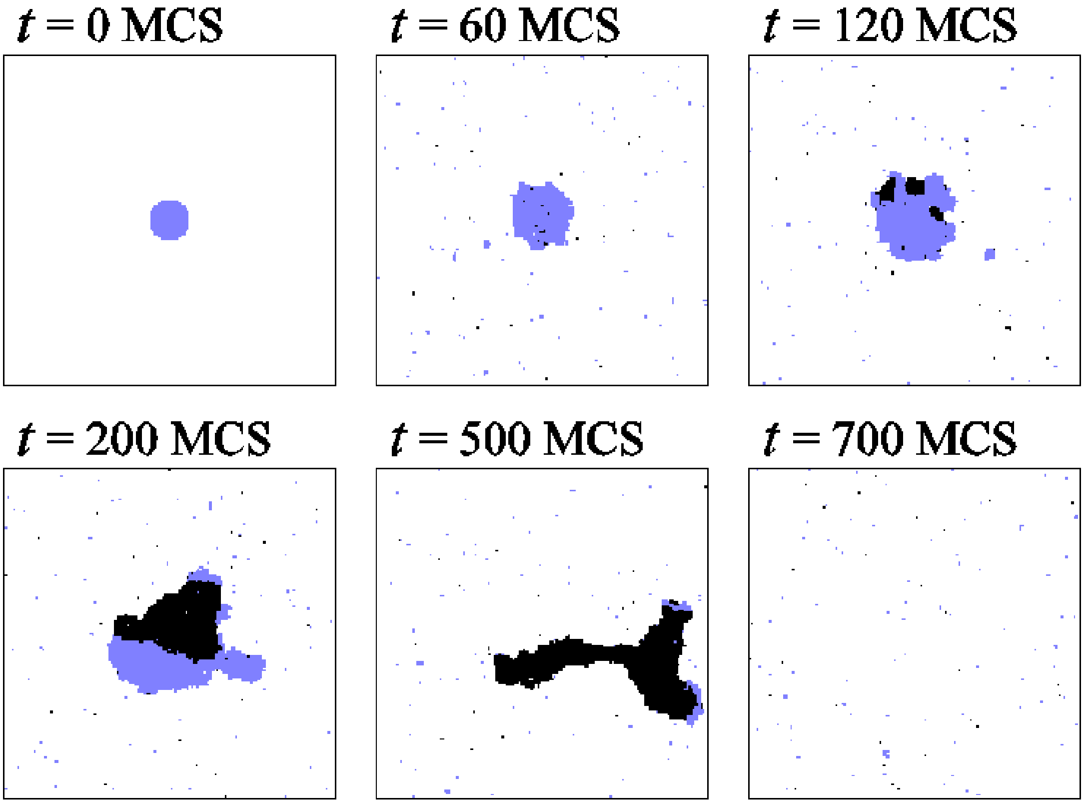

***Figure 8.1**. Evolution of strategy distribution if a sufficiently large circular island of strategy 3 (blue pixels) is inserted into the sea of strategy 2 (white pixels). The growth of the island of strategy 3 is reversed when the strategy 1 (black pixels) occurs and invades the territory of 2s. Sooner or later, however, the black domains are also shrunken via the same mechanism.*

In the homogeneous states the sufficiently large predator domains can occur via a nucleation mechanism which is well described in material sciences. The curiosity of these phenomena is that here two (or more) consecutive nucleation processes drive the system back to the state dominated by strategy 2. Notice that for three-state cyclic dominance the most aggressive strategy cannot expand after having eliminated its prey and finally its predator invades the whole system because of the extinction of its predator.

In these systems similar bursts can occur anywhere via the stochastic processes mentioned above. The frequency of these bursts is proportional to the system size and it decreases with the noise. At the same time the maximum extension of these bursts increases when the noise level is reduced. Fig. 8.2 shows the frequency of strategy 3 for parameters when the bursts are well separated in time.

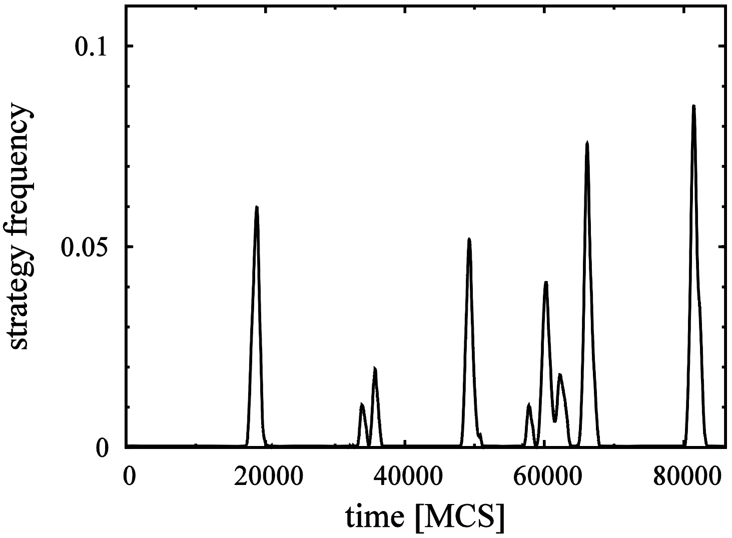

Figure 8.2. *Typical time-dependence of the frequency of strategy 3 in a large system for low noise levels when the bursts (illustrated in Fig. 1) occur rarely. In these Monte Carlo simulations we used large linear system size (it is varied from L=1000 to 2800), thus these bursts may include more than 100,000 lattice sites.*

The quantitative analyses of the fluctuations in the strategy frequencies have indicated huge increase at low noises despite of the relevant reduction of the average bursts frequencies.

Finally it is worth mentioning that the above model represents a type of social dilemma when the paradoxical effect of cyclic dominance drives the system into a social trap where the average income is not optimal at low noise levels. It is found, however, that in a narrow range of noise level these systems can achieve higher average income [Ref.8.1].

Seasonal payoff variations and the evolution of cooperation in social dilemmas

OTKA K120785

A. Szolnoki and M. Perc

Varying environmental conditions affect relations between interacting individuals in social dilemmas, thus affecting also the evolution of cooperation. Oftentimes these environmental variations are seasonal and can therefore be mathematically described as periodic changes. Accordingly, we here study how periodic shifts between different manifestations of social dilemmas affect cooperation. We observe a non-trivial interplay between the inherent spatiotemporal dynamics that characterizes the spreading of cooperation in a particular social dilemma type and the frequency of payoff changes. In particular, we show that periodic changes between two available games with global ordering best be fast, while periodic changes between global and local ordering games best be slow for cooperation to thrive. We also show that the frequency of periodic changes between two local ordering social dilemmas is irrelevant, because then the process is fast and simply the average cooperation level of the two is returned. The structure of the interaction network plays an important role too in that lattices promote local ordering, whilst random graphs hinder the formation of compact cooperative clusters. Conversely, for local ordering the regular structure of the interaction network is only marginally relevant as role-separating checkerboard patterns do not rely on long-range order.

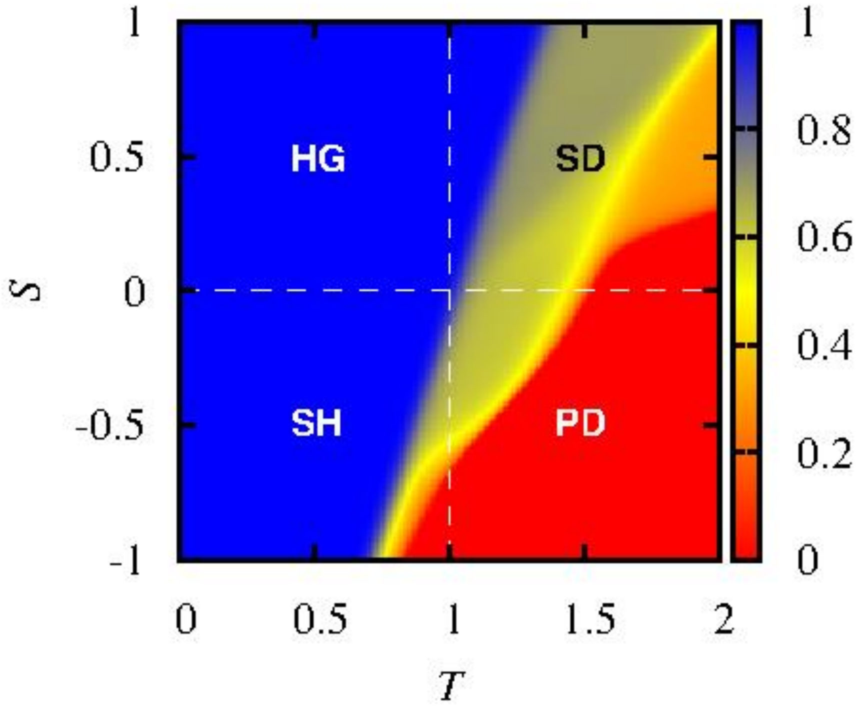

Figure 8.3. *Colour maps encoding the stationary density of cooperators on the full T−S plane obtained on square lattice. The payoff values (T1 = 0.9, S1 = 0.1) and (T2 = T, S2 = S) are exchanged periodically with period τ = 1. In the snowdrift quadrant (SD), seasonal effects have a very similar impact on cooperation regardless of the applied interaction network. Conversely, in the stag-hunt (SH) and the prisoner's dilemma quadrant (PD), cooperators fare better under seasonal variations.*

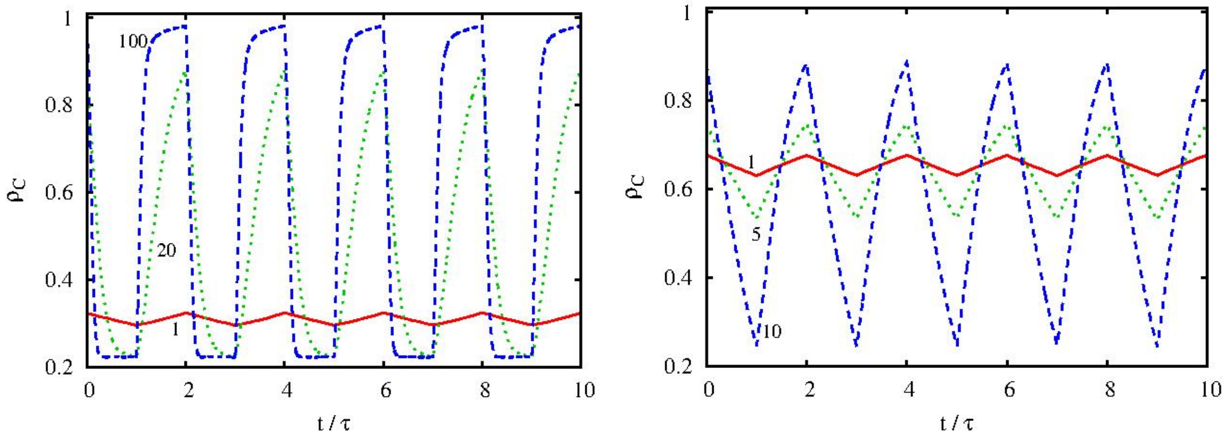

Figure 8.4. *Left: Time evolution of the cooperation level fC in the stationary state, as obtained for different values of τ in the snowdrift game (T=2, S=0.5). Right: Time evolution of the cooperation level fC in in the stag-hunt game (T=0.92, S=−0.5). It can be observed that the relaxation dynamics for the snowdrift game is fast, while for the harmony game and the stag-hunt game, it is comparatively much slower.*

We have shown that there exists a non-trivial interplay between the inherent spatio-temporal dynamics that characterizes the spreading of cooperation in a particular social dilemma type and the frequency of payoff changes. The inherent spatiotemporal dynamics is affected by the parameterization of the two games entailed in the switch, and by the structure of the interaction network. In particular, when cooperation proliferates by means of compact clusters, as is the case in the harmony game, the stag-hunt game, and the prisoner's dilemma game, the relaxation times are longer and the translation invariant feature of an interaction graph promotes the local emergence of a coordinated state that is necessary for a spreading process to reach a global ordering. Accordingly, we have shown that periodic changes between two games with global ordering should be fast for cooperation to be promoted, and preferably unfold on a network without long-range links, like a square lattice. If an interaction network with long-range links is used, like a regular random graph, then the irregular structure hinders the formation of compact clusters, which in turn impairs the evolution of cooperation. Since the observed behaviour is strongly related to the diverse speed of spreading at different payoff values, we may expect conceptually similar behaviour in scale-free and multilayer complex networks as well. [Ref.8.2].

Critical synchronization dynamics of the Kuramoto model on connectome and small world graphs

OTKA K128989

G. Ódor, J. Kelling, R. Juhász and G. Deco

We considered the Kuramoto model on sparse random networks such as the Erdős–Rényi graph or its combination with a regular two-dimensional lattice and study the dynamical scaling behaviour of the model at the synchronization transition by large-scale, massively parallel numerical integration. By this method, we obtain an estimate of critical coupling strength more accurate than obtained earlier by finite-size scaling of the stationary order parameter. Our results confirm the compatibility of the correlation-size and the temporal correlation-length exponent with the mean-field universality class [Ref.8.3.].

The hypothesis, that cortical dynamics operates near criticality also suggests, that it exhibits universal critical exponents which marks the Kuramoto equation, a fundamental model for synchronization, as a prime candidate for an underlying universal model. Here, we determined the synchronization behavior of this model by solving it numerically on a large, weighted human connectome network, containing 836733 nodes, in an assumed homeostatic state. Since this graph has a topological dimension $d < 4$, a real synchronization phase transition is not possible in the thermodynamic limit, still we could locate a transition between partially synchronized and desynchronized states. At this crossover point we observe power-law–tailed synchronization durations, with $\tau t \simeq 1.2(1)$, away from experimental values for the brain. For comparison, on a large two-dimensional lattice, having additional random, long range links, we obtain a mean-field value: $\tau t \simeq 1.6(1)$. However, below the transition of the connectome we found global coupling control-parameter dependent exponents $1 < \tau t \leq 2$, overlapping with the range of human brain experiments. We also studied the effects of random flipping of a small portion of link weights, mimicking a network with inhibitory interactions, and found similar results. The control parameter dependent exponent suggests extended dynamical criticality below the transition point [Ref.8.4., Ref.8.5.].

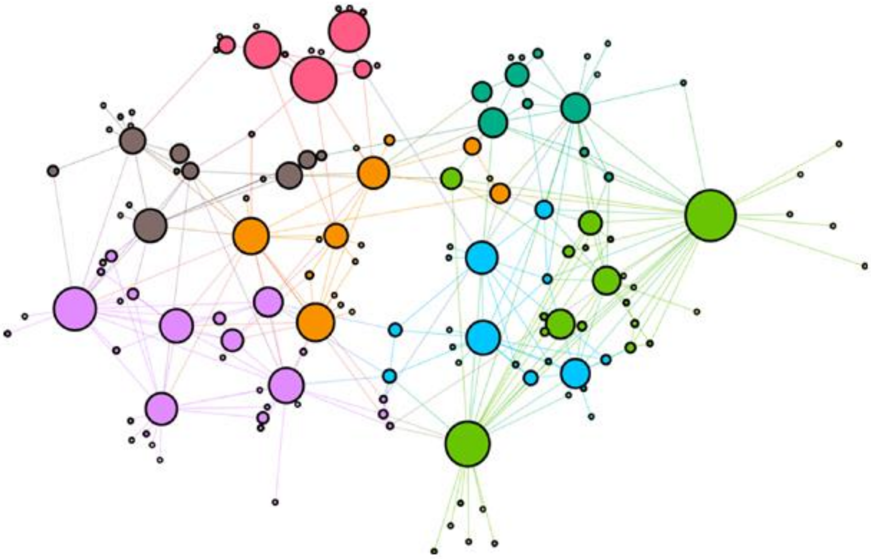

Figure 8.5. *Network of the modules of the KKI-18 human connectome graph is shown. The size of circles is proportional with the number of nodes.*

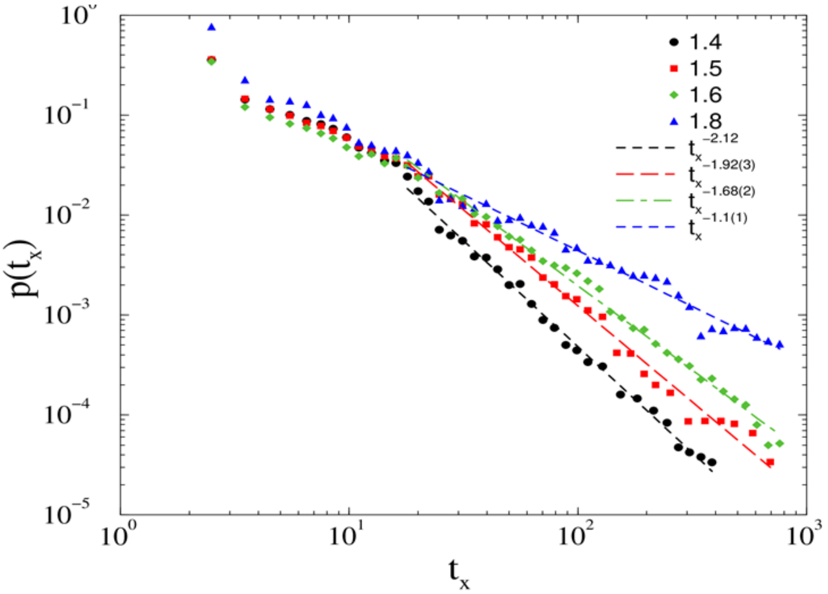

Figure 8.6. *Duration distribution of on the KKI-18 model for growth K = 1.4 (bullets), 1.5 (boxes), 1.6 (diamonds), 1.8 (triangles). The dashed line shows PL fits to the tail region: tx > 20.*

REFERENCES

[Ref.3.1.] Zoltan Labadi, Benjamin Kalas, Andras Saftics, Levente Illes, Hajnalka Jankovics, Éva Bereczk-Tompa, Anett Sebestyén, Éva Tóth, Balázs Kakasi, Carmen Moldovan, Bogdan Firtat, Mariuca Gartner, Marin Gheorghe, Ferenc Vonderviszt, Miklos Fried, Peter Petrik, "Sensing layer for Ni detection in water created by immobilization of bio-engineered flagellar nanotubes on gold surfaces", accepted in ACS Biomaterials Science & Engineering.

[Ref.3.2.] Kalas, B., Zolnai, Z., Safran, G., Serenyi, M., Agocs, E., Lohner, T., Nemeth, A., Fried, M., Petrik, P., Micro-combinatorial sampling of the optical properties of hydrogenated amorphous Si1−xGex for the entire range of compositions towards a database for optoelectronics, under publication in Scientific Reports.

[Ref.3.3.] T. Lohner, E. Szilágyi, Z. Zolnai, A. Németh, Z. Fogarassy, L. Illés, E. Kótai, P. Petrik, M. Fried, Determination of the Complex Dielectric Function of Ion-Implanted Amorphous Germanium by Spectroscopic Ellipsometry, Coatings. 10 (2020) 480. https://doi.org/10.3390/coatings10050480

[Ref.3.4.] Szekrenyes, D. P.; Pothorszky, S.; Zambo, D.; Osváth, Z.; Deák, A. Investigation of Patchiness on Tip-Selectively Surface Modified Gold Nanorods. J. Phys. Chem. C 2018, 122 (3), 1706–1710. https://doi.org/10.1021/acs.jpcc.7b11211

[Ref.3.5.] Pothorszky, Sz.; Zámbó, D.; Deák, T.; Deák, A. Assembling Patchy Nanorods with Spheres: Limitations Imposed by Colloidal Interactions. Nanoscale 2016, 8 (6), 3523–3529. https://doi.org/10.1039/C5NR08014B

[Ref.3.6.] Pothorszky, S.; Zámbó, D.; Szekrényes, D.; Hajnal, Z.; Deák, A. Detecting Patchy Nanoparticle Assembly at the Single-Particle Level. Nanoscale 2017, 9 (29), 10344–10349. https://doi.org/10.1039/C7NR02623D

[Ref.3.7.] Szekrényes, D. P.; Pothorszky, S.; Zámbó, D.; Deák, A. Detecting Spatial Rearrangement of Individual Gold Nanoparticle Heterodimers. Phys. Chem. Chem. Phys. 2019, 21 (19), 10146–10151. https://doi.org/10.1039/C9CP01541H

[Ref.3.8.] Zámbó, D.; Radnóczi, G. Z.; Deák, A. Preparation of Compact Nanoparticle Clusters from Polyethylene Glycol-Coated Gold Nanoparticles by Fine-Tuning Colloidal Interactions. Langmuir 2015, 31 (9), 2662–2668. https://doi.org/10.1021/la504600j

[Ref.3.9.] E. Albert, B. Tegze, Z. Hajnal, D. Zámbó, D. P. Szekrényes, A. Deák, Z. Hórvölgyi, N. Nagy, "Robust Contact Angle Determination for Needle-in-Drop Type Measurements" ACS OMEGA, vol. 4, iss. 19, 18465-18471, 2019.

[Ref.3.10.] N. Nagy, "Contact Angle Determination on Hydrophilic and Superhydrophilic Surfaces by Using r–θ-Type Capillary Bridges" LANGMUIR, vol. 35, iss. 15, 5202-5212, 2019.

[Ref.3.11.] F. Riesz, "The effects of the global surface curvature on Makyoh-topogaphy imaging," PHOTONICS LETTERS OF POLAND, vol. 11, no. 1, 4-6, 2019.

[Ref. 5.1.] F. Bíró, Z. Hajnal, I. Bársony and Cs. Dücső, MEMS microhotplate constraints, open access book Advances in Microelectronics: Reviews, Vol. 2, Book Series, published by IFSA Publishing, S.L. February, 2019

[Ref. 5.2.] N. Samotaev, A. Pisliakov, A. Gorshkova, I. Bársony, Cs. Dücső, F. Bíró, Al2O3 Nanostructured Gas Sensitive Material for Silicon Based Low Power Thermocatalytic Sensor, International Scientific Conference "Materials Science: Composites, Alloys and Materials Chemistry" (MS-CAMC-2019, Nov 20-21), Szentpétervár, Oroszország

[Ref. 5.3.] A Zátonyi, G. Orbán, R. Modi, G. Márton, D. Meszéna, I. Ulbert, A. Pongrácz, M. Ecker, W.E. Voit, A. Joshi-Imre, Z. Fekete, A softening laminar electrode for recording single unit activity from the rat hippocampus, SCIENTIFIC REPORTS 9 (2019) 37237, IF: 4.011

[Ref. 5.4.] A. Zátonyi, M. Madarász, Á. Szabó, T. Lőrincz, R. Hodován, B. Rózsa, Z. Fekete, Transparent, low-autofluorescence microECoG device for simultaneous Ca2+ imaging and cortical electrophysiology in vivo, JOURNAL OF NEURAL ENGINEERING (2020) in press, DOI: 10.1088/1741-2552/ab603f, IF: 4.551

[Ref. 5.5.] M. Csernai, S. Borbély, K. Kocsis, D. Burka, Z. Fekete, V. Balogh, S Káli, Z Emri, P. Barthó, Dynamics of sleep oscillations is coupled to brain temperature on multiple scales, THE JOURNAL OF NEUROPHYSIOLOGY 597 (2019) 4069-4086, IF: 4.950

[Ref. 5.6.] Ö. C. Boros, Á. C. Horváth, S. Beleznai, Ö. Sepsi, D. Csősz, Z. Fekete, P. Koppa, Optimization of an optrode microdevice for infrared neural stimulation APPLIED OPTICS 58 (2019) 3870-3876, IF: 1.973

[Ref. 5.7.] D. Petrovszki, S. Valkai, E. Gora, M. Tanner, A. Bányai, P. Fürjes, A. Dér, Dielectrophoretically enhanced detection of E. coli cells by an integrated optical biosensor system, 45th International Conference on Micro & Nanoengineering, Rhodes, Greece, 2019

[Ref. 5.8.] Petrovszki D., Valkai S., Gora E., Tanner M., Bányai A., Fürjes P., Dér A., E. coli sejtek dielektroforetikusan erősített detektálása integrált optikai bioszenzorral, a Magyar Biofizikai Társaság XXVII. Kongresszusa, Debrecen, Magyarország, 2019

[Ref. 5.9.] A. Bányai, P. Hermann, O. Hakkel, Z. Hajnal, P. Fürjes, Shape design dependent performance of DLD (deterministic lateral displacement) based particle separation systems - FEM modelling and validation, Lab-on-a-Chip Europe Conference, Rotterdam, The Netherlands, 2019

[Ref. 5.10.] I. Rigó, M. Veres, T. Váczi, E. Holczer, O. Hakkel, A. Deák, P. Fürjes, Preparation and Characterization of Perforated SERS Active Array for Particle Trapping and Sensitive Molecular Analysis, BIOSENSORS 9:3 Paper:93, 9p., 2019 (CiteScore: 3.57)

[Ref. 5.11.] O. Hakkel , I. Rigó , M. Veres , P. Fürjes, Microfluidically Integrated SERS Actice Cell Trap Array for Sensitive Analysis of Red Blood Cells Transducers & Eurosensors 2019 Conferences, Berlin, Germany, 2019

[Ref. 5.12.] P. Hermann, Zs. Szomor, O. Hakkel, Z. Hajnal, P. Fürjes, Effects of hydrodynamic parameters of droplet formation in two-phase microfluidic structures, Lab-on-a-Chip Europe Conference, Rotterdam, The Netherlands, 2019

[Ref. 5.13.] Z. Szabó, Wide emission-spectrum NIRLED based on efficient photon-recycling, E-MRS 2019 Spring Meeting, Nizza, France, 2019

[Ref.6.1.] T. Gerecsei, I. Erdődi, B. Peter, Cs. Hős, S. Kurunczi, I. Derényi, B. Szabó and R. Horvath, "Adhesion force measurements on functionalized microbeads: An in-depth comparison of computer controlled micropipette and fluidic force microscopy,"JOURNAL OF COLLOID AND INTERFACE SCIENCE, vol 555, 2019

[Ref.6.2.] Á. G. Nagy, J. Kámán, R. Horváth, and A. Bonyár, „Spring constant and sensitivity calibration of FluidFM micropipette cantilevers for force spectroscopy measurements," SCIENTIFIC REPORTS, vol 9, 10287, 2019.

[Ref.6.3.] R. Ungai-Salánki, B. Peter, T. Gerecsei, N. Orgovan, R. Horvath and B. Szabó,"A practical review on the measurement tools for cellular adhesion force," ADVANCES IN COLLOID AND INTERFACE SCIENCE, vol 269, 2019.

[Ref.6.4.] B. Kovacs and R. Horvath, "Modeling of label-free optical waveguide biosensors with surfaces covered partially by vertically homogeneous and inhomogeneous films," JOURNAL OF SENSORS, 1762450, 2019.

[Ref.6.5.] A. Saftics, B. Türk, A. Sulyok, N. Nagy, T. Gerecsei, I. Szekacs, S. Kurunczi and R. Horvath, "Biomimetic Dextran-Based Hydrogel Layers for Cell Micropatterning over Large Areas Using the FluidFM BOT Technology," LANGMUIR, vol. 35, 2019.

[Ref.6.6] B. Peter, A. Saftics, B. Kovacs, S. Kurunczi and R. Horvath, „Oxidization increases the binding of EGCG to serum albumin revealed by kinetic data from label-free optical biosensor with reference channel," ANALYST, 2019.

[Ref.6.7.] I. Székács, P. Tokarz, R. Horvath, K. Kovács, A. Kubas, M. Shimura, J. Brasun, V. Murzing, W. Caliebe, Z. Szewczuk, A. Paluch, L. Wojnárovits, T. Tóth, J. S.Pap and Ł. Szyrwiel, "In vitro SOD-like activity of mono- and di-copper complexes with a phosphonate substituted SALAN-type ligand," CHEMICO-BIOLOGICAL INTERACTIONS, vol. 306, 2019.

[Ref.6.8.] T. Visnovitz, X. Osteikoetxea, B. W. Sódar, J. Mihály, P. Lőrincz, K. V. Vukman, E. Á. Tóth, A. Koncz, I. Székács, R. Horváth, Z. Varga and E. I. Buzás, "An improved 96 well plate format lipid quantification assay for standardisation of experiments with extracellular vesicles," JOURNAL OF EXTRACELLULAR VESICLES, 1565263, 2019.

[Ref.7.1.] K. Balázsi, M. Furkó, Z. Liao, J. Gluch, D. Medved, R. Sedlák, J. Dusza, E. Zschech, C. Balázsi, Porous sandwich ceramic of layered silicon nitride-zirconia composite with various multilayered graphene content, Journal of alloys and compounds, (2020) p. 154984

[Ref.7.2.] K. Balázsi, M. Furkó, Z. Liao, Z. Fogarassy, D. Medved, E. Zschech, J. Dusza, C. Balázsi,
Graphene added multilayer ceramic sandwich (GMCS) composites: Structure, preparation and properties, Journal of the European Ceramic Society, (2020), accepted for publ.

[Ref.7.3.] K. Balazsi, M. Furkó, P. Klimczyk, C. Balázsi, Influence of Graphene and Graphene Oxide on Properties of Spark Plasma Sintered Si3N4 Ceramic Matrix, Ceramics 3 : 1 (2020) 40-50.

[Ref.7.4.] C. Balázsi, Zs. Fogarassy, O. Tapasztó, A. Kailer, C. Schröder, M. Parchoviansky, D. Galusek, J. Dusza, K. Balázsi, Si3N4/graphene nanocomposites for tribological application in aqueous environments prepared by attritor milling and hot pressing, Journal of the European Ceramic Society, 37 :12 (2017) 3797-3804.

[Ref.7.5.] M. Furkó, Zs. Fogarasy, K. Balázsi, C. Balázsi, An economic and facile method for graphene oxide preparation from graphite powder, Resolution and Discovery 4 (2019) 21-25.

[Ref.7.6.] T. Zagyva, K. Balázsi, C. Balázsi, Examination of novel electrosprayed biogenic hydroxyapatite coatings on Si3N4 and Si3N4/MWCNT ceramic composite, Processing and Application of Ceramics 13 : 2 (2019) 132-138.

[Ref.7.7.] C. Balázsi, M. Furkó, F. Szira, K. Balázsi, Research on Technical Ceramics and their Industrial Application: Preparation Techniques and Properties of Transparent AlON Ceramics
Acta Materialia Transylvania 2 : 1 (2019) 7-12.

[Ref.7.8.] K. Balázsi, M. Furkó, C. Balázsi, Nitrid kerámiák környezetkímélő előállítása és vizsgálata, In: Barabás, István (szerk.) XXVIII. OGÉT (2020) 33-36.

[Ref.7.9.] S. Lamnini, Z. Károly, E. Bódis, K. Balázsi, C. Balázsi, Influence of structure on the hardness and the toughening mechanism of the sintered 8YSZ/MWCNTs composites, Ceramic International 45:4 (2019) 5058-65.

[Ref.7.10.] S. Lamnini, C. Balázsi, K. Balázsi, Wear mechanism of spark plasma sintered MWCNTs reinforced zirconia composites under dry sliding conditions, Wear 430–431 (2019) 280-289.

[Ref.7.11.] A.S. Racz, D. Zambo, G. Dobrik, I. Lukacs, Z. Zolnai, A. Nemeth, P. Panjan, A. Deak, G. Battistig, M. Menyhard, Novel method for the production of SiC micro and nanopatterns, Surface and Coatings Technology 372 (2019) 427-433.

[Ref.7.12.] E. Mugnaioli, J. Reyes-Gasga, U. Kolb, J. Hemmerlé, É.F. Brés, Evidence of non-centrosymmetry of human tooth hydroxyapatite crystals, Chem. Eur. J. 20 (2014) 6849–6852.

[Ref.7.13.] V.K. Kis, Z. Czigány, Z. Dallos, D. Nagy, I. Dódony, HRTEM study of individual bone apatite nanocrystals reveals symmetry reduction with respect to P63/m apatite. Mat. Sci. Eng. C 104 (2019) 109966.

[Ref.7.14.] R. Astala, M.J. Stott, First-principles study of hydroxyapatite surfaces and water adsorption, Phys. Rev. B 78 (2008) 075427.

[Ref.7.15.] M. Gajdics, T. Spassov, V. Kovács Kis, E. Schafler, Á. Révész, Microstructural and morphological investigations on Mg-Nb2O5-CNT nanocomposites processed by high-pressure torsion for hydrogen storage applications, Int. J. Hydrogen Energy 45 (2020) 7917-7928.

[Ref.7.16.] Á. Révész, T. Spassov, V. Kovács Kis, E. Schafler, M. Gajdics, The influence of preparation conditions on the hydrogen sorption of Mg-Nb2O5-CNT produced by ball milling and subsequent high-pressure torsion, J. Nanoscience Nanotechnology 20 (2020) 4587-4590.

[Ref.7.17.] M. Gajdics, T. Spassov, V. Kovács Kis, F. Béke, Z. Novák, E. Schafler, Á. Révész, Microstructural investigation of nanocrystalline hydrogen-storing Mg-titanate nanotube composites processed by high-pressure torsion, Energies 13 (2020) 563.

[Ref.7.18.] E. Schilirò, F. Giannazzo, C. Bongiorno, S. Di Franco, G. Greco, F. Roccaforte, P. Prystawko, P. Kruszewski, M. Leszczyński, M. Krysko, A. Michon, Y. Cordier, I. Cora, B. Pecz, H Gargouri, R. Lo Nigro: Structural and electrical properties of AlN thin films on GaN substrates grown by plasma enhanced-Atomic Layer Deposition, Materials Science in Semiconductor Processing 97 (2019) 35–39.

[Ref.7.19.] S. Mirzaei, M. Alishahi, P. Souček, L. Zábranský, V. Buršíková, M. Stupavská, V. Peřina, K. Balázsi, Zs. Czigány and P. Vašina, Effects of bonding structure on hardness of fracture resistance of W-B-C coatings with varying B/W ratio, Surface and Coatings Technology 358 (2019) 843-849

[Ref.7.20.] M. Kroker, Zs. Czigány, Z. Weiss, M. Fekete, P. Souček, K. Balázsi, V. Sochora, M. Jílek, P. Vašina, On the Origin of Multilayered Structure of W-B-C Coating Prepared by Non-Reactive Magnetron Sputtering from a Single Segmented Target, Surface and Coatings Tehnology 377 (2019) 124864

[Ref.7.21.] S. Mirzaei, M. Alishahi, P. Souček, J. Ženíšek, D. Holec, N. Koutná, V. Buršíková, M. Stupavská, L. Zábranský, F. Burmeister, B. Blug, K. Balázsi, Zs. Czigány, R. Mikšová, P. Vašina, The effect of chemical composition on the structure, chemistry and mechanical properties of magnetron sputtered W-B-C coatings: Modelling and experiments, Surface and Coatings Technology 383 (2020) 125274

[Ref.7.22.] L. Zábranský, P. Souček, P. Vašina, J. Dugáček, P. Sťahel, J. Buršík, M. Svoboda, R. Mikšová, V. Peřina, K. Balázsi, Zs. Czigány, V. Buršíková, Microstructural changes of amorphous Mo-B-C coatings upon thermal annealing, Surface and Coatings Technology 379 (2019) 125052

[Ref.7.23.] T. Kolonits, Zs. Czigány, L. Péter, I. Bakonyi, J. Gubicza, J, Influence of Bath Additives on the Thermal Stability of the Nanostructure and Hardness of Ni Films, Processed by Electrodeposition. Coatings, 9 (2019) 644.

[Ref.7.24.] G. Sáfrán. Hung. Patent No. P150 050 0 (2015)

[Ref.7.25.] G. Sáfrán, “One-sample concept” micro-combinatory for high throughput TEM of binary films, Ultramicroscopy 187(2018) 50–55.
[Ref.7.26.] T. Lohner, et al. Refractive index variation of magnetron-sputtered a-Si1-xGex by ”One-Sample Concept”, Combinatory. Appl. Sci. 8 (2018) 826.
[Ref.7.27] E. Kotai, Computer methods for analysis and simulation of RBS and ERDA spectra. Nucl. Inst. Meth. B 85, (1994) 588–596.
[Ref.7.28] H.R. Ben Zine, K. Balázsi, C. Balázsi, Effect of the □-Si3N4 addition on the tribological properties of 316L stainless steel prepared by attrition milling and spark plasma sintering, Anyagok Világa (Materials World) 1 (2018) 9-16.
[Ref.7.29.] C. Balázsi, H. R. Ben Zine, M. Furko, Z. Czigány, L. Almásy, V. Ryukhtin, H. Murakami, G. Göller, O. Yucel, F.C. Sahin, K. Balázsi, S. Kobayashi, A. Horváth, Microstructural and magnetic characteristics of ceramic dispersion strengthened sintered stainless steels after thermal ageing, Fusion Engineering and Design 145 (2019) 46-53

[Ref.8.1]. Hódsági and Szabó, Physica A 525 (2019) 1379 and by Király and Szabó, Front. Phys. 8 (2020) 59
[Ref.8.2].A. Szolnoki and M. Perc, Scientific Reports, vol. 9, no. 12575, 2019.
[Ref.8.3] R. Juhász, J. Kelling, and G. Ódor, Critical dynamics of the Kuramoto model on sparse random networks, J. Stat. Mech. (2019) 053403
[Ref.8.4] G. Ódor and J. Kelling, Critical synchronization dynamics of the Kuramoto model on connectome and small world graphs, Scientific Reports 9 (2019) 19621.
[Ref.8.5.] Géza Ódor, Jeffrey Kelling and Gustavo Deco The effect of noise on the synchronization dynamics of the Kuramoto model on a large human connectome graph, arXiv:1912.06018

SEMINAR TALKS IN 2019

2019.02.27 „Merre fejlődik az optikai mikroszkóp méréstechnikai szemszögből?” Agócs Emil (EK MFA)

2019.03.06 „Topologikus, alacsonydimenziós elektronrendszerek vizsgálata” Nemes-Incze Péter (EK MFA)

2019.03.13 "A gép forog, az alkotó pihen(het?)" Hajnal Zoltán (EK MFA)

2019.03.20 „Energiagyűjtővel ellátott vezeték nélküli szenzorhálózatok” Szappanos Miklós (EK MFA)

2019.04.10 „Ferromágneses anyagok roncsolásmentes vizsgálata mágneses hiszterézis alhurkok mérése alapján” Vértesy Gábor (EK MFA)

2019.04.17 „Többkomponensű (HEA) vékonyrétegek növekedési (nano)szerkezete” Radnóczi György (EK MFA)

2019.04.25 „Szerves szennyezőanyagok a vizeinkben és azok lebontása nagyenergiájú ionizáló sugárzással” Tóth Tünde (EK EKBI)

2019.04.30 „Making Graphene Auxetic” Krzysztof W. Wojciechowski (Institute of Molecular Physics, Polish Academy of Sciences, Poznan, Poland)

2019.05.15 „A jövő a felfedezésben: gravitációs hullámok a detektoroktól az asztrofizikáig” Márka Szabolcs (Department of Physics, Columbia University, New York)

2019.05.29 „A kétszínű lepke színeváltozásai” Márk Géza (EK MFA)

2019.06.05 „Mit csinálnak az orvosok a lézerekkel … no meg a betegekkel?” Horváth Zoltán (Wigner SzFI)

2019.06.19 „Egy minta elvű mikrokombinatorika kétkomponensű vékonyrétegek összetétel-függő tulajdonságainak TEM, RBS, XRD, nanoindentációs és ellipszometriás vizsgálatára” Sáfrán György (EK MFA)

2020.07.05 „Metallurgical Phenomena and Hot Cracking Behavior During Welding” Kota Kadoi (Joining and Welding Research Institute, Osaka University)

2019.09.03 „Investigation of optrodes for infrared stimulation in the deep tissue” PhD házivédés, Horváth Ágoston Csaba (EK MFA)

2019.09.04 „Fázisátalakulások evolúciós potenciáljátékokban” PhD házivédés, Király Balázs (EK MFA)

2019.11.06 „Miért zöldek a falevelek?” Márk Géza (EK MFA)

2019.11.13 „Közösségi tragédiát okozó kölcsönhatások és folyamatok az evolúciós játékelméletben” Szabó György (EK MFA)

2019.11.20 „Számítógép által vezért mikropipetta felhasználása biofizikai és kolloidikai kutatásokban” Gerecsei Tamás (EK MFA)

2020.12.04 „Rákos sejtek adhéziójának vizsgálata Epic optikai bioszenzorral: a glikokálix enzimatikus emésztésének hatásai” Kanyó Nicolett (EK MFA)

2020.12.11 „Bioaktív üvegek TEM vizsgálata: nano-skálájú inhomogenitások szerepe a foszfátképződésben” Kovács Kis Viktória (EK MFA)

FULL LIST OF MFA PUBLICATIONS IN 2019

[1] G. Sáfrán, “Berendezés vékonyrétegek mikro-kombinatorikus növesztésére anyagtudományi -elsősorban transzmissziós elektronmikroszkópos- vizsgálatokhoz,” 2019. patent

[2] M. Furko, E. D. Bella, M. Fini, and C. Balázsi, “Corrosion and biocompatibility examination of multi-element modified calcium phosphate bioceramic layers,” MATERIALS SCIENCE & ENGINEERING C-MATERIALS FOR BIOLOGICAL APPLICATIONS, vol. 95, pp. 381–388, 2019.

[3] N. G. Galkin, S. A. Dotsenko, K. N. Galkin, A. M. Maslov, D. B. Migas, V. O. Bogorodz, A. B. Filonov, V. E. Borisenko, I. Cora, B. Pécz, D. L. Goroshko, A. V. Tupkalo, E. A. Chusovitin, and E. Y. Subbotin, “Conductive CaSi2 transparent in the near infra-red range,” JOURNAL OF ALLOYS AND COMPOUNDS, vol. 770, pp. 710–720, 2019.

[4] L. Heuken, M. Alshahed, A. Ottaviani, M. Alomari, M. Heuken, C. Wächter, T. Bergunde, I. Cora, L. Tóth, B. Pécz, and J. Burghartz, “Temperature Dependent Vertical Conduction of GaN HEMT Structures on Silicon and Bulk GaN Substrates,” PHYSICA STATUS SOLIDI A-APPLICATIONS AND MATERIALS SCIENCE, vol. 216, no. 1, 2019.

[5] P. Jenei, C. Balázsi, Á. Horváth, K. Balázsi, and J. Gubicza, “The influence of carbon nanotube addition on the phase composition, microstructure and mechanical properties of 316L stainless steel consolidated by spark plasma sintering,” JOURNAL OF MATERIALS RESEARCH AND TECHNOLOGY, vol. 8, no. 1, pp. 1141–1149, 2019.

[6] P. Sipos, A. Tóth, V. Kovács Kis, R. Balázs, I. Kovács, and T. Németh, “Partition of Cd, Cu, Pb and Zn among mineral particles during their sorption in soils,” JOURNAL OF SOILS AND SEDIMENTS, vol. 19, no. 4, pp. 1775–1787, 2019.

[7] I. Kovács, T. Németh, G. Kiss, V. Kis, Á. Tóth, and Z. Benkó, “Rare aluminium phosphates and sulphates (APS) and clay mineral assemblages in silicified hydraulic breccia hosted by a Permian granite (Velence Mts., Hungary) as indicators of a high sulfidation type epithermal system,” MINERALOGY AND PETROLOGY, vol. 113, no. 2, pp. 217–228, 2019.

[8] N. He, X. Chen, and A. Szolnoki, “Central governance based on monitoring and reporting solves the collective-risk social dilemma,” APPLIED MATHEMATICS AND COMPUTATION, vol. 347, pp. 334–341, 2019.

[9] S. Lamnini, Z. Károly, E. Bódis, K. Balázsi, and C. Balázsi, “Influence of structure on the hardness and the toughening mechanism of the sintered 8YSZ/MWCNTs composites,” CERAMICS INTERNATIONAL, vol. 45, no. 4, pp. 5058–5065, 2019.

[10] M. Németh, G. Sáfrán, A. Horváth, and F. Somodi, “Hindered methane decomposition on a coke-resistant Ni-In/SiO2 dry reforming catalyst,” CATALYSIS COMMUNICATIONS, vol. 118, pp. 56–59, 2019.

[11] S. Mirzaei, M. Alishahi, P. Souček, L. Zábranský, V. Buršíková, M. Stupavská, V. Peřina, K. Balázsi, Z. Czigány, and P. Vašina, “Effect of bonding structure on hardness and fracture resistance of W-B-C coatings with varying B/W ratio,” SURFACE AND COATINGS TECHNOLOGY, vol. 358, pp. 843–849, 2019.

[12] I. Cora, Z. Baji, Z. Fogarassy, Z. Szabó, and B. Pécz, “Structural study of MgO and Mg-doped ZnO thin films grown by atomic layer deposition,” MATERIALS SCIENCE IN SEMICONDUCTOR PROCESSING, vol. 93, pp. 6–11, 2019.

[13] T. Nagyne-Kovacs, A. Malik, A. Szenkovits, I. E. Lukacs, I. M. Szilagyi, and G. Pokol, “Effect of Different Anions Upon the WO3 Morphology and Structure,” JOURNAL OF NANOSCIENCE AND NANOTECHNOLOGY, vol. 19, no. 1, pp. 498–501, 2019.

[14] T. Visnovitz, X. Osteikoetxea, B.W. Sódar, J. Mihály, P. Lőrincz, K. V. Vukman, E. Á. Tóth, I. Székács, R. Horváth, Z. Varga, and E. I. Buzás, “An improved 96 well plate format lipid quantification assay for standardization of experiments with extracellular vesicles,” JOURNAL OF EXTRACELLULAR VESICLES, vol. 8, no. 1, 2019.

[15] Á. Vass, I. Borbáth, I. Bakos, Z. Pászti, G. Sáfrán, and A. Tompos, “Stability issues of CO tolerant Pt-based electrocatalysts for polymer electrolyte membrane fuel cells: comparison of Pt/Ti0.8Mo0.2O2–C with PtRu/C,” REACTION KINETICS MECHANISMS AND CATALYSIS, vol. 126, no. 2, pp. 679–699, 2019.

[16] G. Ódor, “Robustness of Griffiths effects in homeostatic connectome models,” PHYSICAL REVIEW E: COVERING STATISTICAL NONLINEAR BIOLOGICAL AND SOFT MATTER PHYSICS (2016-), vol. 99, no. 1, 2019.

[17] D. Zsuzsa, P. Matjaz, and S. Attila, “Knowing the past improves cooperation in the future,” SCIENTIFIC REPORTS, vol. 9, 2019.
[18] O. Tapasztó, V. Puchy, Z. E. Horváth, Z. Fogarassy, E. Bódis, Z. Károly, K. Balázsi, J. Dusza, and L. Tapasztó, “The effect of graphene nanoplatelet thickness on the fracture toughness of Si3N4 composites,” CERAMICS INTERNATIONAL, vol. 45, no. 6, pp. 6858–6862, 2019.
[19] B. Kalas, E. Agocs, A. Romanenko, and P. Petrik, “In Situ Characterization of Biomaterials at Solid-Liquid Interfaces Using Ellipsometry in the UV-Visible-NIR Wavelength Range,” PHYSICA STATUS SOLIDI A-APPLICATIONS AND MATERIALS SCIENCE, vol. 216, no. 13, 2019.
[20] B. Ferenc, H. Zoltán, B. István, and D. Csaba, “MEMS Microhotplate Constraints,” in Advances in Microelectronics: Reviews, vol. 2, 2019, pp. 49–67.
[21] G. Szabó, I. Borsos, and E. Szombati, “Games, graphs and Kirchhoff laws,” PHYSICA A - STATISTICAL MECHANICS AND ITS APPLICATIONS, vol. 521, pp. 416–423, 2019.
[22] L. Kócs, D. Zámbó, E. Albert, P. Basa, G. Sáfrán, and Z. Hórvölgyi, “Nanoszerkezetű, transzparens bevonatok előállítása kolloidkémiai módszerekkel,” MAGYAR KÉMIAI FOLYÓIRAT - KÉMIAI KÖZLEMÉNYEK (1997-), vol. 125, no. 1, pp. 25–34, 2019.
[23] F. Roccaforte, F. Giannazzo, A. Alberti, M. Spera, M. Cannas, I. Cora, B. Pécz, F. Iucolano, and G. Greco, “Barrier inhomogeneity in vertical Schottky diodes on free standing gallium nitride,” MATERIALS SCIENCE IN SEMICONDUCTOR PROCESSING, vol. 94, pp. 164–170, 2019.
[24] K. Kertész, G. Piszter, Z. Bálint, and L. P. Biró, “Biogeographical patterns in the structural blue of male Polyommatus icarus butterflies,” SCIENTIFIC REPORTS, vol. 9, no. 1, 2019.
[25] A. Zátonyi, G. Orbán, R. Modi, G. Márton, D. Meszéna, I. Ulbert, A. Pongrácz, M. Ecker, W. E. Voit, A. Joshi-Imre, and Z. Fekete, “A softening laminar electrode for recording single unit activity from the rat hippocampus,” SCIENTIFIC REPORTS, vol. 9, no. 1, 2019.
[26] A. Saftics, B. Türk, A. Sulyok, N. Nagy, T. Gerecsei, I. Szekacs, S. Kurunczi, and R. Horvath, “Biomimetic Dextran-Based Hydrogel Layers for Cell Micropatterning over Large Areas Using the FluidFM BOT Technology,” LANGMUIR, vol. 35, no. 6, pp. 2412–2421, 2019.
[27] G. Vértesy, I. Tomáš, B. Skrbek, T. Uchimoto, and T. Takagi, “Investigation of Cast Iron Matrix Constituents by Magnetic Adaptive Testing,” IEEE TRANSACTIONS ON MAGNETICS, vol. 55, no. 3, 2019.
[28] P. Petrik, A. Romanenko, B. Kalas, L. Péter, T. Novotny, E. Perez-Feró, B. Fodor, E. Agocs, T. Lohner, S. Kurunczi, M. Stoica, M. Gartner, and Z. Hózer, “Optical Properties of Oxidized, Hydrogenated, and Native Zirconium Surfaces for Wavelengths from 0.3 to 25 μm − A Study by Ex Situ and In Situ Spectroscopic Ellipsometry,” PHYSICA STATUS SOLIDI A-APPLICATIONS AND MATERIALS SCIENCE, vol. 216, no. 8, 2019.
[29] J. Gubicza, A. Heczel, M. Kawasaki, J.-K. Han, Y. Zhao, Y. Xue, S. Huang, and J. L. Lábár, “Evolution of microstructure and hardness in Hf25Nb25Ti25Zr25 high-entropy alloy during high-pressure torsion,” JOURNAL OF ALLOYS AND COMPOUNDS, vol. 788, pp. 318–328, 2019.
[30] N. Vouroutzis, J. Stoemenos, N. Frangis, G. Z. Radnóczi, D. Knez, F. Hofer, and B. Pécz, “Structural characterization of poly-Si Films crystallized by Ni Metal Induced Lateral Crystallization,” SCIENTIFIC REPORTS, vol. 9, no. 1, 2019.
[31] G. Ódor and B. Hartmann, “A heterogenitások hatásai villamos hálózati modelleken,” FIZIKAI SZEMLE, vol. 69, no. 2, pp. 50–54, 2019.
[32] B. Sánta, Z. Balogh, A. Gubicza, L. Pósa, D. Krisztián, G. Mihály, M. Csontos, and A. Halbritter, “Universal 1/f type current noise of Ag filaments in redox-based memristive nanojunctions,” NANOSCALE, vol. 11, no. 11, pp. 4719–4725, 2019.
[33] E. Bodis, I. Cora, P. Nemeth, O. Tapaszto, M. Mohai, S. Toth, Z. Karoly, and J. Szepvolgyi, “Toughening of silicon nitride ceramics by addition of multilayer graphene,” CERAMICS INTERNATIONAL, vol. 45, no. 4, pp. 4810–4816, 2019.
[34] I. Bakonyi, V. A. Isnaini, T. Kolonits, Z. Czigány, J. Gubicza, L. K. Varga, E. Tóth-Kádár, L. Pogány, L. Péter, and H. Ebert, “The specific grain-boundary electrical resistivity of Ni,” PHILOSOPHICAL MAGAZINE, vol. 99, no. 9, pp. 1139–1162, 2019.
[35] G. Vértesy, A. Gasparics, I. Szenthe, F. Gillemot, and I. Uytdenhouwen, “Inspection of Reactor Steel Degradation by Magnetic Adaptive Testing,” MATERIALS, vol. 12, no. 6, 2019.
[36] G. Piszter, K. Kertész, Z. Bálint, and L. P. Biró, “The structural colors of the Blue butterflies: from sexual signaling to chemically selective vapor sensing,” PROCEEDINGS OF SPIE - THE INTERNATIONAL SOCIETY FOR OPTICAL ENGINEERING, vol. 10965, 2019.

[37] G. Szabó, E. Albert, J. Both, L. Kócs, G. Sáfrán, A. Szöke, Z. Hórvölgyi, and L. M. Mureşan, “Influence of embedded inhibitors on the corrosion resistance of zinc coated with mesoporous silica layers,” SURFACES AND INTERFACES, vol. 15, pp. 216–223, 2019.
[38] E. Dodony, G. Radnoczi, and I. Dodony, “Low temperature formation of copper rich silicides,” INTERMETALLICS, vol. 107, pp. 108–115, 2019.
[39] H. R. Ben Zine, K. Balázsi, and C. Balázsi, “The Effect of the Chemical Composition to the End-Properties of Ceramic Dispersed Strengthened 316L/Y2O3 Composites,” PERIODICA POLYTECHNICA-CHEMICAL ENGINEERING, vol. 63, no. 3, pp. 370–377, 2019.
[40] B. Kovacs and R. Horvath, “Modeling of Label-Free Optical Waveguide Biosensors with Surfaces Covered Partially by Vertically Homogeneous and Inhomogeneous Films,” JOURNAL OF SENSORS, vol. 2019, 2019.
[41] J. Pavo, S. Gyimothy, B. Balint, S. Bilicz, G. Vertesy, and I. Tomas, “Magnetic flux simulation for the inspection of local thinning of ferromagnetic plates,” INTERNATIONAL JOURNAL OF APPLIED ELECTROMAGNETICS AND MECHANICS, vol. 59, no. 4, pp. 1377–1384, 2019.
[42] P. Kun, G. Kukucska, G. Dobrik, J. Koltai, J. Kürti, L. P. Biró, L. Tapasztó, and P. Nemes-Incze, “Large intravalley scattering due to pseudo-magnetic fields in crumpled graphene,” NPJ 2D MATERIALS AND APPLICATIONS, vol. 3, 2019.
[43] F. Riesz, “The effects of the global surface curvature on Makyoh-topogaphy imaging,” PHOTONICS LETTERS OF POLAND, vol. 11, no. 1, pp. 4–6, 2019.
[44] M. Serényi, A. Csík, A. Hámori, B. Kalas, I. Lukács, Z. Zolnai, and C. Frigeri, “Diffusion and reaction kinetics governing surface blistering in radio frequency sputtered hydrogenated a-SixGe1-x ($0 \leq x \leq 1$) thin films,” THIN SOLID FILMS, vol. 679, pp. 58–63, 2019.
[45] L. Kolaklieva, V. Chitanov, A. Szekeres, K. Antonova, P. Terziyska, Z. Fogarassy, P. Petrik, I. N. Mihailescu, and L. Duta, “Pulsed Laser Deposition of Aluminum Nitride Films: Correlation between Mechanical, Optical, and Structural Properties,” COATINGS, vol. 9, no. 3, 2019.
[46] N. Oláh, “Titán-karbid/amorf szén nanokompozit bevonat előállítása és jellemzése,” Szegedi Tudományegyetem, 2019. PhD thesis
[47] K. Balázsi, “Magnetron sputtered TiC/a:C nanocomposite thin films: Deposition parameters vs. properties,” VACUUM, vol. 164, pp. 121–125, 2019.
[48] B. Tegze, E. Albert, B. Fodor, G. Sáfrán, and Z. Hórvölgyi, “Photoinduced processes of adsorbed and associated dye molecules in mesoporous titania coatings,” DYES AND PIGMENTS, vol. 167, pp. 109–119, 2019.
[49] K. Hódsági and G. Szabó, “Bursts in three-strategy evolutionary ordinal potential games on a square lattice,” PHYSICA A - STATISTICAL MECHANICS AND ITS APPLICATIONS, vol. 525, pp. 1379–1387, 2019.
[50] N. Nagy, “Contact Angle Determination on Hydrophilic and Superhydrophilic Surfaces by Using r–θ-Type Capillary Bridges,” LANGMUIR, vol. 35, no. 15, pp. 5202–5212, 2019.
[51] Z. Juhász, E. Dudás, A. Vágó-Zalán, and H. Pamjav, “A simultaneous search for footprints of early human migration processes using the genetic and folk music data in Eurasia,” MOLECULAR GENETICS AND GENOMICS, vol. 294, no. 4, pp. 941–962, 2019.
[52] C. BALÁZSI, K. BALÁZSI, M. FURKO, and T. ZAGYVA, “Korszerű műszaki kerámiák kutatása és ipari alkalmazásai: Si3N4/grafén nanokompozitok,” in XXVII. Nemzetközi Gépészeti Konferencia OGÉT 2019, 2019, pp. 27–30.
[53] E. Schiliro, F. Giannazzo, C. Bongiorno, F. S. Di, G. Greco, F. Roccaforte, P. Prystawko, P. Kruszewski, M. Leszczynski, M. Krysko, A. Michon, Y. Cordier, I. Cora, B. Pecz, H. Gargouri, and N. R. Lo, “Structural and electrical properties of AlN thin films on GaN substrates grown by plasma enhanced-Atomic Layer Deposition,” MATERIALS SCIENCE IN SEMICONDUCTOR PROCESSING, vol. 97, pp. 35–39, 2019.
[54] I. Székács, P. Tokarz, R. Horvath, K. Kovács, A. Kubas, M. Shimura, J. Brasun, V. Murzin, W. Caliebe, Z. Szewczuk, A. Paluch, L. Wojnárovits, T. Tóth, J. S. Pap, and Szyrwiel, “In vitro SOD-like activity of mono- and di-copper complexes with a phosphonate substituted SALAN-type ligand,” CHEMICO-BIOLOGICAL INTERACTIONS, vol. 306, pp. 78–88, 2019.
[55] Z. Fan, B. Jóni, G. Ribárik, É. Ódor, Z. Fogarassy, and T. Ungár, “The Microstructure and strength of a V–5Cr–5Ti alloy processed by high pressure torsion,” MATERIALS SCIENCE AND ENGINEERING A-STRUCTURAL MATERIALS PROPERTIES MICROSTRUCTURE AND PROCESSING, vol. 758, pp. 139–146, 2019.
[56] R. Ungai-Salánki, B. Peter, T. Gerecsei, N. Orgovan, R. Horvath, and B. Szabó, “A practical review on the measurement tools for cellular adhesion force,” ADVANCES IN COLLOID AND INTERFACE SCIENCE, vol. 269, pp. 309–333, 2019.

[57] Ö. C. Boros, Á. C. Horváth, S. Beleznai, Ö. Sepsi, D. Csősz, Z. Fekete, and P. Koppa, “Optimization of an optrode microdevice for infrared neural stimulation,” APPLIED OPTICS, vol. 58, no. 14, pp. 3870–3876, 2019.

[58] E. Schilirò, N. R. Lo, F. Roccaforte, I. Deretzis, M. A. La, A. Armano, S. Agnello, B. Pecz, I. G. Ivanov, R. Yakimova, and F. Giannazzo, “Seed-Layer-Free Atomic Layer Deposition of Highly Uniform Al2O3 Thin Films onto Monolayer Epitaxial Graphene on Silicon Carbide,” ADVANCED MATERIALS INTERFACES, vol. 6, no. 10, 2019.

[59] O. Kéri, L. Kócs, Z. Hórvölgyi, Z. Baji, K. László, V. Takáts, Z. Erdélyi, and I. M. Szilágyi, “Photocatalytically Active Amorphous and Crystalline TiO2 Prepared by Atomic Layer Deposition,” PERIODICA POLYTECHNICA-CHEMICAL ENGINEERING, vol. 63, no. 3, pp. 378–387, 2019.

[60] B. Fodor, “Ellipsometric study of nanostructured silicon materials,” 2019. PhD thesis

[61] J. Gubicza, J. L. Lábár, J. Lendvai, and N. Q. Chinh, “The influence of artificial aging on the microstructure and hardness of an Al–Zn–Mg–Zr alloy processed by equal-channel angular pressing,” JOURNAL OF MATERIALS SCIENCE, vol. 54, no. 15, pp. 10918–10928, 2019.

[62] G. Piszter, K. Kertész, G. Molnár, A. Pálinkás, A. Deák, and Z. Osváth, “Vapour sensing properties of graphene-covered gold nanoparticles,” Nanoscale Advances, vol. 1, no. 6, pp. 2408–2415, 2019.

[63] D. Bazeia, B. F. de Oliveira, and A. Szolnoki, “Invasion-controlled pattern formation in a generalized multispecies predator-prey system,” PHYSICAL REVIEW E: COVERING STATISTICAL NONLINEAR BIOLOGICAL AND SOFT MATTER PHYSICS (2016-), vol. 99, no. 5, 2019.

[64] D. Gregušová, L. Tóth, O. Pohorelec, S. Hasenöhrl, Š. Haščík, I. Cora, Z. Fogarassy, R. Stoklas, A. Seifertová, M. Blaho, A. Laurenčíková, T. Oyobiki, B. Pécz, T. Hashizume, and J. Kuzmík, “InGaN/(GaN)/AlGaN/GaN normally-off metal-oxide-semiconductor high-electron mobility transistors with etched access region,” JAPANESE JOURNAL OF APPLIED PHYSICS, vol. 58, 2019.

[65] G. Kapoor, L. Péter, É. Fekete, J. L. Lábár, and J. Gubicza, “Stored energy in nanocrystalline Ni-Mo films processed by electrodeposition,” JOURNAL OF ALLOYS AND COMPOUNDS, vol. 796, pp. 307–313, 2019.

[66] G. I. Márk, K. Kertész, G. Piszter, Z. Bálint, and L. P. Biró, “Modeling the Reflectance Changes Induced by Vapor Condensation in Lycaenid Butterfly Wing Scales Colored by Photonic Nanoarchitectures,” NANOMATERIALS, vol. 9, no. 5, 2019.

[67] D. Merkel, A. Lengyel, G. Hegedus, C. Bogdan, Z. Horvath, and E. Szilagyi, “Iron self-diffusion in Fe5Ge3 thin film,” MATERIALS RESEARCH EXPRESS, vol. 6, no. 8, 2019.

[68] S. Lamnini, C. Balázsi, and K. Balázsi, “Wear mechanism of spark plasma sintered MWCNTs reinforced zirconia composites under dry sliding conditions,” WEAR, vol. 430–431, pp. 280–289, 2019.

[69] A. S. Racz, D. Zambo, G. Dobrik, I. Lukacs, Z. Zolnai, A. Nemeth, P. Panjan, A. Deak, G. Battistig, and M. Menyhard, “Novel method for the production of SiC micro and nanopatterns,” SURFACE AND COATINGS TECHNOLOGY, vol. 372, pp. 427–433, 2019.

[70] D. Nesheva, P. Petrik, T. Hristova-Vasileva, Z. Fogarassy, B. Kalas, M. Šćepanović, S. Kaschieva, S. N. Dmitriev, and K. Antonova, “Changes in composite nc-Si-SiO2 thin films caused by 20 MeV electron irradiation,” NUCLEAR INSTRUMENTS & METHODS IN PHYSICS RESEARCH SECTION B-BEAM INTERACTIONS WITH MATERIALS AND ATOMS, vol. 458, pp. 159–163, 2019.

[71] R. Juhász, J. Kelling, and G. Ódor, “Critical dynamics of the Kuramoto model on sparse random networks,” JOURNAL OF STATISTICAL MECHANICS-THEORY AND EXPERIMENT, vol. 2019, no. 5, 2019.

[72] T. Nagyné-Kovács, G. Shahnazarova, I. E. Lukács, A. Szabó, K. Hernadi, T. Igricz, K. László, I. M. Szilágyi, and G. Pokol, “Effect of pH in the Hydrothermal Preparation of Bi2WO6 Nanostructures,” MATERIALS, vol. 12, no. 11, 2019.

[73] C. Balázsi, H. R. B. Zine, M. Furko, Z. Czigány, L. Almásy, V. Ryukhtin, H. Murakami, G. Göller, O. Yucel, F. C. Sahin, K. Balázsi, S. Kobayashi, and Á. Horváth, “Microstructural and magnetic characteristics of ceramic dispersion strengthened sintered stainless steels after thermal ageing,” FUSION ENGINEERING AND DESIGN, vol. 145, pp. 46–53, 2019.

[74] H. Liliom, P. Lajer, Z. Bérces, B. Csernyus, Á. Szabó, D. Pinke, P. Lőw, Z. Fekete, A. Pongrácz, and K. Schlett, “Comparing the effects of uncoated nanostructured surfaces on primary neurons and astrocytes,” JOURNAL OF BIOMEDICAL MATERIALS RESEARCH PART A, vol. 107, no. 10, pp. 2350–2359, 2019.

[75] Z. Szabó, J. Volk, Z. E. Horváth, Z. Medveczky, Z. Czigány, K. Vad, and Z. Baji, “Atomic layer deposition and annealing of Ga doped ZnO films,” MATERIALS SCIENCE IN SEMICONDUCTOR PROCESSING, vol. 101, pp. 95–102, 2019.

[76] J. Gubicza, P. T. Hung, M. Kawasaki, J.-K. Han, Y. Zhao, Y. Xue, and J. L. Lábár, "Influence of severe plastic deformation on the microstructure and hardness of a CoCrFeNi high-entropy alloy: A comparison with CoCrFeNiMn," MATERIALS CHARACTERIZATION, vol. 154, pp. 304–314, 2019.

[77] G. Vértesy, A. Gasparics, I. Szenthe, and F. Gillemot, "Magnetic nondestructive inspection of reactor steel cladded blocks," GLOBAL JOURNAL OF ADVANCED ENGINEERING TECHNOLOGIES AND SCIENCES, vol. 6, no. 6, pp. 1–9, 2019.

[78] T. Zagyva, K. Balázsi, and C. Balázsi, "Examination of novel electrosprayed biogenic hydroxyapatite coatings on Si3N4 and Si3N4/MWCNT ceramic composite," PROCESSING AND APPLICATION OF CERAMICS, vol. 13, no. 2, pp. 132–138, 2019.

[79] G. Szenes and L. Tóth, "Basic restrictions for theories of ion-induced track formation: ignored relationships between experimental data," PHYSICA SCRIPTA, vol. 94, 2019.

[80] J.-M. Zuo, J. L. Lábár, J. Zhang, T. E. Gorelik, and U. Kolb, "Electron powder diffraction," in International Tables for Crystallography, 2019, pp. 102–117.

[81] R. Dedoncker, G. Radnóczi, G. Abadias, and D. Depla, "Reactive sputter deposition of CoCrCuFeNi in oxygen/argon mixtures," SURFACE AND COATINGS TECHNOLOGY, vol. 378, 2019.

[82] S. Wang, X. Chen, and A. Szolnoki, "Exploring optimal institutional incentives for public cooperation," COMMUNICATIONS IN NONLINEAR SCIENCE AND NUMERICAL SIMULATION, vol. 79, 2019.

[83] M. Csernai, S. Borbély, K. Kocsis, D. Burka, Z. Fekete, V. Balogh, S. Káli, Z. Emri, and P. Barthó, "Dynamics of sleep oscillations is coupled to brain temperature on multiple scales.," JOURNAL OF PHYSIOLOGY-LONDON, vol. 597, no. 15, pp. 4069–4086, 2019.

[84] S. Lamnini, Z. Fogarassy, Z. Horváth, S. Toth, K. Balázsi, and C. Balázsi, "The role of the attrition milling on the grain size and distribution of the carbon nanotubes in YSZ powders," BOLETIN DE LA SOCIEDAD ESPANOLA DE CERAMICA Y VIDRIO, vol. 58, no. 3, pp. 126–133, 2019.

[85] M. Cardinot, C. O'Riordan, J. Griffith, and A. Szolnoki, "Mobility restores the mechanism which supports cooperation in the voluntary prisoner's dilemma game," NEW JOURNAL OF PHYSICS, vol. 21, no. 7, 2019.

[86] V. K. Kis, Z. Czigány, Z. Dallos, D. Nagy, and I. Dódony, "HRTEM study of individual bone apatite nanocrystals reveals symmetry reduction with respect to P63/m apatite," MATERIALS SCIENCE & ENGINEERING C-MATERIALS FOR BIOLOGICAL APPLICATIONS, vol. 104, 2019.

[87] Á. G. Nagy, J. Kámán, R. Horváth, and A. Bonyár, "Spring constant and sensitivity calibration of FluidFM micropipette cantilevers for force spectroscopy measurements," SCIENTIFIC REPORTS, vol. 9, no. 1, 2019.

[88] C. Balázsi, M. Furkó, F. Szira, and K. Balázsi, "Research on Technical Ceramics and their Industrial Application: Preparation Techniques and Properties of Transparent AlON Ceramics," ACTA MATERIALIA TRANSYLVANICA (EN), vol. 2, no. 1, pp. 7–12, 2019.

[89] D. P. Szekrényes, S. Pothorszky, D. Zámbó, and A. Deák, "Detecting spatial rearrangement of individual gold nanoparticle heterodimers," PHYSICAL CHEMISTRY CHEMICAL PHYSICS, vol. 21, no. 19, pp. 10146–10151, 2019.

[90] M. Kroker, Z. Czigány, Z. Weiss, M. Fekete, P. Souček, K. Balázsi, V. Sochora, M. Jílek, and P. Vašina, "On the Origin of Multilayered Structure of W-B-C Coatings Prepared by Non-Reactive Magnetron Sputtering from a Single Segmented Target," SURFACE AND COATINGS TECHNOLOGY, vol. 377, 2019.

[91] S. Molnar, R. Bohdan, G. Nagy, I. Rajta, L. Illes, A. Csik, and S. Kokenyesi, "Direct surface patterning of amorphous chalcogenide layers with high- energy H+ and He+ ion beams," JOURNAL OF MATERIALS SCIENCE: MATERIALS IN ELECTRONICS, vol. 30, no. 16, pp. 15331–15338, 2019.

[92] M. Furko, Z. Fogarassy, K. Balázsi, and C. Balázsi, "An economic and facile method for graphene oxide preparation from graphite powder," RESOLUTION AND DISCOVERY, vol. 4, no. 1, pp. 21–25, 2019.

[93] I. Rigó, M. Veres, T. Váczi, E. Holczer, O. Hakkel, A. Deák, and P. Fürjes, "Preparation and Characterization of Perforated SERS Active Array for Particle Trapping and Sensitive Molecular Analysis," BIOSENSORS, vol. 9, no. 3, 2019.

[94] T. Gerecsei, I. Erdődi, B. Peter, C. Hős, S. Kurunczi, I. Derényi, B. Szabó, and R. Horvath, "Adhesion force measurements on functionalized microbeads: An in-depth comparison of computer controlled micropipette and fluidic force microscopy," JOURNAL OF COLLOID AND INTERFACE SCIENCE, vol. 555, pp. 245–253, 2019.

[95] N. G. Galkin, K. N. Galkin, A. V. Tupkalo, S. A. Dotsenko, Z. Fogarassi, and B. Pecz, "Ca Silicide Films on Si(1 0 0) and Si(1 1 1) Substrates: Structure, Optical and Electrical Properties," INTERNATIONAL JOURNAL OF NANOSCIENCE, vol. 18, no. 3–4, 2019.

[96] P. Vancsó, Z. I. Popov, J. Petö, T. Ollár, G. Dobrik, J. S. Pap, C. Hwang, P. B. Sorokin, and L. Tapasztó, “Transition metal chalcogenide single layers as an active platform for single-atom catalysis,” ACS ENERGY LETTERS, vol. 4, no. 8, pp. 1947–1953, 2019.

[97] P. B. Barna, D. Biro, M. F. Hasaneen, L. Székely, M. Menyhárd, A. Sulyok, Z. E. Horváth, P. Pekker, I. Dódony, and G. Radnóczi, “Cross sectional complex structure analysis is a key issue of thin film research: A case study on the preferential orientation crossover in TiN thin films,” THIN SOLID FILMS, vol. 688, 2019.

[98] A. Szolnoki and M. Perc, “Seasonal payoff variations and the evolution of cooperation in social dilemmas,” SCIENTIFIC REPORTS, vol. 9, no. 1, 2019.

[99] N. Q. Chinh and G. Sáfrán, “High strength of ultrafine-grained Al–Mg films and the relevance of the modified Hall–Petch-type relationship,” MRS COMMUNICATIONS, vol. 9, no. 3, pp. 1111–1114, 2019.

[100] Z. Czigány, S. Mirzaei, M. Alishahi, P. Soucek, L. Zábransky, V. Buršíková, M. Stupavská, V. Peřina, K. Balázsi, and P. Vašina, “Structure and mechanical properties of hard and tough WBC layers.” 2019.

[101] S. György, B. István, and L. Borbála, “Statistical analyses of cyclic and starlike hierarchical dominances in directed graphs,” PHYSICAL REVIEW E: COVERING STATISTICAL NONLINEAR BIOLOGICAL AND SOFT MATTER PHYSICS (2016-), vol. 100, no. 3, 2019.

[102] S. Márton, P. András, S. Péter, and O. Zoltán, “Anisotropic strain effects in small-twist-angle graphene on graphite,” PHYSICAL REVIEW B, vol. 100, no. 12, 2019.

[103] G. Piszter, K. Kertesz, Z. Balint, and L. P. Biro, “Optical Detection of Vapor Mixtures Using Structurally Colored Butterfly and Moth Wings,” SENSORS, vol. 19, no. 14, 2019.

[104] O. Hakkel, I. Rigo, M. Veres, and P. Furjes, “Microfluidically Integrated SERS Active Cell Trap Array for Sensitive Analysis of Red Blood Cells,” in 20th International Conference on Solid-State Sensors, Actuators and Microsystems and Eurosensors XXXIII, TRANSDUCERS 2019 and EUROSENSORS XXXIII, 2019, pp. 964–967.

[105] G. Nagy, A. Beck, G. Sáfrán, Z. Schay, S. Liu, T. Li, B. Qiao, J. Wang, and K. Lázár, “Nanodisperse gold catalysts in oxidation of benzyl alcohol: comparison of various supports under different conditions,” REACTION KINETICS MECHANISMS AND CATALYSIS, vol. 128, no. 1, pp. 71–95, 2019.

[106] I. Bányász, E. Szilágyi, I. Rajta, G. Nagy, S. Pelli, C. G. Nunzi, S. Berneschi, V. Havránek, V. Vosecek, N. Nagy, Z. Szabó, M. Veres, and A. Speghini, “Fabrication of low loss channel waveguide in tungsten-tellurite glass by 11 MeV carbon ion microbeam for telecom C band,” OPTICAL MATERIALS: X, vol. 4, 2019.

[107] P. Vancso, I. Hagymasi, P. Castenetto, and P. Lambin, “Stability of edge magnetism against disorder in zigzag MoS2 nanoribbons,” PHYSICAL REVIEW MATERIALS, vol. 3, no. 9, 2019.

[108] A. S. Rácz, “Szilícium-karbidban gazdag nano-védőrétegek tervezése és vizsgálata,” 2019. PhD thesis

[109] T. Kolonits, Z. Czigány, L. Péter, I. Bakonyi, and J. Gubicza, “Influence of Bath Additives on the Thermal Stability of the Nanostructure and Hardness of Ni Films Processed by Electrodeposition,” COATINGS, vol. 9, no. 10, 2019.

[110] G. I. Márk, K. Kertész, G. Piszter, Z. Bálint, and L. P. Biró, “First- and second order light scattering processes in biological photonic nanostructures,” in Fundamental and Applied Nano-Electromagnetics II, 2019, pp. 135–150.

[111] L. Zábranský, P. Souček, P. Vašina, J. Dugáček, P. Sťahel, J. Buršík, M. Svoboda, R. Mikšová, V. Peřina, K. Balázsi, Z. Czigány, and V. Buršíková, “Microstructural changes of amorphous Mo–B–C coatings upon thermal annealing,” SURFACE AND COATINGS TECHNOLOGY, vol. 379, 2019.

[112] T. Borbála, A. Emőke, D. Boglárka, M. János, S. György, and H. Zoltán, “Thin layer photocatalysts of TiO2-Ag composites,” STUDIA UNIVERSITATIS BABES-BOLYAI CHEMIA, vol. 64, no. 3, pp. 81–98, 2019.

[113] G. Vértesy, B. Bálint, S. Gyimóthy, and J. Pávó, “INFLUENCE OF THE SIZE OF SAMPLE IN MAGNETIC ADAPTIVE TESTING,” GLOBAL JOURNAL OF ADVANCED ENGINEERING TECHNOLOGIES AND SCIENCES, vol. 6, no. 9, pp. 1–9, 2019.

[114] A. A. Koós, P. Vancsó, M. Szendrö, G. Dobrik, S. D. Antognini, Z. I. Popov, P. B. Sorokin, L. Henrard, C. Hwang, L. P. Biró, and L. Tapasztó, “Influence of Native Defects on the Electronic and Magnetic Properties of CVD Grown MoSe2 Single Layers,” JOURNAL OF PHYSICAL CHEMISTRY C, vol. 123, no. 40, pp. 24855–24864, 2019.

[115] E. Albert, B. Tegze, Z. Hajnal, D. Zámbó, D. P. Szekrényes, A. Deák, Z. Hórvölgyi, and N. Nagy, “Robust Contact Angle Determination for Needle-in-Drop Type Measurements,” ACS OMEGA, vol. 4, no. 19, pp. 18465–18471, 2019.

[116] L. Liu, X. Chen, and A. Szolnoki, “Evolutionary dynamics of cooperation in a population with probabilistic corrupt enforcers and violators,” MATHEMATICAL MODELS & METHODS IN APPLIED SCIENCES, vol. 29, no. 11, pp. 2127–2149, 2019.

[117] S. Rose, P. Nemes-Incze, M. Pratzer, V. Caciuc, N. Atodiresei, and M. Morgenstern, “Protection of one-dimensional Si chains embedded in Pt(111) and protected by a hexagonal boron-nitride monolayer,” SURFACE SCIENCE, vol. 685, pp. 24–33, 2019.

[118] J. Pető, G. Dobrik, G. Kukucska, P. Vancsó, A. A. Koós, J. Koltai, P. Nemes-Incze, C. Hwang, and L. Tapasztó, “Moderate strain induced indirect bandgap and conduction electrons in MoS2 single layers,” NPJ 2D MATERIALS AND APPLICATIONS, vol. 3, no. 1, 2019.

[119] Z. Bálint, G. P. Katona, Z. E. Horváth, K. Kertész, G. Piszter, and L. P. Biró, “High accuracy of color-generating nanoarchitectures is kept in lowland and mountainous populations of Polyommatus dorylas (Lepidoptera: Lycaenidae: Polyommatinae),” ARTHROPOD STRUCTURE & DEVELOPMENT, vol. 53, 2019.

[120] K. Bali, B. Dúzs, G. Sáfrán, B. Pécz, and R. Mészáros, “Effect of Added Surfactant on Poly(Ethylenimine)-Assisted Gold Nanoparticle Formation,” LANGMUIR, vol. 35, no. 43, pp. 14007–14016, 2019.

[121] R. B. Z. HAROUNE, C. S. FILIZ, C. ZSOLT, B. KATALIN, and B. CSABA, “NOVEL SiC DISPERSION STRENGHTENED AUSTENITIC STEELS PREPARED BY POWDER TECHNOLOGY,” ARCHIVES OF METALLURGY AND MATERIALS, vol. 64, no. 4, pp. 1519–1526, 2019.

[122] G. Németh, D. Datz, Á. Pekker, T. Saito, O. Domanov, H. Shiozawa, S. Lenk, B. Pécz, P. Koppa, and K. Kamarás, “Near-field infrared microscopy of nanometer-sized nickel clusters inside single-walled carbon nanotubes,” RSC ADVANCES, vol. 9, no. 59, pp. 34120–34124, 2019.

[123] Z. Scherübl, A. Pályi, G. Frank, I. E. Lukács, G. Fülöp, B. Fülöp, J. Nygård, K. Watanabe, T. Taniguchi, G. Zaránd, and S. Csonka, “Observation of spin–orbit coupling induced Weyl points in a two-electron double quantum dot,” COMMUNICATIONS PHYSICS, vol. 2, 2019.

[124] B. Peter, R. Ungai-Salanki, B. Szabo, A. G. Nagy, I. Szekacs, S. Bosze, and R. Horvath, “High-Resolution Adhesion Kinetics of EGCG-Exposed Tumor Cells on Biomimetic Interfaces: Comparative Monitoring of Cell Viability Using Label-Free Biosensor and Classic End-Point Assays (vol 3, pg 3882, 2018),” ACS OMEGA, vol. 4, no. 6, pp. 10474–10474, 2019.

[125] P. Petrik, A. Romanenko, E. Agócs, B. Kalas, T. Lohner, F. E. Perezné, T. Novotny, and Z. Hózer, “Fűtőelemek cirkóniumburkolatának optikai felületvizsgálata,” NUKLEON, vol. XII, no. 7, pp. 32–35, 2019.

[126] J. Pap, D. Lukacs, M. Nemeth, L. Szyrwiel, L. Illes, B. Pecz, S. Shen, and L. Vayssieres, “Behavior of Cu-Peptides under Water Oxidation Conditions – Molecular Electrocatalysts or Precursors to Nanostructured CuO Films.” 2019.

[127] D. Lukács, M. Németh, Ł. Szyrwiel, L. Illés, B. Pécz, S. Shen, and J. S. Pap, “Behavior of a Cu-Peptide complex under water oxidation conditions – Molecular electrocatalyst or precursor to nanostructured CuO films?,” SOLAR ENERGY MATERIALS AND SOLAR CELLS, vol. 201, 2019.

[128] G. Piszter, K. Kertész, Z. E. Horváth, Z. Bálint, and L. P. Biró, “Reproducible phenotype alteration due to prolonged cooling of the pupae of Polyommatus icarus butterflies,” PLOS ONE, vol. 14, no. 11, 2019.

[129] A. Ballabio, S. Bietti, A. Scaccabarozzi, L. Esposito, S. Vichi, A. Fedorov, A. Vinattieri, C. Mannucci, F. Biccari, Á. Nemcsis, L. Toth, L. Miglio, M. Gurioli, G. Isella, and S. Sanguinetti, “GaAs epilayers grown on patterned (001) silicon substrates via suspended Ge layers,” SCIENTIFIC REPORTS, vol. 9, no. 1, 2019.

[130] K. Bán, M. Nagy, and Z. Fogarassy, “Direct (SEM) and indirect structural analysis of heat affected zone after laser cutting at finemet and metglas alloys,” in 17th Czech and Slovak Conference on Magnetism Book of Abstracts, 2019, pp. 126–126.

[131] D. Zalka, L. Péter, M. El-Tahawy, J. Gubicza, G. Molnár, and I. Bakonyi, “Structure and Giant Magnetoresistance of Co-Fe/Cu Multilayer Films Electrodeposited from Various Bath Formulations,” JOURNAL OF THE ELECTROCHEMICAL SOCIETY, vol. 166, no. 16, pp. D923–D934, 2019.

[132] B. Gyüre-Garami, B. Blum, O. Sági, A. Bojtor, S. Kollarics, G. Csősz, B. Márkus, J. Volk, and F. Simon, “Ultrafast sensing of photoconductivity decay using microwave resonators,” JOURNAL OF APPLIED PHYSICS, vol. 126, no. 23, 2019.

[133] G. Sáfrán, B. Kalas, and M. Serényi, “Determination of the optical properties of a-SixGe1-X facilitated by micro-combinatory,” AIP CONFERENCE PROCEEDINGS, vol. 2186, 2019.

[134] I. Bányász, G. U. L. Nagy, I. Rajta, V. Havránek, V. Vosecek, M. Fried, P. Petrik, E. Agócs, B. Kalas, M. Veres, and R. Holomb, “Swift heavy ion irradiated planar waveguides in a rare earth doped tungsten Tellurite glass and a tungstate crystal,” AIP CONFERENCE PROCEEDINGS, vol. 2186, no. 1, 2019.

[135] Z. Bálint, G. Katona, and K. Kertész, “A new species of Penaincisalia (Lepidoptera: Lycaenidae) from Peru,” OPUSCULA ZOOLOGICA (BUDAPEST), vol. 50, no. 2, pp. 137–144, 2019.

[136] L. P. Biró, K. Kertész, G. Piszter, Z. E. Horváth, and Z. Bálint, “Anyagtudósok kalandozása a biológiában: A lepkék szárnyainak szerkezeti színei,” ACTA MATERIALIA TRANSYLVANICA (HU), vol. 2, no. 2, pp. 69–72, 2019.
[137] L. P. Biró, K. Kertész, G. Piszter, Z. E. Horváth, and Z. Bálint, “Roaming of Materials Scientists in Biology: Structural Colours of Butterfly Wings,” ACTA MATERIALIA TRANSYLVANICA (EN), vol. 2, no. 2, pp. 69–72, 2019.
[138] P. Fürjes, “Controlled focused ion beam milling of composite solid state nanopore arrays for molecule sensing,” MICROMACHINES, vol. 10, no. 11, 2019.
[139] G. Ódor and J. Kelling, “Critical synchronization dynamics of the Kuramoto model on connectome and small world graphs,” SCIENTIFIC REPORTS, vol. 9, no. 1, 2019.
[140] B. Kakasi, T. Gerecsei, B. Kovács, R. Horváth, H. Jankovics, and F. Vonderviszt, “Flagellin-based monolayers with tuneable characteristics for cell adhesion studies.” 2019.
[141] N. G. Husztiné, L. Pap, M. Pósfai, and F. Vonderviszt, “Magnetit-kötő flagelláris filamentumok kötési tulajdonságainak vizsgálata eltérő morfológiájú magnetit nanorészecskékkel.” 2019.
[142] M. Pósfai, P. Pekker, M. Fodor, and F. Vonderviszt, “Interfaces of interest in environmental mineralogy.” 2019.
[143] G. Vértesy, A. Gasparics, I. Uytdenhouwen, and R. Chaouadi, “INFLUENCE OF SURFACE ROUGHNESS ON NON-DESTRUCTIVE MAGNETIC MEASUREMENTS,” GLOBAL JOURNAL OF ADVANCED ENGINEERING TECHNOLOGIES AND SCIENCES, vol. 6, no. 12, pp. 25–33, 2019.
[144] T. Shumilova, N. Maximenko, A. Zubov, N. Kovalchuk, V. Ulyashev, and V. Kis, “Varieties of Impactites and Impact Diamonds of the Kara Meteorite Crater (Pay-Khoy, Russia),” IOP CONFERENCE SERIES: EARTH AND ENVIRONMENTAL SCIENCE, vol. 362, no. 1, 2019.
[145] E. Dodony, I. Dódony, B. Rudd, and G. Z. Radnóczi, “Measuring Diffracted Intensities In TEM.” 2019.
[146] A. R. Temming, G. Dekkers, F. S. van de Bovenkamp, H. R. Plomp, A. E. H. Bentlage, Z. Szittner, N. I. L. Derksen, M. Wuhrer, T. Rispens, G. Vidarsson, and Z. Szittner, “Human DC-SIGN and CD23 do not interact with human IgG,” SCIENTIFIC REPORTS, vol. 9, no. 1, 2019.
[147] Z. Bálint, G. Katona, and K. Kertész, “Description of two new species of the groundstreak genus Arzecla Duarte et Robbins, 2010 (Lepidoptera: Lycaenidae: Theclinae: Eumaeini) from Colombia. Описание двух новых видов рода Arzecla Duarte et Robbins, 2010 (Lepidoptera: Lycaenidae: Theclinae: Eumaeini) из Колумбии.,” CAUCASIAN ENTOMOLOGICAL BULLETIN, vol. 15, no. 2, pp. 367–374, 2019.
[148] A. G. Nagy, J. Kaman, R. Horvath, and A. Bonyar, “Spring constant and sensitivity calibration of FluidFM micropipette cantilevers for force spectroscopy measurements (vol 9, 10287, 2019),” SCIENTIFIC REPORTS, vol. 9, 2019.
[149] C. A. Pintérné, L. Illés, and G. Z. Radnóczi, “Magas hőmérsékleten oxidált cirkónium gyűrűminták elektronmikroszkópos vizsgálatai,” NUKLEON, vol. XII, 2019.
[150] Z. Lábadi, H. Jankovics, P. Szekér, É. Tóth, A. Saftics, B. Kalas, M. Fried, and P. Petrik, “Detection of arsenic in water using bacterial flagellin variants.” 2019.